Transport and Bottom Boundary Layer Observations of the North Atlantic Deep Western Boundary Current at the Blake Outer Ridge

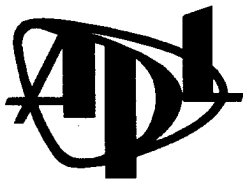by Frederick R. Stahr

19990112 020

Applied Physics Laboratory   University of Washington
1013 NE 40th Street   Seattle, Washington 98105-6698

TRANSPORT AND BOTTOM BOUNDARY
LAYER OBSERVATIONS OF THE NORTH
ATLANTIC DEEP WESTERN BOUNDARY
CURRENT AT THE BLAKE OUTER RIDGE

by

Frederick R. Stahr

A dissertation submitted in partial fulfillment of the
requirements for the degree of

Doctor of Philosophy

University of Washington

1998

Approved by _____
Chairperson of Supervisory Committee

Program Authorized
to Offer Degree   School of Oceanography

Date _____ 13 November 1998 _____

In presenting this dissertation in partial fulfillment of the requirements for the Doctoral degree at the University of Washington, I agree that the Library shall make its copies freely available for inspection. I further agree that extensive copying of this dissertation is allowable only for scholarly purposes, consistent with "fair use" as prescribed in the U.S. Copyright Law. Requests for copying or reproduction of this dissertation may be referred to University Microfilms, 1490 Eisenhower Place, P.O. Box 975, Ann Arbor, MI 48106, to whom the author has granted "the right to reproduce and sell (a) copies of the manuscript in microform and/or (b) printed copies of the manuscript made from microform."

Signature _____

Date _____13 Nov 1998_____

FOREWORD

This report is a duplication of the dissertation submitted in partial fulfillment of the requirements for the Doctor of Philosophy degree at the University of Washington in November 1998. Dr. Thomas B. Sanford was the chairperson of the supervisory committee.

University of Washington

Abstract

TRANSPORT AND BOTTOM BOUNDARY LAYER OBSERVATIONS OF THE NORTH ATLANTIC DEEP WESTERN BOUNDARY CURRENT AT THE BLAKE OUTER RIDGE

by Frederick R. Stahr

Chairperson of the Supervisory Committee:
Professor Thomas B. Sanford
School of Oceanography

The North Atlantic Deep Western Boundary Current (DWBC) was surveyed at the Blake Outer Ridge over 14 days in July and August 1992 to determine its volume transport and to investigate its bottom boundary layer (BBL). This site was chosen because previous investigations showed a strong and bottom-intensified DWBC on the ridge's flanks with a thick BBL. The primary instrument used was the Absolute Velocity Profiler, a free-falling velocity and conductivity-temperature-depth device. Two sections across the width of the current produced volume transports of 17 ± 1 Sv and 18 ± 1 Sv (1 Sv $= 1 \times 10^6$ m^3 s^{-1}) for all water flowing equatorward below a potential temperature of 6°C. Transport values were derived using both absolute velocities and AVP-referenced geostrophic velocities and were the same within experimental uncertainty. Good agreement was found between these results and historical ones when both were similarly bounded and referenced. The mean of a nine-day time series of absolute velocity profiles was the same as the means of year-long current-meter records at three depths in the same location suggesting these observations reflect the mean DWBC. A turbulent planetary BBL was found everywhere under the current. Frictional bottom stress was mostly balanced by an along-stream change in the current's external potential energy evidenced by a change in depth of the velocity core along the ridge. The thickness of the bottom mixed layer (BML) (where density, nutrient, and suspended sediment concentrations are vertically uniform) was asymmetrical across the current and up to five times thicker than the BBL. There was little velocity shear in the BML above the BBL and the across-slope density gradient was minimal. Observations suggest a combination of processes maintains the thick BML including large-scale turbulence, downwelling Ekman transport in the BBL and up-slope return flow in the BML, and buoyant convection into the BML.

Table of Contents

List of Figures

iv

v

List of Tables

List of Abbreviations

AABW: Antarctic Bottom Water

APL/UW: Applied Physics Laboratory, University of Washington

AVP: Absolute Velocity Profiler

BBL: Bottom Boundary Layer

BML: Bottom Mixed Layer

BOR: Blake Outer Ridge

BW: Bottom Water

CTD: Conductivity, Temperature, and Depth

DWBC: Deep Western Boundary Current

LNADW: Lower North Atlantic Deep Water

LSW: Labrador Sea Water

SLSW: Shallow Labrador Sea Water

Preface

This thesis expands on a paper to be published in Deep-Sea Research II (Vol. 46, Issue 2, 1998, in press) by Stahr and Sanford (1998). It also includes and enlarges on material in the Applied Physics Laboratory technical report "R/V *Endeavor* 239: Cruise Report and Preliminary Results", Sanford, *et al.*, 1996.

Acknowledgments

Dedication

This dissertation is dedicated to the memory of my grandfather, Burgess Dempster (1907-1986), and my grandmother Dudley Stahr (1902-1986), who influenced me more strongly than they ever knew.

Chapter 1: Introduction and Motivation

1.1 DWBC Volume Transport and Global Climate

The North Atlantic Deep Western Boundary Current (DWBC) couples the global atmospheric climate to the ocean interior, making it an important component of the global climate system. Formed primarily by high-latitude deep convection, this density-driven current flows south from the Irminger Basin near Greenland along the continental slope of the western Atlantic to the Southern Ocean, where it mixes with Circumpolar Deep Water and spreads throughout the global abyssal basins. The DWBC was first inferred by Wüst (1935) and Iselin (1936), analytically predicted by Stommel (1958), and directly observed by Swallow and Worthington (1961). Because of its role in the climate system, and our lack of knowledge about deep ocean currents, investigations of the DWBC continue in an effort to understand its full nature (Fine, 1995).

Glacial cycles in the planet's climate are reflected in the volume transport of the DWBC, as shown by stable carbon isotope investigations (Mix and Fairbanks, 1985), trace element studies (Lea and Boyle, 1990), faunal analysis (Schitker, 1979), and sediment grain size analysis (Haskell, 1991). A full understanding of the ocean and atmospheric processes that actually control the magnitude and existence of the DWBC is not yet at hand. However, there is evidence that a high surface salinity (>35)[1] in the Greenland, Norwegian, and Icelandic Seas is necessary to maintain the deep convection that fills those basins and, in turn, supplies the DWBC via their deep overflows. The DWBC starts in the Irminger Basin and its magnitude is reasonably stable over long periods, despite the winter-time nature of the deep convection (Dickson and Brown, 1994). During the last deglaciation, after several thousand years of warming, the global climate suddenly returned to glacial temperatures for a 1000 year period known as the Younger Dryas cold event. Analysis of ice cores from Greenland indicates the climate shifted into and out of the Younger Dryas in a very short period, as little as 1–3 years (Alley et al., 1993) or 5–20 years (Taylor et al., 1993). It has been suggested that this sudden global temperature decline was caused by, or at least magnified by, a large

---

[1] Salinities are measured using the unitless 1978 Practical Salinity Scale (PSS-78).

decrease in the volume transport of the DWBC as evidenced through the studies mentioned above. The freshwater flux necessary to change the high-latitude surface salinity and cause a change in DWBC transport may have come from a sudden influx of glacial meltwater via the St. Lawrence drainage, or alternately from a change in a "salt oscillator" operating in glacial times (Broecker, 1990). Whatever the exact causes are, it is apparent from a number of ocean records that the DWBC is weak or non-existent during glacial periods and strong during interglacial periods.

Just as past climate changes have affected the strength of the DWBC, it is likely future ones will also. Manabe and Stouffer's (1994) coupled ocean-atmosphere model indicates that if atmospheric carbon dioxide concentration doubles, the DWBC may cease in 200 years. If the concentration quadruples, the current may stop even more quickly, with a significant decrease in as little as 50 years. Stocker and Schmittner (1997) confirmed these results and their numerical model further tested the climate's sensitivity to the rate of increase and final concentration of atmospheric CO_2. In their model runs, the DWBC experiences a permanent collapse for final concentrations greater than 650 ppm or rate increases greater than 0.5% yr^{-1} . Thus, both observations and numerical models suggest that a significant change in the DWBC volume transport indicates a change in the global climate.

1.2 DWBC Topographic Interaction

Along its path from the North Atlantic to the Southern Ocean, the DWBC encounters seamounts, ridges, and small basins that impede the current and lead to spatial and dynamic complexity. It is also slowed by bottom friction but it persists for the whole length of the Atlantic (~14,000 km). It has been hypothesized that currents like the DWBC continue for such great distances because they create a "slippery" boundary layer for themselves due to the slope they are on (MacCready and Rhines, 1993). This boundary layer reduces, or even eliminates, the effects of bottom friction (Chapman and Lentz, 1997). These currents also have large amounts of available potential energy which may be drawn upon to help overcome bottom friction (MacCready, 1994). Further, it has been suggested that the global vertical diffusivity in the ocean is accounted for by intense mixing in frictional bottom boundary layers at basin edges (Armi, 1978).

The simultaneous observations of velocity, bottom stress, and density within the DWBC presented here are useful to examine these issues.

One of the topographic "impediments" to the DWBC is the Blake Outer Ridge (BOR), also known as the Blake-Bahamas Outer Ridge, which juts out of the continental shelf south of Cape Hatteras and north of the Bahama Islands. It is a sedimentary feature thought to have been formed by the DWBC itself. Over millions of years, the DWBC has deposited sediment here carried from northern sources, although it is unclear whether this process continues at present. The deposition occurred here because this is where the DWBC was slowed by the Florida Current (or Gulf Stream) coming off the continental shelf and crossing over the deeper current. With the slight reduction of speed due to this interaction, the DWBC could not maintain its whole suspended sediment load, so enough dropped out over a long period to form the BOR (Bryan, 1970). One piece of evidence for this is that much of the BOR is red clay from the St. Lawrence drainage. Further, the sediment composition and layering here is one of the pieces of evidence for the connection between climate change and the strength of the DWBC (Heezen et al., 1966; Johnson et al., 1988; Haskell, 1991). It is unclear whether the suspended sediment in the present-day DWBC's bottom boundary layer is depositing on the ridge, or if it has been suspended by erosion from the ridge.

Prior studies show the DWBC has a very thick bottom boundary layer (BBL), particularly at the Blake Outer Ridge. This layer is seen in profiles of temperature, density and suspended particulate (sediment) concentration (Amos et al., 1971; Eittreim et al., 1975; Haskell and Johnson, 1993). However, early studies could not determine if the whole layer was being turbulently mixed because of bottom friction (Amos et al., 1971) or if it was unstratified because of other processes, such as down-slope heat transport and subsequent convection (Eittreim et al., 1975). Most prior deep-ocean bottom boundary layer experiments measured either water properties or velocities, but not both. In order to determine the actual effects of bottom friction on the current and its BBL, a combination of simultaneous velocity, turbulent kinetic energy dissipation, and water property data is necessary.

As the DWBC moves around topographic barriers such as seamounts and ridges, it may break from the continental boundary and join abyssal recirculation gyres. Several studies show recirculation gyres adjacent to the DWBC in abyssal sub-basins

(McCartney, 1992; Schmitz and McCartney, 1993). Attempting to make transport measurements of the DWBC where it interacts with such recirculations can be difficult. This has been demonstrated in the results from a long-term current-meter array off the Bahamas at 26°30'N (McCartney, 1993; Lee et al., 1996). Therefore it is useful to seek places to monitor volume transport that have no recirculation gyres, such as the northeast side of the BOR. The nearest known recirculation gyre is in the Blake-Bahama basin south of the BOR (Leaman and Vertes, 1996).

The ridge may affect the DWBC dynamically as it flows over and around it. One effect that has been observed is the formation of mid-water column (~2000 m) cyclonic eddies traced by floats released east of the ridge during 1973 and entrained by the DWBC as they crossed the tip of the ridge. They were tracked for two years as they moved along the south side of the ridge and past the Bahamas (Riser et al., 1978). Another later experiment started floats south of the BOR to investigate the recirculation gyre in the Blake-Bahama basin (Leaman and Vertes, 1996). These occasionally exhibited cyclonic eddy motion along the Blake Escarpment, but more often showed anti-cyclonic eddies generated as they passed the San Salvador Spur at 24°N, another topographic impediment to the DWBC. To fully examine this type of effect, a spatially large and dense velocity profile survey along the BOR crest and tip would be necessary.

This dissertation reports on a survey specifically designed to address the issues of the DWBC's volume transport, whether or not the bottom boundary layer is "slippery" (i.e., not exhibiting the character and effects of bottom friction), and the cause of the unusually thick bottom mixed layer at the BOR. The methods and some of the resulting high-resolution observations of velocity and water properties are presented in Chapter 2 and several appendices. Transport was determined using both absolute and geostrophic velocity fields and is compared to results from prior studies in Chapter 3. The results of a BBL investigation with simultaneous velocity, turbulent kinetic energy dissipation rate, and water properties measurements is presented in Chapter 4. Chapter 5 summarizes the experiment and results as a whole.

Chapter 2: Methods and Observations

This chapter reports on the design of the experiment, the principal instruments used to gather the data, how they were analyzed, and some of the basic results pertinent to both the transport and bottom boundary layer issues. The appendices provide further details to support this chapter. Observational results relating to specific issues in the context of volume transport and the bottom boundary layer are included in subsequent chapters.

2.1 Experiment Design

Our observations were made over two weeks in late July and early August 1992 from the R/V *Endeavor* as the second half of a two-leg cruise (leg 1 was off Cape Hatteras, see Sanford *et al.*, 1996). We chose to observe the DWBC at the Blake Outer Ridge because it is easily accessible and previous studies show a strong current and large bottom boundary layer there (Amos *et al.*, 1971; Jenkins and Rhines, 1980; Pickart and Smethie, 1993). For the majority of the measurements, especially those for volume transport, we chose the northeast side of the ridge because there was no indication of a recirculation gyre present to confound the results.

The survey pattern for this experiment started with two adjoining sections across the current referred to as Sections 0 and 1 (see Fig. 1). The primary purpose of these sections was to capture the whole width of the current and measure its volume transport, although the data were also used in the bottom boundary layer analysis. Section 0 was distinguished by the fact that the orientation and magnitude of the continental slope under the DWBC changes little in the previous 200 km, so this section served as a comparison to those further downstream where the topography steepens and steers the current. Section 1 was located where the ridge begins to separate from the continental shelf and the current is clearly turning in response to the ridge. We then sampled along the crest of the ridge (Section R) to estimate flow going over it, although the station spacing was too large to accurately measure volume transport.
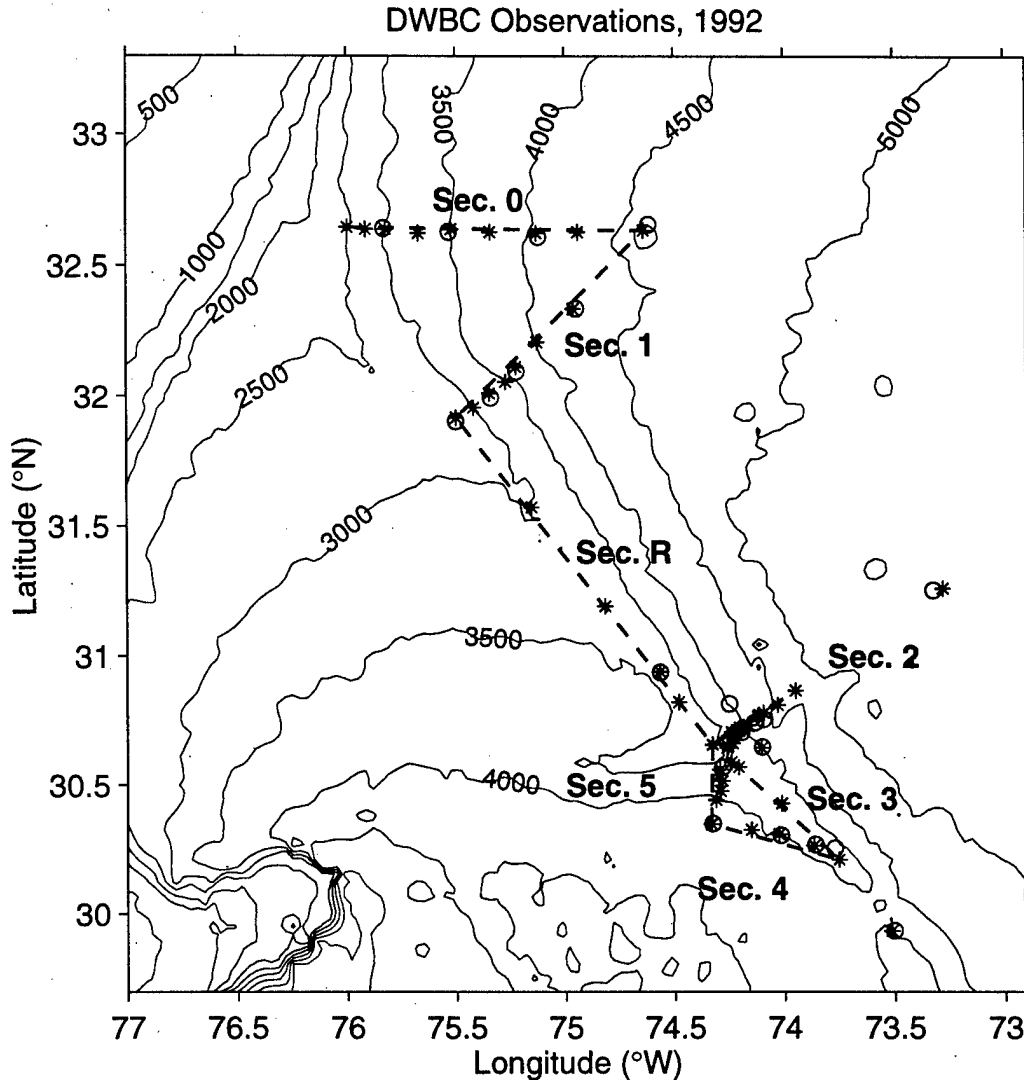
Figure 1: Blake Outer Ridge and locations of observations from R/V *Endeavor* cruise 239 in July–August 1992. Thick dashed lines show sections; (∗) indicates AVP observation and (o) indicates CTD observation. Bathymetry is from Smith and Sandwell (1997); depth is in meters.

Section 2 crossed the current 180 km downstream of Section 1 and was primarily designed to investigate the dynamics of the bottom boundary layer. Its location corresponds to that of a year-long current-meter record (Jenkins and Rhines, 1980) that indicated the DWBC was particularly strong and bottom intensified here. Our stations

along this section were clustered tightly to focus on the BBL but transport was calculated here as well. Sections 3, 4, and 5 were taken adjacent to Section 2 approximately where the 3800–m isobath crosses the ridge. These were intended to examine how the DWBC crossed the ridge crest and formed a return flow along the south side. Appendix A lists the times and locations of all observations shown in Figure 1.

For this experiment, a velocity profiling approach was chosen over fixed current meters for several reasons. One was to cover a large horizontal scale along the ridge on a nearly synoptic time scale with high vertical resolution. Another was to have flexibility during the experiment to change the sampling pattern to best observe moving or developing flow features. This flexibility is demonstrated in the narrative of the chief scientist from the cruise (Appendix B), which helps explain why some of the observations were made when and where they were. One disadvantage of any synoptic survey is a lack of long-term averages. We addressed that deficiency by taking a nine-day time series of measurements at the exact location of a year-long current meter record and comparing the results, as well as by invoking the ergodic hypothesis (i.e., that spatial averages from independent observations may be used to approximate the corresponding temporal averages). The comparison of averages from the time-series and the current-meter record indicates that DWBC velocities during our two week survey were typical of the year-long average.

2.2 Instrument Systems

The principal instruments used for this experiment were the Absolute Velocity Profiler (AVP), a free falling velocity and water-property measuring device, and a standard Conductivity-Temperature-Depth (CTD) and water sampling system. These two systems complemented each other well. They both measured basic water properties (temperature, salinity, and pressure). Additionally, the AVP measured velocity and turbulent kinetic energy dissipation rate while the CTD gathered data on transmissivity, oxygen concentration, and collected water for direct measurements of salinity, oxygen, nutrients and suspended sediments. Operating them on opposite watches (AVP during the day, CTD at night) permitted a more complete synoptic survey by more efficient use of ship-time.

2.2.1 Absolute Velocity Profiler

The Absolute Velocity Profiler (AVP) (Sanford *et al.*, 1985) simultaneously measures absolute horizontal velocity, conductivity, temperature, pressure, and turbulent kinetic energy dissipation rate as it free-falls from the surface to the bottom. The absolute velocity is determined by combining two systems: one electromagnetic and one acoustic Doppler. The electromagnetic system measures relative horizontal velocity from the voltage induced as the instrument and the surrounding water move through the Earth's magnetic field. The acoustic Doppler system measures the instrument's absolute velocity when it nears the bottom. The combination of the two measurements provides the absolute horizontal velocity through the full water column to an accuracy of $\pm$ 1 cm s^{-1} (Elliot and Sanford, 1982). To measure water properties the AVP carries a pumped and ducted Sea-Bird Electronics CTD system with an oxygen sensor. To measure turbulent kinetic energy dissipation rate, a particularly useful value for determining the bed stress in the bottom boundary layer, the AVP has two airfoil-type shear probes of a design similar to that of Oakey (1982) and fabricated at the Applied Physics Laboratory, University of Washington (APL/UW).

The AVP is launched and recovered from the side of a ship (see Fig. 2). It drops through the water at a rate of about 1 m s^{-1} due to weights attached to it with a line ~ 1.5 m long. The weights are released by a simple mechanism when the first one hits the bottom. Syntactic foam under the skin causes the AVP to rise at about 1 m s^{-1}. Accurate velocities are typically obtained to within 5 m of the bottom and water properties to within 3 m due to the location of the various sensors on the instrument and its change in vertical speed after the weights release. The lower end contains most of the sensors, including the acoustic Doppler transceiver array for determining absolute velocity near the bottom. It operates at about 300 kHz, pinging every minute until bottom echoes are strong enough to process then every half second for high-accuracy measurements. The narrow dark band about 1 m up the skin houses the two-axis electric field array that measures the relative velocity throughout the water column. The blades on the upper end cause the AVP to rotate at a period of about 6 s, allowing any electrode offset or drift to be removed. The upper end also contains the launch and recovery hardware. A computer-activated mechanism releases the beach-ball flotation after the ship moves away. A VHF radio transmitter and xenon flasher help locate the instrument after it surfaces. The

sensors at the bottom end of the instrument include the Sea-Bird Electronics temperature and conductivity pair (center of Fig. 3) and the shear probes for sensing turbulent dissipation (tips hang just below the crash cage on right and left in Fig. 3). Also on the bottom end but not visible in Figure 3 are a 10-kHz tracking pinger and an optical backscatter device. The Sea-Bird pump and oxygen sensor are under the skin just above the temperature and conductivity sensors.

Figure 2: The Absolute Velocity Profiler being launched.
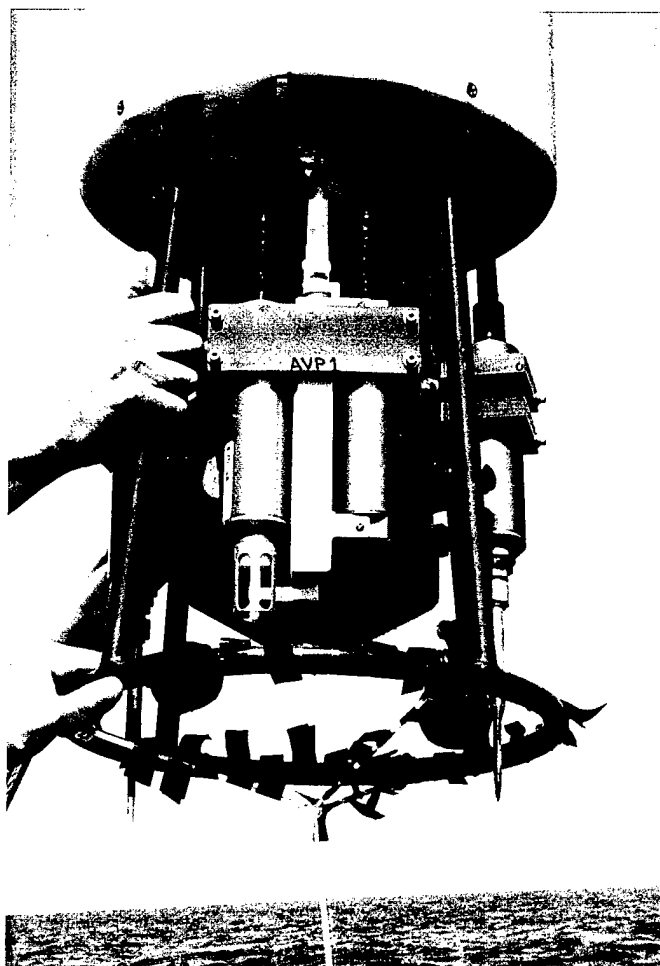
Figure 3: Close up of AVP lower end and sensors.

Originally created in the 1970's, two of these instruments (denominated AVP1 and AVP2) were redesigned and rebuilt for these experiments. New sensors and support electronics were added, old systems were updated, and a new data-acquisition system was installed. The new sensors included the Sea-Bird CTD and oxygen units, a Paroscientific pressure gauge, a D&A Instruments optical backscatter device, and two APL/UW fabricated shear-foil dissipation sensors. The new data-acquisition system is a Tattletale Model 7 microcomputer, which required new circuit boards, extensive rewiring of the backplane, and special programming. The electrode arms were redesigned to include an integral preamplifier so the signal would come into the pressure case after a gain of 500. Only the pressure cases, guard rings, flotation, acoustic Doppler hardware, tilt sensors, and three-axis magnetometers came from the original instruments. Table 1

details the subsystems and sensors contained in the finished product. AVP2 was completed on-board between legs 1 and 2 of the cruise. Because its systems were not as well-calibrated as AVP1, very few of its profiles were used for any of the data analysis. During its fifth deployment, a water leak destroyed much of the internal electronics and rendered it useless for the remainder of the cruise.

Table 1: AVP sensors and systems.

Sensor/System	Manufacturer	Model No.	Sample Rate	Accuracy
Microcomputer	Onset Computers	Tattletale 7	—	—
Pressure	Paroscientific	410KT	24 Hz	2.8 dbar
Temperature	Sea-Bird Electronics	SBE-3	24 Hz	0.002°K
Conductivity	Sea-Bird Electronics	SBE-4	24 Hz	0.0002 S/m
Dissolved oxygen	Sea-Bird Electronics	SBE-23	5 Hz	0.2 ml/l
Optical backscatter	D&A Associates	OBS-3	1 Hz	100 mg/l
Electromagnetic velocity	APL-UW	—	5 Hz	0.002 m/s
Acoustic Doppler velocity	APL-UW	—	2 Hz	0.01 m/s
TKE dissipation rate*	APL-UW	—	2 Hz	factor of 2
Magnetometer	Develco	9200	5 Hz	±18 mG
Tilt	Lucas Schaevitz	LSRP-14-5	5 Hz	0.1°
10-kHz pinger	International Transducer Co.	ITC 3025	once/8 s	—
Radio	NovaTech	RF700A1	1 Hz	—
Xenon flasher	Ocean Applied Research	SF-500	1 Hz	—

* Sensors sampled at 400 Hz, TKE dissipation rate computed from spectra every 0.5 sec.

The AVP measures absolute velocity in the following way (see Sanford *et al.*, 1985, for more details): The voltage between two electrodes on opposite sides of the instrument is determined by a very sensitive voltmeter that completes a circuit through the electrodes

and seawater around the instrument. This voltage is the sum of four parts. The first part is due to the AVP's vertical motion through the horizontal component of the Earth's magnetic field, and the second is due to its horizontal motion through the vertical component of the same field. Both of these voltages are induced along the section of the circuit that forms a line through the center of the instrument. By Faraday's law, the potential V induced across a line of length $\mathbf{l}$ moving through a magnetic field $\mathbf{B}$ at speed $\mathbf{v}$ is given by $V = \mathbf{l} \cdot \mathbf{v} \times \mathbf{B}$. The electrodes are at the same height and on opposite sides of the AVP, so the vector $\mathbf{l}$ is a horizontal line through the center of it. The third part of the voltage is through the circuit line around the outside of the instrument. It arises from the vertically averaged horizontal velocity of the entire water column (i.e., the barotropic flow) moving through the vertical component of the Earth's magnetic field. It is essentially constant with water depth and together with the second part of the voltage corresponds to the horizontal velocity of the instrument relative to the vertically averaged velocity of the water column at any point of the profile. The fourth part of the voltage comes from heterogeneities in the electrodes themselves and from thermosaline differences in the water they encounter and is called the "electrode offset." In summary, the AVP measures the voltage induced by its own motion through the Earth's magnetic field (as driven by the surrounding water and gravity), plus the voltage due to the electric field generated by the horizontal velocity of the whole water column, plus the electrode offset.

In order to separate the voltage due to horizontal velocity of the water from the other voltages, the AVP incorporates three additional features. First, pressure measurements are made to calculate the fall rate of the AVP (about 1 m s^{-1}) so the voltage arising from vertical motion can be determined. We assume the water is not moving vertically, therefore the vertical velocity of the AVP relative to the surrounding water is the absolute fall rate of the instrument. Second, to determine the electrode offset, the AVP rotates about its vertical axis approximately once every six seconds due to flow over the vanes on its upper endcap. The electrode offset is independent of instrument orientation which is measured by an on-board compass. Thus, combining orientation and magnetic field strength data, the electrode offset voltage can be determined. After the fall-rate component and the electrode offset have been removed, the AVP velocity profile still has the depth-independent offset from the motion of the whole water column through the Earth's magnetic field. This velocity offset is determined by comparing the remaining

electromagnetic velocity profile to an absolute velocity profile determined from the acoustic Doppler system. This system echoes 300 kHz pulses off the seafloor producing a profile for 300 m above the bottom. The shapes of these two profiles are typically the same, and the difference between them is the vertically uniform portion of the water velocity. Correcting the electromagnetic (or relative) velocity profile with the acoustic Doppler (or absolute) profile yields an accurate, high-resolution (~2 m) absolute velocity profile over the full water column.

2.2.2 Conductivity-Temperature-Depth and Water Sampling System

We used a standard conductivity-temperature-depth (CTD) package on a wire-lowered cage with a rosette of twelve 5-liter Niskin bottles, a Sea-Bird 911+ CTD system, which was pumped and ducted and had dual temperature-conductivity sensors and an oxygen sensor. The cage also carried a 25-cm Sea-Tech transmissometer and an altimeter so it could be lowered to within 3-5 m of the sea floor (see Table 2). The Sea-Bird system on the CTD cage provided in-situ comparisons for the identical systems on the AVPs, a form of calibration, as well as adding to our data-set in general. Several times during the experiment the temperature-conductivity sensor pair from one of the AVPs was substituted for the secondary pair on the CTD for direct comparison. Pre- and post-cruise factory calibrations were also used, as well as comparing electronic to "bottle" values. The light transmission and oxygen concentration data were used to examine the spatial extent of mixing in the bottom boundary layer.

The water samples captured in the Niskin bottles were used for multiple analyses. We analyzed the water to determine values of dissolved oxygen, nitrate, phosphate, silicate, and salinity. The salinity values from the bottles were used to check the electronic CTD systems. In a similar fashion, the oxygen concentration was used to adjust the parameters in the algorithm for processing the electronic oxygen sensor data. This adjustment provided more accurate oxygen concentration profiles over the full water column. We also filtered the water to capture the suspended sediment for later analysis. This provided information on particulate size and composition through electron microscopy and X-ray fluorescence.

Table 2: CTD sensors and systems.

Sensor/System	Manufacturer	Model No.	Sample Rate	Accuracy
Rosette (12 btls.)	General Oceanics	COM 1015	5 l/btl.	NA
Pressure	Paroscientific	410KT	24 Hz	2.8 dbar
Temperature (qty. 2)	Sea-Bird Electronics	SBE-3	24 Hz	0.002°K
Conductivity (qty. 2)	Sea-Bird Electronics	SBE-4	24 Hz	0.0002 S/m
Dissolved oxygen	Sea-Bird Electronics	SBE-23	5 Hz	0.2 ml/l
Optical backscatter	D&A Associates	OBS-3	1 Hz	100 mg/l
Transmissometer (25 cm)	Sea-Tech Company	TR5025	24 Hz	0.5%
Altimeter	Benthos	2110	2 Hz	0.2 m
12-kHz pinger	(unknown)	(unknown)	1 Hz	NA

2.3 Data Processing and Results

This section concentrates on the processing and results of those parts of the experiment different from standard hydrographic observations. The details of processing temperature, salinity, pressure, oxygen, and nutrient concentrations are covered in Appendix C, "Water Property Measurement Techniques and Calibrations".

2.3.1 Velocity Data

Absolute horizontal velocity measured by the AVP is created by combining the pressure, electromagnetic, acoustic Doppler, magnetometer, and tilt sensor data with the proper calibration parameters in the fashion described in Section 2.2.1 above. The calibration parameters include geometric ones for the spatial relationship of the sensors on the instrument and geomagnetic ones for the latitude and longitude of the observations. With one exception, only data from the down-profile (surface to the bottom) were used in this study because the dynamic characteristics of the whole instrument (spin rate, tilt angles, and vertical speed) were more stable in that direction providing easily processed

and cleaner signals. The exception is that both down- and up-profiles of acoustic Doppler data were used to create the bottom referenced velocity because the averaging helped reduce the noise inherent in that system. This noise arises because the system only produces a data-point every 12 m of travel and the signal processing of the echoes is difficult on sloping bottoms with variable reflection characteristics.

As noted in Table 1, the various sensors and systems produced data at different rates, sometimes dependent on proximity to the bottom (e.g., the acoustic Doppler system). The microprocessor program accounted for this with a special interrupt routine that read the different data channels in a particular pattern when they were ready. It then performed some computations immediately to make the data more compact before writing it to the hard-disk. The program produced a final output data rate of 8 Hz, which was sufficiently high relative to the 1 m s^{-1} vertical velocity to provide good vertical resolution and allow further smoothing in post-cruise processing. More details on AVP data processing can be found in Drever *et al.* (1984). The microprocessor programming and other basic routines were written by John Dunlap and Jane Verrall of the Applied Physics Laboratory, University of Washington.

For the purposes of this dissertation, the 8 Hz data were gridded to 2 Hz (~0.5 m in the vertical). Then the absolute velocity profiles were filtered with a 12 m boxcar window to further remove noise from instrument rotation. Finally, the profiles and other data were gridded to 2 m for general purpose use, starting at 20 m depth and getting as close to the bottom as possible (typically 3-5 m) without using poor quality velocity data.

A density field could be constructed between any two AVP drops because it also sampled water properties. As with regular hydrographic data, the density field can be related to the velocity normal to a line between the drops by the geostrophic approximation integrated in x from drop A to drop B with the result expressed as

$$\rho^B(z) - \rho^A(z) = (-\rho_0(z)/g) \; (x^B - x^A) f \, v_z(z) \,,$$

where $v_z(z)$ is the vertical shear of the normal flow averaged between drops. Down-profile density data were used to construct surface-relative geostrophic profiles on all sections. These profiles were then referenced to the mean absolute velocity profile between the depths of 1300 and 2400 m. This depth range was chosen because it was

below the main thermocline and the magnitude of the velocity shear was usually low. The average difference between the geostrophic and absolute reference profile was used as an offset for the whole geostrophic profile. The geostrophic profiles were extrapolated to the bottom by assuming a constant velocity shear below the last valid measurement point on the shallowest profile.

To make smooth profiles of absolute velocity to compare to geostrophic ones and to construct contour plots, the absolute profiles were filtered with a 300 m Bartlett window. This window length was chosen by comparing the mean vertical shear of the geostrophic profiles with the mean vertical shear of filtered absolute profiles for various filter lengths. On average, a 300 m filter created absolute profiles with a mean shear close to that of the geostrophic profiles and usually no more than 1.5 times greater than the geostrophic shear. Figure 4 shows an example of the absolute velocity filtering scheme and geostrophic velocity profile for two AVP drops (445 and 446 from Section 1) that were taken 14 km and 3.7 hours apart. Each absolute profile is shown at 2 m resolution (the jagged blue and green lines) and with the 300 m filter (thick line of same color). The reference velocity that was constructed from these between 1300 and 2400 m is shown as a black dashed line, and the referenced geostrophic velocity profile is the red line. The difference between the geostrophic and absolute velocities is a function of ageostrophic effects, such as internal waves, that are most prevalent above the main thermocline. In the lower water column, where we measured the DWBC transport, the profiles are similar.

In an attempt to improve the overall quality of the velocity field for transport calculations, a Kalman filter technique was explored as a means to combine the absolute and geostrophic velocities. If absolute velocity profiles are used alone to determine transport, it is necessary to assume they represent a laterally smooth velocity field and are not aliased by lateral variations. Alternately, geostrophically computed velocity profiles are lateral averages, but each profile is uncertain to within a constant. The combination of the two types of profiles should provide a more robust velocity field because the local nature of the absolute profiles will complement the spatially averaged character of geostrophic profiles. Also, they are nearly independent and simultaneous observations (velocity and density) with uncorrelated errors. Each data set partially compensates for deficiencies in the other such that the combination should be more accurate than the arithmetic mean of the two.

Velocity Profiles, AVPs 445 (blue) & 446 (green)
Dist. between: 14.0 km, Time between: 3.7 hrs.

Velocity (m s⁻¹), Absolute (blue & green)
Geostrophic (red), Ref. for geos. (—)
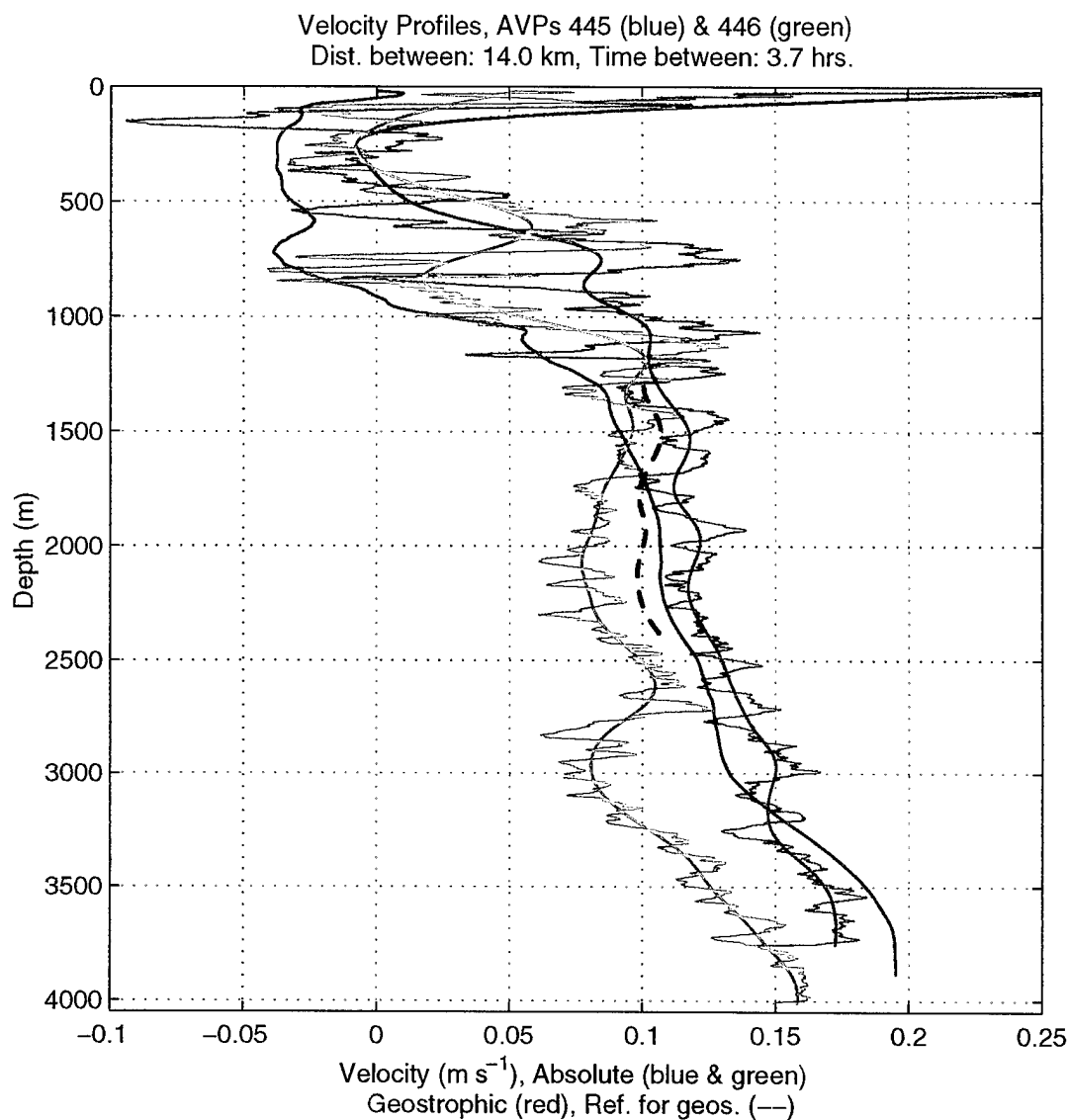
Figure 4: Absolute velocity profiles drop 445 and 446 with smoothed versions and associated geostrophic and reference profile.

The Kalman filter formulation was a least-squares-fit type combination of the two velocities weighted with uncertainties related to each data set. It used the geostrophic approximation with density and the directly measured velocity on pairs of AVP drops. The principal uncertainties were from direct measurements of vertical and lateral shear and

the curvature of the flow. In the deep part of the water column where the DWBC was being measured for transport, the Kalman filter results were little different than either the geostrophic or absolute velocity profiles. Because of this similarity and a desire to report both results, the transport was calculated from each velocity field separately. The Kalman filter combination may have advantages in more general situations because it provides an optimized velocity field based on expected uncertainties in each data set.

2.3.2 Turbulent Kinetic Energy Dissipation Rate

The two airfoil shear probes on the AVP measure the dissipation rate of turbulent kinetic energy (ε) just ahead of the instrument (see Fig. 4). They are mounted at a tilt to point into the flow as the AVP spins on its axis. John Toole designed the basic probes based on work by Neil Oakey (1982). Shear probe data were collected only during the last 2000 m of the down-profiles because we were interested primarily in the bottom boundary layer and the data occupied significant disk space. There are two probes because they are often subject to noise that does not affect both probes simultaneously, such as plankton hits or the wake of the drop weights.

The conversion of raw data to values of ε (in W kg^{-1} or m^2 s^{-3}) was developed by John Dunlap following the work of Mike Gregg for the Advanced Microstructure Profiler. The dissipation rate is calculated by integrating the shear spectrum from the probes between 2 and 10 cycles per meter. The shear spectra are assumed to be in the shape of the universal turbulent shear spectra of Panchev and Keisch (1969) and the data are low-pass filtered to eliminate high-frequency noise from the instrument. The processing used the parameters of fall rate and probe calibration, combining these with the dynamic responses of the probe and circuitry to yield final values of dissipation rate in the range of 10^{-10} to 10^{-5} m^2 s^{-3}, adequately covering what we expected in a deep ocean bottom boundary layer.

In general, our signals were fairly noisy with standard deviations of up to half an order of magnitude around the mean. In many drops, the two probes exhibited apparently different mean levels of background dissipation (i.e., the dissipation in regions of the drop away from the bottom). Our data typically had a noise floor of between 10^{-8} and

10^{-9} m^2 s^{-3}, which is higher than turbulence detected in the main thermocline (Gregg, 1987). Part of this noise likely comes from the probes passing through the turbulent wake produced by the drop weights ahead of the vehicle. Also, some combinations of amplifiers and probes produced above-average levels of electronic noise. Despite this noise floor, we expected (and found) dissipation levels several orders of magnitude higher in the bottom boundary layer, reaching values as high as 10^{-6} m^2 s^{-3}. Dissipation profiles were eliminated from further analysis if the mean background level was more than one order of magnitude greater than that of the other probe on the same drop or it showed no response in the BBL where the other probe did. Figure 5 shows data from the both probes on AVP drops 435 and 438. Using the above criteria, the data from channel 2 of AVP 435 were eliminated while both channels of AVP 438 were retained. Note the increased level of dissipation rate in the bottom boundary layer (20-30 m above the bottom), averaging about 10^{-7} m^2 s^{-3}. The bottom mixed layer was 78 m thick for AVP 435 and 164 m thick for AVP 438, but the shear probes showed no change in dissipation rate at those heights above the bottom.
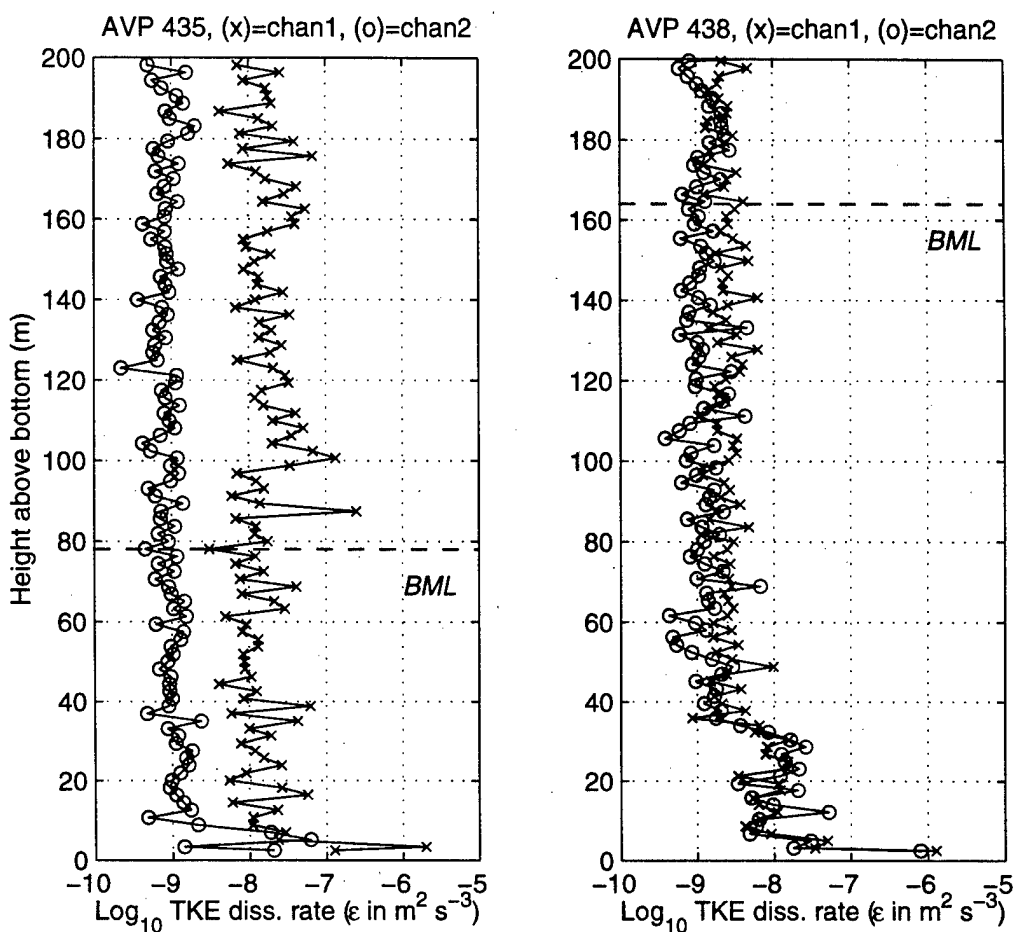
Figure 5: TKE dissipation rate (ε) for AVPs 435 and 438 (Section 0). Dashed lines mark top of Bottom Mixed Layer.

2.3.3 Suspended Sediment Analysis

In prior observations at the BOR, thick near-bottom nepheloid layers consisting of suspended sediments were found (Eittreim *et al.*, 1975). Knowing the BOR is a sedimentary feature, we attempted to measure sediment flux at the ridge by combining our velocity measurements with simultaneous measures of suspended sediment concentration. The ridge may be growing from sediment deposited by the DWBC, or shrinking because the strong current resuspends deposited sediments and transports them off the ridge. Of course, the sediment suspended in the bottom mixed layer could be neither falling out nor from local resuspension. It may simply accumulate from the water column above or have

been transported with the current as remnants of benthic storms further north in the DWBC (Gardner and Sullivan, 1981).

To measure flux, we attempted to measure velocity and the suspended sediment concentration simultaneously in the DWBC by attaching an optical backscatter device (OBS) to the AVP. In order to calibrate the OBS, we also mounted it to the CTD cage, which carried a 25-cm transmissometer and provided direct water sampling from which the sediments could be filtered. Unfortunately, the OBS failed to provide useful data because modifications made to detect the concentrations expected at the BOR were inadequate and the extreme pressure cycling broke the transducer element. Further, the planned analysis of the filtered samples for concentration values was unsuccessful due to inadequate filter pre-weighing procedures (see Appendix C). However, the filtered material was used for a particle size analysis, and the transmissometer on the CTD cage provided useful data (see Fig. 6) that were converted to sediment concentration values with information from a prior investigation at the BOR (Haskell and Johnson, 1993). Because the velocity survey could not be well connected to the sediment concentrations, no flux calculations were undertaken.
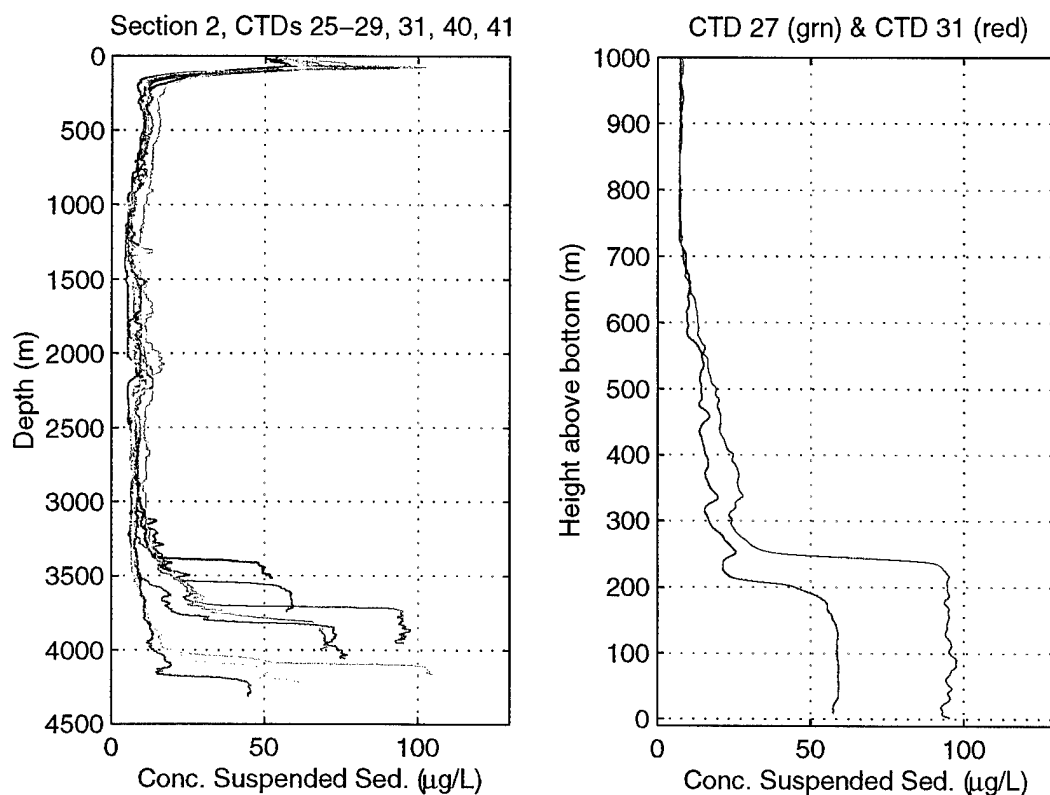
Figure 6: Profiles of suspended sediment concentrations for Section 2.

The suspended sediment in the bottom mixed layer acts as a tracer of mixing processes there. Because it settles out at a rate dependent on its effective diameter and density, it can be a tracer of the upward vertical velocity necessary to keep it suspended. For this reason, a size and composition analysis was pursued on some of the filtered samples from within the BML. These were first examined by X-ray fluorescence (XRF) to determine mineral composition and then by scanning electron microscope (SEM) and to determine the mean size and distribution of the suspended sediment. These filters were primarily from the center of the current where the transmissometer showed high suspended sediment concentrations through the whole BML in CTDs 22 (Section 1), 26, and 27 (Section 2). The size analysis was performed by imaging five random locations on each filter (typically about 400 particles per image), digitizing each image and analyzing it to determine size and shape of the particles. This showed that, on average, the particles were 1 μm in effective diameter (Waddell diameter) from top to bottom of the BML and on both sections. The XRF analysis also showed no spatial pattern to the material and

that it was primarily silica, calcium, and aluminum. The images showed mud grains and diatom tests, many of which were broken or partially dissolved (see Fig. 7). The only organic-looking matter seen were sparse patches of bacterial mats in small areas of two filters.

The size and composition analysis of the filtered sediment samples suffers one significant drawback in helping determine dynamics within the BML. The particles on the filters are mostly disaggregated because of the filtering process itself and therefore do not accurately reflect the mean in-situ particle diameters and distribution. It is common in abyssal nepheloid layers such as these to have effective particle diameters of several hundred microns due to aggregation, with associated higher settling velocities (R. Sternberg, personal communication). The resulting uncertainty this raises will be further discussed in Chapter 4.

The nature of the surface sediment below the DWBC was examined to address the issue of local deposition or resuspension. On its last drop, AVP2 hit the bottom and returned with a small amount of mud on its shear probes. This was saved and analyzed for size in a Sequoia Scientific Lab-LISST particle analyzer and for composition by XRF. The size distribution peaked at about 2.5 μm, but the minimum detection limit for the Lab-LISST is 1.2 μm. The XRF analysis showed mineral ratios similar to those for the suspended samples. This single sample hardly represents the whole area, but the similarity to the suspended analysis results suggests that the bottom sediment is similar to the suspended sediment. Haskell (1993) conducted an extensive study of surface sediments on the Blake Outer Ridge and found a size distribution peaked at about 11 μm from surface box cores, although his analysis technique included only particles in the size range 6 to 70 μm. These cores also showed slow sedimentation rates and significant bioturbation. Bottom photographs from the flanks of the ridge revealed a smooth sea floor with crag and tail lineations indicating strong abyssal flow.

Particle sizes can be used in a diagram of curves, such as that provided by McCave (1984a), which relate suspended sediment transport and deposition regimes to particle size and bottom friction velocity (defined as $u_* = \sqrt{\tau/\rho}$, where τ is bottom stress and ρ is density). The diagram shows that for 1 μm diameter particles, a u_* of at least 0.3 cm s^{-1} is necessary to keep them suspended, while 11 μm diameter particles need a u_* of at least

0.7 cm s^{-1}. We observed an average u_* of about 1.0 cm s^{-1} close to the bottom in the highly turbulent BBL and about 0.3 cm s^{-1} above that in the more weakly turbulent part of the BML (see Chapter 4 for details). Unfortunately, curves that accurately represent erosion regimes for values of u_* versus particle size are not available. As mentioned before, it is not necessary to invoke local resuspension to have high suspended sediment concentrations in the BML. Detritus constantly falls from the surface zone and raises suspended concentrations in the region 1000 m above the sea floor with the highest concentration in the BML. The shape of the curve above the BML is typically logarithmic and profiles like those shown in Figure 6 have been found in many deep ocean observations, including areas outside strong currents (McCave, 1986).
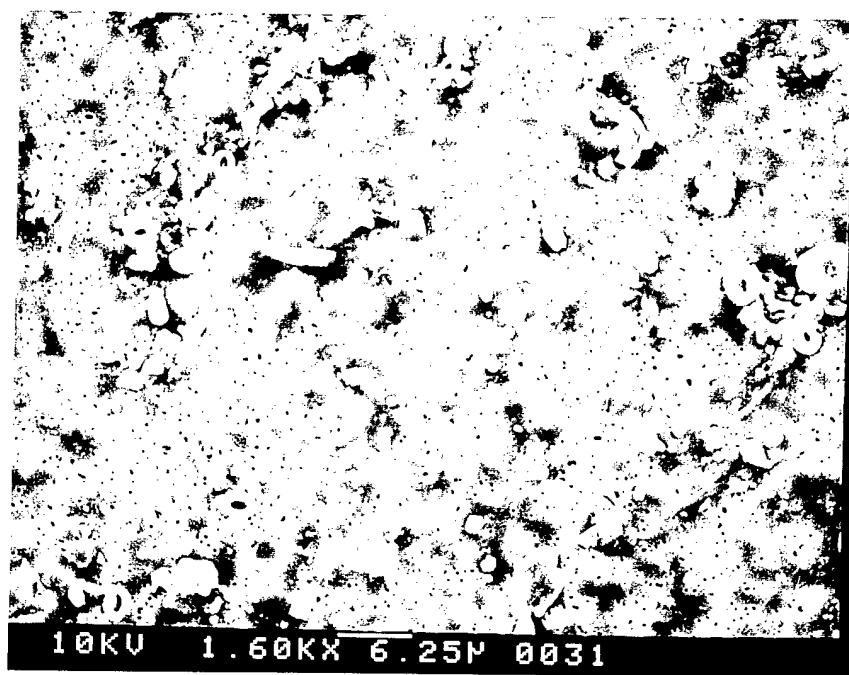
Figure 7: Scanning electron microscope photograph of a filter from CTD 22. The sample was taken 100 m above bottom where the transmissometer measured 86 μg l^{-1} concentration. Image magnification is 1600x; note the 6.25 μm scale bar at the bottom of the frame. Filter holes are the small black shapes (average size 0.4 μm) sediment is the white shapes (average size 1 μm).

Chapter 3: Volume Transport

3.1 Transport Results

Volume transport is the integral of a current's velocity over a defining area and is typically derived from a line of observations forming a synoptic section. In this survey it was determined by combining simultaneous velocity and density measurements from the AVP across each section. Potential temperature levels and flow direction defined the DWBC boundaries and therefore area. Velocity fields were generated from both directly measured absolute profiles and geostrophic profiles constructed from density data and referenced to the absolute velocities. Except for the pressure data and the reference velocity applied to the geostrophic profiles, the two velocity fields were independent of one another, thus providing independent transport values. In general, the reference velocities averaged about 4 cm s^{-1}. This value is not insignificant relative to the mean velocity of the current (~7 cm s^{-1}) and indicates the importance of using a good absolute velocity reference with geostrophic profiles when measuring the transport of the DWBC.

The water being carried by the DWBC was split into four principal water masses labeled (from shallowest to deepest) Shallow Labrador Sea Water (SLSW), Labrador Sea Water (LSW), Lower North Atlantic Deep Water (LNADW), and Bottom Water (BW). They were distinguished by potential temperature (θ) ranges which were based partly on definitions from prior studies and partly on our dissolved-oxygen data (see Fig. 8). These ranges, and the approximate equivalent in potential density (σ_3) and depth, are given in Table 3. We lacked measurements of anthropogenic tracers, specifically CFC-11, that have been used in the past to define the core of the current.

The shallowest category, SLSW, consisted primarily of water from the upper part of the Labrador Sea formed along the western boundary (Pickart *et al.*, 1997). Previous studies found elevated CFC concentrations in this water mass at the BOR (Johns *et al.*, 1997; Pickart and Smethie, 1993). In the next deeper category, LSW, our data showed elevated oxygen concentrations but not the maximum (see Fig. 8). The third category, LNADW, exhibited the highest oxygen concentration below the main thermocline. The

potential density boundaries for this class were the same as those selected by Pickart and Smethie (1993) for their study of how the Gulf Stream crosses over the DWBC. LNADW originates in high latitude overflows such as the Denmark Strait and is considered the original element of the DWBC.

Our deepest category, BW, was included in the transport analysis because it contained the highest DWBC velocities. However, it constituted only about 15% of the overall transport owing to its small area. It had lower oxygen but higher silicate concentrations than the LNADW above it, indicating it was a mixture of LNADW and Antarctic Bottom Water (AABW) which is high in silicate from its source region. Our temperature-salinity data for the LNADW and BW categories fell directly on top of those Amos et al. (1971) observed southeast of our Section 2, indicating our BW consisted of 10–16% AABW as they found for their data. The DWBC creates a thick bottom mixed layer along the flanks of the BOR possibly entraining AABW from the adjacent Hatteras Abyssal Basin to raise the silicate concentrations in the BW. If this were the case, an increase in silicate concentration along-stream (i.e., from Section 0 to 1 to 2, etc.) might be expected. However, our samples in the DWBC showed no such increase, suggesting the LNADW and AABW that form BW mixed somewhere north of Section 0 (see Fig. 9).

The contoured velocity fields and potential temperature boundaries used to calculate transport are shown in Figures 10 and 11. A 300-m vertical filter was applied to each absolute profile to obtain smooth contours. The reference for the geostrophic velocities was derived by minimizing the rms difference between the geostrophic profile and the mean of adjacent absolute profiles between depths of 1300 and 2400 m (e.g., see Fig. 4). This depth interval was chosen because it is below the main thermocline and the velocity is typically closer to zero than in any other part of the profile; this most closely corresponds to the level of no motion used in previous studies. Geostrophic velocities were extrapolated in the bottom triangles by maintaining a constant velocity shear from the deepest valid observations. The absolute velocity measurements typically reached within 5 m of the bottom.

Table 3: Limits and characteristics of water masses used for DWBC transport calculations.

Water mass	Pot. Temp. Range	Approx. Pot. Density Range	Approx. Depth (m)
SLSW	$6° > \theta \geq 4°C$	$41.00 < \sigma_3 \leq 41.27$ kg m^{-3}	1000–1800
LSW	$4° > \theta \geq 2.8°C$	$41.27 < \sigma_3 \leq 41.44$ kg m^{-3}	1400–2800
LNADW	$2.8° > \theta \geq 1.9°C$	$41.44 < \sigma_3 \leq 41.55$ kg m^{-3}	2500–4100
BW	$\theta < 1.9°C$	$\sigma_3 > 41.55$ kg m^{-3}	3400–bottom
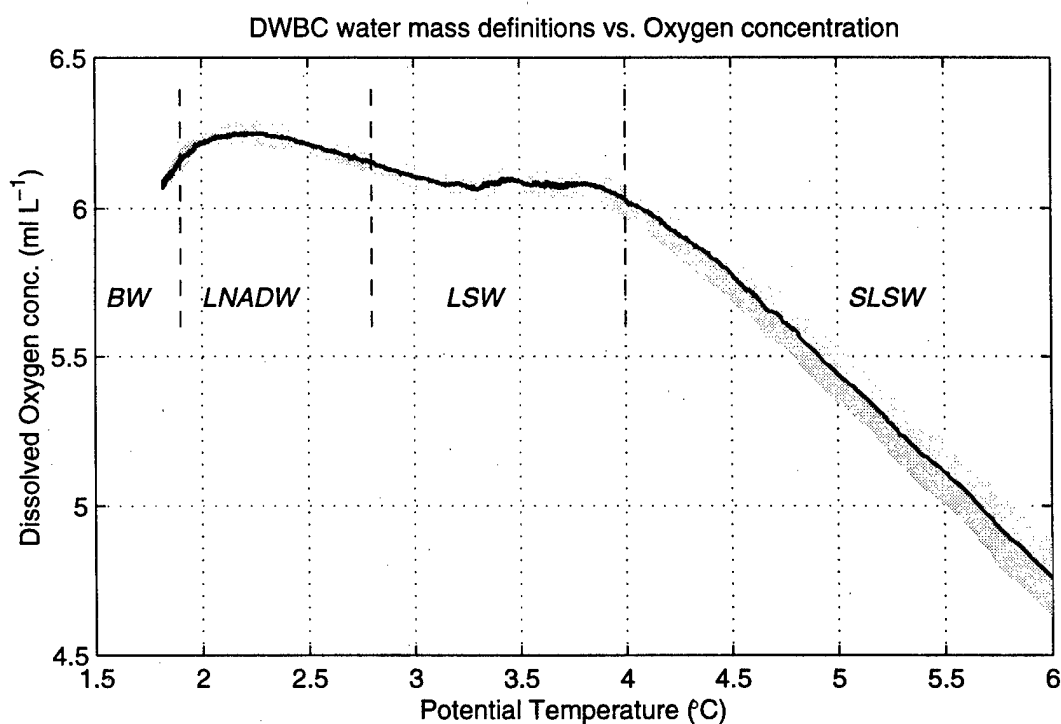
Figure 8: Water mass categories used in volume transport calculations as defined by observed potential temperature versus oxygen concentration. The heavy line is the mean for all casts; the gray area is two standard deviations around the mean. Data were collected by a SBE 911+ CTD system with a Model 23 oxygen sensor calibrated by water sample analysis.
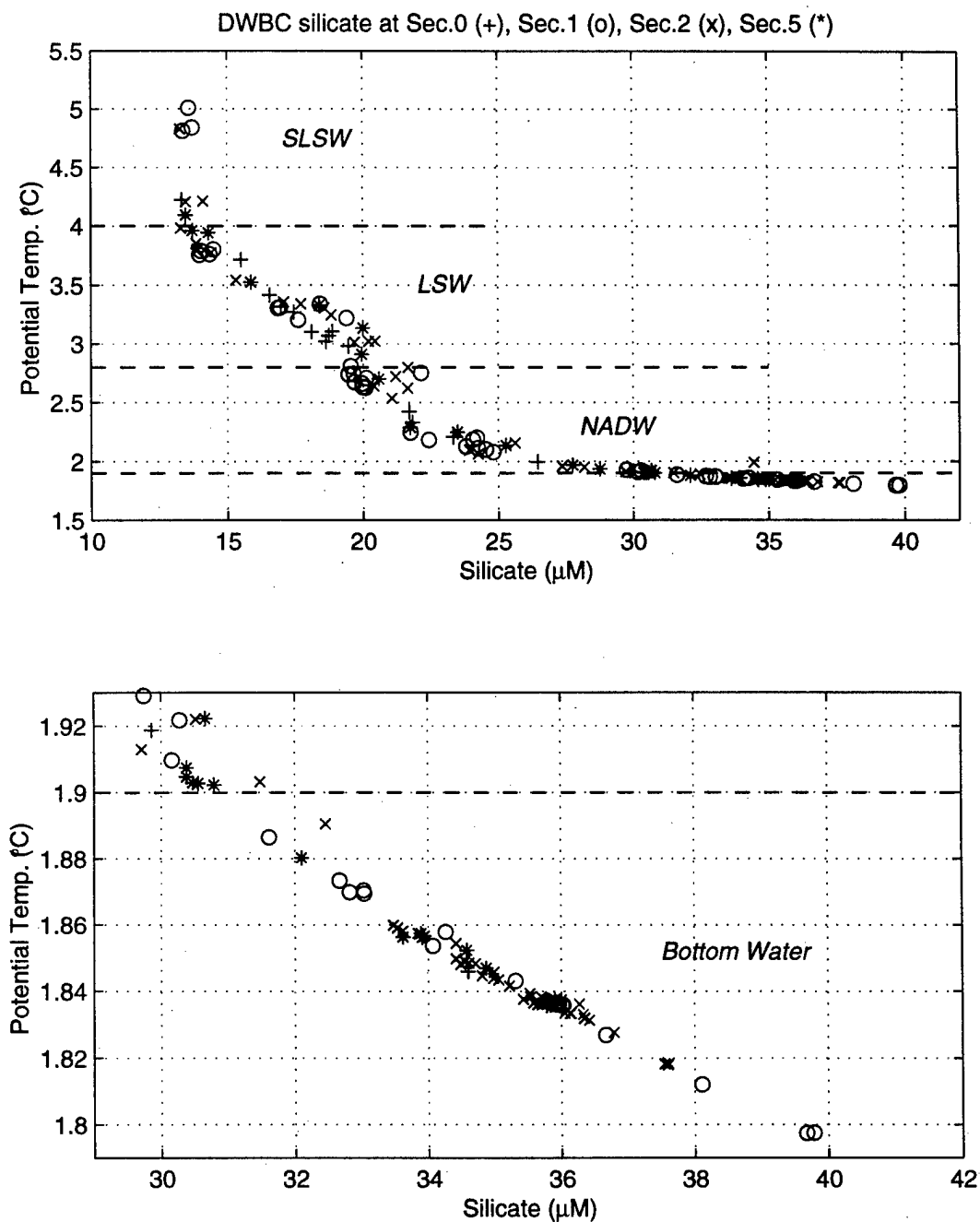
Figure 9: Silicate versus potential temperature distribution by section. The upper panel shows all DWBC water masses. The lower panel contains an expanded scale for Bottom Water.

Figure 10: Contours of the absolute velocity component normal to the sections and potential temperature. Contour intervals are every 2 cm s^{-1} with the 0 and ± 10 cm s^{-1} intervals labeled. The coordinate system is along-stream with positive flow equatorward. Potential temperature contours that divide transport categories are labeled to the right of each panel. The height of the bottom mixed layer is indicated by the dashed line near the bottom. AVP drop numbers are indicated at the top of each panel, with the leading digit (4) removed; in Section 2, some labels have been removed for clarity. Panel (a) is Section 0, (b) is Section 1, (c) is Section 2, and (d) is Section R. Panel (e) is a small version of Fig. 1 to clarify section locations.

a) Section 0, Absolute Velocity & Pot. Temp. Contours

b) Section 1, Absolute Velocity & Pot. Temp. Contours

Distance across–slope (km)

c) Sec. 2, Abs. Vel.

Velocity (cm/s)

e)

Longitude (°W)

d) Section R, Absolute Velocity & Pot. Temp. Contours

Distance along Ridge (km)
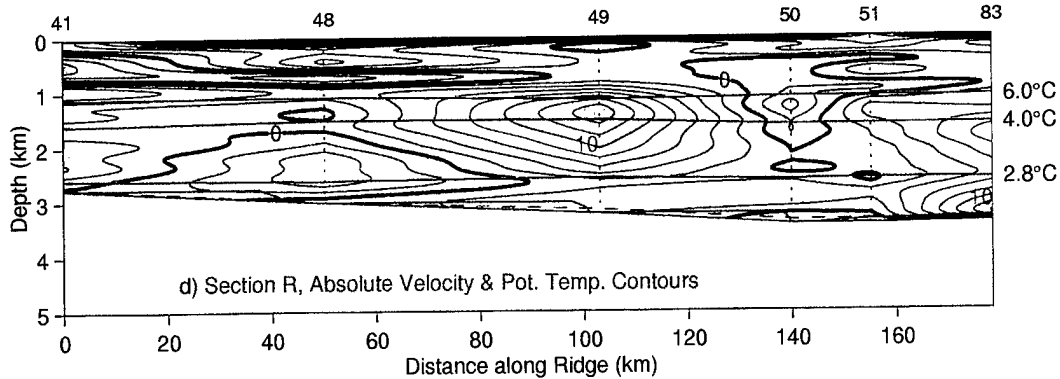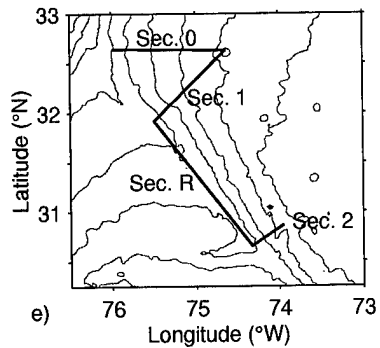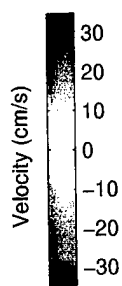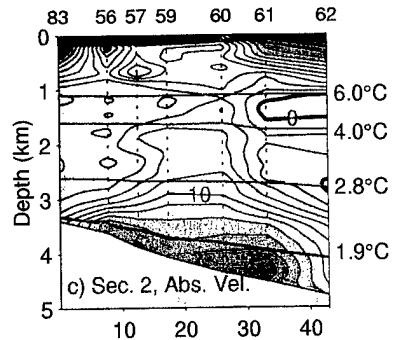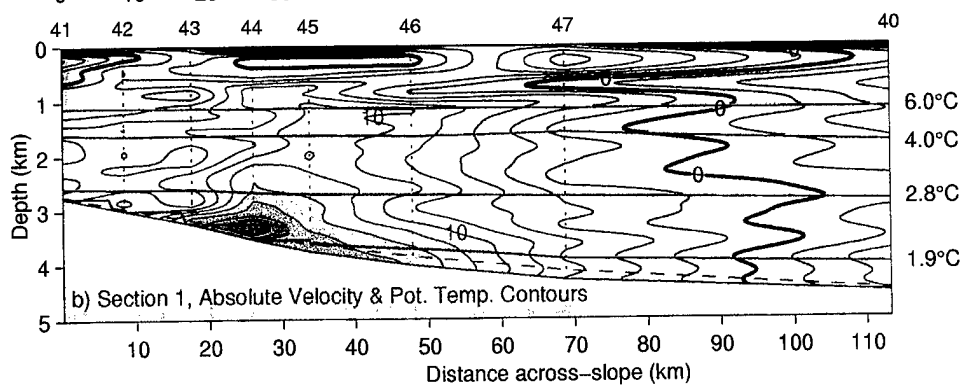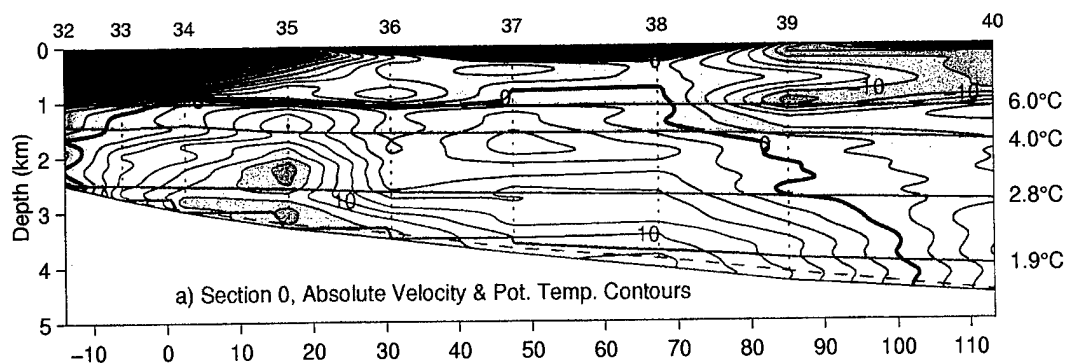
Figure 11: Contours of referenced geostrophic velocity (normal to the sections) and potential temperature. Geostrophic profiles were referenced to absolute profiles at depths of 1300 to 2400 m. Contour intervals are every 2 cm s^{-1} with the 0 and $\pm$10 cm s^{-1} intervals labeled. The coordinate system is along-stream with positive flow equatorward. Potential temperature contours that divide transport categories are labeled to the right of each panel. The height of the bottom mixed layer is indicated by the dashed line near the bottom. AVP drop numbers are indicated at the top of each panel, with the leading digit (4) removed. In Section 2, not all drops were used to more accurately represent a synoptic section. Panel (a) is Section 0, (b) is Section 1, (c) is Section 2, and (d) is Section R. Panel (e) is a small version of Fig. 1 to clarify section locations.

a) Section 0, Geostrophic Velocity & Pot. Temp. Contours

b) Section 1, Geostrophic Velocity & Pot. Temp. Contours

Distance across–slope (km)

c) Sec. 2, Geos. Vel.

Velocity (cm/s)

e)

Longitude (°W)

d) Section R, Geostrophic Velocity & Pot. Temp. Contours

Distance along Ridge (km)
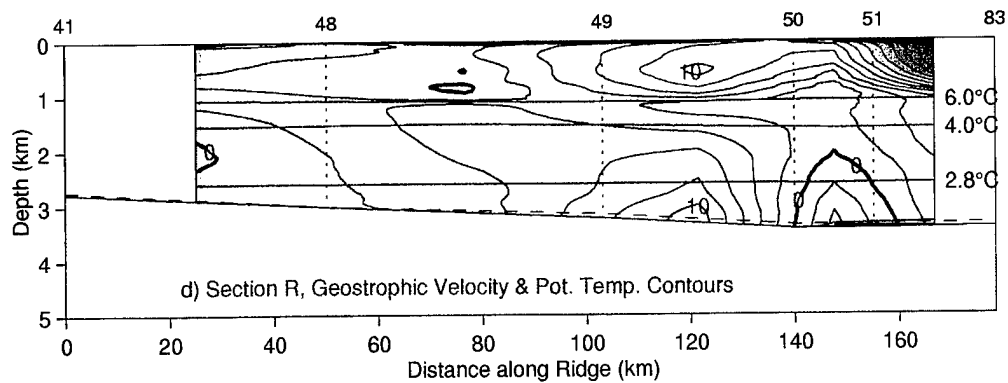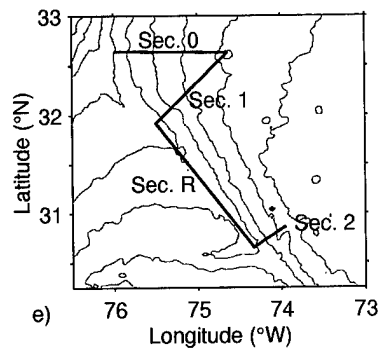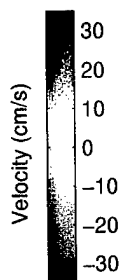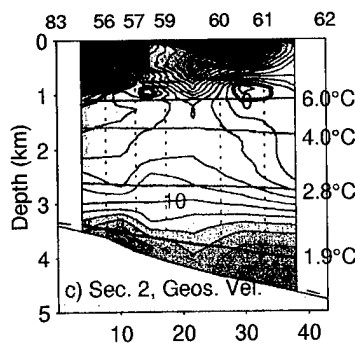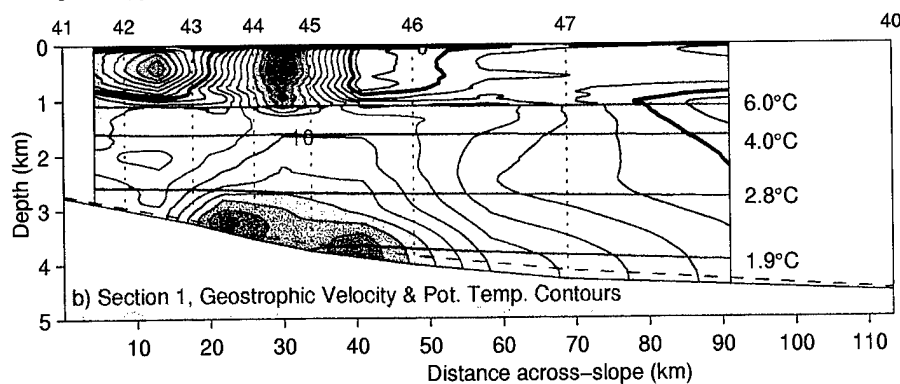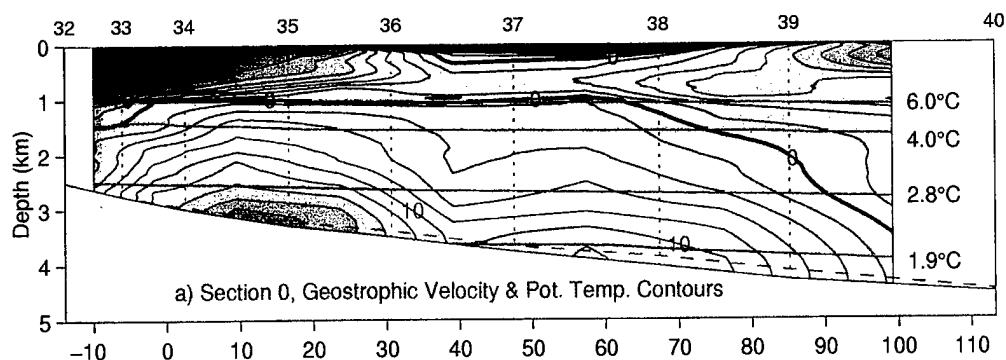
Table 4: Transport of the DWBC at the Blake Outer Ridge in July/August 1992.

Sec #	Sec. length (km)	Normal dir. (°T)	# of stn	SLSW transport* (Sv)	LSW transport (Sv)	LNADW transport (Sv)	BW transport (Sv)	Total transport (Sv)
0	127	180°	9	A: 1.2 ± 0.2	5.8 ± 0.7	7.6 ± 0.5	1.9 ± 0.4	16.6 ± 1.4
				G: 1.2 ± 0.1	5.8 ± 0.4	7.7 ± 0.6	1.5 ± 0.5	16.2 ± 1.2
1	113	135°	8	A: 2.8 ± 0.1	6.3 ± 0.2	7.3 ± 0.2	1.9 ± 0.4	18.3 ± 0.7
				G: 2.6 ± 0.2	5.7 ± 0.2	7.4 ± 0.4	2.0 ± 0.3	17.8 ± 0.8
2	43	149°	10	A: 0.5 ± 0.1	1.8 ± 0.1	4.6 ± 0.1	2.9 ± 0.2	9.7 ± 0.2
				G: 0.6 ± 0.1	1.7 ± 0.1	5.2 ± 0.3	3.1 ± 0.2	10.7 ± 0.5
R	183	220°	6	A: 3.3 ± 1.6	5.9 ± 2.9	1.9 ± 0.4	0	11.1 ± 4.9
				G: 2.1 ± 0.4	5.6 ± 1.1	4.4 ± 1.5	0	12.1 ± 3.0
5	34	271°	5	A: 0.4 ± 0.1	1.3 ± 0.1	2.5 ± 0.2	1.3 ± 0.3	5.5 ± 0.5
				G: 0.5 ± 0.1	1.3 ± 0.1	2.5 ± 0.5	1.2 ± 0.3	5.4 ± 0.9

* Note that in the transport columns, the top line (A:) refers to transport derived from absolute velocity and the bottom line (G:) to those from geostrophic velocity.

Transport results and uncertainties using both absolute and geostrophic velocity fields are presented in Table 4. The uncertainties are discussed later in this chapter. In Section 0, the zero-velocity contour reached the bottom on both sides of the current, indicating this section captured the whole DWBC. The mean transport was 16.4 Sv ($1\ \mathrm{Sv} = 10^6\ \mathrm{m}^3\ \mathrm{s}^{-1}$). No similar zero-velocity contour was apparent on the inner end of Section 1, implying some of the current may have flowed over the ridge between sections. However, the transport of SLSW increased by about 1.5 Sv between Sections 0 and 1 owing to higher along-stream velocities (both absolute and geostrophic) in that category. The overall transport increased by the same amount. It is possible the difference in this shallow water category resulted from the inshore end of Section 0 being somewhat retarded by the nearby Gulf Stream. However, no T-S evidence supports this proposition. Alternately, the difference might be from a large-scale eddy present during our survey, but no direct evidence supports this either. Regardless of the cause, the difference in transport between Sections 0 and 1 is within the total uncertainty and statistically insignificant within one standard deviation.

The geostrophic and absolute velocity fields generally agree, particularly below about 1300 m. On Section R, however, big differences were noted around AVP drop 449, where a strong mid-water eddy appeared. No temperature or salinity anomalies were observed with the anomalous velocity, suggesting the profile may have been in the outer edge of an anticyclonic eddy where the inertial acceleration was balanced by the Coriolis acceleration, as seen by Elliot and Sanford (1986). The AVP profiles on either side of drop 449 were more than 50 km away and showed no evidence of the eddy. This is not unexpected because eddies previously observed in the area were only 40 km in diameter (Riser et al., 1978). The large velocity anomaly from this eddy was partly responsible for the large uncertainty in transport for Section R.

At Section 2, transport is reduced by about one-half because almost all the SLSW and LSW, and some of the LNADW, has flowed over the ridge. Because this section was not intended to fully capture DWBC transport, the offshore edge of the current was not observed. An estimated 0.5 Sv of transport beyond our section end was missed and is not included in Table 4. This estimate was made by extrapolating the transport per unit width curve from the observed stations to where it became zero. We occupied one station along the line of Section 2 and 77 km from its end in the Hatteras Abyssal Basin. Its density field indicated a northward flowing velocity between it and the nearest inner station, and its absolute velocity profile showed a weak baroclinic flow structure. Both observations suggested it would be inappropriate to extrapolate between this station and the nearest inner station. However, this station was used to provide background density data for calculating anomalies for other analyses. Section R should have captured most of the transport going over the ridge but the relatively large station spacing (some > 50 km) and the previously mentioned eddy made the transports more uncertain than at Sections 0 and 1. Nonetheless, a sum of the total transport of Sections 2 and R yields approximately 22 Sv, which is within 25% of the 18 Sv found in Section 1. These two estimates agree within the 5 Sv uncertainty on Section R.

Section 5 was located on the southwest side of the ridge and had a transport of about 5.5 Sv. At this point the DWBC has negotiated the ridge and is proceeding west towards the continental shelf. This section was likewise not intended to observe the whole current width and an estimated 1 Sv of transport was included. Without other sections on this side of the ridge, it is difficult to determine whether the transport here should be the same or different from that in Section 2. The structure and magnitude of the current core,

density field, and bottom mixed layer on Section 5 were very similar to those on Section 2 as seen in Figure 11. The symmetrical density structure across the ridge supports the geostrophically balanced flow on both sides. The associated pressure field prevents strong cross-ridge flow, even well above the ridge crest. Low cross-ridge flow speeds were observed in most ridge-crest AVP profiles.
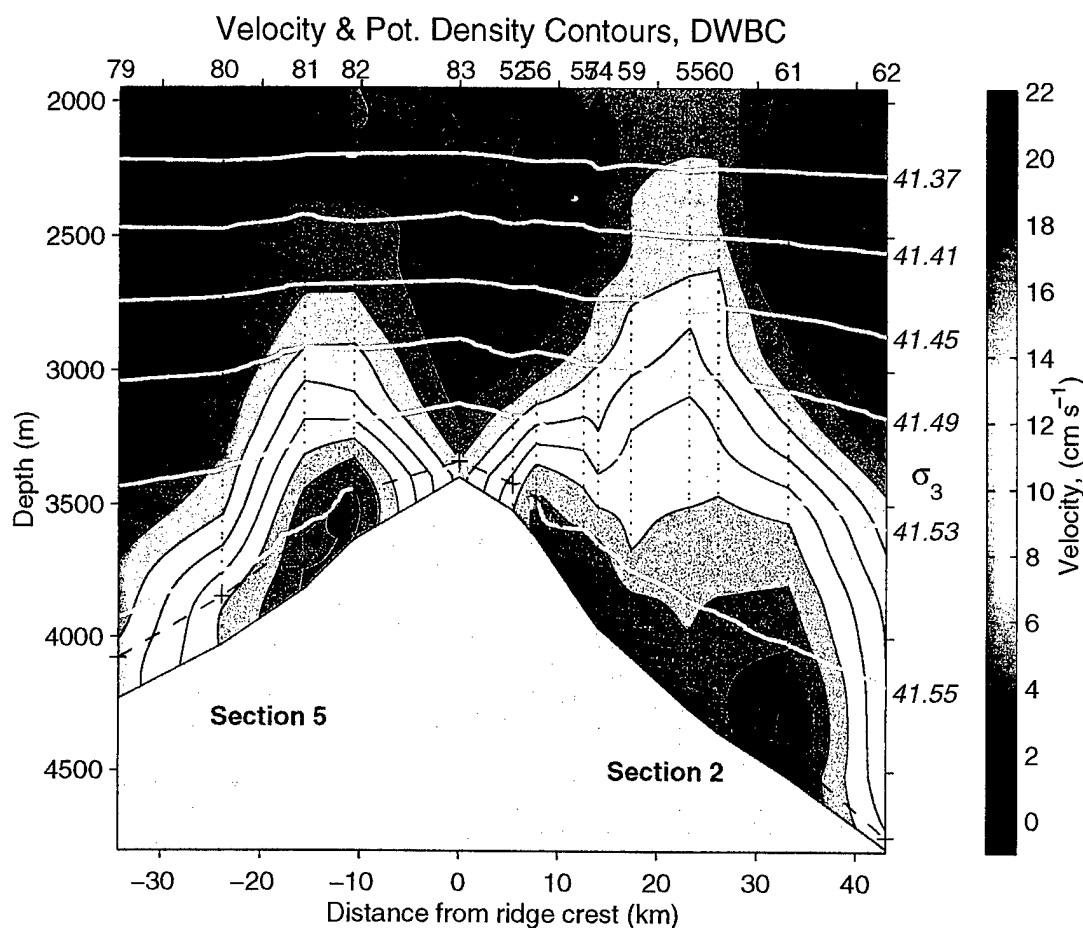
Figure 12: Contours of along-slope velocity magnitude, potential density (white lines), bottom mixed layer height (dashed line), and topography on Sections 2 and 5 as seen from the southeast (see Fig. 1 for general orientation). Locations of AVP drops are marked at the top with the leading digit (4) removed for clarity. Distance is defined as positive to the northeast for Section 2 and negative to the south for Section 5. Absolute velocities were filtered with a 300-m Bartlett filter. Contours are of magnitude only; actual direction is out of the page on Section 2 and into the page on Section 5. The BML height was calculated as the point where the buoyancy frequency squared drops below 2×10^{-7} s^{-2} and remains so to the bottom.

3.2 Uncertainty Analysis

To understand the accuracy limits of this experiment's transport results, an uncertainty analysis was conducted of various components employing several techniques. Confidence intervals for transport values depend not only on the performance of the instruments but also on the spatial and temporal extent over which the transport is measured. Ideally, one can use some property or tracer to define the horizontal and vertical limits of the current. However, even tracers such as CFCs do not always succeed because of dilution due to entrainment. Therefore most investigations, including this one, use isotherms or isopycnals to bound the transport area vertically because water mass characteristics can be accurately determined. For lateral boundaries, a combination of topography, station locations, or velocity reversals is often used. For this study, the ridge crest was the inshore boundary and the offshore boundary was established where the southward transport per unit width approached zero, (i.e., where the velocity reversed from south to north). This offshore boundary is a reasonable choice at the BOR where there is no recirculation gyre.

Temporal variability in the velocity field, such as advecting eddies, planetary waves, tides, and internal waves, as well as non-synoptic sampling, confound the determination of low-frequency transport. In the context of a velocity profiling survey, much of that variability can be removed by vertically smoothing and temporally averaging the profiles. Temporal variations in the current influence the absolute and geostrophic velocity fields differently because the methods used to calculate these fields are based on different principles and represent different responses to ocean structures. The directly-measured absolute velocity is local but spatially independent of other observations. The density-derived geostrophic velocity is spatially integrated but relies on synopticity. If hydrographic stations are even one day apart, confounding density features can create velocity errors. In this experiment, transport was estimated from both absolute and geostrophic velocities to compare the methods and to realize the advantages of both by averaging the two. An absolute reference velocity for the geostrophic profiles and the pressure data were the only connections between the two velocity fields.

The overall uncertainties listed in Table 4 with the transport values are a combination of uncertainties due to method deficiencies and natural variability. This overall value was estimated by exchanging observed profiles in a full section with interpolated ones. One

profile at a time was removed from the section and replaced with one formed by interpolating from the adjacent profiles, then the transport was recalculated. This process was not applied to the profiles at the ends of the section for lack of surrounding ones from which to interpolate. The difference between the transports calculated using interpolated profiles and those using real profiles is an estimate of the total uncertainty in the whole observation. These estimates were assumed to be random so they were squared and averaged over all realizations to produce the overall variance for the section. The uncertainty listed in Table 4 is the square root of this overall variance, the rms value. Because each profile was subject to the combined effects of instrument and sampling errors, as well as natural fluctuations (e.g., tides and internal waves), it is believed that this uncertainty reasonably estimates the sum of all components.

The part of this overall uncertainty contributed by spatial variability in the DWBC source field was estimated by examining the conservation of volume transport between sections within a topographically constrained water mass. Sections 0 and 1 shared a common eastern end station and were bounded on the west by the continental slope and the beginning of the ridge. A topographically trapped isopycnal ($\sigma_3 = 41.469$ kg m^{-3}) was used as an upper boundary and transport was calculated between it and the bottom for both sections. The results were 8.2 Sv for Section 0 and 7.9 Sv for Section 1. If the uncertainties on the two sections are of similar size, then the difference of 0.3 Sv indicates a random potential error of 0.2 Sv for each section. Another conservation test compared the transport of the Bottom Water (BW) category at Sections 0, 1, and 2. Unfortunately, the outer edge of the current on Section 2 was not observed, so BW transport was estimated by extrapolation of the transport function curve (transport per unit width) to where it crossed zero. Using a parabola matching the data available within the section, about 0.5 Sv of BW was estimated to be outside our calculated transport. Adding this to the 1 Sv increase over BW transport at Section 1, and assuming a random nature to it, the overall uncertainty implied is 0.9 Sv on any section, which is similar to the total uncertainty found by the profile replacement technique on Sections 0 and 1.

Variance due to internal wave and inertial motions was examined through a time series of four drops at the same location taken over one-half an inertial period (11.4 hours). These were treated in a fashion similar to that described for the overall uncertainty (i.e., removing drops and recalculating the mean velocity profile). For the

whole DWBC ($\theta < 6°C$), the resulting rms uncertainty was 0.005 m s^{-1}. Assuming this is random, errors were estimated for each section by multiplying the transport area of the section by 0.005 m s^{-1} and then dividing by the square root of the number of independent realizations within the section. The latter was determined by dividing the length of the section by a horizontal spatial correlation length for internal waves, estimated by Sanford (1991) to be 15 km. For Sections 0 and 1, transport uncertainty due to internal wave and inertial motions was about 0.4 Sv.

Uncertainty in the absolute velocity field due to the instrument itself was estimated by comparing an independent measurement of barotropic velocity with that determined from the AVP data. Depth-averaged velocity (V_{nav}) was computed from the locations and times the AVP left the surface and returned, much as with a dropsonde device. The difference between V_{nav} and the depth-averaged velocity measured by the instrument (V_{avp}) for a number of drops on this and a more recent cruise exhibited no systematic trend and had a random error of 0.005 m s^{-1}. Again, transport uncertainty for a section was calculated by multiplying this velocity error by the section area and dividing by the square root of the number of drops in the section. This yielded uncertainty values of about 0.2 Sv for Sections 0 and 1.

To address whether the observations represented the long-term mean DWBC, Site 2-5 on Section 2 was specifically positioned where a current-meter mooring was located in 1977–78 (Jenkins and Rhines, 1980). Table 5 lists the average and standard deviations of magnitude and direction of the DWBC for both the year-long current-meter records and for our nine-day time series of eight profiles. The AVP profile data were averaged over 20 m above and below the nominal depth of the current meters because the pressure record from the upper-most current meter exhibited this range of mooring motion. The mean and standard deviation of the time-series profiles is shown in Figure 13 in along-slope and across-slope component form with the same for the current meter records. The close agreement in both magnitude and direction at each level confirms that during our experiment period, the DWBC was typical of its long-term mean. The agreement also supports the idea that our experimental uncertainties are largely uncontaminated by long-term natural variability.

Means of 9–day AVP time series and 1–yr. current–meter record

Potential Density, σ_3 (kg m^{-3})
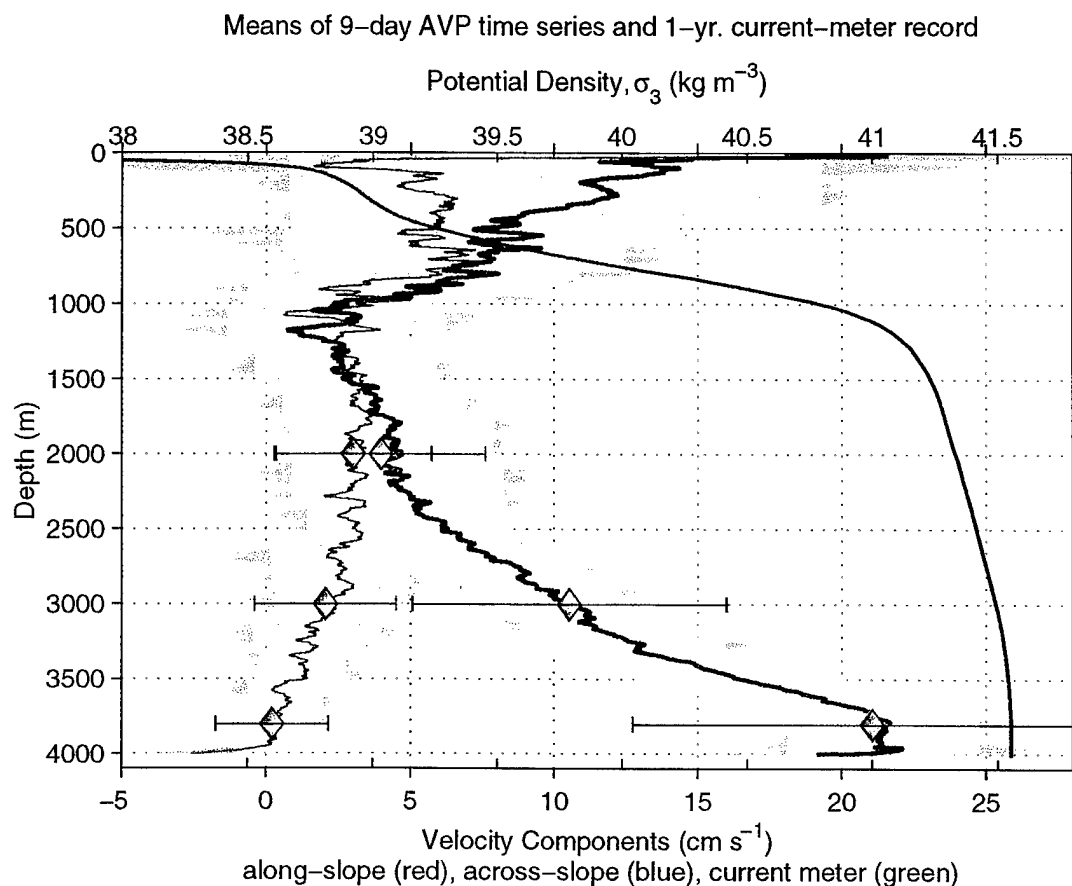
Figure 13: Average velocity and potential density profiles of a 9-day AVP time series at Site 2-5 in the center of the DWBC. The red line represents the average along-slope velocity component of eight AVP profiles (454, 464, 465, 467, 469, 484, 489, and 492); the blue line is across-slope velocity (positive up-slope), and the gray area represents ± one standard deviation. Positive along-slope direction is 149° T; positive across-slope direction is 239° T. The black line is potential density with scale at top. Symbols (♦) mark mean values from year-long current-meter mooring at the same site with bars indicating one standard deviation from means (Jenkins and Rhines, 1980).

Table 5: Mean DWBC magnitude and direction at Site 2-5.

Depth (m)	Current Meters, 1 yr., 1977–78	AVP, 9-day time series, 1992
2002	6.1 ± 2.9 cm s^{-1} at 190° ± 45°	6.2 ± 2.3 cm s^{-1} at 188° ± 28°
3003	11.1 ± 5.2 cm s^{-1} at 161° ± 25°	11.0 ± 1.9 cm s^{-1} at 160° ± 10°
3803	21.3 ± 7.8 cm s^{-1} at 149° ± 24°	21.6 ± 3.2 cm s^{-1} at 150° ± 5°

To further investigate whether long-term natural variations, such as topographic Rossby waves, may comprise part of our velocity signals and provide greater uncertainty in the transport results, the current-meter records were studied for energy peaks in a wave frequency range that could be sustained on a bottom slope like that at the BOR. The bottom slopes at all our sections (0.018-0.038) fall between two limiting cases developed by Rhines (1970) for low-frequency waves on sloping bottoms in a fully stratified rotating ocean. The upper frequency limit is when $\alpha \cong f/N$, where α is bottom slope, f is the inertial frequency, and N is the average buoyancy frequency below the main thermocline. In this case, the frequency of a bottom-trapped wave is nearly the inertial frequency. For the values of f and N at Section 2 (7.46 x 10^{-5} s^{-1} and 1.2 x 10^{-3} s^{-1}, respectively) the slope would have to be 0.063 to support such a wave, much steeper than is found there. The lower limit is when $\alpha << f/N$, or a slope less than 0.006 for this stratification, much more gradual than anywhere on the BOR. The wave frequency in this case is approximately equal to f^2/N, or a period of about 15.7 days. Figure 14 shows variance preserving spectra of current speed from each current-meter. Thick vertical dashed lines indicate the inertial (~1 cycle per day) and 15.7 day (6.4 x 10^{-2} cpd) periods. Only nine percent of the variance from any of the three current meters is contained in the frequency range of interest. Most of the variance occurs at lower frequencies with peaks at 4.5 x 10^{-2} and 1.4 x 10^{-3} cpd (22 and 70 day periods) which are marked with thin dashed lines in Figure 14.

It seems unlikely that our observed velocities had large components from low frequency variations in them because the AVP time series averages closely correlated with the year-long current-meter averages. Further, the distributions of velocity and direction data from the year-long current-meter records are not normal, but peaked around the means and skewed toward it. The kurtosis values for velocity at each depth are slightly positive (0.2 to 1.1), where normal distributions have zero kurtosis, and they are very positive (2.6 to 38.8) for the direction data. This indicates a higher than normal probability of observing these mean values during a re-occupation of the area for further transport measurements.
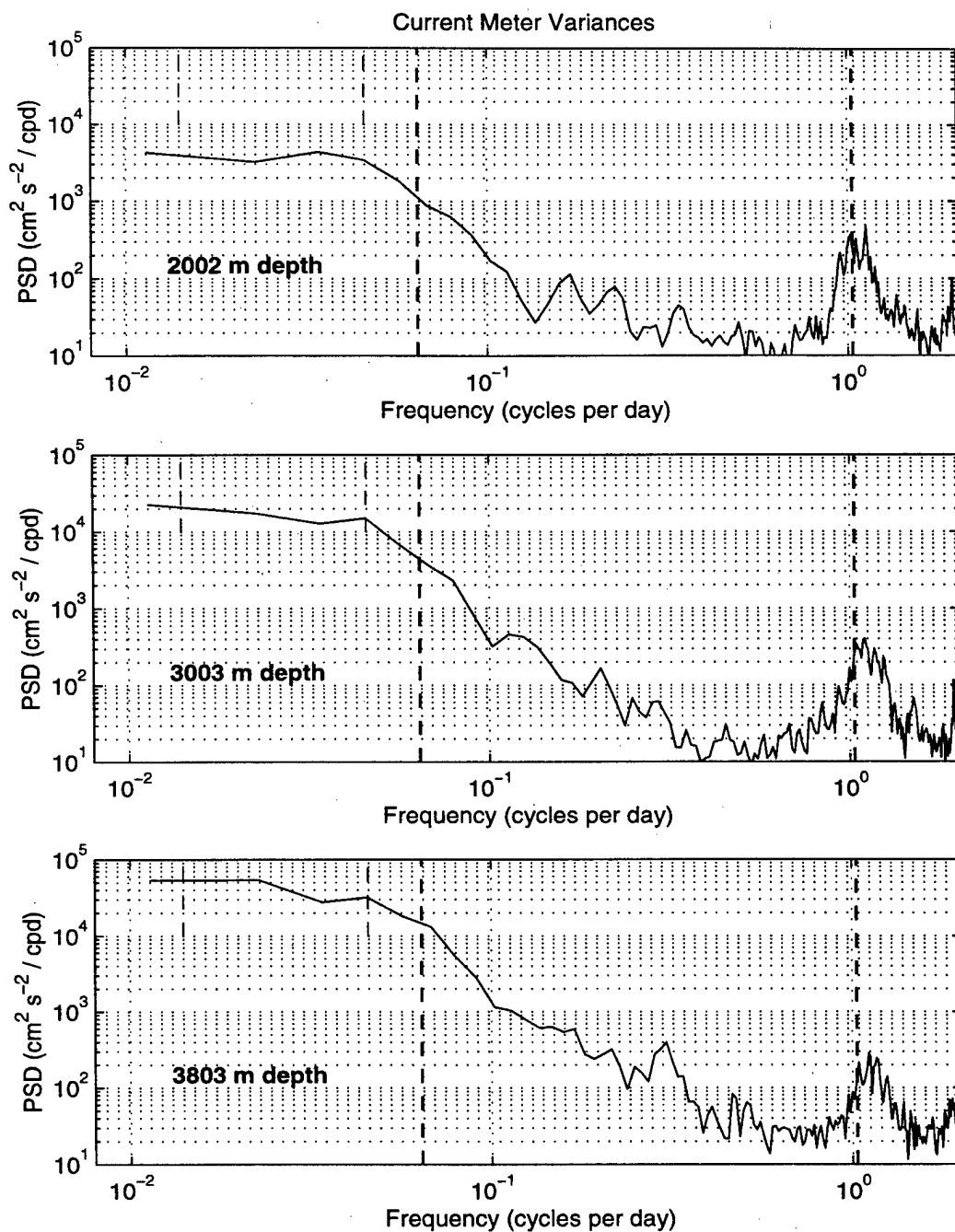
Figure 14: Variance spectra of current meter speeds at each depth level. Thick dashed lines mark 1.03 and 15.7 day periods, thin dashed lines mark 22 and 70 day periods.

For yet another estimate of transport uncertainty due to low-frequency phenomena, an 18-km portion of Section 2 was reoccupied seven days after the initial observations.

Transport for the whole DWBC ($\theta < 6°C$) was measured at 4.0 ± 0.2 Sv during the first occupation and 5.7 ± 0.5 Sv during the second. Most of the increase (1.4 of the 1.7 Sv) was due to higher velocities in the BW and LNADW categories during the second occupation. This difference includes both experimental error and natural fluctuations. Assuming a steady transport over these seven days, the difference would represent experimental uncertainty. However, the time series at Site 2-5 (part of this short section) indicates the difference is largely from a natural fluctuation shown by consistently higher bottom velocities late in the time series. Because the purpose of the error analysis is to derive bounds on the experimental error and not to estimate the total potential variability of the transport, this value is taken as an upper limit for experimental error, confirming the overall uncertainty estimates of approximately 1.5 Sv for Section 0.

In summary, experimental uncertainty of the transport results in this experiment was estimated by various techniques. These included a replacement estimation for overall values, two conservation calculations, a half-inertial period time series of profiles, a vertically averaged velocity to check instrument error, and a repeat sub-section occupation after seven days. Also, a nine-day time series of profiles was compared to the results from a year-long current meter mooring showing this experiment occurred during a period typical of the mean DWBC. Further, that current meter record was examined for low frequency velocity variance that could be sustained on the slopes of the BOR and little was found. All these analyses suggest that the overall experimental uncertainties given in Table 4 are accurate.

3.3 Comparison to Prior Transport Results

Volume transport estimates for the DWBC in the vicinity of the Blake Outer Ridge range from 3 to 40 Sv (Riser *et al.*, 1978; Swallow and Worthington, 1961). The reasons for this range are threefold: (1) different boundaries have been used to define the cross-sectional area of the current; (2) different techniques have been used to measure velocity or provide a reference for geostrophic velocity; and, (3) some natural variability exists in the transport of the current. Schmitz (1996) summarized basin-wide transports in the North Atlantic and reported a general value of 12 Sv of transport for the DWBC just north of the BOR. He defined the DWBC as water in the potential temperature range of 1.6 to 4°C, and within that same range on Section 0 we found a transport of 15 Sv.

Comparing our results to this general summary is not as good as comparing them to specific studies in the same area. Transport comparisons at the BOR are available from several prior surveys that overlap our observations (see Fig. 15). These comparisons, however, must be undertaken carefully to ensure that current boundaries and velocity references are properly considered.

Previous DWBC Observations near Blake Outer Ridge
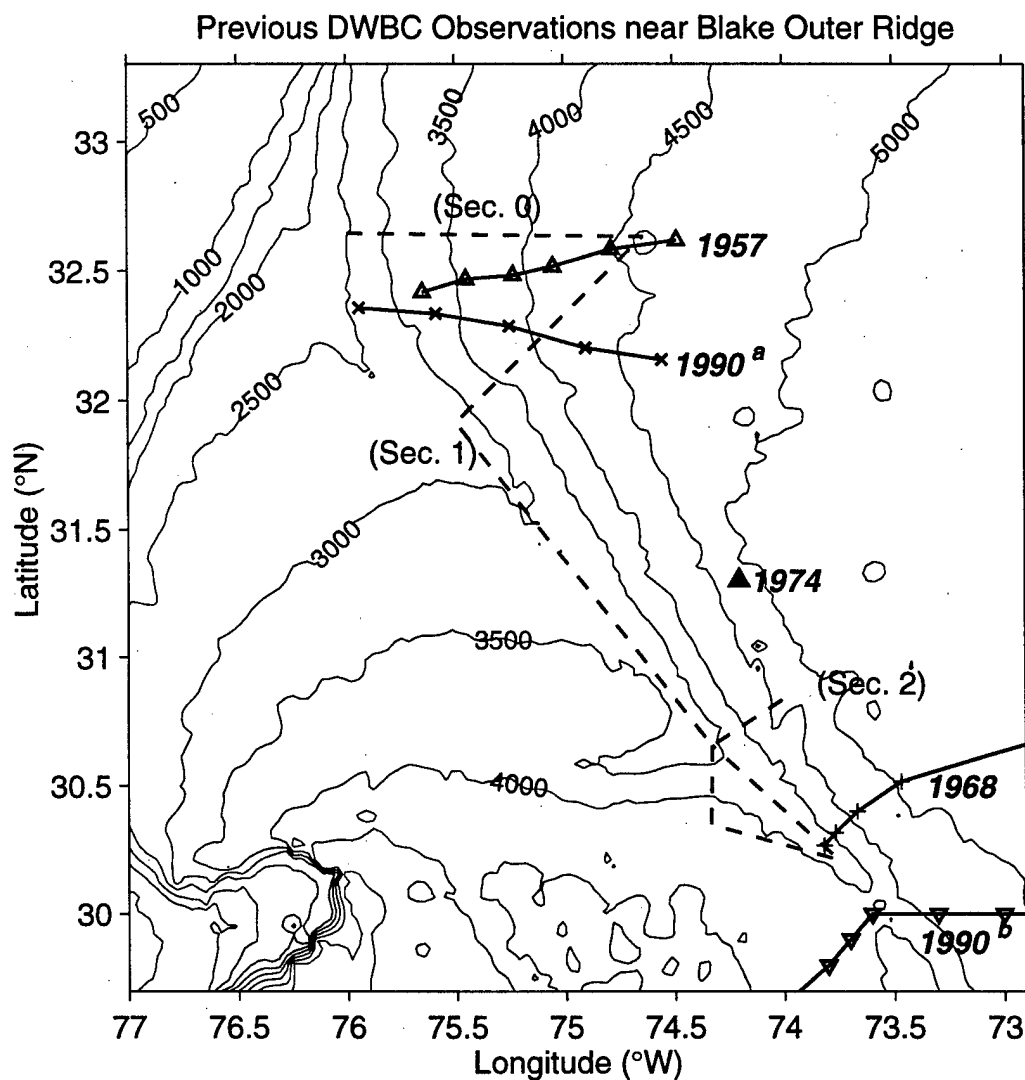
Figure 15: Prior DWBC observations near the Blake Outer Ridge.

Swallow and Worthington (1961) were the first to observe the DWBC, doing so in 1957 near Section 0. They pioneered the use of neutrally-buoyant isobaric floats to obtain

absolute velocity references for geostrophic profiles. They deployed several at depths between 1500 and 2900 m. One float with a nearly zero mean velocity crossed a CTD section, so they defined this isotherm, $\theta = 3.43°C$ (approximately 2100 m), as the level of no motion (LNM) for referencing all geostrophic profiles on that section. Also using that isotherm as an upper boundary, they calculated a transport of 6.8 Sv between it and the bottom and out to the edges of their section. Using the same boundaries and LNM with our geostrophic velocities, we found 6.5 Sv on Section 0. However, using the absolute velocities as a reference for our geostrophic profiles (instead of assuming zero velocity at $\theta = 3.43°C$), we found 12.5 Sv. This difference demonstrates that the current structure was laterally more complex than could be accounted for using a single float to obtain one section-wide reference velocity.

In 1968, Amos *et al.* (1971) conducted a hydrographic survey across the Blake Abyssal Plain and Blake Outer Ridge to determine the deep circulation in the area. Their survey line crossed the ridge southeast of our Section 2 and continued 150 km out into the Hatteras Abyssal Basin. Instead of using a float to establish reference velocities, they considered the LNM for each geostrophic profile to be the center of a depth interval where the vertical shear of horizontal velocity was a minimum. These LNMs ranged from 1500 to 2100 m in depth on the northeast side of the BOR where they calculated a DWBC transport of 22 Sv. The LNMs defined by the minimum shear zone were also used as area boundaries for the transport calculation. Because our survey did not extend as far as theirs, we calculated the portion of their transport from the four stations that overlapped our Section 2 to be 17.7 Sv. Using the same definition for LNMs (i.e., the middle of the minimum shear in each geostrophic velocity profile) and boundaries (i.e., from the LNM to the bottom and from the ridge crest to the outer station), our data yielded 6.9 Sv of transport, less than half their estimate. If we use our absolute velocities to reference our geostrophic velocities at the same LNM depths, the result is 9.8 Sv. This again indicates that knowledge of the full velocity field is important.

The large difference between the results of the two studies is primarily due to the area to which Amos *et al.* attribute high DWBC velocities. Where we observed an area 10-km wide and 300-m thick with velocities >18 cm s^{-1}, they reported an area 36-km wide and over 1500-m thick with velocities > 20 cm s^{-1}. Part of this difference is from spatial resolution. Where they had four stations, we had ten. Also, the accuracy of the salinity-

temperature-depth system available at the time for determining density (and geostrophic velocity) was considerably less than the systems we used. The transport difference could also be due to natural variability in the flow, but their values at this location (far down the ridge) are not corroborated by any other study. Although no uncertainties were reported, they are probably large due to the absence of independent reference velocities and large bottom-triangle extrapolations used in calculating transport. In light of these differences, incongruent numbers are expected.

The current meter mooring with which we compared our AVP time series in the previous section was part of an array of five moorings that crossed the BOR (Mills and Rhines, 1979). Three of these were placed on the northeast side of the ridge along the line of our Section 2. Unfortunately, the middle of the three was lost, presumably swept away by the strong current, and transport could not be estimated from the remaining two owing to their > 80 km separation. Our time series comparison was with the mooring closest to the ridge crest.

In 1990, Pickart and Smethie (1993) used five hydrographic sections centered around Cape Hatteras to study how the Gulf Stream crosses over the DWBC. Their current boundary definitions differed from other studies because they selected only those density classes that showed high F-11 concentrations and excluded the middle of the water column (see Fig. 16). Our SLSW category corresponds roughly to their shallowest two categories, our LSW to that which they excluded, and our LNADW exactly to their deepest category. They referenced their geostrophic profiles using a dropsonde device (POGO float) to measure the vertically averaged velocity from the surface to 3000 m, nearly the full depth of the water column. A transport of 10.1 Sv was observed in the central part of their southernmost section which overlaps with our Sections 0 and 1 (see Fig. 15). Using the same density boundaries and depth range for reference velocities with the AVP, we determined an average value of 9.6 Sv for Sections 0 and 1. This agreement is satisfying given their data were collected with instruments similar to ours and two years before our survey. Again, it illustrates the importance of boundary definitions in determining transport.
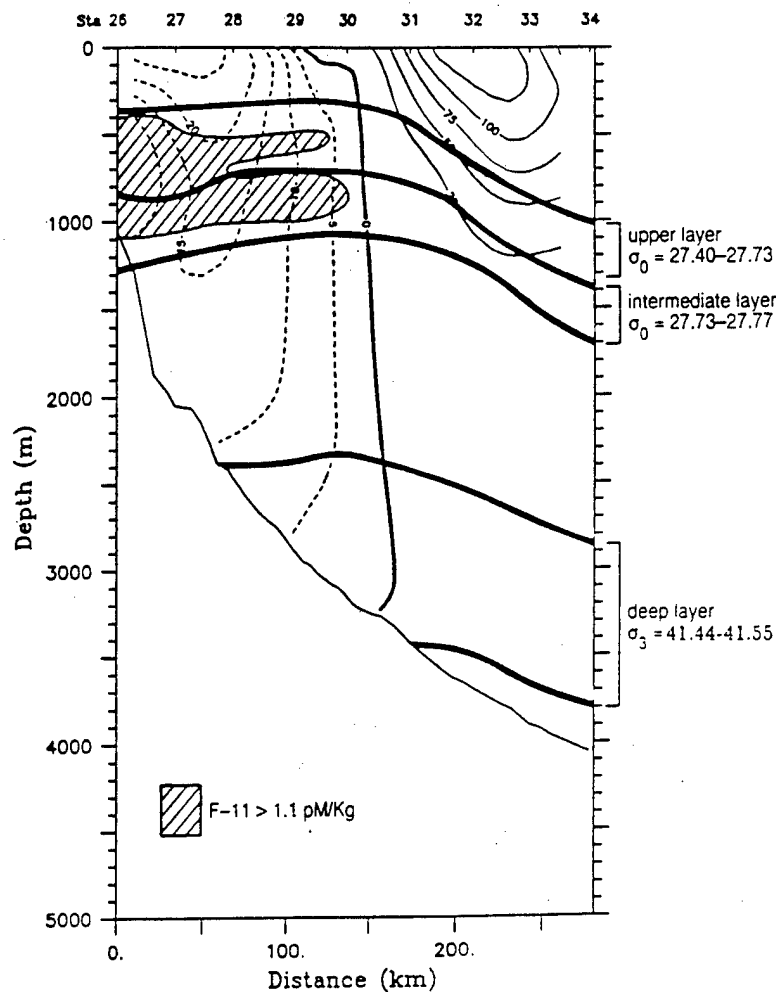
Figure 16: Pickart and Smethie's (1993) boundary definitions for the DWBC (thick lines) overlaid on absolute geostrophic velocity contours on their Section 2 (36–38°N). The hatched region is the F-11 core of the shallow DWBC. (Reprinted by permission from the American Meteorological Society.)

Johns *et al.* (1997) conducted a hydrographic survey in 1990 to determine the details and extent of deep transport and recirculation gyres within the Blake Abyssal Basin south of the BOR. The northern boundary of their survey crosses the Blake Escarpment and Abyssal Basin at 29°N, then turns northeast across the ridge near the Amos *et al.* (1971) section, then east again along 30°N (see Fig. 15.) Our water mass definitions are similar to theirs, however, our transport results differ. For transport calculations, they obtained reference velocities for geostrophic profiles by using current meters and dropsondes along

26.5°N and closing the volume transport and CFC-11 budgets over the rest of the survey area. They reported 20 Sv of the DWBC coming across the ridge and another 11 Sv flowing around its tip for a total of 31 Sv through their boundary (see Fig. 17).
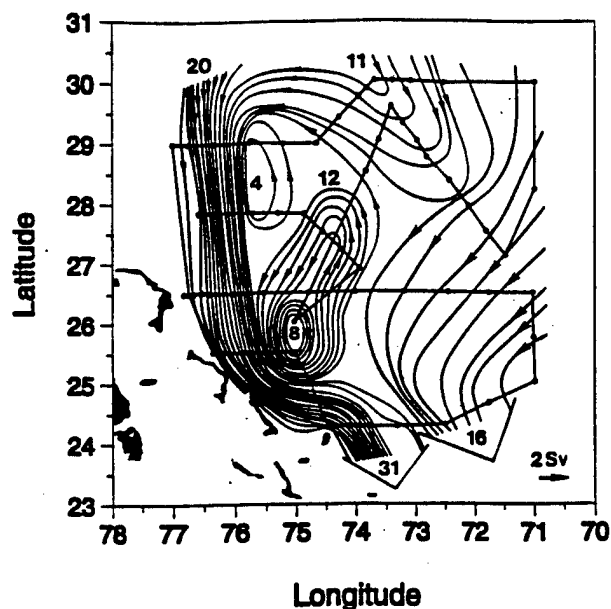
Figure 17: Transport schematic for the whole DWBC (all water below 6°C potential temperature), from Johns *et al.* (1997). Streamlines represent 2 Sv each. Along the northern boundary, 11 Sv flows around the BOR while 20 Sv crosses over the ridge.

The 11 Sv coming around the tip of the ridge compares favorably with our 10 Sv result at Section 2. And the 20 Sv flowing directly south compares reasonably to our 17 Sv at Section 0. However, the results for Sections 0 and 2 are not additive because transport at the latter is directly from the former; the current is diverted by the ridge. It seems unlikely that the 20 Sv they show flowing directly south never negotiates the BOR, particularly in light of the zero-velocity contour we observed at Section 0 and the similar transport results for Sections 0 and 1. Their results for individual water masses show approximately 8 Sv in the two deepest categories ($\theta < 2.4°C$) coming straight south as part of the 20 Sv. This potential temperature range is largely blocked by the ridge until Section 2. Therefore, it seems probable that 31 Sv is an overestimate of DWBC transport by approximately this amount, 8 Sv. However, direct comparison with our results is difficult because of reference velocity technique differences and spatial coverage.

Typically, when boundary definitions are similar and appropriate reference velocities are used, our results agree well with prior studies. A summary of the comparisons discussed above is presented in Table 6. If future work is carried out to monitor long-term climate change by monitoring the transport of the DWBC, some common definitions must be agreed upon. In particular, a common definition for the boundaries of the DWBC and an accepted method for determining the velocity field (or at least a reference for geostrophic velocities) are necessary for effective long-term monitoring.

Table 6: Comparison of prior DWBC volume transports with results from this study when the most appropriate choices of boundaries and/or reference velocities are used. Dates are for publication of results; see Figure 15 for dates of observations.

DWBC Transport	Swallow and Worthington (1961)	Amos *et al.* (1971)	Pickart and Smethie (1993)	Schmitz (1996)	Johns *et al.* (1997) (Sec. 2 only)
Prior study	6.8 Sv	17.7 Sv	10.1 Sv	12 Sv	11 Sv
This study	6.5 Sv	6.9 Sv	9.6 Sv	15 Sv	10 Sv

3.4 Potential Vorticity

Planetary and relative vorticity contributions to potential vorticity (PV) were calculated within each water mass on Sections 0, 1, 2 and 5 to investigate whether they changed as the DWBC flowed along and around the ridge. Planetary potential vorticity was calculated in the standard fashion for each profile using fN^2/g. Relative vorticity (ζ) was calculated by averaging the absolute velocities normal to the section within each water mass, then taking the difference between drops to find shear and expressing the contribution as $\zeta N^2/g$. The average relative vorticity was about two orders of magnitude smaller than the planetary vorticity. Both were conserved to within a standard deviation from section to section within each water mass (see Tables 7 and 8). The only water mass exhibiting change in its across-stream distribution of PV was the LNADW between Sections 1 and 2 (see Fig 18). In this water mass, isopycnals stretched slightly at the off-

shore end. This may have been caused by the bottom isopycnal of this water mass staying close to the top of the bottom mixed layer which was nearly bottom parallel. This change between sections led to a slight decrease in PV on Section 2 relative to Section 1, although insignificant relative to the uncertainties (see Table 7). There is no significant change in relative vorticity between Sections 1 and 2 in the LNADW.

Table 7: DWBC planetary vorticity component of PV by water mass and section.

Water Mass	Section 0 x 10^{-11} m^{-1} s^{-1}	Section 1 x 10^{-11} m^{-1} s^{-1}	Section 2 x 10^{-11} m^{-1} s^{-1}	Section 5 x 10^{-11} m^{-1} s^{-1}
SLSW	3.01 ± 1.18	3.42 ± 0.37	2.99 ± 0.27	2.93 ± 0.43
LSW	1.06 ± 0.04	1.06 ± 0.05	1.05 ± 0.03	1.06 ± 0.03
LNADW	1.00 ± 0.18	0.94 ± 0.14	0.82 ± 0.14	0.88 ± 0.17
BW	0.14 ± 0.02	0.12 ± 0.01	0.12 ± 0.04	0.13 ± 0.01

Table 8: DWBC relative vorticity component of PV by water mass and section.

Water Mass	Section 0 x 10^{-13} m^{-1} s^{-1}	Section 1 x 10^{-13} m^{-1} s^{-1}	Section 2 x 10^{-13} m^{-1} s^{-1}	Section 5 x 10^{-13} m^{-1} s^{-1}
SLSW	1.71 ± 0.15	2.32 ± 0.12	0.46 ± 1.8	0.68 ± 7.90
LSW	0.82 ± 6.36	0.50 ± 4.20	0.31 ± 5.62	1.43 ± 3.46
LNADW	0.87 ± 4.13	2.04 ± 5.68	2.05 ±4.58	0.27 ± 5.70
BW	0.03 ± 0.27	–0.08 ± 0.34	–0.12 ± 0.78	–0.07 ± 1.51
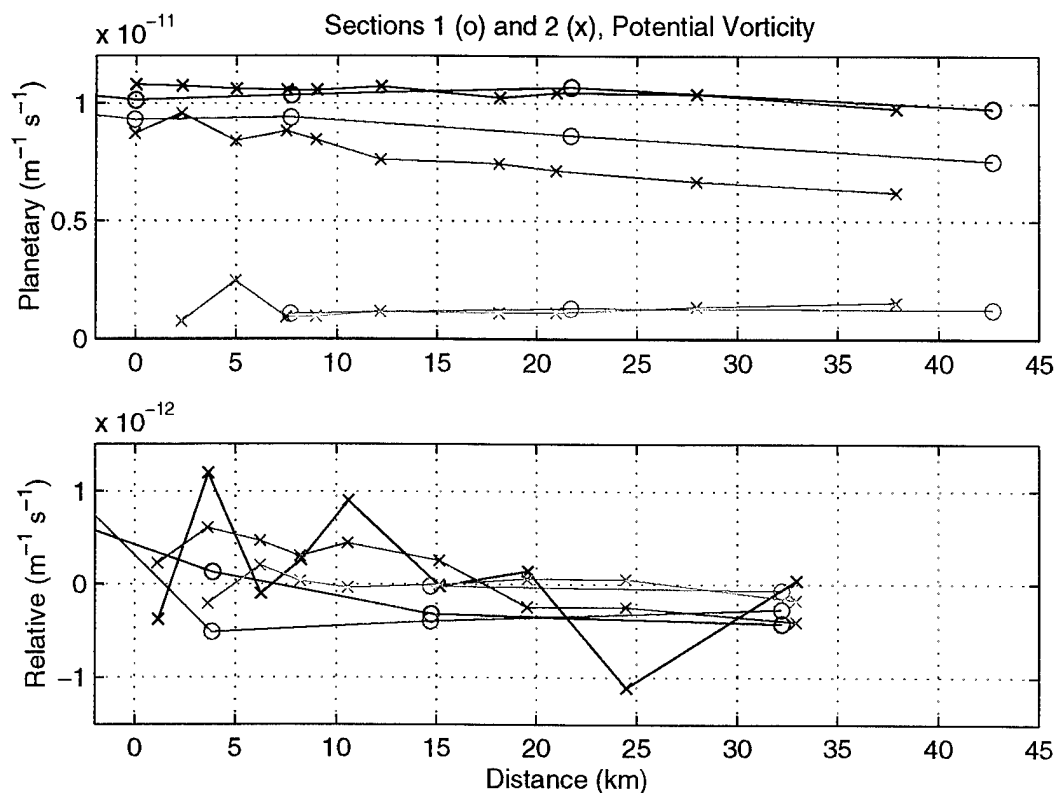
Figure 18: Relative and planetary components of potential vorticity across Sections 1 (o) and 2 (x) for the deep water masses (LSW = black, LNADW = red, BW = green). Note decade change in vertical scale between panels.

Stommel and Arons (1972) considered a DWBC with a constant potential vorticity and variable transport values flowing over idealized bottom slopes to explain why these currents are so wide. They concluded that a small slope will widen a constant PV abyssal current to many times its natural Rossby radius (R) with the final value being dependent on slope (α) and transport (T). At the BOR, the bottom slope increases from section to section, so this is a natural place to test their formulation for width.

The necessary parameters from our observations are given in Table 9. The current width was clearly observed only at Section 0, where the zero-velocity contour intersects the bottom on either side of the southward flow. For the other sections, the current width given is an approximation calculated by fitting a parabola to the transport-per-unit-width curve and computing where it intersects the bottom. The mean current thickness (H) was calculated by dividing the integral area used for transport by the current width. Likewise,

the mean velocities were calculated by dividing the transports by the integral areas. The values for reduced gravity, $g' = g\ \delta\rho/\rho$, were derived from the differences in the mean density of the whole current and the mean density in the same depth range at a background station taken in the Hatteras Abyssal Basin near Section 2. The baroclinic Rossby radius was calculated as $R = (g'H)^{1/2}/f$. Stommel and Arons divided their solutions into small and large slopes using the non-dimensional parameter $\sigma = R\alpha/H$, where H is the current height (or thickness) and R and α are Rossby radius and slope respectively. Our values for σ range from 0.06 to 0.11, so the BOR is in the small-slope regime despite its steeper than ordinary slope. The other non-dimensional parameter they defined, τ, relates transport (T) to height and f: $\tau = T(f/g'H^2)$. Current width is then determined as the Rossby radius times the ratio (τ/σ). For our parameters this produces widths of 142 ± 13 km at Section 0, 147 ± 8 km at Section 1, and 55 ± 6 km at Section 2 using average transport and transport uncertainties in determining τ. These widths are larger than we observed (see Table 9) by factors of 1.2 to 1.9, depending on which end of the uncertainty range is used. However, while the values are not the same, the trend is correct in that a steeper slope corresponds to a narrower current. The difference may be due to the assumptions that PV is exactly constant across the width of the current, which is not necessarily true (see Fig. 18), and that bottom friction is unimportant.

Table 9: Mean DWBC characteristics at the Blake Outer Ridge.

Sec #	Mean slope	Trans-port (Sv)	Width (km)	Height (m)	Vel. (m s^{-1})	Density (kg m^{-3})	Density Anomaly (kg m^{-3})	$g' \times 10^{-3}$ (m s^{-2})	$f \times 10^{-4}$ (s^{-1})	R (km)
0	0.018	16.4	83	2974	0.064	1038.0	0.0180	0.169	0.787	9.3
1	0.023	18.0	94	2634	0.075	1038.5	0.0166	0.155	0.775	8.9
2	0.038	10.2	43	2837	0.083	1039.9	0.0135	0.127	0.746	8.1

Pickart and Huang (1995) expanded this analysis by creating a DWBC model that allowed for an across-stream variation of PV. They compared their model to the Stommel and Arons model using a realistic across-stream PV function calculated from data taken in the North Atlantic DWBC at 35.5°N. The difference between the two models decreased approaching the equator. We calculated across-stream PV in the same manner and found a similarly shaped function with lower magnitudes due to different values of reduced gravity and transport. They also replaced the linear bottom slope with an exponential one (similar to that at the BOR) in their model, creating an across-stream pattern of maximum velocity consistent with our observations; asymmetrical and stronger further up-slope. Further, they added a model ridge to examine how such a topographic feature might impede along-slope transport and force fluid into the interior. While the BOR topography does not exactly match their model ridge (uniform height and perpendicular to a southward flow), it is worth testing our observations against the model to see if the BOR may have a similar effect. Within the model, a ridge height which prevents continuous along-slope flow is reached when $H_b < (f/f_o)H$, where H_b is bottom depth (measured from the top of the current as defined by H, DWBC thickness), f_o is the Coriolis parameter where the current was formed, and f is local Coriolis parameter. Taking f_o from 55°N, and f and H from Table 9, we find the DWBC would be blocked at the BOR if $H_b < 1960$ m below the top of the DWBC. At the inner end of Section 1, $H_b \approx 1670$ m, but it continually increases along the ridge as the crest slopes down to the abyssal plain. Therefore, every part of the DWBC can cross the ridge crest at some point along its length. This is evidenced by the strong current at Section 5 and in many other data sets showing flow along the southwest side of the ridge (Amos *et al.*, 1971; Riser *et al.*, 1978; Mills and Rhines, 1979; Lai, 1984).

Chapter 4: Bottom Boundary Layer

4.1 Prior BBL Results

The region near the seafloor in which the solid boundary affects the currents and water properties immediately above it is generically known as the bottom boundary layer. It can be divided into two regions, one within the other, which are easily separable on the Blake Outer Ridge. The larger and more easily observed of the two is the bottom mixed layer (BML), where density and tracer concentrations are vertically uniform. BMLs have been observed in many abyssal areas (Eittreim *et al.*, 1969; Armi and Millard, 1976; McCave and Tucholke, 1986), and particularly under the DWBC (Amos *et al.*, 1971; Eittreim *et al.*, 1975; Biscaye and Eittreim, 1977). They are particularly thick (O 150 m) where the current flows along a slope that favors downwelling bottom Ekman-layer transport (Trowbridge and Lentz, 1991; De Madron and Weatherly, 1994; Ramsden, 1995). The smaller included layer is the dynamic bottom boundary layer (BBL) close to the seafloor (O 40 m) where bottom friction significantly reduces the current's velocity and increases turbulent mixing. This layer is less easily observed but more important to the dynamics of bottom-trapped currents. The BML is often taken to represent the BBL based on the theory that velocity shear drives steady mixing that keeps the layer unstratified, but beyond this active region the ocean restratifies. This correlation between BML and BBL heights has been observed frequently on the continental shelf (Caldwell, 1978). Deep ocean measurements of velocity and turbulence near the bottom are fewer.

Various models have been developed that relate bottom slope, stratification, rotation, and stress to the height of the BBL under persistent and transient current velocities. These 1- and 2-D models also seek to quantify the dynamic effect the BBL has on the overlying current, particularly as it relates to friction (Weatherly and Martin, 1978; Trowbridge and Lentz, 1991; MacCready and Rhines, 1993; MacCready, 1994; Chapman and Lentz, 1997). In a few deep ocean studies using current meters, some models successfully predicted BBL velocity and structure but were less successful in predicting the thicker BML that was observed (Bird *et al.*, 1982; D'Asaro, 1982). Armi and Millard (1976) observed a BML up to six times thicker than the BBL in the Hatteras Abyssal

Plain. Our observations also show a BML up to five times thicker than the BBL on the slope of the BOR.

4.2 Observations at the BOR

A frictional bottom boundary layer was observed everywhere under the DWBC, where velocities rotate approaching the bottom in the correct sense for an Ekman spiral. The along-slope flow was bottom intensified with the highest speeds observed at or near the top of the bottom mixed layer. The vertical structure of velocity below the main thermocline (i.e., within the DWBC) was fairly consistent across the current and typified by the profile shown in Figure 13. Velocity continuously increased toward the bottom until uniform stratification within the BML ended the shear. A thick BML was expected here because the slope is favorable for downwelling under a current in the direction of DWBC. A dynamic bottom boundary layer 20–50 m thick formed at the bottom of the BML in which velocity decreased toward zero. The temporal steadiness of the vertical structure is shown by the gray area in Figure 13. This site was near the center of the current so the along-slope velocities were high, but the vertical structure was typical within the DWBC, even where velocities were lower.

The BML velocities were very well aligned with the topography as expected for a bottom-trapped current (see Fig 19). The flow went around the ridge, but only where topography permitted (see Fig. 19b). Some of the current at Section 5 probably passed around the ridge considerably further southeast and traveled back along isobaths as shown by the velocities in Section 4. The velocity and density structure at Sections 2 and 5, as well as the BML heights for each drop, are shown in Figure 12. The BML height was considered to be the point where the buoyancy frequency squared (N^2) (unfiltered) dropped below 2×10^{-7} s^{-2} and remained so to the bottom. The average N^2 10 m above this point was typically 10^{-6} s^{-2}. Note the smooth transition in the overlying isopycnals from nearly horizontal at 2000 m to roughly parallel to the slope near the top of the BML. This symmetrical density structure across the ridge supports the geostrophically balanced deep flow on both sides. Furthermore, the associated pressure field prevents strong cross-ridge flow, even at heights well above the ridge crest.
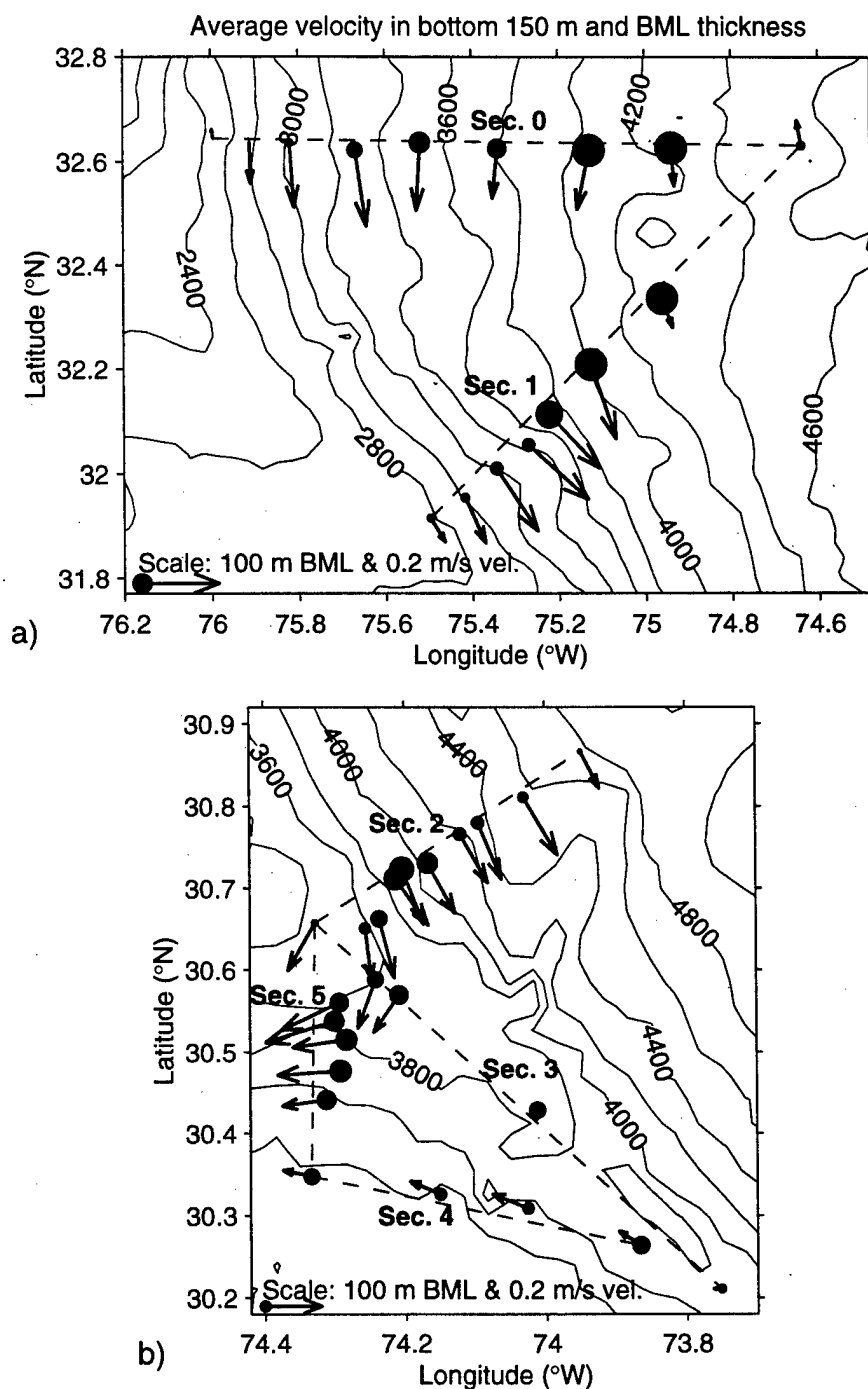
Figure 19: Average velocity vectors in bottom 150 m and thickness of the bottom mixed
layer (BML) on (a) Sections 0 and 1, and (b) Sections 2, 3, 4, and 5. Dot diameter at
base of vectors is proportional to the thickness of the BML. Note different scale
vectors in lower left corner of each panel. Bathymetry is from Smith and Sandwell
(1997); depth is in meters.

Across much of the DWBC at the BOR, the tops of the BML and BBL were not coincident. In regions where the BML was very thick, the BBL remained thinner suggesting that processes other than continuous strong turbulence must be keeping the mixed layer uniform. This is evident when velocity, density, tracer concentrations, and turbulent kinetic energy dissipation rates are examined in the BML (see Fig. 20). In this nine-day time series from Site 2-5, the thickness and density of the BML were steady (Fig. 20a). There was little shear in the along-slope velocity between the top of the BML and the top of the BBL, although there was some variance that could generate low-level turbulence on large scales (O 10 m). Within the BBL, turbulent dissipation of kinetic energy rose several orders of magnitude above the noise floor of the sensors (Fig. 20f). The current rotated in the BBL in a planetary sense such that the across-slope flow became negative (i.e., down-slope) as seen in Fig. 20e. Oxygen and suspended sediment concentrations (Figs. 20b and 20c), derived from nearby CTD casts over the same period as the time series, demonstrated a vertical uniformity like density throughout the BML. The suspended sediment data came from transmissometer measurements of optical beam attenuation, which is a function of the concentration and size of suspended particles in the water (see section 2.3.3). Suspended sediment is useful evidence of mixing because a dynamic process is typically required to keep the concentration vertically uniform against settling forces.

Figure 20: Individual profiles (thin colored lines) and mean profiles (thick black lines) from the bottom 400 m of the nine-day time series at Site 2-5 and nearby CTD casts. For clarity, the leading digit (4) on AVP drop numbers has been omitted. a) Profiles of potential density (σ_3) from all eight AVP drops. b) Profiles of suspended sediment concentration measured by the transmissometer on the CTD using the conversion formula of Haskell (1993). CTD cast 27 was at Site 2-5 and 12 hours after the beginning of the time series (AVP 54). Casts 40 and 41 were 5 km up- and down-stream on the same isobath at 7 and 2 hours, respectively, before AVP 89 near the end of the time series. c) Profiles of oxygen concentration from CTD water samples using modified-Winkler titration method. d) Profiles of along-slope velocity (axis rotation 149˚ from true north). The mean profile is for all eight AVP drops in the time series; however, drops 54, 64, 65, 67, and 69 (the latter four of which were only 11.4 hours apart) were in a slower along-slope current regime than drops 84, 89, and 92, which were taken 4-6 days later. e) Profiles of across-slope velocity (axis rotation 239˚ from north, positive up-slope). f) Profiles of turbulent kinetic energy dissipation rate from AVP drops with good quality data.

a) AVPs 54 64 65 67 69 84 89 92
Potential Density (σ_3 kg/m^3)

b) CTDs 27 40 41
Sus. Sed. Concentration (µg/L)

c) CTDs 27 40 41
Oxygen Concentration (ml/L)

d) AVPs 54 64 65 67 69 84 89 92
Along-slope Velocity (cm/s)

e) AVPs 54 64 65 67 69 84 89 92
Across-slope Velocity (cm/s)

f) AVPs 54 64 65 67 84 89
KE Dissipation Rate (m^2/s^3)
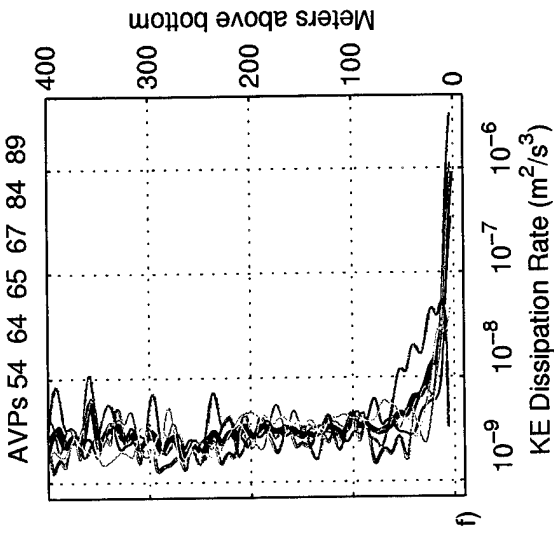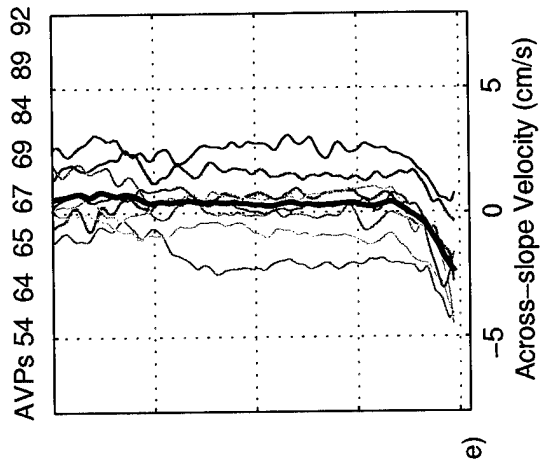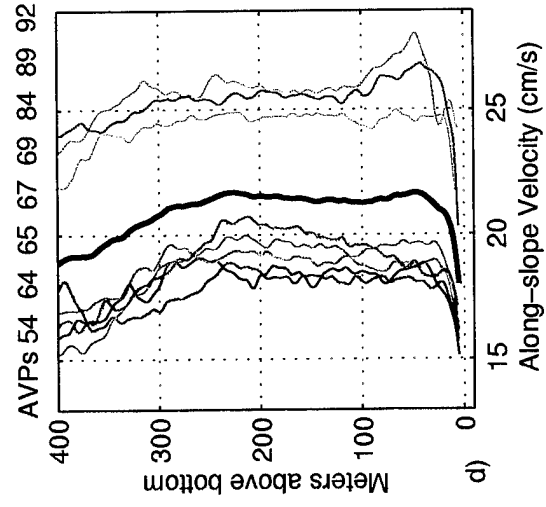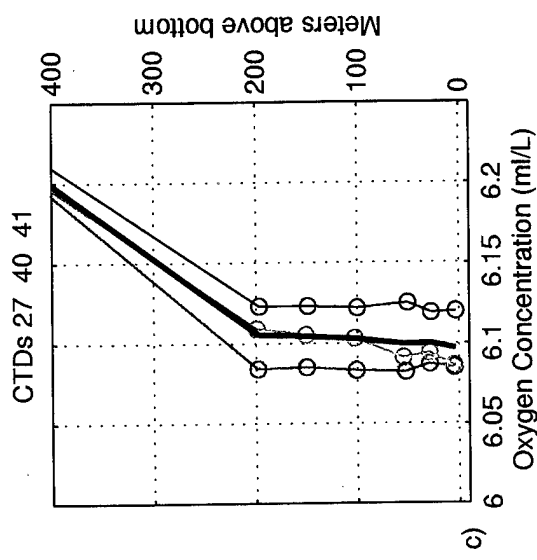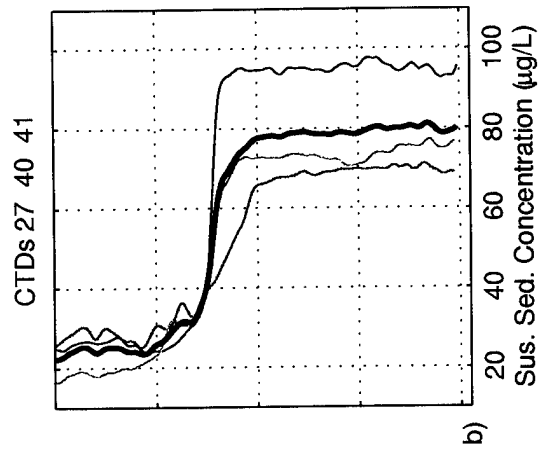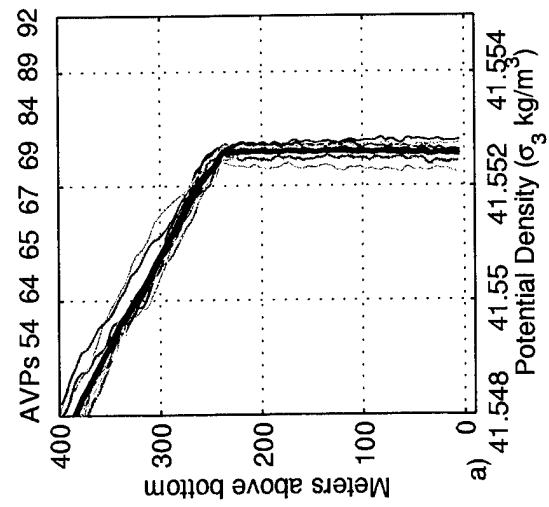
4.3 Bottom Stress

Bottom stress (τ) can be determined from the relationship $\tau = \rho u_*^2$, where ρ is density and u_* is the bottom friction velocity, a useful parameter in BBL studies. In our case, u_* can be calculated from either turbulent kinetic energy dissipation rates or velocity profiles. We applied both methods to 38 AVP drops from Sections 0, 1, 2, and 5, which had DWBC velocities of over 10 cm s^{-1} representing the bulk of the current. To use the measurements of turbulent kinetic energy dissipation rate (ε), one assumes a balance of production and dissipation of kinetic energy in the BBL that leads to the equation $u_{*_\varepsilon} = (\kappa z \varepsilon)^{1/3}$ (Johnson et al., 1994a), where κ is von Karman's constant (taken here as 0.41), and z is distance above the bottom. For the 38 drops, an average $u_{*_\varepsilon} = 0.56 \pm 0.19$ cm s^{-1} was found from ε measurements in the last 15 m of the profile (AVP measured to within 5 m of the bottom). Alternately, one can fit a log function to the near-bottom velocity profile based on the relationship $U(z) = u_* ln(z/z_0)/\kappa$, where z_0 is a bottom roughness length defined by $U(z_0) = 0$ (Newberger and Caldwell, 1981). For the same 38 drops, with velocities rotated into the direction of maximum stress and a typical fit length of 10 m of each profile, this method produced an average $u_{*_v} = 0.96 \pm 0.56$ cm s^{-1}. The bottom stress and turbulent dissipation increase with increased velocity in the overlying DWBC, as expected. Under the high-speed core of the current (22 drops on Sections 2 and 5 where the BML velocity is > 18 cm s^{-1}) we found an average of $u_{*_v} = 1.2$ cm s^{-1} and up to 2.6 cm s^{-1} for one drop. The values of stress calculated by each method for each drop used in the analysis is shown in Figure 21 with the average values being $\tau_\varepsilon = 0.033$ Pa and $\tau_v = 0.096$ Pa.
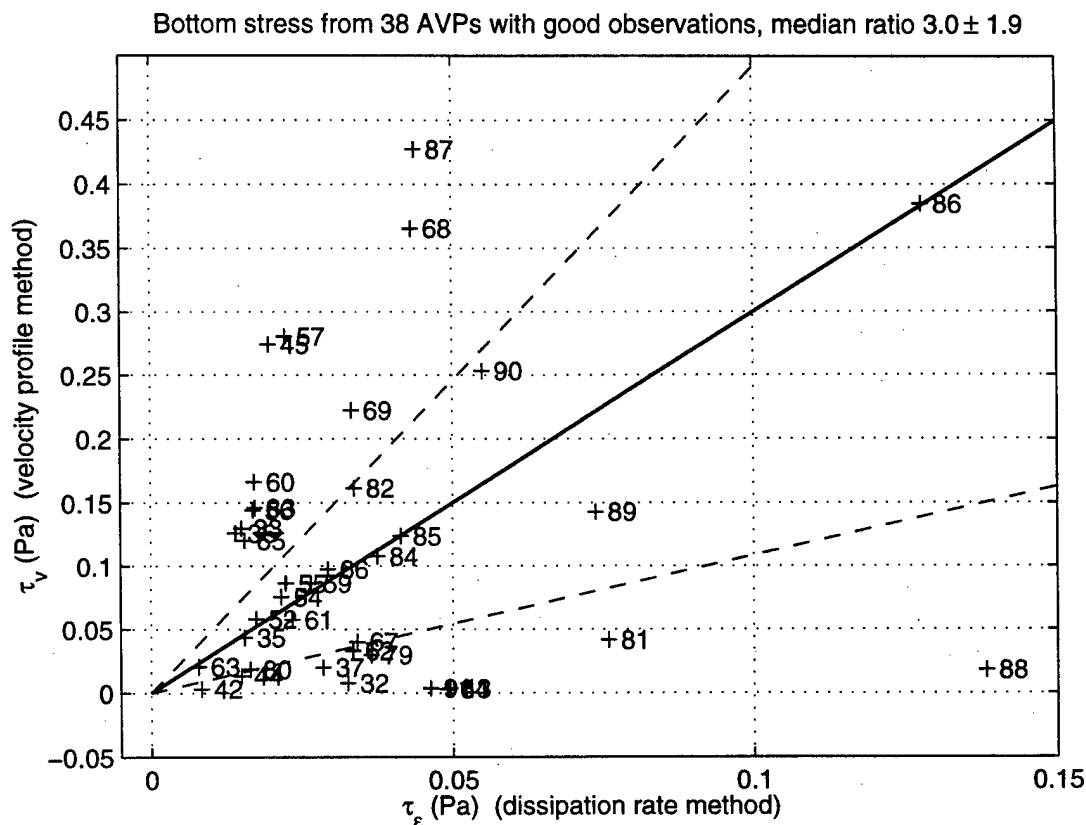
Figure 21: Bottom stress calculated by both velocity profile and dissipation rate methods from 38 AVP observations with good data for dissipation rate. Median ratio of 3:1 is shown (solid line) with standard deviation of ± 1.9 (dashed lines). Drops are labeled with leading digit (4) removed.

The fact that τ_v (velocity method) is about three times higher than τ_ε (dissipation method) is not unexpected. Johnson *et al.* (1994a) found the two methods differed by a factor of 3.1 in the Mediterranean outflow, and Dewey and Crawford (1988) found a difference of about 4.5 on the continental shelf. Sanford and Lien (1998) investigated the different methods with observations in a tidal channel and found that the methods matched only within the bottom 3 m; above that, the velocity profile followed a different log-curve which yielded a stress about three times higher than the dissipation-derived value. All three studies suggest that form drag from meter-scale and larger bottom topography is responsible for the difference. This probably occurs at the BOR as well, based on bottom photographs from the area (Heezen *et al.*, 1966) showing irregular features. Several AVP profiles showed increasing velocity in the last few data points (typically 5-8 m above the

bottom) suggesting the current was reacting to local bottom roughness such as sand waves or slumps. Johnson *et al.* (1994b) found the best closure of the overall energy budget in the Mediterranean overflow was provided by the stress estimated using the velocity-profile method.

Because u_{*_v} and u_{*_ε} are sometimes not clearly determined from the observations, a third method for calculating friction velocity was used. The overlying DWBC flow that drives the turbulent BBL can be related to friction velocity through an empirical drag coefficient, $C_d = u_*^2/U^2$. A drag coefficient is typically used for parameterizing bottom stress in models. Observational values for C_d are usually created from U measured 1 m off the sea bed (Weatherly and Martin, 1978). But without measurements in that range, we used the mean velocity above the BBL within the BML. For the 38 drops used to find the mean values before, we found $C_d = 4 \times 10^{-3}$ using u_{*_v} with the overlying velocity, or $C_d = 1.9 \times 10^{-3}$ using u_{*_ε} instead. These values bracket the 2.5×10^{-3} value that is often used in models (MacCready, 1994) and the upper value is the same as that found by Lueck and Lu (1997) in a tidal channel. The primary advantage of using u_{*_d} (friction velocity from $(C_d U^2)^{1/2}$) is that it is less susceptible to near-bottom variability and provides more uniformity in parameters calculated from it, such as the height of the BBL, $h = \kappa u_*/f$ (Wimbush and Munk, 1970). Defining the BBL height directly from observations of velocity shear and turbulence is more difficult due to the variability in those observations. To illustrate this, the BBL height for Section 1 was calculated using the values of u_{*_v}, u_{*_ε}, u_{*_d}, and then determined by examining the observations of velocity and ε for the height at which they become the same as the "background" levels. As seen in Figure 22, the BBL height found using u_{*_d} best reflect the velocity of the overlying DWBC. Other parameters calculated from u_{*_d}, such as bottom stress, would similarly reflect the strength of the DWBC better.
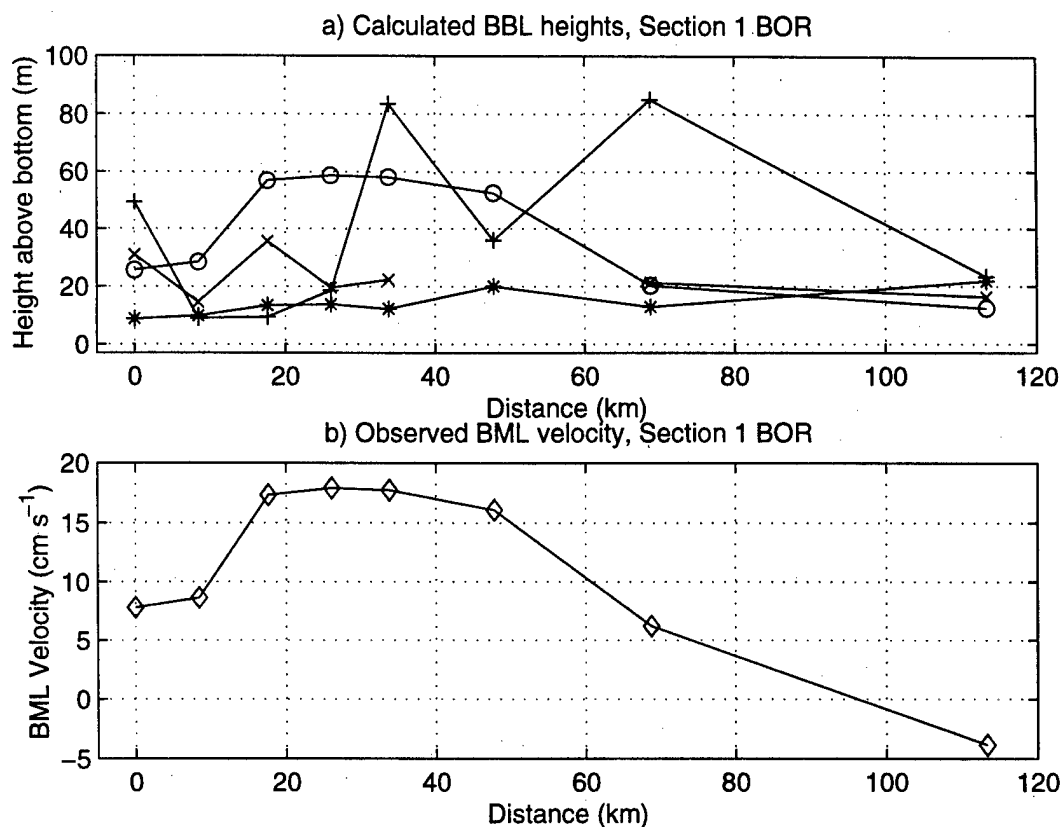
Figure 22: a) Bottom boundary layer heights in Section 1 calculated from u_{*_v} (+), u_{*_ε}(x), u_{*_d} (o) (using $C_d = 4 \times 10^{-3}$), and direct interpretation of velocity and ε profiles (*). b) Velocity of the DWBC within the BML in Section 1.

The effect of the observed bottom stress on the energy and momentum balance of the DWBC can be considered in light of two general models. The first is that of a stream-tube flowing along a slope as described by Smith (1975). Although this model was developed to examine overflows, solutions were presented for the case far down-stream of the overflow point where entrainment is negligible, the current is principally along isobaths, and bottom stress is still important. At the BOR, the bottom-intensified velocity structure, the thick BML with almost uniform across-slope density, and a noticeable drop in the depth of the velocity core as it proceeds along the ridge suggest such a formulation applies with the thick BML as the stream-tube. Smith related bottom and entrainment stress to the current velocity by the formula $\rho K U^2 = \int (\tau_b + \tau_e)dx$, where ρ is the density, K is a friction parameter, U is the mean velocity, τ_b is the bottom stress, τ_e is the

entrainment stress, and x is the across-slope direction. Based on Smith's work, Griffiths (1986) found in the far down-stream case (where there is no entrainment, a homogenous environment, constant velocity, constant area, and constant density contrast) the angle between the isobaths and the direction of the flow is related to the bottom stress by the formula $\beta = KU/fA$, where β is the angle, and A is the area of the stream-tube. From our observations of the BML at Sections 1 and 2, we determined $\beta \approx 0.06$ by solving Smith's equation for K using our values for stress and velocity, and then using values from Table 10 with the derived K in Griffith's equation for β. Multiplying β by the 180-km distance between the sections, the core of the current should move down-slope across isobaths by 10.8 km, which it approximately did (see Fig. 10). Determining the center of the observed velocity core by a velocity-weighted calculation yields a depth of 3517 m at Section 1 and 4076 m at Section 2, a difference of 559 m. The along-slope distance between those isobaths at Section 2 is 12.5 km, close to the 10.8 km derived using the model. Section 0 was not used in this analysis because it shared a common end station with Section 1, making it difficult to define an accurate along-stream distance.

Table 10: Mean bottom mixed layer characteristics at the Blake Outer Ridge.

Sec. #	Core Vel. (m s^{-1})	Depth of Vel. Core (m)	Mean BML Density (kg m^{-3})	Mean Density Anomaly (kg m^{-3})	Area (10^6 m^2)	Width (km)	Mean Height (Area/W) (m)	Mean Bottom Stress (Pa)
0	0.115	3550	1043.8	0.0212	11.3	83	136	0.078
1	0.127	3517	1043.8	0.0127	10.9	94	116	0.069
2	0.168	4076	1046.0	0.0138	5.2	43	122	0.113
avg. Sec. 1&2	0.148	(Δ = 559)	1044.9	0.0133	8.1	68.5	119	0.092

Baringer and Price (1997) also used Smith's work to examine the Mediterranean outflow and developed the following along-stream momentum balance:

$$\frac{\partial}{\partial y}\left(\rho_o \bar{v}^2 \bar{h} W\right) + W\frac{\partial}{\partial y}\left(\frac{1}{2}g\delta\rho\bar{h}^2\right) - g\delta\rho\bar{h}W\frac{\partial \overline{D}}{\partial y} = -W(\bar{\tau}_b + \bar{\tau}_e)$$

where overbar indicates the mean within the stream-tube, y is the along-stream direction, ρ_o is a background density, v is the velocity, h is the thickness, W is the width, $\delta\rho$ is the density anomaly between the stream-tube and the background, and D is the velocity-weighted depth of the current core. The first term denotes the along-stream change in the kinetic energy and the second is the change in the internal potential energy. The third term represents the change in the external potential energy as driven by the change in depth of the velocity core, and the righthand side of the equation is the stress. We can use the values given in Table 10 to estimate the terms of this balance between Sections 1 and 2. Note that τ_e is taken to be zero and the along-stream distance between sections is 180 km.

The first term (ΔKE) is about 0.3×10^8 J m^{-1} and the second (ΔIPE) about 0.05×10^8 J m^{-1}, both small. The larger terms are the third one (ΔEPE), about 6.6×10^8 J m^{-1}, and the stress term on the righthand side, about 10.2×10^8 J m^{-1}. These two terms approximately balance one another. One reason these terms may not balance more closely in this case is that the stress on the top of the mixed layer (usually from entrainment) may be of an opposite sign to that of the bottom stress, i.e., a higher flow speed pushing the top of BML instead of retarding it as entrainment would. This would reduce the value of the stress term and seems plausible given that velocity increased from the mid-water column to the top of the BML, indicating BML speed would be higher if not for bottom stress and the unstratified BML. By these calculations, it is evident the dominant terms here are external potential energy and bottom stress. This was also true at the Mediterranean outflow, except that there entrainment stress was also important.

Two caveats should be noted with regard to the stream-tube analysis and results. First, this reflects only the velocity core of the DWBC which is not necessarily coincident with its tracer core. We did not measure CFC or other anthropogenic tracer concentrations to locate a DWBC tracer core as others have (Pickart and Smethie, 1993). However, the velocity core at Section 2 was located where the DWBC tritium core was found in observations along the same section taken by Jenkins and Rhines (1980); both

were tightly trapped to the bottom and about 20 km down-slope from the ridge crest. This provides some confirmation that the stream-tube model is accurate for the velocity core between Sections 1 and 2. The second caveat is that the DWBC cannot sustain this amount of along-stream deepening in its core depth for any great distance. By this model, change in core depth is a function of bottom stress, which is a quadratic function of mean current speed. Where the speed and stress are smaller (as under most other parts of the current) there may be little along-stream deepening of the current core. In some places further north in the Atlantic, the tracer core even appears to rise along-stream (R. Pickart, personal communication).

The second general model of how bottom stress affects an abyssal current flowing on a slope draws upon the overlying density structure to modify the current's BBL and overcome the bottom stress. This model is partly based on the tenet that the return of the down-slope Ekman transport within the BBL manifests itself throughout the current above. The area affected by the return flow is an ellipsoid whose dimensions are defined by the relationship $NH/fL \approx 1$, where N is the buoyancy frequency, and H and L are the height and width of the current (Garrett et al., 1993). Using the values in Table 9 for H, L, and f, and an observed value of 1.2×10^{-3} s^{-1} for N, this is satisfied only at Section 2, while at Sections 0 and 1, $NH/fL \approx 1/2$. MacCready (1994) suggested the longevity of the DWBC arises from a high ratio of internal potential energy to kinetic energy within the current and the sloping bottom plays a key role in modifying the across-slope BBL density structure to reduce friction. Chapman and Lentz (1997) created a similar model that indicates the bottom velocity is completely stopped by an across-slope flow within the BBL such that no stress impinges on the overlying current despite bottom friction. Both models assume a uniform horizontal density field surrounds and intersects the top of the BBL, which is taken to be the same as the BML. In the Chapman and Lentz model, a fairly strong horizontal density gradient is required within the BML to create the along-slope flow necessary to arrest the velocity at the bottom (see Fig. 23). However, our observations reveal a density field nearly parallel to the top of the BML intersecting it at very slight angles on the up-slope side of the current only (see Fig. 24). Little across-slope density gradient was detected within the BML and the BBL was typically thinner than the BML across much of the current (see Fig. 25).
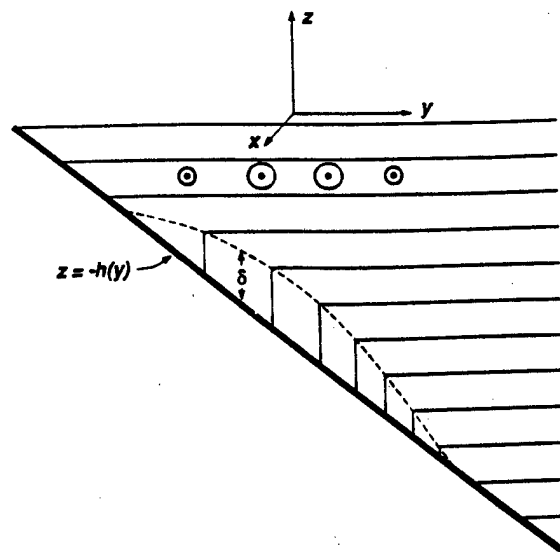
Figure 23: Model geometry and stratification from Chapman and Lentz (1997). Isopycnals are continuous across the top of the bottom boundary layer which is completely mixed in the vertical.
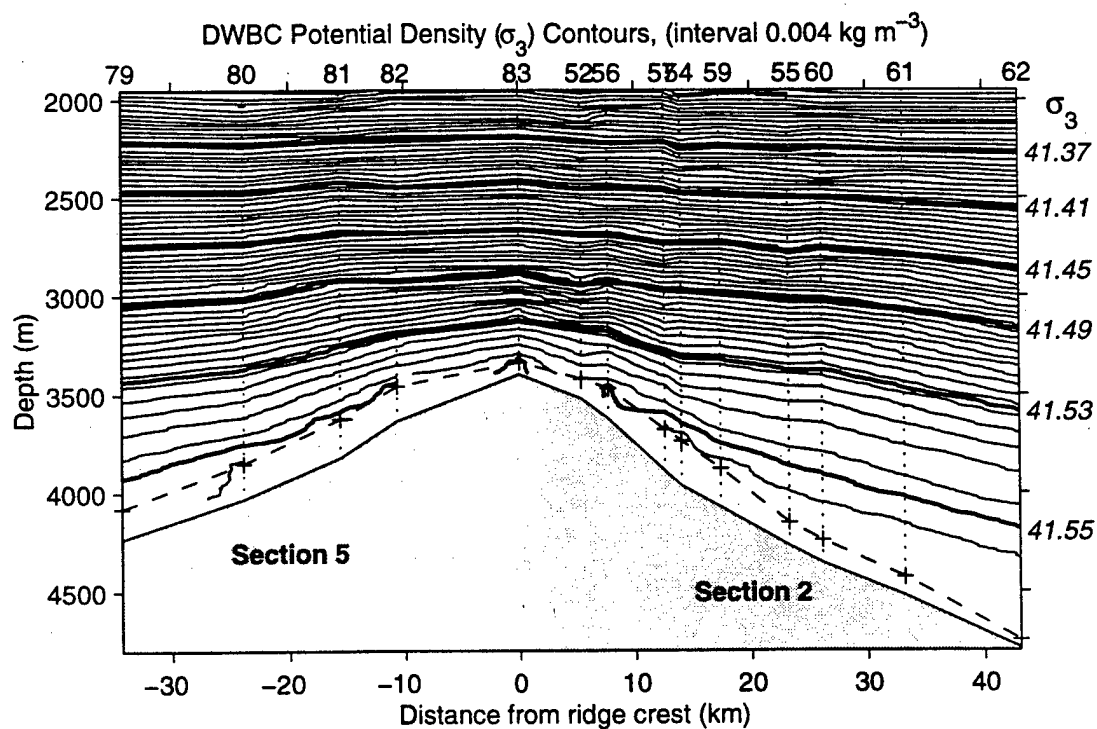
Figure 24: Potential density (σ_3) field across the BOR at Sections 5 and 2.

MacCready (1994) calculated spin-down times (i.e., the time needed for the energy to decrease by a factor of 1/e) for abyssal currents flowing on slopes using various values of background stratification, bottom slope, and kinetic energy dissipation due to bottom stress. From an analytic model he suggested the ratio of potential to kinetic energy relates to the buoyancy frequency (N) and bottom slope (α) by $PE/KE = (f/N\alpha)^2$. At the BOR, α ranges from 0.018 at Section 0 to 0.038 at Section 2 and $N/f \cong 15.5$ on all sections. By this formulation the PE/KE ratio at the BOR should range from 13 to 3. Using observations from two previously published DWBC data sets, MacCready ascertained PE/KE ratios of 10 and 41 . He suggested an average ratio > 25 helps explain the longevity of the current. Using the same technique to determine PE and KE from our data, we found ratios between 14 and 4 (see Table 11). While these are close to the range calculated using the model (13-3), they are not close to the value of 25 MacCready suggested sustains the current. However, the model indicates the ratio is sensitive to bottom slope, which is larger here than in other areas of the basin. The high ratio at Section 0 is primarily due to an elevated density structure on the near-shore end (high PE), while the lower ratios on subsequent sections are from high current velocities (high KE). PE was calculated using the mean vertical elevation (Δz) of isopycnals (in divisions of 0.01 kg m^{-3}) on inner stations relative to the outer-most station of a section. The outer station served as a proxy for one unaffected by the current. The Δz values were used in the equation PE (per unit length along stream) $= \Sigma(1/2)\rho N^2 \Delta z A$, where A is the area of each isopycnal increment, N is the mean buoyancy frequency for the DWBC (nearly constant), and the summation is for each drop and across each section. KE was calculated using the equation KE (per unit length along stream) $= \Sigma(1/2)\rho v^2 A$, where v is the velocity in each element and the summation is the same as for PE.

Table 11: Potential and kinetic energy per unit length along-stream for DWBC.

	Section 0	Section 1	Section 2
PE (J/m)	8.97×10^9	3.39×10^9	3.72×10^9
KE (J/m)	6.52×10^8	7.61×10^8	5.84×10^8
Ratio PE/KE	13.8	4.5	6.4

To determine the actual spin-down time, an estimate of the time needed for bottom stress to drain the current's energy by kinetic dissipation is required. This was calculated by dividing the vertical integral of the current's *KE* by the vertical integral of the *KE* dissipation rate. We used the equation $\varepsilon = u_{*_v}{}^3/\kappa z$ (Newberger and Caldwell, 1981) to calculate a dissipation rate rather than the direct ε observations because u_{*_v} more accurately represents the full drag on the DWBC. Using $u_{*_v} = 0.96$ cm s^{-1} to find ε in the BBL and assuming $\varepsilon \sim 10^{-10}$ m^2 s^{-3} above that, we found a time of 14 days by integrating from 5 to 2800 m above the bottom (see Table 9). Multiplying this by the *PE/KE* ratios of 14 and 4, we determined spin-down times of 196 to 56 days. Assuming the current sustains a speed of 7.5 cm s^{-1}, it could travel 1270 km in 196 days, a long distance but not basin scale. Another technique to calculate spin-down time is to use the relationship MacCready (1994) derived from his model that $T_{sd} = (PE/KE)(H/2C_dV)$, where T_{sd} is spindown time, H is the average height of the current, V is the average velocity of the current, and C_d is a drag coefficient. Typically, C_d is taken as 2.5×10^{-3}, but in this we can use our calculated value of 4×10^{-3}. Employing data from Table 9 and a *PE/KE* ratio of 14, we found a spin-down time of ~750 days. This allows the current to travel ~4900 km, closer to basin scale but still not the full length it travels. These calculations are for local values of speed and stress just as for the stream-tube model. The steeper slope at the BOR leads to stronger local velocities than for most of the DWBC. The higher velocities lead to higher local stresses and, therefore, lower spin-down times.

4.4 Bottom Mixed Layer Structure

Determining the effects of bottom stress on the DWBC was the primary reason for investigating the bottom boundary layer but the observations also allow an examination of the processes that shape and sustain the thick bottom mixed layer under the DWBC. A number of models have been proposed for BML development under a steady, stratified, along-isobath current flowing over a frictional sloping bottom (Weatherly and Martin, 1978; Trowbridge and Lentz, 1991; MacCready and Rhines, 1991; Ramsden, 1995; Chapman and Lentz, 1997). In general, the models are 1-D and assume the mixed layer thickness is characterized by (1) turbulent mixing due to bottom stress or velocity shear, (2) a vertically uniform current above the mixed layer, (3) uniform and horizontal overlying stratification, and (4) planetary rotation (Weatherly and Martin, 1978). On a slope in the northern hemisphere which is shallower to the right of the current looking down-stream, the bottom Ekman transport increases the thickness of the BML by moving lighter water down-slope, thus eroding the overlying stratification. A density profile such as that shown in Figure 20a is produced by all BML models for this current and slope regime. Density profiles such as these were also observed in deep boundary currents on slopes in South Atlantic (De Madron and Weatherly, 1994). In flat regions, the density profile has a strong capping stratification (steeper slope than the background above) produced by local bottom mixing, such as shown by Armi and Millard (1976).

Most of these models, however, include some assumptions that are inconsistent with our observations. Typically, the BML and BBL are thought to have the same thickness based on the theory that vertical uniformity of properties is only sustainable by strong mixing driven by velocity shear due to bottom friction. This appears not to be the case at the BOR where most of the BML velocity is unsheared, except in the dynamic BBL (see Fig. 20). Spectral analysis of BML velocities above the BBL shows variance over vertical wavelengths of 20-100 m that is consistent with isotropic turbulence ($\varepsilon \approx 10^{-9}$ m^2 s^{-3}), but this is unaccounted for in the models. In addition, all models assume the BML velocity is less than the overlying interior velocity, but at the BOR the opposite is true (see Fig. 13). Finally, most models assume the BML intersects a horizontal interior density structure over a large range of densities and at a distinct angle, while the observed density structure at the BOR transitions smoothly from horizontal to nearly bottom parallel before intersecting the top of the BML over a very small range of isopycnals (see Fig. 12).

The across-stream structure of the current was examined at Sections 0 and 1 (see Fig. 25). These sections were chosen because they cover the full width of the current and range of DWBC speeds. The structure of the boundary layers in Section 0 and 1 is asymmetrical, with the thicker part down-slope, whereas the along-slope velocity is asymmetrical up-slope of the center (see Figs. 19 and 25). The bottom Ekman layer transport is maximum approximately under the core of the current. At the point where the sign of the gradient changes (i.e., the transport becomes convergent), the BML starts thickening beyond the height of the BBL. This continues as more light water is advected down-slope and the BML thickens to 5 times that of the BBL in Section 2. The overlying density stratification is very weak, offering little resistance to the thickening. The across-slope density difference within the BML, and the density contrast between the BBL and BML, diminish after the Ekman transport inflection point (see Fig. 25e). Farther down-slope, the density difference being driven by the Ekman transport is very weak. Also the Ekman transport decreases because the DWBC velocity decreases. Both effects tend to reduce the BML height back toward that of the BBL. Some fluid may escape the BML at the down-slope end but our observations were insufficient to observe this.
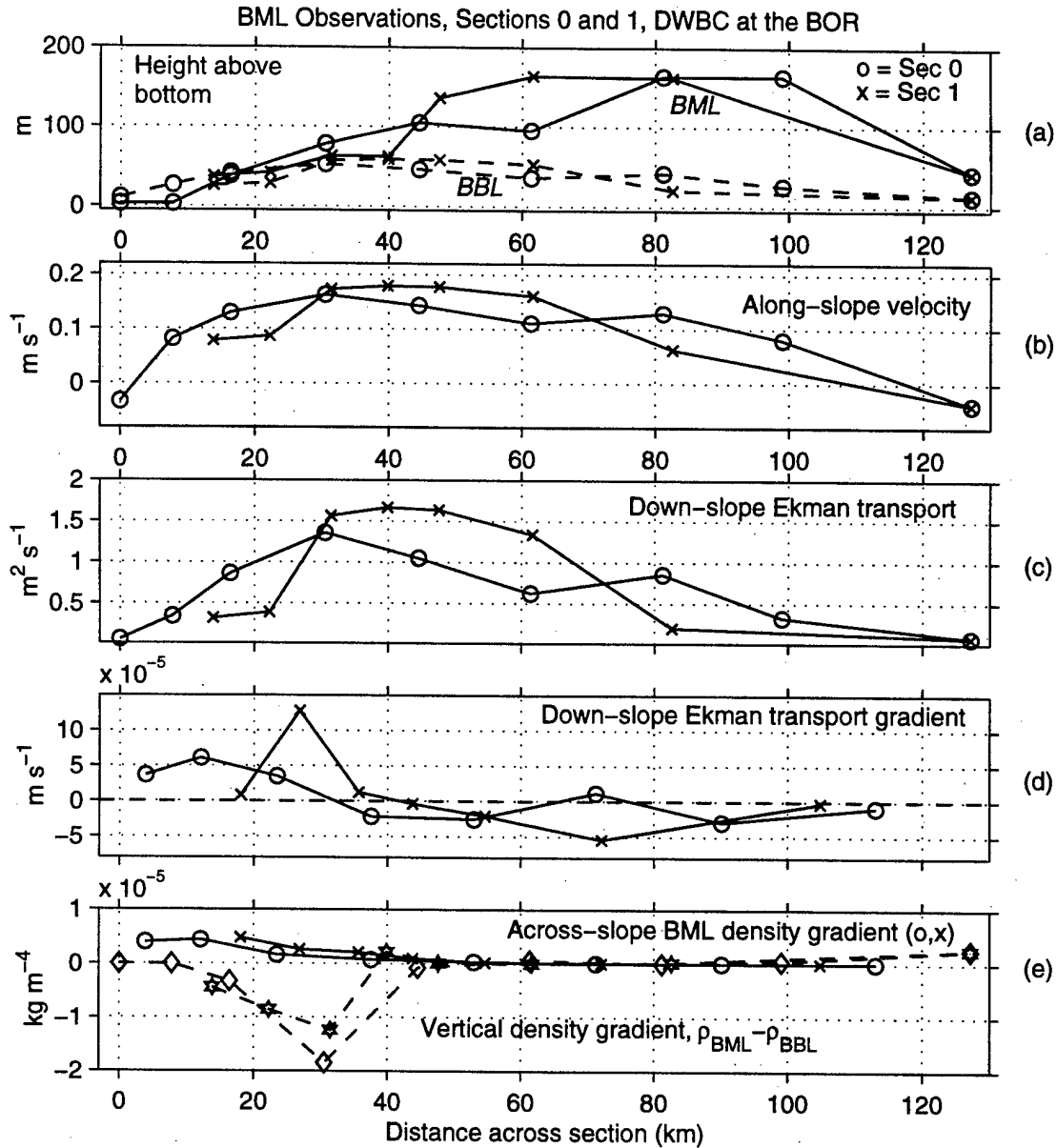
Figure 25: Observations from the bottom mixed layer (BML) in Sections 0 (o) and 1 (x). The outer-most station is the same for each section. (a) Heights of the BML (solid line) and Ekman-like bottom boundary layer (BBL) (dashed line). (b) Mean along-slope DWBC velocity within the BML but above the BBL. (c) Ekman volume transport per unit width within the BBL. (d) Across-slope gradient of Ekman volume transport per unit width. (e) Across-slope (horizontal) gradient of average density within the whole BML (solid lines), and vertical gradient of average density difference between the upper BML and BBL (dashed lines, ♦ for Sec. 0, * for Sec. 1).

The vertically uniform concentrations of suspended sediment shown by the transmissometer (see Fig. 20b) provide the most direct evidence that a dynamic process is at work in the upper BML because the sediment is always under the influence of gravity. The settling velocity of sediment particles is related to size, which we measured through scanning electron microscopy of our filters and laser particle sizing of one bottom sample. The microscopy yielded an average particle diameter of about 1 μm and the laser sizing showed an average of 2.5 μm. Aggregation of particles in abyssal boundary layers is common and an important component of determining settling velocity (McCave, 1984b). The filtered samples were mostly disaggregated by the filtering process, although the bottom sample may not have been. Regardless, the 1 μm diameter acts as a lower bound and has a settling velocity of 3.6×10^{-7} m s^{-1} from the model of McCave (1984). Typical aggregate sizes are much larger, $O(250 \mu$m), rendering a settling velocity of $\sim 5 \times 10^{-4}$ m s^{-1} (R. Sternberg, personal communication). The maximum time required for the particle concentration to return to a stratified background shape can be determined by multiplying the height of the BML by the settling velocity, establishing a range of 6 to 7700 days. Particle size and aggregation are therefore the key parameters determining what vertical velocity is needed to maintain a uniform suspended sediment concentration in the BML.

Both advective and diffusive mechanisms could create this uniform concentration. Within the BBL, values of the turbulent diffusion coefficient were estimated from the near-bottom turbulent log-layer as $K_v = \kappa u_* z$, and from the Ekman layer heights as $K_v = 1/2 \, h^2 f$, giving a range from 2 to 8×10^{-2} m^2 s^{-1}. Using concentrations of excess radon at bottom sites on the BOR, Eittreim et al. (1975) reported values between 1 and 2.6×10^{-2} m^2 s^{-1} for K_v in the bottom 300 m including both the BBL and BML. However, high in the BML, where turbulence is low and concentrations remain uniform, diffusion seems less likely because property gradients are low.

To investigate an advective–diffusive balance for suspended sediments within the BML, an expression modified from that of Taylor and Dyer (1977) can be used:

$$\frac{\partial \overline{C}}{\partial t} + \nabla \cdot \overline{VC} = -\frac{\partial w_s \overline{C}}{\partial z} - \nabla \cdot K_s \nabla \overline{C}$$

where the overbar denotes a time average, C is the sediment concentration (assumed to be for single sized particles), V is the water velocity, w_s is the particle settling velocity, and K_s is a turbulent diffusion coefficient. Note that w_s is negative for grains more dense than seawater. The steady-state, 1-D balance in the vertical is

$$(\overline{W} + w_s)\overline{C} = -K_s \frac{\partial \overline{C}}{\partial z} + G$$

where G is an arbitrary function independent of z and assumed to be zero. There is little vertical variation to $\overline{C}$, which has a mean of 80 μg l^{-1} at Site 2-5 (see Fig. 20b) and a vertical gradient of about 10^{-2} μg l^{-1} m^{-1}. In the BML, K_s is greater than the value of the molecular diffusivity of momentum (about 10^{-6} m^2 s^{-1}) and less than the K_v computed above for the BBL. Using the maximum value of K_s as an upper bound (8×10^{-2} m^2 s^{-1}), then the upper bound on $(\overline{W} + w_s)$ is 10^{-5} m s^{-1}. This velocity is sufficiently small that in the BML the balance could simply be $(\overline{W} + w_s) = 0$ and the vertical component of the local advective velocity $(\overline{W})$ is opposite of and greater than or equal to the settling velocity of the sediment grains (w_s).

The advective velocity necessary to keep the upper BML uniform could come from weak turbulence on large spatial scales which is undetectable by the shear probes. BMLs up to five times thicker than the associated Ekman layers were observed in the Hatteras Abyssal Basin by Armi and Millard (1976). D'Asaro (1982) analyzed the current meter records from those sites for evidence of turbulence above the Ekman layers and suggested the entire BML is at least intermittently turbulent due to velocity fluctuations at near-inertial and tidal frequencies. To investigate whether large scale BML velocity fluctuations at the BOR are responsible for the uniform tracer structure, the velocity profiles of the nine-day time series at Site 2-5 were examined in the region above the BBL but below the top of the BML. The mean for each profile was removed and the resulting mean standard deviations (rms) for all profiles were 0.66 cm s^{-1} in the along-slope direction and 0.46 cm s^{-1} in the across-slope direction (see Fig. 26). These values correspond to the magnitude reported by Armi (1977) above a turbulent Ekman layer. He noted that for fully developed turbulence, velocity fluctuations (u') are to the mean velocity (U) according to $u' \approx U/40$. Using that formula with our mean velocity (21 cm

s^{-1}), fluctuations should be about 0.53 cm s^{-1}, a value very close to the observed ones, especially the mean rms for the two components (0.57 cm s^{-1}).
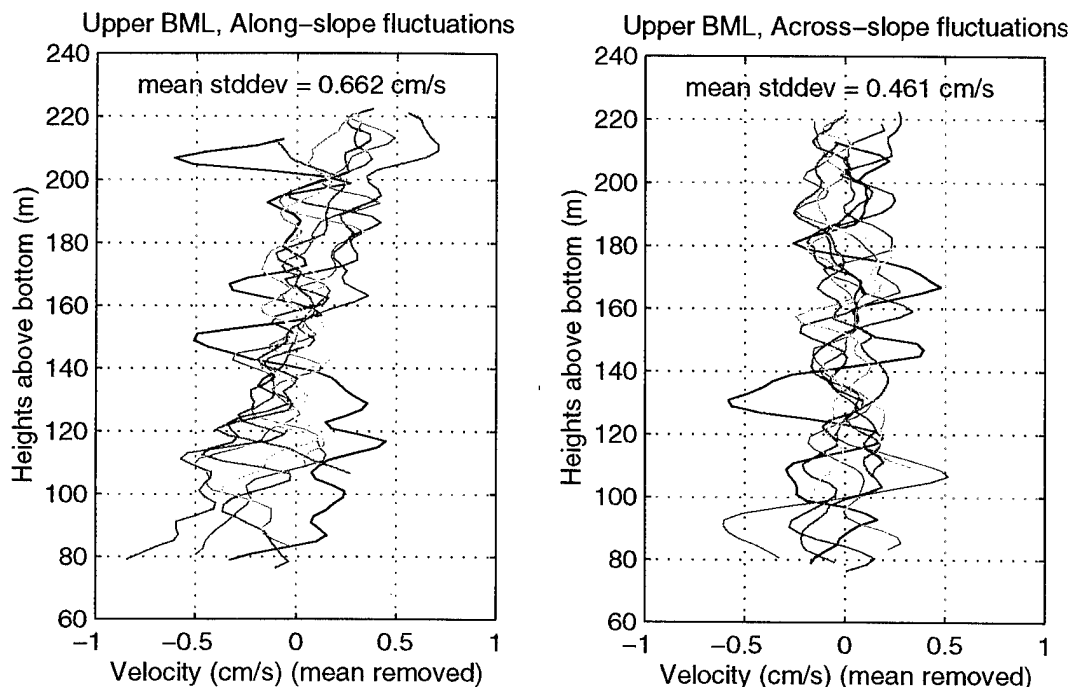
Figure 26: Velocity fluctuation profiles from AVP time series at Site 2-5.

To determine if these fluctuations represent instrument noise or the actual environment, spectra of the velocity fluctuations were calculated from the unfiltered profiles (i.e., 2 m data) of the time series in the upper BML (see Fig. 27). A mean spectrum with no relation to vertical wavenumber (k_z) is expected for instrument noise. However, the mean spectrum for these drops has a dependence of $k_z^{-5/3}$ in the range 1-5 x 10^{-2} cpm (wavelengths 20-100 m) indicating isotropic turbulence in the inertial subrange (Tennekes and Lumley, 1972). The noise level of the instrument appears below wavelengths of 20 m where the mean spectrum is white and has a value of 3.5 x 10^{-5} m^2 s^{-2} cpm^{-1}. This corresponds to an rms velocity fluctuation of about 0.3 cm s^{-1}. Turbulent dissipation rate (ε) can be calculated from the formula $\phi_v(k_z) = (4/3)(18/55)\alpha\varepsilon^{2/3}k_z^{-5/3}$, where α is taken as 1.5 and $\phi_v(k_z)$ is the velocity

spectral density (Tennekes and Lumley, 1972). From these spectra, an ε of about 1.5 x 10^{-9} m^2 s^{-3} was calculated and plotted on Figure 27 (dashed line). The spectra were calculated using a multitaper technique (Percival and Walden, 1993).

Using this value of turbulent dissipation rate, we can estimate the Reynolds stress ($\overline{u'w'}$) from the equation $\varepsilon = \overline{u'w'}\,(dU/dz)$, where dU/dz is the mean along-slope shear in the BML. Examining the along-slope fluctuations in Figure 26, a mean shear of 3.6 x 10^{-5} m^2 s^{-1} is estimated. Combining this with ε from the mean spectrum, Reynolds stress is estimated as 4.2 x 10^{-5} m^2 s^{-2}. The square root of this is 0.65 cm s^{-1}, approximately the rms of the along-slope velocity fluctuation, implying a relation such as $\overline{u'w'} \approx u_{rms}'^2$. However, for this to be true, u' and w' should be well correlated, which is neither expected nor observed in homogeneous turbulent boundary layers. Sanford and Lien (1998) report $\overline{u'w'}^{1/2} \approx 0.4 u_{rms}'$ in a fully turbulent homogenous tidal flow. The relationship $\varepsilon = \overline{u'w'}\,(dU/dz)$ ignores temporal changes in TKE and vertical buoyancy flux, which may play an important role in this boundary layer.

Both analyses demonstrate the velocity fluctuations in the BML above the BBL produce a fully turbulent layer with large spatial scales (O 10's of meters) and low dissipation rates. Other advective components, such as upslope recirculation and buoyant convection, are probably acting in addition to this turbulence to keep tracer concentrations uniform.

BML velocity spectra from 9–day time series at Site 2–5
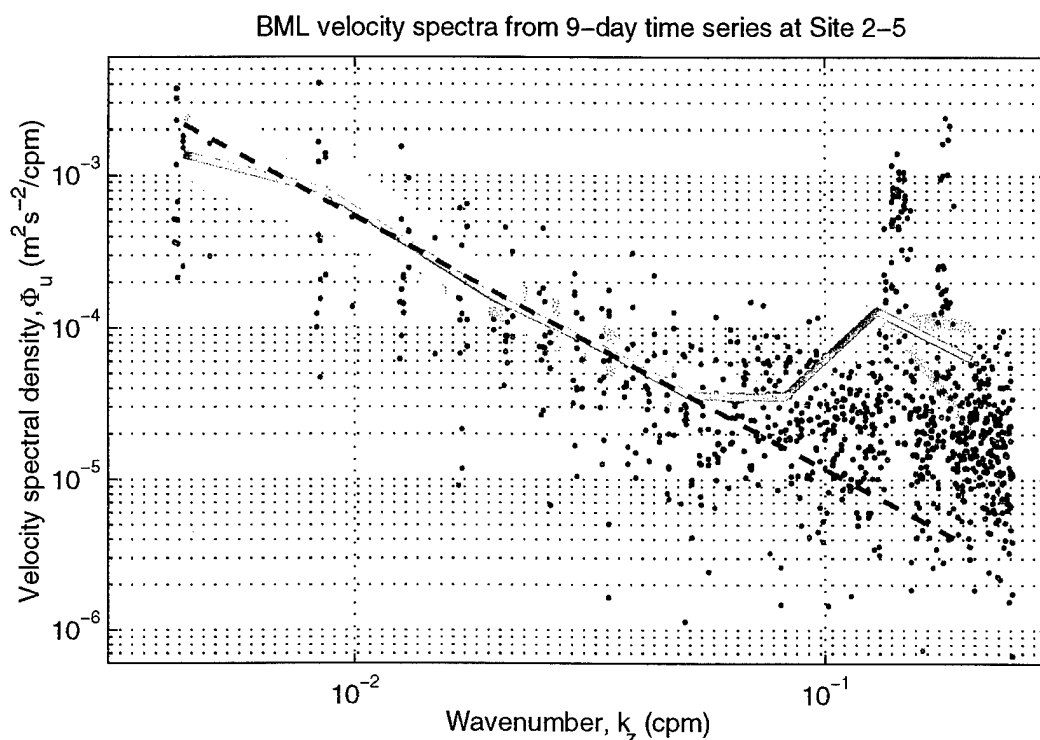
Figure 27: Velocity spectral density versus vertical wavenumber for BML above BBL in nine-day time series of eight AVP profiles. Blue dots denote data from along-slope velocity fluctuations and red dots are from across-slope data. Green line is the mean spectrum of both components; gray area is the 95% confidence limit. Dashed line has a slope of -5/3 and a magnitude appropriate for $\varepsilon = 1.5 \times 10^{-9}$ m^2 s^{-3}.

The vertical component of an up-slope return flow within the upper BML is another mechanism that could keep concentrations uniform and the sediments suspended. If 2-D conservation of mass holds within the whole BML system, then the volume transport up-slope in the upper BML equals down-slope Ekman transport in the lower BML (i.e., the BBL). This hypothesized return flow could provide some fluid to the divergent Ekman transport near the top of the slope. If we use the nine-day time series mean velocities (see Fig. 20), the thin down-slope Ekman transport in the BBL balances to within 25% by a thick, but weak, up-slope velocity in the upper BML. In order to oppose the vertical settling velocities for suspended particles calculated above, across-slope velocities of between 1.4 x 10^{-5} and 0.019 m s^{-1} are needed on a slope at the angle of Section 2 (0.038). From the time series, the mean up-slope flow in the BML above the BBL is

about 0.003 m s^{-1}, which is within this range, although the variability around this mean is very large. Furthermore, the exact direction of the local topography is uncertain so the rotation of velocity components may have an error of a few degrees. A two degree change in angle of a 0.2 m s^{-1} along-slope flow produces an across-slope flow of 0.007 m s^{-1}, more than double the estimated mean up-slope flow.

A second advective mechanism at work is the upward buoyant convection of light water from the BBL up into the BML. Based on deep ocean observations, Eittreim *et al.* (1975) originally proposed that buoyant convection from the downwelling Ekman layer was an important factor in maintaining a thick BML and a uniform concentration of suspended sediment. Thermal convection from the BBL was supported by Weatherly and Martin (1978) based on both a model and observations. (In early observations, salinity measurements were not accurate enough to verify a true density flux in the Ekman layer, so heat flux was reported.) Our observations also affirm this buoyant convection from the BBL. Fifteen of the 84 AVP drops and CTD casts showed statically unstable layers just above the seafloor that correlate in size with the BBL (see Fig. 28 for an example). The average difference of all these density steps is $1.7 \pm 0.7 \times 10^{-4}$ kg m^{-3}. These steps also provide evidence that a down-slope buoyancy flux actually occurs.

In order for these steps to convect up into the BML, the Rayleigh number must be sufficiently high (> 1710) to indicate the viscous forces can be overcome (Turner, 1973). A minimum Rayleigh number was found to be about 3.1×10^4 using the formula $Ra = g'd^3/\kappa\nu$, where g' is the reduced gravity (1.6×10^{-6} m s^{-2} for the average step), d is the distance over which the step acts (taken to be 1 m as a lower bound), κ is vertical diffusivity (taken as 3×10^{-5} m^2 s^{-1}) and ν is the kinematic viscosity ($\sim 1.7 \times 10^{-6}$ m^2 s^{-1} here). The vertical velocity provided by these overturns can be calculated based on a scaling from the atmospheric boundary layer of $w_*^3 = \overline{(w'b')}h$, where w_* is the free convective vertical velocity scale, $\overline{(w'b')}$ is the buoyancy flux (primes denote variations from horizontal means and overbar denotes horizontal average of whole layer), and h is the layer thickness (Garratt, 1992). Here, buoyancy flux can be estimated as $K_v g'/\delta z$, where K_v is in the range taken from the BBL (1 to 8×10^{-2} m^2 s^{-1}), g' is for the density

step itself, δz is the thickness of that step (taken as the whole thickness of the BBL as upper bound), and h can be taken as the thickness of the BBL. For the range of BBL thickness encountered and the range of g' for the various density steps observed, this formulation provides values for w_* that range between 0.001 and 0.012 m s^{-1}. For the atmospheric case, the typical size of velocity fluctuations is about $0.6w_*$, so for our case the actual velocities may only be 9-72 x 10^{-4} m s^{-1}, but this is well within the range necessary to keep sediment particles in suspension. It should be noted that while this mechanism may not be as continuous as the large scale turbulence or the vertical component of the up-slope recirculation, it could balance the typical 5 x 10^{-4} m s^{-1} settling velocity of the particles.
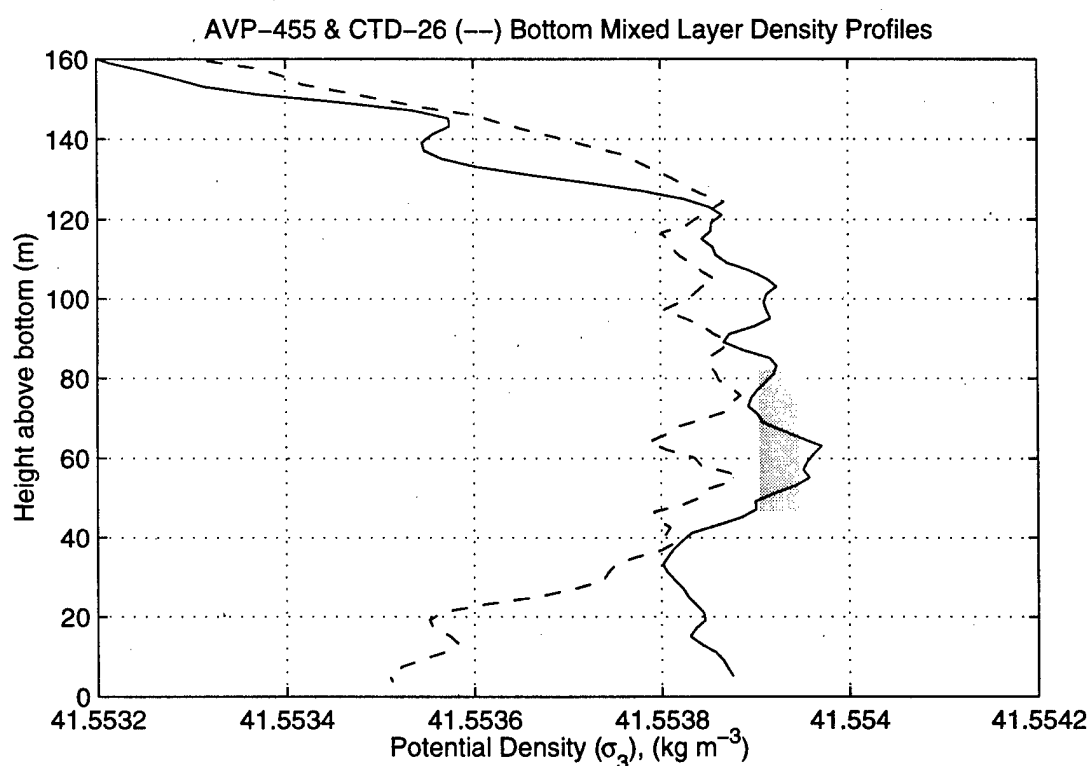
Figure 28: Statically unstable step in bottom mixed layer observations of AVP 455 and CTD 26, taken at Site 2-7 about five hours apart. Gray bar represents one standard deviation from mean of four AVP drops over 11.4 hour time series at Site 2-5, representing a statistical uncertainty for AVP density measurements.

Based on the BML observations represented in Figures 20 and 25 and the discussion above, a 2–D conceptual model (see Fig. 28) was developed offering a plausible explanation for most, if not all, observed phenomena. Because the DWBC is approximately steady in this location, we believe the processes within the BML may also be steady enough to create a 2–D balance across the slope that adjusts in a short time scale to changing topography and forcing. Given that the flow is in geostrophic balance, then the time scale could be considered the length of time it takes the down-slope Ekman transport to cover one Rossby radius across the slope, approximately five days. In the illustration, the shape of the BML is vertically exaggerated for clarity. The down-slope BBL transport returns up-slope in a weak BML recirculation which is not resisted by any across-slope stratification within the layer. The BML height results from the combined effects of 1) fluid entrainment into the BBL ($w < 0$) on the up-slope side to compensate for Ekman transport divergence, 2) flow up into the BML ($w > 0$) from the BBL on the down-slope side due to Ekman transport convergence (which then recirculates up-slope), 3) weak buoyant convection out of the BBL, and 4) weak turbulence from large-scale velocity fluctuations (O 10' of meters) within the upper BML. There is a small amount of down-slope buoyancy flux resulting from mixing with a weak overlying pycnocline up-slope of the current center as seen in Figure 25e. Both the Ekman transport and along-slope density difference drop rapidly approaching the outer edge of the current where the BML height returns to the BBL height. The uniformity of sediment and nutrient concentrations throughout the BML support this model. The overlying isopycnals are not shown in Figure 28 but are nearly parallel with the top of the BML, particularly down-slope of the current core.
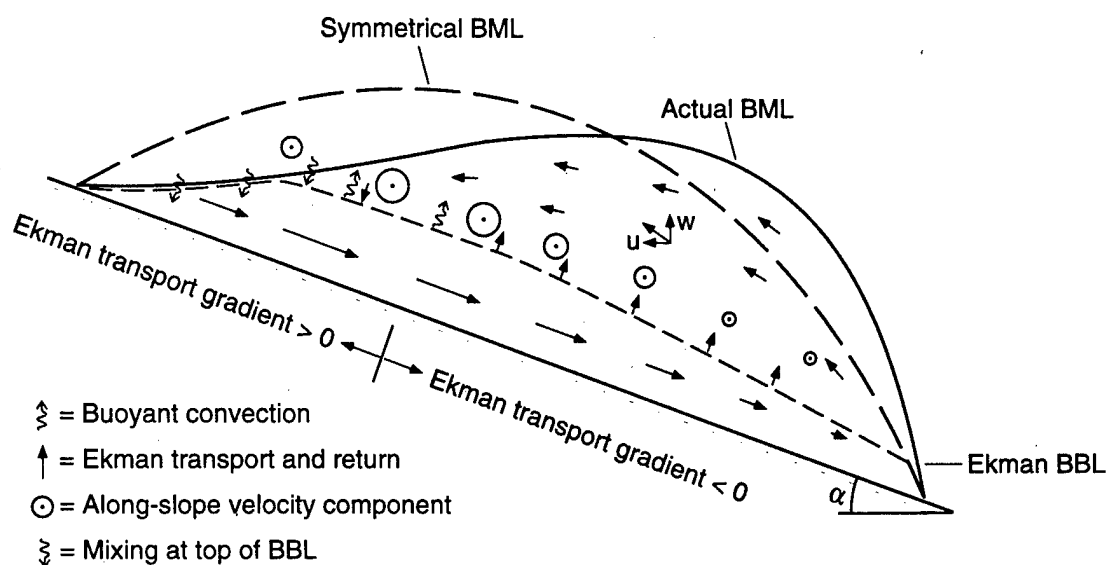
Figure 29: An illustration of an asymmetrical bottom mixed layer (BML) on a slope based on observations of the DWBC at the Blake Outer Ridge.

One of the problems with this 2-D model is that the entrainment apparent on the up-slope side in the divergent region in not balanced by any detrainment on the down-slope side. Only one AVP drop was made on the down-slope end of Sections 0 and 1, which is insufficient to rule out the possibility of detrainment from the BML into the interior. The deepest isopycnals stretch apart slightly in the offshore direction (see Fig. 24) indicating this may be the case. But the stretch may also just represent the normal offshore density gradient as it appears adjacent to the ridge.

A 3-D model better addresses this issue of "excess" entrainment. As in the 2-D model above, we assume the BML boundary is closed on the down-slope side such that the BBL transport recirculates back up-slope within the BML. However, the recirculation does not provide all the water necessary for the Ekman divergence at the up-slope side. Some extra water is entrained all along this up-slope edge and the total volume of the BML increases along-stream, gradually thickening it and perhaps leading to the observed asymmetry across-slope. Our observations endorse this in one respect; the highest points of the BML at Section 1 are about 170 m above bottom, while at Section 2 they are about 240 m. Unfortunately, the complex nature of the DWBC on the BOR does not yield a simple image at Section 2 so a straightforward test of the along-stream BML development

is difficult. At Section 2 the ridge crest is deep and a thick BML exists directly on top of it, so there is no well defined up-slope end such as at Sections 0 and 1 (see Fig. 24). Furthermore, our observations did not extend enough to see the outer end of the BML, leading to what appears to be a rather symmetrical across-slope shape. However, a few rough estimates can be made to test this "inflating bag" model.

In a steady state, there should be a balance between the along-stream change in volume transport and the along-stream integral of Ekman transport in the BBL minus a recirculation amount from Ekman convergence down-slope. The "inflation" of the BML is only from the "excess" entrainment, which is less than the maximum down-slope Ekman transport by the amount of recirculation. This balance can be roughly tested between Sections 1 and 2 because the isopycnal defining the Bottom Water transport category ($\sigma_3 = 41.55$) nearly coincides with the top of the BML at both sections. The increase in transport from Section 1 to 2 is about 1 Sv (see Table 4) and the Ekman transport is a maximum of 1.5 m^2 s^{-1} at Section 1. Over the 185 km between sections, this transport should add about 0.27 Sv into the BML, which is less than the measured increase by about a factor of four. This calculation neglected recirculation within the BML, which would only increase the difference. The difference further increases if the unobserved portion of the BW transport is added (~0.5 Sv). Absence of a topographically closed boundary on the up-slope end of Section 2 may also be responsible for the imbalance. Testing the idea over a longer distance, say from the start of the DWBC to Section 1, might render a different view. In this case, we assume no significant BML where the current starts, take a slightly lower value of 1 m^2 s^{-1} for BBL Ekman transport (assuming a slightly weaker average current), and use a length of ~7000 km. This yields about 7 Sv of transport into the BML through the BBL, again neglecting the recirculation. We observed 2 Sv at Sections 0 and 1, indicating the recirculation factor may be about 70% if the 2 Sv represents the "excess" entrainment over that distance. Based on this rough calculation, it is plausible this mechanism accounts for the enlarged BML, but observations where the BML boundaries are more easily distinguished would help verify this model.

Chapter 5: Summary

This study provides several new insights about the DWBC and its bottom boundary layer as it flows along the Blake Outer Ridge. Surveying the current with a full depth profiling instrument simultaneously measuring absolute velocity and density produced a more comprehensive view of the current, including its thick bottom mixed layer, than heretofore available. In the deep water, the geostrophic and absolute velocity fields agreed well, demonstrating that the DWBC is in geostrophic balance as it flows along and around the ridge. Planetary potential vorticity is conserved and relative vorticity is an order of magnitude lower. A time series of profiles on Section 2, where a year-long current-meter record was taken, confirmed our observations were representative of the mean DWBC.

5.1 Volume Transport

Our first two sections, 0 and 1, were designed to capture the full volume transport of the current. For all water masses combined, we determined values of 17 ± 1 Sv and 18 ± 1 Sv from absolute and geostrophic velocity fields respectively. A comprehensive uncertainty analysis was conducted on these results to establish experimental errors and estimate the natural variability in our observations. Transport at Section 2, about 180 km down-stream of Section 1, indicated about half the current had crossed the ridge by that point, as verified (within a large uncertainty) by Section R. We compared our values with those obtained in previous transport investigations in the same region. When boundaries and velocity references were adjusted to be in close agreement, the results of Swallow and Worthington (1961), Pickart and Smethie (1993), and Schmitz (1996) agreed with our results. The 11 Sv transport reported by Johns *et al.* (1997) coming around the tip of the ridge was similar to what we observed on Section 2. But the full 31 Sv of transport they found disagreed with our total of ~18 Sv. Our results also disagreed with the 22 Sv reported by Amos *et al.* (1971) in a section near our Section 2. However, neither Johns *et al.* or Amos *et al.* had absolute reference velocities or dense spatial coverage in this region to make comparisons with our study satisfactory.

In the deep water, our geostrophic and directly measured velocity fields agreed well, demonstrating the current is in geostrophic balance as it flows along and around the ridge. Potential vorticity is conserved and interacts with changing bottom slope as predicted by Stommel and Arons (1972) to change the width of the current. Further, the across-slope distribution of potential vorticity is similar to that modeled by Pickart and Huang (1995), where the potential vorticity is elevated on the near-shore side. Comparing our observations to their model flow around a ridge shows that no part of the DWBC is ultimately blocked by the BOR.

To return to one of the original motivations for this experiment, it appears the DWBC can be monitored at the BOR for evidence of global climate change. The volume transport was measured clearly at Sections 0 and 1 where the current is confined and free of recirculation gyres. Influence from low frequency phenomena, such as topographic Rossby waves, appears to be small at the BOR as demonstrated by the peaked statistical distribution of the current-meter records. Making future results effective would require definition of an easily measured standard tracer boundary (e.g., potential density or oxygen concentration) and velocity measurements with a reliable and repeatable technique (e.g., absolute profiles or well-referenced geostrophic profiles). Because the current's transport may change significantly in the span of 5-20 years in response to climate change, or perhaps forcing it, monitoring the current at sufficient frequency (more or less biannually for decadal scale changes) would be necessary. This study demonstrates that a velocity-profile survey is a useful technique for monitoring DWBC transport and that observations at the BOR could provide valuable information to predict or confirm climate change.

5.2 Bottom Boundary and Mixed Layer

Profiles of velocity, density, turbulent dissipation, suspended sediment, oxygen, and nutrients through the bottom boundary layer were used to examine the structure and dynamics therein. Bottom stress was present everywhere under the current, creating a strongly turbulent ($\varepsilon \approx 10^{-7}$ m^2 s^{-3}) planetary bottom boundary layer with an average friction velocity of about 1 cm s^{-1}. This value was determined by fitting the velocity profiles to a log curve, while a lower value was derived from turbulent dissipation measurements in the BBL. The factor of three ratio between the bottom stress derived

from the two different values is similar to that seen in other boundary layer flows. The bottom mixed layer above the BBL was also turbulent, but much more weakly ($\varepsilon \approx 10^{-9}$ $m^2 \ s^{-3}$). Velocity fluctuations in the upper BML at Site 2-5 exhibited kinetic energy spectra with a $-5/3$ dependence on vertical wavenumber indicating turbulence over wavelengths 20-100 m.

The energy dissipated by this bottom stress fit a stream-tube formulation for the distance down-slope the velocity core of the DWBC moved between Sections 1 and 2. Our observations agreed with a model relating velocity, bottom stress, density, area, and Coriolis parameter to the angle the current core makes with the isobaths. Further, our observations were tested with an along-stream momentum balance in which the external potential energy term was 65% of the stress term. Both these terms were at least an order of magnitude larger than the terms representing along-stream changes in kinetic energy and internal potential energy. The depth change observed (and supported by the model) for the DWBC velocity-core along the BOR cannot be extrapolated to the DWBC over the whole North Atlantic basin however. This is because the velocity and stress are higher here than along most of the DWBC, the depth change is large compared to distance along-stream, and this model may not hold as well in regions of weaker flow.

Observed values for the current as a whole were compared to a formulation for spin-down time based on the overall energy balance of the current. The ratios of internal potential energy to kinetic energy at various sections of our survey were similar to those calculated using a model including bottom slope as a key parameter. However, these ratios were small compared to the value thought necessary to sustain the current for a great distance. The small ratios were probably because the slope at the BOR is steeper than under most parts of the DWBC and the current speed is higher. Accordingly, these results are difficult to extrapolate to larger spatial scales for the DWBC.

Our bottom mixed layer observations were examined in light of BML models in which an across-slope density gradient creates an along-slope shear flow that reduces the effect of bottom stress on the current. The density field assumed in the models was not detected at the BOR. The observed across-slope density gradient in the BML was very small and the overlying isopycnals intersected the BML at shallow angles. A typical result of the models is an along-slope velocity shear, but little was found within the BML. Most models assume a higher velocity above the BML. But at the BOR, the highest

velocities were in the BML, decreasing above it with a minimum near the main thermocline.

Two conceptual models were presented regarding the shape of and flow within the BML to explain the observations in a consistent manner. In the first, a 2-D balance within the BML is assumed. The down-slope advection of mass and buoyancy within the planetary BBL creates an asymmetrically shaped BML, with Ekman transport convergence down-slope being the principal driving force. The upward vertical velocity from the convergence drives a weak up-slope return flow of the Ekman transport. In addition to this recirculation, buoyant convection from the BBL and large spatial scale turbulence in the upper BML keep density, suspended sediment, and other tracer concentrations uniform throughout the BML.

The second model attempts to account for the enlarged BML through the entrainment observed in the up-slope region of the BML. This model suggests a 3-D structure in which the BML is not only asymmetrical across-slope but also thickens slowly along-stream. Although the volume transport balance proposed did not hold between Sections 1 and 2, it may hold over longer distances, such as at basin scales.

References

Alley R. B., D. A. Meese, C. A. Shuman, A. J. Gow, K. C. Taylor, P. M. Grootes, J. W. C. White, M. Ram, E. D. Waddington, P. A. Mayewski and G. A. Zielinski (1993) Abrubt increase in Greenland snow accumulation at the end of the Younger Dryas event. *Nature,* **362,** 527-529.

Amos A. F., A. L. Gordon and E. D. Schneider (1971) Water masses and circulation patterns in the region of the Blake-Bahama Outer Ridge. *Deep-Sea Research,* **18,** 145-165.

Armi L. (1977) The dynamics of the bottom boundary layer of the deep ocean. Presented at Bottom Turbulence, Proc. of the 8th Int. Liege Colloq. on Ocean Hydrodynamics. 306.

Armi L. (1978) Some evidence for boundary mixing in the deep ocean. *Journal of Geophysical Research,* **83,** (C4), 1971-1979.

Armi L. and R. C. Millard, Jr. (1976) The bottom boundary layer of the deep ocean. *Journal of Geophysical Research,* **81,** (27), 4983-4990.

Armstrong F. A. L., C. R. Stearns and J. D. H. Strickland (1967) The measurement of upwelling and subsequent biological processes by means of the Technicon AutoAnalyzer and associated equipment. *Deep-Sea Research,* **14,** (3), 381-389.

Baringer M. O. and J. Price (1997) Momentum and Energy Balance of the Mediterranean Outflow. *Journal of Physical Oceanography,* **27,** (8), 1678-1692.

Bernhardt H. and A. Wilhelms (1967) The continuous determination of low level iron, soluble phosphate and total phosphate with the AutoAnalyzer. *Technicon Symposium, 1967,* **1,** 386.

Bird A. A., G. L. Weatherly and M. Wimbush (1982) A study of the bottom boundary layer over the eastward scarp of the Bermuda Rise. *Journal of Geophysical Research,* **87,** (C10), 7941-7954.

Biscaye P. E. and S. L. Eittreim (1977) Suspended particulate loads and transports in the nepheloid layer of the abyssal Atlantic Ocean. *Marine Geology,* **23,** 155-172.

Broecker W. S. (1990) Salinity History of the Northern Atlantic During the Last Deglaciation. *Paleoceanography,* **5,** (4), 459-467.

Bryan G. M. (1970) Hydrodynamic model of the Blake Outer Ridge. *Journal of Geophysical Research*, **75**, (24), 4530-4537.

Caldwell D. R. (1978) Variability of the bottom mixed layer on the Oregon shelf. *Deep-Sea Research*, **25**, 1235-1243.

Carpenter J. H. (1965) The Chesapeake Bay Institute technique for the Winkler dissolved oxygen method. *Limnology and Oceanography*, **10**, 141-143.

Chapman D. C. and S. J. Lentz (1997) Adjustment of Stratified Flow over a Sloping Bottom. *Journal of Physical Oceanography*, **27**, 340-356.

D'Asaro E. (1982) Velocity Structure of the Benthic Ocean. *Journal of Physical Oceanography*, **12**, 313-322.

De Madron X. D. and G. Weatherly (1994) Circulation, transport and bottom boundary layers of the deep currents in the Brazil Basin. *Journal of Marine Research*, **52**, (4), 583-638.

Dewey R. K. and W. R. Crawford (1988) Bottom stress estimates from vertical dissipation rate profiles on the continental shelf. *Journal of Physical Oceanography*, **18**, (8), 1167-1177.

Dickson R. R. and J. Brown (1994) The production of North Atlantic Deep Water: Sources, rates and pathways. *Journal of Geophysical Research*, **99**, (C6), 12,319-12,341.

Drever R. G., J. H. Dunlap and T. B. Sanford (1984) *The Design and Performance of an Acoustic Doppler and Electromagnetic Velocity Profiler*. APL-UW 9-84, Applied Physics Laboratory, University of Washington.

Eittreim S., P. E. Biscaye and A. F. Amos (1975) Benthic Nepheloid Layers and Ekman Thermal Pump. *Journal of Geophysical Research*, **80**, (36), 5061-5067.

Eittreim S., M. Ewing and E. M. Thorndike (1969) Suspended matter along the continental margin of the North American Basin. *Deep-Sea Research*, **16**, 613-624.

Elliot B. A. and T. B. Sanford (1982) *Error Analysis of Absolute Velocity Profiler in the Local Dynamics Experiment of POLYMODE*. APL-UW 8207, Applied Physics Laboratory, University of Washington.

Elliot B. A. and T. B. Sanford (1986) The subthermocline lens D1. Part I: Description of water properties and velocity profiles. *Journal of Physical Oceanography*, **16**, (3), 532-548.

Fine R. A. (1995) Tracers, time scales, and the thermohaline circulation: The lower limb in the North Atlantic Ocean. *Reviews of Geophysics,* **Supplement,** (July 1995), 1353-1365.

Gardner W. D. and L. G. Sullivan (1981) Benthic Storms: Temporal Variability in a Deep-Ocean Nepheloid Layer. *Science,* **213,** (329-331), .

Garratt J. R. (1992) *The Atmospheric Boundary Layer,* Cambridge University Press, Cambridge, 316 pp.

Garrett C., P. MacCready and P. Rhines (1993) Boundary mixing and arrested Ekman layers: Rotating stratified flow near a sloping boundary. *Annual Review of Fluid Mechanics,* **25,** 291-323.

Gregg M. C. (1987) Diapycnal mixing in the thermocline: a review. *Journal of Geophysical Research,* **92,** (C5), 5249-5286.

Griffiths R. W. (1986) Gravity currents in rotating systems. *Annual Review of Fluid Mechanics,* **18,** 59-89.

Haskell B. J. (1991) The influence of deep Western North Atlantic circulation on late quaternary sedimentation on the Blake Outer Ridge. Ph.D. dissertation, Duke University.

Haskell B. J. and T. C. Johnson (1993) Surface sediment response to deepwater circulation on the Blake Outer Ridge, western North Atlantic: paleoceanographic implications. *Sedimentary Geology,* **82,** (1), 133-144.

Heezen B. C., C. D. Hollister and W. F. Ruddiman (1966) Shaping of the continental rise by deep geostrophic contour currents. *Science,* **152,** (3721), 502-508.

Iselin C. O. (1936) A study of the circulation of the Western North Atlantic. *Pap. Phys. Oceanogr. Meteor,* **4,** (4), 1-101.

Jenkins W. J. and P. B. Rhines (1980) Tritium in the deep North Atlantic Ocean. *Nature,* **286,** 877-880.

Johns E., R. A. Fine and R. L. Molinari (1997) Deep Flow along the Western Boundary South of the Blake Bahama Outer Ridge. *Journal of Physical Oceanography,* **27,** 2187-2208.

Johnson G. C., R. G. Lueck and T. B. Sanford (1994a) Stress on the Mediterranean outflow plume: Part II. Turbulent dissipation and shear measurements. *Journal of Physical Oceanography,* **24,** 2084-2092.

Johnson G. C., T. B. Sanford and M. T. O. N. Baringer (1994b) Stress on the Mediterranean outflow plume: Part I. Velocity and water property measurements. *Journal of Physical Oceanography,* **24,** 2072-2083.

Johnson T. C., E. L. Lynch, W. J. Showers and N. C. Palczuk (1988) Pleistocene fluctuations in the Western Boundary Undercurrent on the Blake Outer Ridge. *Paleoceanography,* **3,** (2), 191-207.

Lai D. Y. (1984) Mean flow and variabilities in the Deep Western Boundary Current. *Journal of Physical Oceanography,* **14,** 1488-1498.

Lea D. W. and E. A. Boyle (1990) A 210,000-year record of barium variability in the deep northwest Atlantic Ocean. *Nature,* **347,** 269-272.

Leaman K. D. and P. S. Vertes (1996) Topographic Influences on Recirculation in the Deep Western Boundary Current: Results from RAFOS Float Trajectories between the Blake-Bahama Outer Ridge and the San Salvador "Gate". *Journal of Physical Oceanography,* **26,** 941-961.

Lee T. N., W. E. Johns, R. J. Zantopp and E. R. Fillenbaum (1996) Moored Observations of Western Boundary Current Variability and Thermocline Circulation at 26.5°N in the Subtropical North Atlantic. *Journal of Physical Oceanography,* **26,** 962-983.

Lueck R. G. and Y. Lu (1997) The logarithmic layer in a tidal channel. *Continental Shelf Research,* **17,** (14), 1785-1801.

MacCready P. (1994) Frictional decay of abyssal boundary currents. *Journal of Marine Research,* **52,** 197-217.

MacCready P. and P. B. Rhines (1991) Buoyant inhibition of Ekman transport on a slope and its effect on stratified spin-up. *Journal of Fluid Mechanics,* **223,** 631-661.

MacCready P. and P. B. Rhines (1993) Slippery Bottom Boundary Layers on a Slope. *Journal of Physical Oceanography,* **23,** (1), 5-22.

Manabe S. and R. J. Stouffer (1994) Multiple-century response of a coupled ocean-atmosphere model to an increase of atmospheric carbon dioxide. *Journal of Climate,* **7,** (1), 5-23.

McCartney M. S. (1992) Recirculating components to the deep boundary current of the northern North Atlantic. *Progress in Oceanography,* **29,** 283-383.

McCartney M. S. (1993) Crossing of the Equator by the Deep Western Boundary Current in the Western Atlantic Ocean. *Journal of Physical Oceanography,* **23,** 1953-1974.

McCave I. N. (1984a) Erosion, transport and deposition of fine-grained marine sediments. *Fine-Grained Sediments,* **15,** (Special Publication), 35-69.

McCave I. N. (1984b) Size spectra and aggregation of suspended particles in the deep ocean. *Deep-Sea Research,* **31,** (4), 329-352.

McCave I. N. (1986) Local and global aspects of the bottom nepheloid layers in the world ocean. *Netherlands Journal of Sea Research,* **20,** (2), 167-181.

McCave I. N. and B. E. Tucholke (1986) Deep current-controlled sedimentation in the western North Atlantic. In: *The Geology of North America, Vol. M, The Western North Atlantic Region, ed.* P. R. Vogt & B. E. Tucholke editors, Geological Society of America, , pp. 451-468.

Mills C. A. and P. B. Rhines (1979) *The Deep Western Boundary Current at the Blake-Bahamas Outer Ridge: Current Meter and Temperature Observations, 1977-78.* Technical Report WHOI-79-85, Woods Hole Oceanographic Institution.

Mix A. C. and R. G. Fairbanks (1985) North Atlantic surface-ocean control of Pleistocene deep-ocean circulation. *Earth and Planetary Science Letters,* **73,** 231-243.

Newberger P. A. and D. R. Caldwell (1981) Mixing and the bottom nepheloid layer. *Marine Geology,* **41,** 321-336.

Oakey N. S. (1982) Determination of the rate of dissipation of turbulent energy from simultaneous temperature and velocity shear microstructure measurements. *Journal of Physical Oceanography,* **12,** 256-271.

Panchev S. and D. Kesich (1969) Energy Spectrum of isotropic turbulence at large wavenumbers. *Comptes rendus de l'Academie bulgare des Sciences,* **22,** 627-630.

Percival D. B. and A. T. Walden (1993) *Spectral analysis for physical applications: multitaper and conventional univariate techniques,* Cambridge University Press, Cambridge, 583 pp.

Pickart R. S. and R. X. Huang (1995) Structure of an inertial deep western boundary current. *Journal of Marine Research,* **53,** 739-770.

Pickart R. S. and W. M. Smethie, Jr. (1993) How does the Deep Western Boundary Current cross the Gulf Stream? *Journal of Physical Oceanography,* **23,** 2602-2616.

Pickart R. S., M. S. Spall and J. R. N. Lazier (1997) Mid-depth ventilation in the western boundary current system of the sub-polar gyre. *Deep-Sea Research I,* **44,** (6), 1025-1054.

Ramsden D. (1995) Response of an Oceanic Bottom Boundary Layer on a Slope to Interior Flow. Part II: Time-Dependent Interior Flow. *Journal of Physical Oceanography, 25*, 1688-1695.

Rhines P. (1970) Edge-, Bottom-, and Rossby waves in a rotating stratified fluid. *Geophysical Fluid Dynamics, 1*, 273-302.

Riser S. C., H. Freeland and H. T. Rossby (1978) Mesoscale motions near the deep western boundary of the North Atlantic. *Deep-Sea Research, 25*, 1179-1191.

Sanford T. B. (1991) Spatial Structure of thermocline and abyssal internal waves. Presented at Dynamic of Oceanic Internal Gravity Waves, 'Aha Huliko'a Hawaiian Winter Workshop, University of Hawaii at Manoa. 109-142.

Sanford T. B., M. D. Allison, J. H. Dunlap, T. Lehman, F. R. Stahr and J. A. Verrall (1996) *R/V Endeavor 239: Cruise Report and Preliminary Results.* Technical Report APL-UW TR 9603, APL, University of Washington.

Sanford T. B., R. G. Drever and J. H. Dunlap (1985) An Acoustic Doppler and Electromagnetic Velocity Profiler. *Journal of Atmospheric and Oceanic Technology, 2*, (2), 110-124.

Sanford T. B. and R.-C. Lien (1998) Turbulent properties in a homogeneous tidal bottom boundary layer. *Journal of Geophysical Research, ,* (in press), .

Schitker D. (1979) The deep waters of the western North Atlantic during the past 24,000 years, and the re-initiation of the Western Boundary Undercurrent. *Marine Micropaleontology, 4*, 265-280.

Schmitz W. J., Jr. (1996) *On the World Ocean Circulation: Volume I.* Technical Report WHOI-96-03, Woods Hole Oceanographic Institution, Woods Hole, Mass.

Schmitz W. J., Jr. and M. S. McCartney (1993) On the North Atlantic Circulation. *Review of Geophysics, 31*, (1), 29-49.

Smith P. C. (1975) A streamtube model for bottom boundary currents in the ocean. *Deep-Sea Research, 22*, 853-873.

Smith W. H. F. and D. T. Sandwell (1997) Global seafloor topography from satellite altimetry and ship depth soundings. *Science, 277*, (5334), 1956-1962.

Stahr F. R. and T. B. Sanford (1998) Transport and Bottom Boundary Layer Observations of the North Atlantic Deep Western Boundary Current at the Blake Outer Ridge. *Deep-Sea Research II, 46*, (2), in press.

Stocker T. F. and A. Schmittner (1997) Influence of CO2 emission rates on the stability of the thermohaline circulation. *Nature*, **388**, 862-865.

Stommel H. (1958) The abyssal circulation. *Deep-Sea Research*, **5**, 80-82.

Stommel H. and A. B. Arons (1972) On the abyssal circulation of the world ocean - V. The influence of bottom slope on the broadening of inertial boundary currents. *Deep-Sea Research*, **19**, 707-718.

Swallow J. C. and L. V. Worthington (1961) An observation of a deep countercurrent in the Western North Atlantic. *Deep-Sea Research*, **8**, 1-19.

Taylor K. C., G. W. Lamorey, G. A. Doyle, R. B. Alley, P. M. Grootes, P. A. Mayewski, J. W. C. White and L. K. Barlow (1993) The 'flickering switch' of late Pleistocene climate change. *Nature*, **361**, 432-436.

Tennekes H. and J. L. Lumley (1972) *A First Course in Turbulence*, MIT Press, Boston, 300 pp.

Trowbridge J. J. and S. J. Lentz (1991) Asymmetric behavior of an oceanic boundary layer above a sloping bottom. *Journal of Physical Oceanography*, **21**, 1171-1185.

Turner J. S. (1973) *Buoyancy Effects in Fluids*, Cambridge University Press, Cambridge, 368 pp.

Weatherly G. L. and P. J. Martin (1978) On the structure and dynamics of the oceanic bottom boundary layer. *Journal of Physical Oceanography*, **8**, 557-570.

Wimbush M. and W. Munk (1970) The benthic boundary layer. In: *The Sea, Vol. 4, ed.* A. E. Maxwell editor, Wiley - Interscience, New York, pp. 731-758.

Wüst G. (1935) Schichtung und Zirkulation des Atlantischen Ozeans, Die Stratosphäre. *Wiss. Ergebn. Dtsch. Atl. Exped.*, **6**, 180.

Appendix A: Locations of AVP and CTD observations

Absolute Velocity Profiler - Blake Outer Ridge - R/V *Endeavor* #239 - 1992

Drop No.	Date	Time (UTC)	Latitude North	Longitude West	Site No.	Comments
432	July 23	0921	32°38.097'	75°59.680'	0-1	good data
433	July 23	1210	32°38.059'	75°54.623'	0-2	good data
434	July 23	1504	32°38.022'	75°49.079'	0-3	good data
435	July 23	1823	32°37.332'	75°40.000'	0-4	good data
436	July 23	2151	32°38.114'	75°31.003'	0-5	good data
437	July 24	0942	32°37.741'	75°20.405'	0-6	good data
438	July 24	1345	32°37.441'	75°07.664'	0-7	good data
439	July 24	1741	32°37.496'	74°56.291'	0-8	good data
440	July 24	2202	32°37.809'	74°38.222'	0-9	good data
441	July 25	1410	31°55.155'	75°29.863'	1-1	dolphins released wt.?, redeployed, OK
442	July 25	1724	31°57.309'	75°25.109'	1-2	good data
443	July 25	2025	32°00.533'	75°20.874'	1-3	good data
444	July 26	0912	32°03.539'	75°16.547'	1-4	good data
445	July 26	1235	32°07.031'	75°13.638'	1-5	good data
446	July 26	1614	32°12.490'	75°07.260'	1-6	write unfinished, OK
447	July 26	2217	32°20.013'	74°57.833'	1-7	good data
448	July 27	1143	31°34.268'	75°09.376'	R-2	good data
449	July 27	1628	31°11.268'	74°48.785'	R-3	good data
450	July 27	2020	30°56.327'	74°34.077'	R-4	good data
451	July 27	2349	30°49.687'	74°28.582'	R-5	good data
452	July 28	1119	30°39.170'	74°15.370'	2-1	good data
453	July 28	1516	30°42.325'	74°14.168'	2-3	good data, 1st drop for AVP2!
454	July 28	1907	30°43.533'	74°12.188'	2-4	good data
455	July 28	2238	30°46.194'	74°07.303'	2-7	good data
456	July 29	0926	30°40.047'	74°14.196'	2-2	good data
457	July 29	1252	30°42.800'	74°19.947'	2-4	good data
458	July 29	1644	30°44.404'	74°09.896'	2-6	good data, AVP2
459	July 29	1700	30°44.091'	74°10.032'	2-6	good data
460	July 29	2108	30°46.983'	74°05.655'	2-8	good data

AVP (cont.)

Drop No.	Date	Time (UTC)	Latitude North	Longitude West	Site No.	Comments
461	July 30	0906	30°48.949'	74°01.993'	2-9	good data
462	July 30	1309	30°52.211'	73°57.065'	2-11	good data
463	July 30	2040	31°15.710'	73°16.247'	2-15	good data
464	July 31	0913	30°43.705'	74°11.261'	2-5	good data
465	July 31	1309	30°43.683'	74°11.425'	2-5	good data
466	July 31	1324	30°43.481'	74°11.320'	2-5	good data, AVP2
467	July 31	1713	30°43.743'	74°11.342'	2-5	good data
468	July 31	1828	30°43.177'	74°12.460'	2-4	good data, AVP2
469	July 31	2050	30°43.685'	74°11.332'	2-5	good data
470	Aug. 1	1440	30°34.407'	74°12.437'	3-2	good data
471	Aug. 1	1544	30°35.651'	74°14.371'	3-1	good data, AVP2
472	Aug. 1	1942	30°25.847'	74°00.618'	3-3	good data
473	Aug. 1	2139	30°15.366'	73°46.768'	3-4	no data, AVP2 flooded
474	Aug. 2	1106	29°55.854'	73°30.927'	3-5	good data
475	Aug. 2	1546	30°12.906'	73°45.068'	3-4	good data
476	Aug. 2	1921	30°15.992'	73°51.905'	4-1	good data
477	Aug. 3	0908	30°18.616'	74°01.641'	4-2	good data, ant. fell off
478	Aug. 3	1303	30°19.713'	74°09.105'	4-3	good data
479	Aug. 3	1700	30°20.901'	74°19.961'	4-4	good data
480	Aug. 3	2041	30°26.485'	74°18.522'	5-7	good data
481	Aug. 4	0911	30°31.098'	74°17.013'	5-4	good data
482	Aug. 4	1246	30°33.810'	74°17.620'	5-2	good data
483	Aug. 4	1620	30°39.637'	74°19.639'	5-0	good data
484	Aug. 4	1950	30°43.442'	74°11.145'	2-5	good data
485	Aug. 5	1236	30°32.441'	74°17.950'	5-3	good data
486	Aug. 5	1607	30°28.872'	74°17.409'	5-5	good data
487	Aug. 5	2013	30°42.344'	74°13.797'	2-3	good data
488	Aug. 5	2341	30°46.560'	74°06.840'	2-7	good data
489	Aug. 6	1128	30°43.366'	74°11.101'	2-5	good data
490	Aug. 6	1502	30°38.863'	74°15.555'	2-1	good data
491	Aug. 6	1817	30°39.024'	74°07.790'	SE25	good data
492	Aug. 6	2146	30°43.476'	74°11.121'	2-5	good data

CTD and Water Samples - Blake Outer Ridge - R/V *Endeavor* #239 - 1992

Cast No.	Date	Time (UTC)	Latitude North	Longitude West	Site No.	Comments
16	July 24	0031	32°37.827'	75°31.219'	0-5	Good
17	July 24	0423	32°37.926'	75°49.373'	0-3	Good
18	July 25	0117	32°37.978'	74°38.186'	0-9	Good
19	July 25	0713	32°37.304'	75°07.744'	0-7	Good
20	July 26	0007	31°54.924'	75°29.917'	1-1	Good, AVP1 TC pair cal.
21	July 26	0326	32°00.361'	75°20.760'	1-3	Good
22	July 27	0114	32°20.269'	74°57.465'	1-7	Good
23	July 27	0610	32°06.852'	75°13.628'	1-5	Good
24	July 28	0324	30°56.515'	74°33.930'	R-4	Good
25	July 28	0830	30°40.640'	74°16.010'	2-1	Good
26	July 29	0148	30°45.553'	74°07.357'	2-7	Good
27	July 29	0536	30°43.243'	74°11.979'	2-5	Good
28	July 30	0015	30°46.289'	74°05.585'	2-8	Good
29	July 30	0405	30°45.584'	74°08.703'	2-6	Good
30	July 31	0100	31°15.015'	73°18.467'	2-15	Good, AVP1 TC pair cal.
31	Aug. 1	0005	30°42.140'	74°14.120'	2-3	Good, AVP2 TC pair cal.
32	Aug. 1	0402	30°40.450'	74°15.820'	2-1	Tow-yo start, no bottles
	Aug. 1	1350	30°37.915'	74°06.664'	~2-5	Tow-yo end, good
33	Aug. 2	0122	30°15.440'	73°46.660	3-4	Good
34	Aug. 2	0609	29°55.860'	73°30.870'	3-5	Good
35	Aug. 2	2250	30°16.170'	73°51.830'	4-1	Good
36	Aug. 3	0241	30°17.870'	74°01.410'	4-2	Good
37	Aug. 4	0007	30°21.010'	74°19.900'	4-4	Good
38	Aug. 4	0421	30°34.050'	74°16.830'	5-2	Good
39	Aug. 5	0031	30°39.657'	74°19.430'	5-0	Tow-yo start, no bottles
	Aug. 5	1135	30°25.800'	74°18.800'	~5-6	Tow-yo end, good
40	Aug. 6	0328	30°48.590'	74°14.540'	NW2	Good
41	Aug. 6	0748	30°39.070'	74°06.510'	SE25	Good, AVP1 TC pair cal.

Appendix B: Narrative of Observations from Chief Scientist

The following is a narrative of Leg 2 of R/V *Endeavor* cruise 239 edited from the log of the Chief Scientist, Tom Sanford. It is included to give some insight into the quality of the observations due to operating conditions, and where tradeoffs were made to accomplish the original goals in light of in-situ data analysis and instrument difficulties.

Narrative

After getting AVP2 operational and ready, we departed Morehead City (North Carolina) at 1700 on 22 July and headed for the first station on the Blake Outer Ridge (BOR). We arrived at 0500 on 23 July at Site "0-1" (for station 1 on Section 0), where the water was 2500 m deep. This section was added to the cruise plan after the others, so it was dubbed "Section 0." We installed new software (version J) on AVP1 and a new shear probe in VG1 after purging the probe holder with Freon. AVP drop 432 began at 0520. While it was running, we drifted more than a mile to the north, even though the ADCP did not indicate strong surface currents. The recovery went smoothly, and the instrument was ready again in 70 minutes. Prior to the next launch, the hydrophone and line scan recorder (LSR) system was checked to ensure the settings were the same as during Leg 1.

Launch and recovery on the next two AVP drops, 433 and 434, went well. However, it appeared that some part of the AVP blocked the pinger output on each rotation. It was also discovered that VG1's canister had leaked (VG is for 'velocity gradient' and refers to the dissipation shear probes). VG4 was installed for AVP drop 435, but it was noisy. It was suggested that it might be noisy because the 10-kHz pinger was taped to its connector and bracket. The pinger was repositioned for AVP drop 436; also, a shorter line was used on the releasable weights in order to get closer to the bottom. CTD casts 16 and 17 that night went well. There seemed to be little current at this site, as evidenced by the amount of wire out being nearly the same as the depth.

AVP drop 437 on the morning of 24 July got off a bit late, but smoothly. The recovery was rather long because the wind was abeam and pushed us away from the instrument as the ship approached it. Little surface current was noticed during AVP drops 437 and 438. On AVP drop 439, the instrument moved to the southwest, which was downwind,

about a mile during the down profile. Data from these drops showed good agreement between down- and up-profile velocities. None of the drops exhibited a very strong bottom-intensified flow, particularly AVP drop 440, so we decided to postpone the planned time-series drops and begin Section 1 in the morning. CTD casts 18 and 19 and steaming to the start of Section 1 took the remainder of the night and part of the next morning.

AVP drop 441 began at about 1000 on 25 July, but the instrument did not submerge after the beach ball was released. It appeared that the weight had been dislodged by dolphins, which were seen cavorting about the ship. The instrument was recovered, reset, and redeployed about half an hour later, this time descending properly. While the drop was in progress, exact station positions were set for the rest of Section 1. AVP drops 442 and 443 were conducted successfully that afternoon.

On the first drop of 26 July, drop 444, the AVP was deployed at about 0500 at Site 1-4 without difficulty. Chirping noises were heard on the hydrophones; we hoped the noises were stormy petrels and not dolphins. Preliminary analysis of the data taken the day before at Sites 1-1, 1-2, and 1-3 showed flows of up to 20 cm/s near the bottom as we anticipated. On AVP drop 445, the instrument was deployed and recovered without incident; however, on drop 446 it exhibited a problem. The last disk-write operation did not occur. Fortunately, the data were recovered from the quasi-static RAM. The cause of the problem was unclear, and AVP drop 447 was delayed for about 2 hours while we investigated. Drop 447 was successful, although later than planned. Two CTD casts (22 and 23) occurred that night.

The next station line, Section R, was along the crest of the Ridge. The sites were selected to estimate cross-ridge volume transport. The planned time-series drops were held in reserve until we found a site that exhibited a strong, jet-like flow for testing the "slippery" boundary layer theory, probably at Section 2.

AVP drop 448 began at 0745 on 27 July. The instrument was deployed by the morning AVP watch with assistance from some of the CTD watch at Site R-2. Recovery was in a squall with a lot of lightning. AVP drop 449 was delayed because we steamed farther south looking for the 3250-m isobath. We finally made the drop in about 3200 m

of water. There was a severe squall again during the launch, but the recovery was textbook; the AVP surfaced about 240 m in front of the ship and was aboard in 6 minutes.

While AVP drop 450 was running, we tested the second instrument, AVP2, and prepared the working area of the deck for both instruments. Two carts had to be available and secured to two separate areas of the deck, yet at the same time be capable of moving from one area to the other without interference. AVP drop 451 at Site R-5 began later than planned, since the previous recovery was with the wind abeam and the mate made an extremely time-consuming approach. The CTD watch took over an hour behind schedule, and CTD casts 24 and 25 and the steaming time between them took longer than expected. We did not arrive at Site 2-1 until about 0430 on 28 July. Moreover, weather conditions had deteriorated, with winds blowing 20 kn. and seas running 4–6 ft.

Launch and recovery on AVP drop 452 at Site 2-1 went smoothly. AVP drop 453 at Site 2-3 was the first for the AVP2 instrument. What a great occasion! It only took 14 years to get a second AVP in the water. The radio frequency of the recovery beacon was 154.585 MHz (AVP1 was operating at 160.785 MHz.). The instrument was deployed and recovered without difficulty. About 3.5 lb. of lead (weight in water) was added in the OBS bracket to help compensate for the extra weight of the oxygen sensor, the TC pair, and the pump. The data were recovered, and the instrument appeared to have performed well. Consequently two simultaneous ("dual") drops were planned for the next day. In the meantime, AVP1 was used for drops 454 and 455, at Sites 2-4 and 2-7, respectively. During these deployments, the winds were still 20 kn. with 4–6-ft seas.

The drops on 29 July were planned to be 250 m apart in depth in order to fill in some intermediate depths between the sites of the day before. AVP drop 456 at Site 2-2 began about 0530, and AVP drop 457 at Site 2-4 began a little ahead of schedule at 0900. The winds remained about 20 kn., but there was more swell now.

AVP2 and AVP1 were deployed almost simultaneously at Site 2–6 on drops 458 and 459, respectively. One purpose was to provide simultaneous profiles for intercomparison of the instruments. Indeed, a peculiar feature in the east velocity component was observed by both profilers, but at different depths. There was clearly a problem with the processing, which might be related to disk writes or some other intermittent process. The deployment was less than ideal owing to communication difficulties (not hardware

related) between the laboratory and the bridge. Nonetheless, the profilers got off as expected. The 3.5 lb. of lead on AVP2 improved the fall rate, but it was still too slow and more weight was added after recovery. AVP drop 460 (with AVP1) at Site 2-8 finished out the day, and the CTD shift took over.

AVP drop 460 at Site 2-8 showed near-bottom velocities of about 20 cm/s, indicating we were still in the Deep Western Boundary Current (DWBC). However, the velocity structure was clearly not uniform in time or along the sections. For a quick look at this issue, we plotted speed vs. pressure for AVP drops 452 to 460. The speeds near the bottom ranged from 14 to 19 cm/s, with the median being about 16 cm/s. The velocity structure changed somewhat above 3750 dbar, and it appeared that we may have recorded the superposition of a topographic Rossby wave (TRW) and the DWBC.

We continued the drops to the northeast trying to find the edge of the DWBC. AVP1 (drop 461) was put over the side soon after 0500 on 30 July in 4500 m of water at Site 2-9. Upon its recovery, we adjusted the two 2-lb. weights to counterbalance the Sea-Bird gear, and made the next drop, 462, at Site 2-11 in 4750 m of water, where we hoped to see a change in the velocity structure and a lower speed near the bottom.

The data from the section thus far showed that the currents did not diminish away from the ridge but rather remained strong or increased. We decided that the velocity profiles needed to be compared with other variables, such as transmissivity and oxygen concentration to look for alternate signatures of the DWBC. The vertical structure of the velocity profiles was clearly bottom intensified, with the maximum speed occurring at or near the bottom, which looked very much like a TRW. The wavelength could be >300 km (from theory) and the wave period was probably about 20 days (from the Peter Rhines' 1978 current-meter data). The question was how to confirm that this was a TRW? If we repeated the series we started 2 days ago in about 4 days, we should be able to observe a quarter to a third of a period. If the wave was at or near its maximum (when the flow is strong and along isobaths), a repeat section in 4 days might reveal a very changed situation. On the other hand, going farther offshore should show the wave's character by changes in the velocity structure.

The case *in favor of* a repeat, or time series, approach was:

- It would give repeat observations in the region of interest, i.e., in the DWBC.

- It might give the time evolution of the structure as a check for wave activity.

The case *against* the time series approach was:

- We would not have enough time to resolve a full period of the wave.

- If the structure changed little, the resolution of the period would be uncertain.

- We might need to sacrifice other observations.

The case in favor of making AVP drops farther out on the Section 2 line was:

- We could do it immediately without waiting.

- Finding the spatial structure would be valid for determining a TRW.

The case *against* going farther out was:

- Bottom slope and buoyancy frequency decrease with distance offshore; thus the length scale would grow.

- Considerable time would be spent steaming to and from drops.

- There was no assurance that the velocity structure would be much changed.

AVP drop 462 (Site 2-11) showed a greatly diminished current amplitude at the bottom, only 11 cm/s vs. 22 cm/s at Site 2-9. This was a change in the right direction and suggested that we would benefit most from a drop farther out along the section line. We had a lot of coherent profiles and needed at least one that was greatly different to get a better determination of the horizontal wavelength.

We decided to forgo a drop at the 5000-m site and instead steamed to the 5250-m site. AVP drop 463 got off well at 1640 on 30 July. After the instrument was recovered (it was a long run at that depth), we made a full-depth CTD cast (CTD-30) with the AVP1 TC sensors on board for calibration purposes. The transmissometer was removed because it was only rated to 5000 dbar. The water-sampling scheme was adjusted to give a more conventional spread as opposed to the bottom-intensified scheme we typically used.

On 31 July, we arrived at Site 2-5 exactly at 0500 as promised by the bridge. The CTD station had gone well, and the seas were down. The ship was able to make 11.5 to

12.0 kn. for most of the run. AVP drop 464 went off smoothly at 0515; the recovery was equally successful.

We then made simultaneous drops with AVP1 (AVP drop 465) and AVP2 (AVP drop 466) at Site 2-5 to continue the time series and to provide intercomparison data. We put AVP1 in the water first, with a 20-minute delay on the surface. AVP2 followed at a horizontal separation of 100 m with a 5-minute surface delay. When they started down, they were 100 m apart along a line at 330°T; when they returned, they were about 160 m apart along a line at 332°T (AVP2 was northwest of AVP1). There appeared to be a surface current to the southeast. The 15-minute interval between putting the instruments into the water worked well. AVP2 again dropped a little more slowly than AVP1.

We followed that dual drop with another. This time we deployed AVP1 at Site 2-5 (AVP drop 467) and AVP2 farther to the southwest in water 3925 m deep at Site 2-4 (AVP drop 468). AVP2 was put over half an hour late because we had to change an O-ring on one of the connectors. The delay was long enough that we decided to deploy AVP1 on drop 469 before recovering AVP2 from drop 468. We lost the acoustic tracking signal from AVP2 after it surfaced at a range of 2400 m. A few pings were heard as we headed toward the deployment site, but the amplitude was very low until we were within 600 m.

CTD cast 31 at Site 2-3 included the TC pair from AVP2 for calibration. CTD cast 32 was a long tow-yo in the bottom boundary layer (BBL) that took from 0000 to 1000 on 1 August. The regular secondary TC was reinstalled, the bottles were removed, and extra weight was added to the frame. We deployed the rig off the J-frame on the side of the ship, but in retrospect we should have deployed it off the A-frame over the back for better maneuverability. The intended path was along 055°T from Site 2-1 to Site 2-5, but the actual path was a large arc bending to the east. We ended at the 4000-m depth but considerably southeast of Site 2-5. The vertical pattern was a sawtooth down through the bottom mixed layer, up about one and a half times its thickness, and back down slowly (30 m/min. vs. 60 m/min.). This yielded a good image of the density structure adjacent to the ridge.

The dual AVP drops 470 (with AVP1) and 471 (with AVP2) at Sites 3-2 and 3-1 did not go quite as planned that morning. Instead of deploying in 3500 m of water, AVP1

went in at 3600 m. We set off looking for the 3500-m site, but after an hour decided to make drop 471 in 3550 m of water instead. Both instruments were recovered successfully. However, it seems we apparently hooked them at too high a ship speed, and they hit the side of the ship during recovery.

We successfully found Site 3-3 (3700 m) and launched AVP1 on drop 472 at 1540. Then we looked for Site 3-4 (3800 m), ~14 n.mi. away. Finding the right depth was not easy, so we settled for about 3770 m and launched AVP2 on drop 473 at 1740.

The instrument went into the water without incident, and the characteristic dual pings were heard; however, it did not release the beach ball and descend when it should have. Moreover, the pinging was interrupted at least once (possibly a reset of the microcomputer) and stopped altogether as we approached the instrument for recovery. But before we could grab it, the instrument descended. It was silent acoustically. We decided to return to Site 3-3 to recover AVP1 as fast as possible and then come back to search for AVP2 after it had time to drop to the bottom and rise again.

About 6 n.mi. from Site 3-3, the high-frequency radio in the laboratory began to pick up faint signals from AVP1, which had been on the surface for an hour or so. At 2 n.mi., the radio direction finder (RDF) on the bridge began receiving sporadic readings, and the ship's radar detected the instrument at a range of 1.5 n.mi.. Shortly thereafter, it was sighted but was not heard acoustically until we were within 600 m. It was recovered at 1925, and we turned to recover AVP2.

We requested and received full ship's speed, about 13.5 kn. On our way, we were treated to a helicopter flying show by some Navy pilots from a carrier operating just over the horizon, who used us a "target." At a range of 3.6 n.mi. from Site 3-4, AVP2's recovery radio was heard on the lab's radio set. Again, the ship's RDF picked it up at about 2 n.mi. and the radar detected it at 1.5 n.mi.. It was dark, so the xenon flasher was useful, but not very visible. We recovered AVP2 at 2055, and while hoisting it aboard we noticed there was mud on the shear probes and guard ring, indicating the instrument had actually touched the bottom. Perhaps there are finer sediments in this area, and the lower weight sank in deeply before releasing the upper weight. We took samples of the sediment for analysis and then laid the instrument in its cart and removed the vent plug. A puff of vapor escaped that smelled like battery acid, and water was

visible inside the pressure tube. The lower electronics section was immediately removed from the tube.

There was a lot of water inside the tube; it was a miracle we got the instrument back. However, all of the electronics had been exposed to salt water and were destroyed. The batteries were shorted out and had to be thrown away. The electronics in the lower section were burnt, and those in the upper section were badly damaged, but we salvaged some sensors including the tilt sensor and magnetometer. The instrument was a total loss for the rest of the cruise. The leak appeared to come from the top of the pressure tube, but the cause was unclear. Later, the pressure transducer on AVP2 was tested and did not leak at either high or low pressure. The connector in the upper endcap for the release solenoid probably was the culprit, as it was loose to the touch. Because of its lead angle, the cable may have cocked the seal allowing water inside while the instrument was at the surface.

Before launching AVP1 on drop 474 the morning of 2 August, we added 1 m of line to the lower weight because we suspected the instrument might hit bottom as AVP2 did on its last drop. While adding the extra line, we noted a discoloration on a line near the release which may have been from bottom mud. When the instrument was recovered from drop 474, we looked closely for signs of mud but found none.

AVP drop 475 went off on schedule in 3800 m of water at Site 3-4. As we approached the site, the bottom was shoaling, and we took the first opportunity to make a drop in 3800 m of water. However, it was apparent there were 50-m hills in the area which may be important when interpreting the data.

AVP drop 476 was the first drop in Section 4 and was over a flat spot at a depth of 3900 m. The run from Site 3-5 to Site 4-1 showed a gentle slope with hills. We started CTD cast 35 about an hour early owing to being ahead of schedule.

The first drop on 3 August (AVP drop 477) went smoothly and began nearly on schedule at 0510. It was easier to find the correct depth over the steeper and more regular slope. As we approached the AVP for recovery, its radio antenna fell off and sank, but otherwise there was no problem. AVP drop 478 was slightly delayed to replace a faulty shear probe, but ran well.

Launch and recovery on AVP drop 479 were difficult owing to poor laboratory–bridge communications. The mate on this watch typically moved the ship around the instrument too fast and too close, especially on recovery. Achieving and maintaining appropriate speeds was a problem. Fortunately, the next drop (AVP 480) went well. Just before 1700, a vertically propagating inertial wave was displayed in the ADCP data; there was a peak in the northward velocity component in the upper 50 m followed by a peak in the eastward component, indicating downward propagation.

CTD cast 37 on the evening of 3 August went smoothly, but there was some concern about the sequence of bottle closings on cast 38 the morning of 4 August. Typically, all the bottles but the last one are tripped, the CTD is brought to the surface to verify that the last is still open and then lowered back to the depth required (~10 m), and the last sample taken. This time the last bottle was already closed. We concluded that the sequence was not out of step, but that the bottle closed prematurely.

AVP drop 481 at Site 5-6 got off smoothly at 0510. We requested 1 kn. of forward speed for the launch and recovery. Other than rain squalls sweeping over us, all went well. The data from drops 480 and 481 agreed well with regard to the structure of the current above the bottom. Launch and recovery on AVP drops 482 and 483 were without problems, in spite of the squalls and lightning.

AVP drop 484 was back at Site 2-5 where we had conducted the half-day time series several days before. Our purpose in returning was to estimate the time dependence of the flow there through multiple occupations over a week-long period.

That night we conducted another long tow-yo, but this time on Section 5 on the backside of the ridge to collect data on the bottom boundary layer. The CTD was rigged to tow from the A-frame using the Markey winch. Again, the bottles were removed and extra weight was added. The tow-yo went smoothly, but took 12 hours to get to Site 5-6.

AVP drop 485 got off as soon as possible (0840) at Site 5-3 on the morning of 5 August. We had sacrificed one AVP launch to complete the tow-yo and decided to invest time in one more drop in Section 5. Data from this drop showed an enhanced flow with bottom speeds of about 25 cm/s. The last AVP drop on the section (drop 486) was at Site 5-5, and then we headed back to Section 2.

The data from AVP drop 484 at Site 2-5 showed a large increase in the velocity at the bottom relative to what we had observed previously on AVP drops 464–469. Additional profiling was needed, but we were running out of time. We planned profiles in a cross pattern around Site 2-5 along with some CTD casts.

AVP drop 487 was at Site 2-3. It showed bottom speeds of 30 cm/s and a velocity structure similar to that at Site 2-5 the previous day. However, drop 488 at Site 2-7 3.5 hours later showed a structure completely different from that at either Site 2-3 or 2-5. The strong, bottom-intensified jet was missing, and the flow was generally weaker throughout the water column. This came as a complete surprise and required another revision of our plans to be sure that we measured the velocity structure around the area.

The evening CTD cast (CTD-40) was 5 n.mi. northwest of Site 2-5 along the 4000-m isobath. The next (CTD-41) was 5 n.mi. southeast of Site 2-5 along the same isobath. AVP drop 489 at Site 2-5 began at 0730 on 6 August, about 2 hours behind schedule owing to the long CTD casts and steaming time. Other sites were considered for drops that day, but this would be our last day of profiling, as we were due to return to Rhode Island by noon on 9 August. The captain agreed to depart from Site 2-5 as late as 2300 that day.

AVP drop 490 at Site 2-1 began at 1100. After the launch, we dropped XBTs on a line to the northwest for 5 n.mi. and later for 5 n.mi. to the southeast of Site 2-1 hoping to identify the center of the mesoscale feature we observed in the AVP profiles.

We conducted AVP drop 491 where CTD cast 41 had been 5 n.mi. southeast of Site 2-5 in hopes of resolving any along-isobath structure. Again, after the launch, we dropped XBTs at 5 and 10 n.mi. from the drop site along a line at 145°T (southeast). We returned just as the AVP was nearing the surface. We were unable to hear it acoustically until we were only 200 m away, as the hot sun and low wind had created a strong diurnal thermocline which trapped the sound.

Our final drop (AVP drop 492) was at Site 2-5 where the velocity structure had been changing so rapidly over the past few days. We decorated the beach ball specially for the occasion, the 92nd drop of the cruise, one drop for each year of the century. We all tried to be extra careful but almost made a bad mistake. The cover for the charging connector was in place but not tightened down. Fortunately, the mistake was noticed as the

instrument was being moved to the launch station and was corrected. The rest of the operation went well, and we were glad to have the profiler aboard at 2020 after a successful drop. We began steaming north toward Narragansett Bay, Rhode Island, but continued to drop more XBTs in an attempt to define any mesoscale eddy structure in the area.

The science team met on 7 August to consider what to do with the special XBTs we brought to test the interference of the TTM2 tow cable with the XBT profiles. Our plan was to deploy TTM2 without its rough-surfaced tail and without the splice in the water. We had six XBTs with resistors (T-7s) and six insulated ones. The units with the resistors were designed to exhibit a fixed temperature of 15°C throughout the drop, and the insulated ones were designed to give the isolation resistance. Before deploying TTM2, we first needed to get the XBTs to operate properly from a hand launcher. The first drop was a complete loss; the next yielded a noisy profile that was confirmed by a third drop. Moving back to the ship's stanchion-mounted launcher did not yield a better profile. It was decided to leave this matter to a future cruise when TTM2 might be operational.

For the rest of that day and all of 8 August, we secured instruments, duplicated files, removed and stowed antennas and cables, and generally broke down the laboratory and packed up gear. Popcorn was made to keep things running smoothly, and we all caught up on sleep. The night watch was canceled so its members could return to a regular daylight schedule. We docked at Quonset Point, Rhode Island, at 0940 on 9 August under rainy skies, off-loaded gear into a waiting truck and headed home.

Appendix C: Water Property Measurement Techniques and Calibrations

C.1 Temperature, Salinity, Pressure and Density

Two pairs of temperature (T) and conductivity (C) sensors were used on the CTD and one pair on each AVP, all of the same model (see Table 12). Paroscientific Digiquartz pressure sensors were used on all instruments. All sensors and the CTD underwater unit were checked and calibrated by Sea-Bird Electronics both pre-cruise (June 1992) and post-cruise (September 1992). The AVP and CTD temperature and conductivity sensors were calibrated simultaneously in a common bath to determine the offset between sensors. Post-cruise calibrations were used for final processing because they were of higher quality due to a calibration-bath design change. Much of the following information is taken from a memo written by Nordeen Larson of Sea-Bird which was sent with our final calibration sheets on November 19, 1992.

Table 12: Sea-Bird temperature, conductivity and oxygen sensors used on R/V *Endeavor* cruise 239.

Platform	Temperature, Model 3	Conductivity, Model 4	Oxygen, Model 23
CTD (primary)	S/N 843	S/N 484	S/N 230313
CTD (secondary)	S/N 844	S/N 485	
AVP1	S/N 1248	S/N 971	S/N 230303
AVP2	S/N 703	S/N 330	S/N 230302

The pressure sensor was found to be healthy both pre- and post-cruise with a +0.15 dbar drift. We used the 1988 calibration coefficients from Paroscientific with a +3.3 dbar offset during the cruise and did not change them in post-cruise processing. Expected accuracy was ± 1.5 dbar under all conditions, and ± 0.75 dbar at depth.

The conductivity sensors were found to be normal and "healthy" with a very slight drift during the cruise period of -0.0005 S/m at 3.5 S/m (about -0.005 PSU equivalent) (see Figures 29 and 30 for calibration sheets). Corrected salinities were better than ± 0.004 PSU (see below for further discussion).

Post-cruise temperature calibrations showed an absolute drift of under 1 mK at temperatures below 10°C for all sensors between pre- and post-cruise calibrations. To achieve a best match to the absolute temperature calibrations of NRCC, a slope of +1.00009568 and offset of +0.0024 mK were applied as recommended (see Figures 31 and 32 for calibration sheets). Despite the low drift, both the primary and secondary temperature sensors on the CTD were found to be "unhealthy" due to a faulty capacitor in the pre-amplifier circuit during the post-cruise calibration. This affected the secondary temperature sensor on the CTD more and therefore it was not used other than as a consistency check on the primary sensor. In addition to the capacitor problem, the thermistor in the primary sensor was not properly soldered to its leads, yielding a time constant of 0.280 seconds compared with a value of about 0.065 seconds for a normal sensor. Fortunately, this long time constant is not critical to performance in the deep ocean where temperature changes are small over great depths. Thus, we used the primary sensor in post-cruise data processing with some confidence.

During the cruise, in-situ comparison between the AVP and CTD TC-sensor pairs was accomplished in two ways. First, on CTD casts 15, 20, 30, and 41, the TC-sensor pair from AVP1 was put on the CTD in place of the normal secondary set. These were referred to as "calibration casts". The same was done for the TC pair from AVP2 on CTD cast 31. (The thermistor soldering problem noted above was detected through analysis of these calibration casts.) Second, several AVP drops and CTD casts were made sequentially in exactly the same location allowing comparison of data in nearly identical natural conditions, but with each sensor pair operating on its "home" platform.

The best environment in which to compare the sensors for offsets is a thick, well-mixed layer with homogeneous temperature and salinity, such as a bottom mixed layer (BML), where response time to gradients is not a significant factor. Some of our calibration and intercomparison sites met this requirement (see Table 13). The CTD primary sensor pair was chosen as the standard because it had the most stable pre- and post-cruise calibration despite its slow time response for temperature. The offsets

necessary to make the AVP TC sensor data match those of the CTD are shown in the last two columns of Table 13. These were determined from the means of the data throughout the most uniform parts of the bottom layers or, in case of stratification, those points closest to the bottom. The offset values from Sites 0-5, 1-7, 2-1, 2-8, 2-5B were chosen to be applied to all AVP1 data because the BMLs were thick, homogenous, and the time differences between casts and drops were minimal. The AVP2 sensor pair was run on one calibration cast. However, significant electronic noise appeared in the AVP sensor channels, so its TC data were not used in any final analysis.

Table 13: In-situ calibrations and comparisons of temperature and conductivity sensors.

CTD cast	AVP drop or (sensors on CTD)	Hrs. btwn	Station location	BML type	Temp. offset (°C)	Cond. offset (Siemens/m)
15	(AVP1 sensors)	0	Leg 1	stratified	-1.4×10^{-3}	$- 5 \times 10^{-5}$
16	436	4.0	Site 0-5	mixed	0	$- 5 \times 10^{-5}$
20	(AVP1 sensors)	0	Site 1-1	stratified	-1.5×10^{-3}	$- 5 \times 10^{-5}$
22	447	4.5	Site 1-7	mixed	-0.2×10^{-3}	-13×10^{-5}
25	452	2.0	Site 2-1	mixed	$+1.5 \times 10^{-3}$	$- 2 \times 10^{-5}$
28	460	4.5	Site 2-8	mixed	$+1.0 \times 10^{-3}$	$- 5 \times 10^{-5}$
30	(AVP1 sensors)	0	Site 2-15	stratified	$+1.4 \times 10^{-3}$	$- 3 \times 10^{-5}$
31	(AVP2 sensors)	0	Site 2-3	mixed	$+1.2 \times 10^{-3}$	0
41	(AVP1 sensors)	0	Site 2-5B	mixed	$+1.0 \times 10^{-3}$	0

SEA-BIRD ELECTRONICS, INC.
1808 136th Place N.E., Bellevue, Washington 98005
Telephone: (206) 643-9866   Telex: 292915 SBEI UR

CONDUCTIVITY CALIBRATION DATA   PSS 1978: C(35,15,0) = 4.2914 Siemens/meter
CALIBRATION DATE 05-Jun-92   *Pre cruise cal NRCC*

SENSOR SERIAL NUMBER = 484 ◄— *PRIMARY*

a = 9.52523993e-06   b = 4.62540767e-01
c = -3.91139143e+00   d = -4.38022747e-05
m = 4.3

BATH TEMP (°C)	BATH SAL (°/oo)	BATH COND (Siemens/m)	INST FREQ (kHz)	INST COND (Siemens/m)	RESIDUAL (Siemens/m)
31.0854	34.9827	5.94861	11.67345	5.94871	0.00010
22.9717	34.9841	5.09373	10.86255	5.09364	-0.00009
15.0455	34.9864	4.29438	10.04385	4.29422	-0.00016
6.8841	34.9864	3.51638	9.17581	3.51634	-0.00004
-0.9926	34.9862	2.81763	8.31815	2.81787	0.00024
26.9915	15.2821	2.61202	8.04812	2.61219	0.00017
19.0823	15.2818	2.21952	7.50480	2.21943	-0.00009
10.9818	15.2813	1.83731	6.93488	1.83723	-0.00008
2.9637	15.2813	1.48287	6.36048	1.48280	-0.00007
0.0000	0.0000	0.00000	2.90766	0.00001	0.00001

Conductivity = $(af^m + bf^2 + c + dt) / [10(1 - 9.57(10^{-8})p)]$ Siemens/meter, where p = pressure in dbars

Residual = instrument conductivity - bath conductivity

NOTE: Multiply Siemens/meter by 10 to obtain mmho/cm
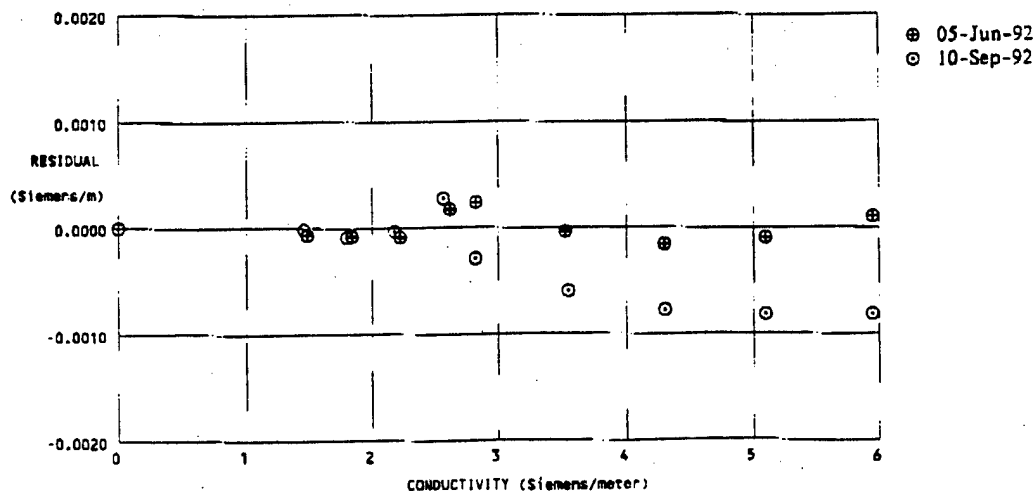
Figure 29: Sea-Bird post-cruise calibration sheet for primary salinity sensor used on CTD (S/N 484).

S E A - B I R D   E L E C T R O N I C S ,   I N C .
1808 136th Place N.E., Bellevue, Washington 98005
Telephone: (206) 643-9866   Telex: 292915 SBEI UR

CONDUCTIVITY CALIBRATION DATA   PSS 1978: C(35,15,0) = 4.2914 Siemens/meter
CALIBRATION DATE: 10-Sep-92

SENSOR SERIAL NUMBER = 971

a = 7.33322396e-06   b = 5.48199118e-01
c = -4.10399641e+00   d = -1.24957256e-04
m = 4.5

| BATH TEMP | BATH SAL | BATH COND | INST FREQ | INST COND | RESIDUAL |
(°C)	(°/oo)	(Siemens/m)	(kHz)	(Siemens/m)	(Siemens/m)
30.9744	35.0197	5.94226	10.73815	5.94233	0.00007
22.9415	35.0211	5.09540	10.00075	5.09532	-0.00008
15.0593	35.0207	4.29950	9.25307	4.29941	-0.00009
7.0887	35.0205	3.53835	8.47537	3.53835	-0.00000
-1.0392	35.0199	2.81612	7.66362	2.81625	0.00013
26.9531	14.9594	2.55971	7.35397	2.55979	0.00008
19.0084	14.9592	2.17308	6.85953	2.17306	-0.00002
10.8452	14.9592	1.79558	6.33936	1.79552	-0.00006
3.0679	14.9590	1.45835	5.83537	1.45832	-0.00003
0.0000	0.0000	0.00000	2.73589	0.00000	0.00000

Conductivity = $(af^m + bf^2 + c + dt) / [10(1 - 9.57(10^{-8})p)]$ Siemens meter, where p = pressure in dbars

Residual = instrument conductivity - bath conductivity

NOTE: Multiply Siemens/meter by 10 to obtain mmho/cm

⊕ 01-Nov-91
⊙ 08-Jul-92
⊗ 10-Sep-92
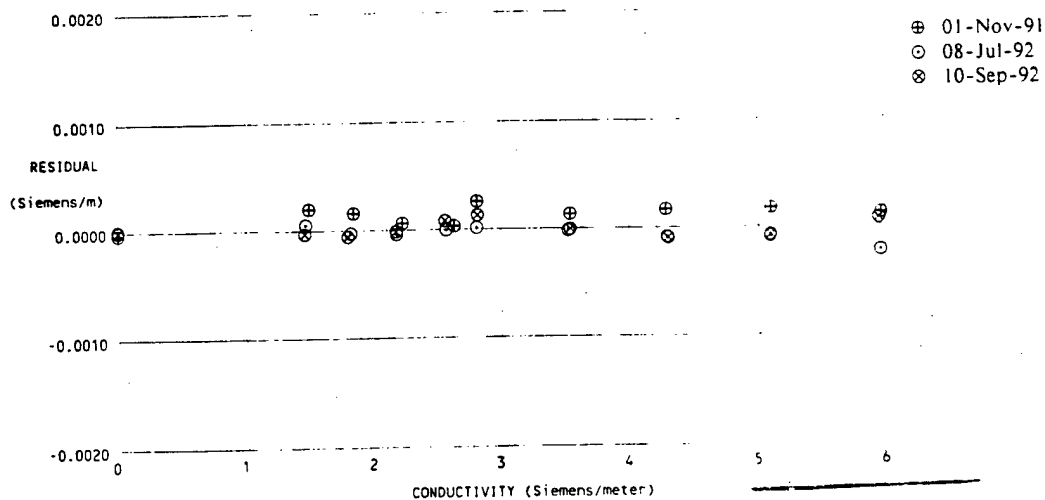
Figure 30: Sea-Bird post-cruise calibration sheet for salinity sensor used on AVP-1 (S/N 971).

SEA-BIRD ELECTRONICS, INC.
1808 136th Place N.E., Bellevue, Washington 98005
Telephone: (206) 643-9866   Telex: 292915 SBEI UR

TEMPERATURE CALIBRATION DATA
CALIBRATION DATE: 09-Sep-92s   *Post Cruise   SBE cal.*

SENSOR SERIAL NUMBER = 843 *Primary*

a = 3.68092273e-03   b = 5.99575485e-04
c = 1.62685039e-05   d = 3.17998992e-06
f_o = 6115.764

BATH TEMP (°C)	INSTRUMENT FREQ (Hz)	INST TEMP (°C)	RESIDUAL (°C)
-1.4789	6115.764	-1.4790	-0.00012
1.0236	6468.829	1.0238	0.00013
4.4980	6983.139	4.4982	0.00012
8.0336	7536.037	8.0335	-0.00003
11.4274	8095.550	11.4273	-0.00014
14.8931	8696.717	14.8930	-0.00014
18.3991	9336.225	18.3991	0.00005
21.8750	10001.998	21.8752	0.00021
25.3802	10705.948	25.3802	0.00004
28.8260	11430.529	28.8259	-0.00017
32.3632	12208.525	32.3632	0.00004

Temperature = $1/\{a + b[ln(f_o/f)] + c[ln^2(f_o/f)] + d[ln^3(f_o/f)]\} - 273.15$ (°C)

Residual = instrument temperature - bath temperature
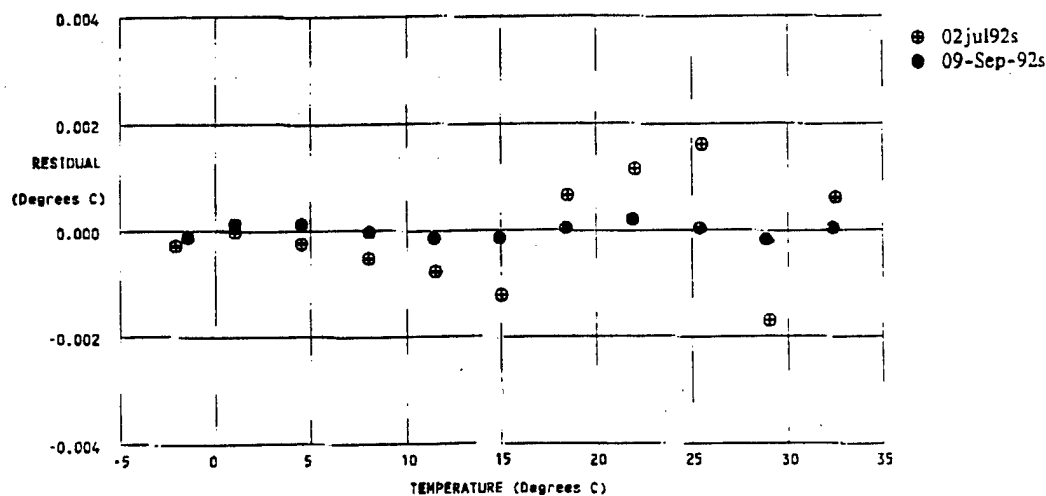
Figure 31: Sea-Bird post-cruise calibration sheet for primary temperature sensor used on CTD (S/N 843).

SEA-BIRD ELECTRONICS, INC.
1808 136th Place N.E., Bellevue, Washington 98005
Telephone: (206) 643-9866   Telex: 292915 SBEI UR

TEMPERATURE CALIBRATION DATA
CALIBRATION DATE: 04-Sept-92   NRCC

SENSOR SERIAL NUMBER = 1248   AVP1

$a = 3.67369109e-03$ $b = 5.99999554e-04$
$c = 1.45123064e-05$ $d = 2.03852176e-06$
$f_o = 6482.98$

2.713151e-6

BATH TEMP (°C)	INSTRUMENT FREQ (Hz)	INST TEMP (°C)	RESIDUAL (°C)
31.1903	12492.38	31.1902	-0.00013
23.0074	10697.38	23.0073	-0.00011
14.9612	9114.43	14.9607	-0.00048
6.9515	7709.70	6.9513	-0.00020
-0.9442	6482.98	-0.9442	-0.00001
26.9740	11543.74	26.9743	0.00029
19.0134	9889.64	19.0135	0.00007
10.9312	8387.05	10.9317	0.00054
2.9885	7074.97	2.9885	0.00003

Temperature $= 1/(a + b[\ln(f_o/f)] + c[\ln^2(f_o/f)] + d[\ln^3(f_o/f)]) - 273.15$ (°C)

Residual = instrument temperature - bath temperature

NRCC shows -3 mK ;3 mo
SBE shows -1 mK /3 mo

⊕ 25-Oct-91
⊙ 02jul92s — SBE
⊗ 04-Sept-92

new old fit.
JUL 02 —
-1.06 09 Sept — 1.84
-1.17 23 Sept — 1.92
-.91 7 Oct — 1.3
Zw ...
; mo
over Jul ...
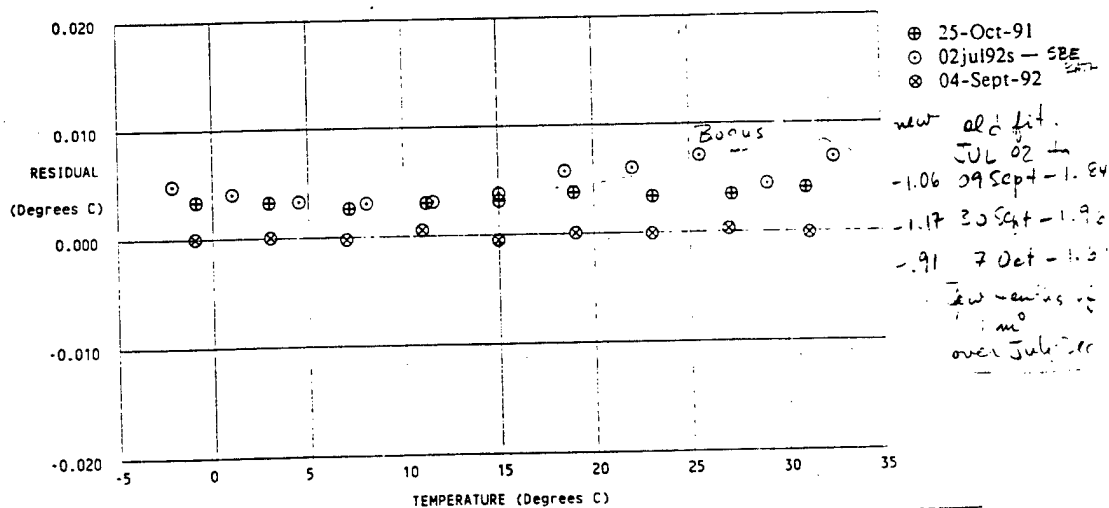
Figure 32: Sea-Bird post-cruise calibration sheet for temperature sensor used on AVP-1 (S/N 1248).

Final data processing was conducted with post-cruise calibration values using SBE SeaSoft software (version 4.213 or later) for the CTD sensors, or the equivalent for the AVP sensors. The following routines and parameters were used. "DATCNV" converted the raw data to engineering units using "PCCALS.CON" file with post-cruise calibration constants and converting pressure, primary and secondary temperature (in IPTS-68), primary and secondary conductivity, oxygen current, oxygen temperature, light transmission, depth and altimeter records. "SPLIT" divided the data into down- and up-cast profiles after which only the down-cast was used (except for oxygen data, see next section). "ALIGNCTD" advanced profiles as follows: primary conductivity = 0 s, primary temperature = 0.280 s, primary oxygen = 4.0 s, secondary conductivity = 0.073 s, secondary temperature = 0 s, secondary oxygen = 0 s. "WILDEDIT" removed wild points with first pass = 3 sigma and second pass = 10 sigma. "CELLTM" corrected the conductivity cell for thermal mass with alpha = 0.03 and 1/beta = 9.0. "LOOPEDIT" removed sections where the CTD was traveling backwards owing to ship roll (fixed minimum velocity = 0.01 m s^{-1}). "DERIVE" generated final values of primary and secondary salinity and oxygen concentration in ml l^{-1} with proper ".CON" files for oxygen sensors. "BINAVG" put profiles into pressure bins of 2 dbar with a first surface bin of 5 m. "DERIVE" (again) added density and sigma-theta values. "BUOYANCY" added values for buoyancy frequency N. "ASCIIOUT" made ASCII files of the data. Values of temperature and pressure were taken from the ".ROS" files with "ROSSUM" for processing nutrient and salinity water sample data.

Salinity was also measured from the Niskin-bottle water-samples to further calibrate the SBE conductivity sensors. Salinities were determined for each sample using an Autosal 8400A on board the ship. About one month after the cruise, a similar model was used at the University of Washington to find the salinity of duplicate samples taken from casts 15, 20, 30, 31, and 41 (i.e., the calibration casts where an AVP sensor pair replaced the usual secondary set on the CTD). An illustration of the differences between these values and the electronic CTD values for CTD cast 20 is shown in Figure 33. The difference between bottle values and electronic values for all casts is shown in Figure 34. The mean of all these differences was –0.00059 ± 0.0033 PSU, and the rms (i.e., square root of the sum of each difference squared) was 0.052 PSU. The uncertainty in bottle salinities was 0.02 PSU. Because no significant trend in salinity differences was detected, no adjustments to the processed data were made.
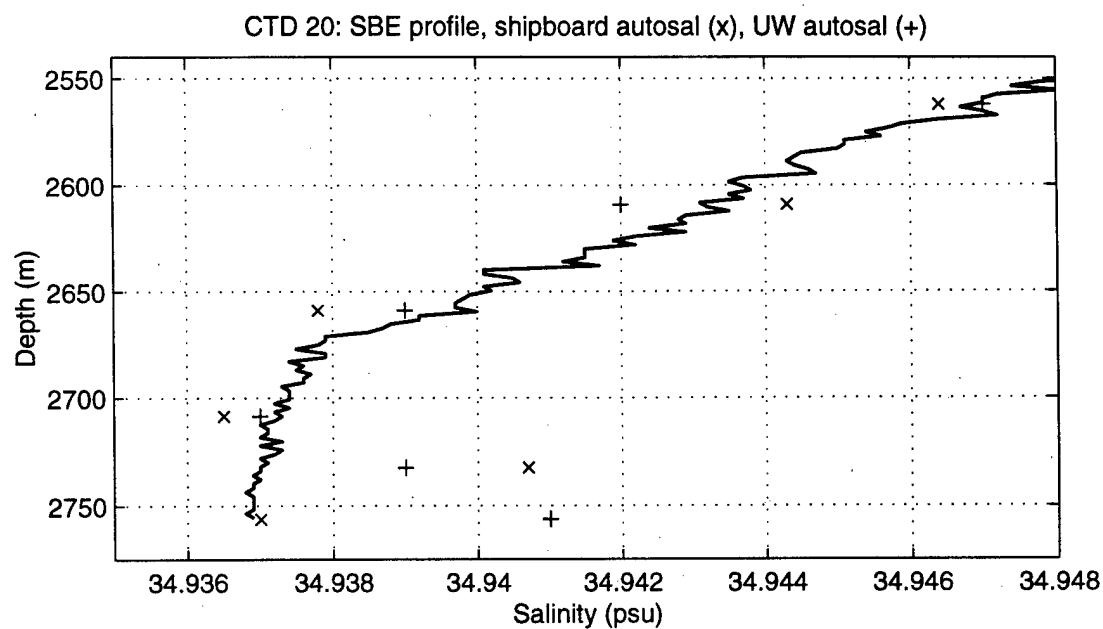
Figure 34: Salinity values for CTD 20. Profile is from Sea-Bird primary temperature and conductivity sensors, (x) from onboard Autosal analysis, (+) from UW Autosal analysis.
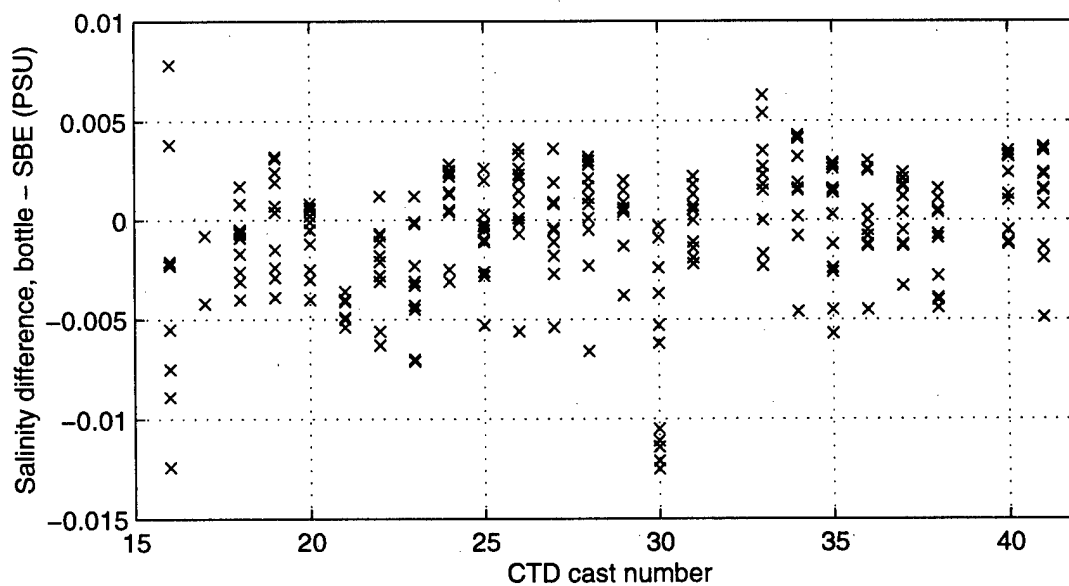
Figure 35: Salinity differences between water-sample derived values and Sea-Bird Electronics sensor derived values.

C.2 Oxygen

Initial processing of the data from the SBE Model 23 oxygen sensors (one on the AVP and one on the CTD) yielded oxygen concentration values significantly different from those measured in the water samples using the modified Winkler titration method (Carpenter, 1965). The reasons were numerous and the remedy only partially satisfactory. (Much of the following information was gathered from conversations with Jim Carlson of SBE in December 1996.) First, the Beckman sensor unit used by SBE has a very long response time to in-situ temperature changes (order three minutes). Therefore, the down-cast signal and up-cast signals do not match well except near the bottom where the temperature changes most slowly. In addition, there is a slight pressure hysteresis effect on the sensor. Second, there was a misprinted coefficient for one of the algorithms used to convert the measure values of sensor temperature, water temperature, salinity, pressure, and sensor current into oxygen concentration. Third, the pre-cruise calibration values for these sensors were only good for the first few casts during leg 1 because sensor drift was rapid and large.

The best way to correct the full-depth SBE profiles for sensor drift and response time was to use the titration-derived water-sample values (a.k.a., "bottle concentrations") as constraints to adjust the processing algorithm parameters for each drop until the electronic-derived concentrations nearly match the bottle concentrations at those particular depths. The bottle concentrations are accurate to within 0.02 ml/l, considerably better than the electronic values. This analysis was only performed on the electronic oxygen data from the CTD as there were no bottles on the AVP to use for referencing its electronic sensor. However, because the spatial density of CTD casts was fairly high, we were able to construct a reasonably good survey in the deep water column.

Because the bottles were taken during the upcast, parameter values were derived using the upcast electronic profiles and then applied to both down- and upcast data. Most investigators use the downcast data exclusively because of the clean flow pattern into the sensor and the simultaneity with the temperature and salinity measurements. However, in this case it was thought that using the upcasts was advantageous because the algorithm parameters were being adjusted for exactly the same water measured by titration and the sensor had more time to equilibrate to the surrounding water temperature. The disadvantage of having a disturbed flow around the sensor from the CTD rosette during

the upcast was partially overcome by stopping for a short soaking period of 30 s at each bottle depth to get a better average value. After adjusting the processing parameters for each cast, the electronic profile and bottle values matched well, as seen for CTD casts 16, 18 (Section 0), and 20–23 (Section 1) in Figure 35. All electronic profiles were filtered with an 8 m boxcar filter to smooth out spikes. Cast 16 had bottle samples spread throughout the water column and demonstrates how well the post-processed electronic profile and bottle values match. All casts after CTD 16 had the bottles concentrated in the bottom mixed layer. When the bottom mixed layer is examined closely, it appears neither the down nor upcast profile exactly matches the bottle concentrations (see Fig. 36), therefore only the bottle samples were used for analysis of the BML.
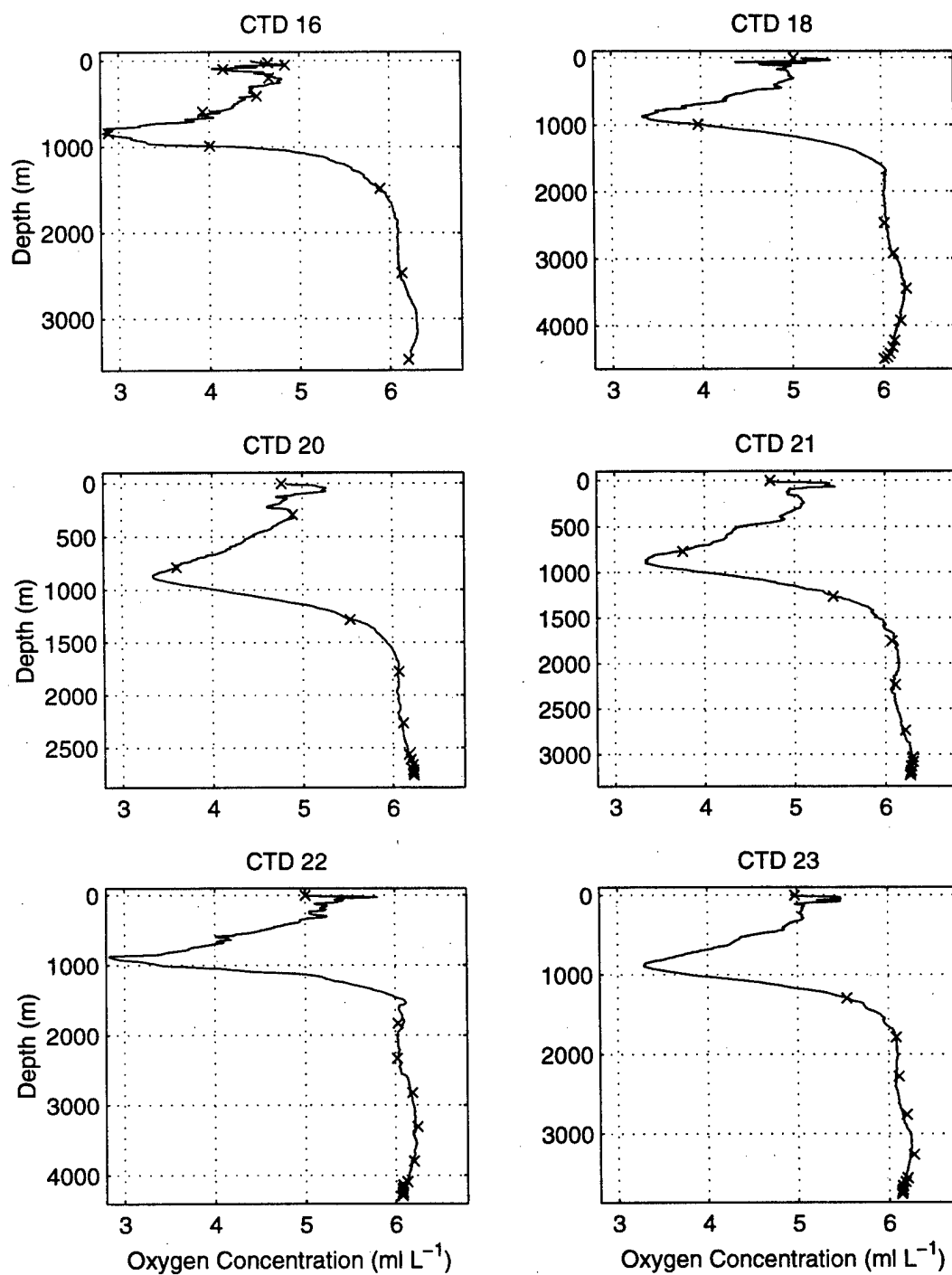
Figure 36: Oxygen concentration profiles from upcasts of CTD 16, 18, 20, 21, 22, 23 on Sections 0 and 1 with water-sample measured values (x).

Dissolved Oxygen from CTD 20
Electronic profiles and bottle values (x)
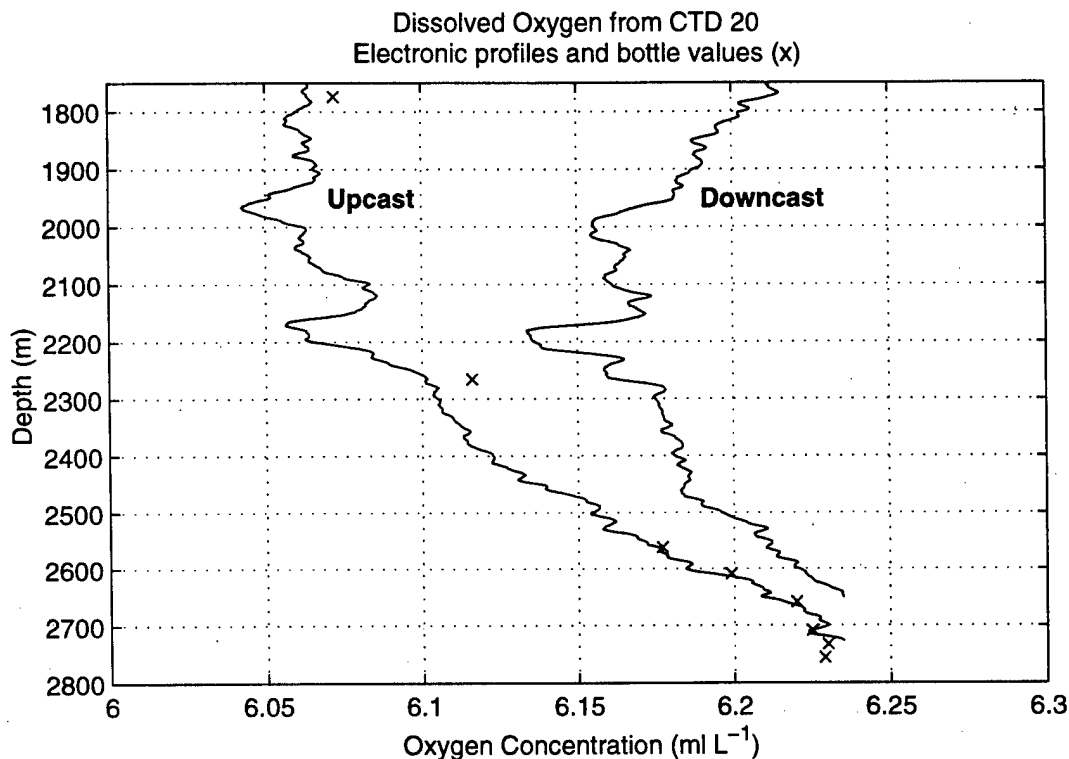
Figure 37: Oxygen concentration profiles from down- and upcasts for deep portion of CTD 20 with water-sample measured values (x).

C.3 Nutrients

Dissolved nutrient concentrations were determined for nitrate+nitrite, nitrite, phosphate, and silicate using a modified continuous-flow autoanalyzer from SIO. Nitrate+ nitrite was analyzed according to the basic method of Armstrong *et al.* (1967). Nitrate is reduced to nitrite in a column of copperized cadmium filings and reacted with sulfanilamide and N-(1-napthyl)ethylenediamine dihydrochloride to form a red azo dye which is analyzed at 542 nm. Nitrite alone is analyzed without reduction and the difference between nitrate+nitrite and nitrite yields the nitrate concentration. The phosphate analysis is a modification of the procedure of Bernhardt and Wilhelms (1967) using dihydrazine sulfate as a reductant. The silicate analysis is a modification of the

method of Armstrong *et al.* (1967) using stannous chloride as the reductant. Both phosphate and silicate analyses are carried out at 820 nm.

Profiles of concentration for nitrate, phosphate and silicate for CTD-16 are shown in Figure 37. This cast had samples taken at a more uniform spacing in the water column and represents the typical full-depth profile for each nutrient. On subsequent casts the samples were concentrated in the BML, which typically has good uniformity in all nutrient concentrations with some occasional small differences that may be related to up- or down-slope advection within the BML (see Fig. 20). Silicate increases with depth due to a high concentration end member, Antarctic Bottom Water (AABW), mixing with North Atlantic Deep Water (NADW) in higher latitude basins. In general, the deeper the cast, the higher the concentration of silicate, indicating increased percentages of AABW. However, there are no changes in the concentration profiles of any nutrient as the DWBC moves along the ridge, indicating no significant sources or sinks here.
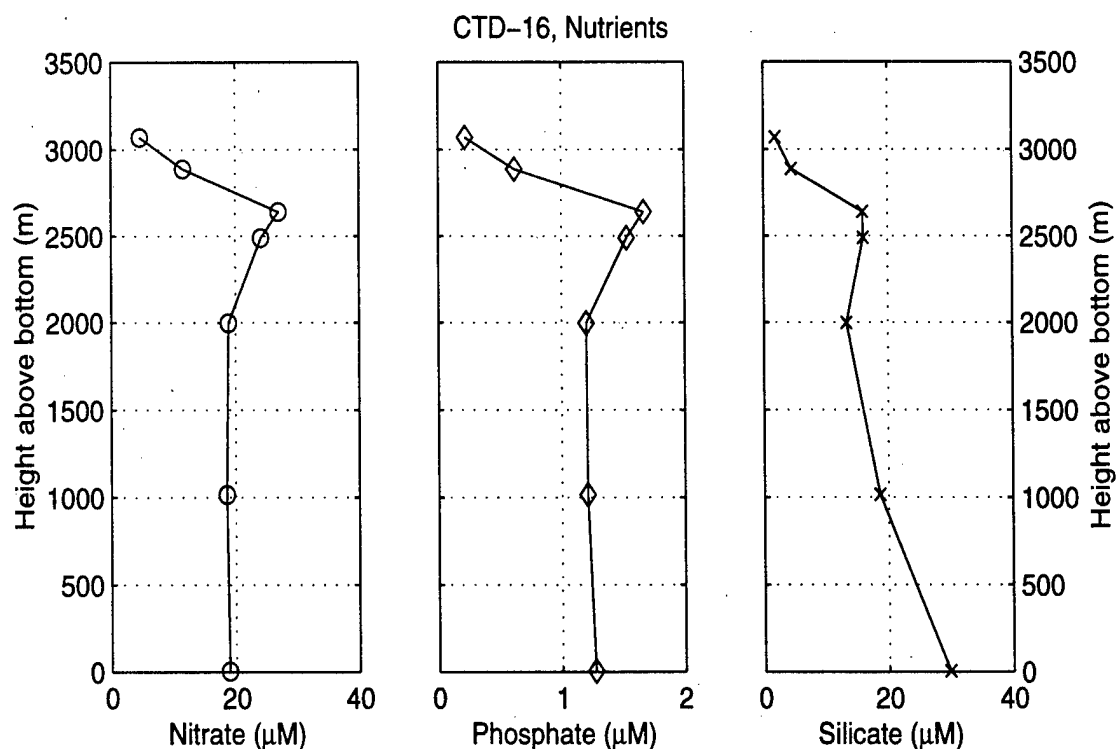
Figure 38: Full depth profiles of nitrate, phosphate and silicate concentrations from CTD-16, Section 0.

C.4 Suspended Sediments

To determine the concentration of suspended particulate material (SPM), two indirect optical measurements and one direct water sample measurement were attempted. The optical instruments were an optical back-scatter (OBS) device from D&A Instrument Company and a 25-cm beam transmissometer from Sea-Tech Company. The OBS was attached alternately to the AVP and to the CTD cage, while the transmissometer was always fixed to the CTD cage. The plan was to calibrate the OBS signals with both the transmissometer data and water samples on the CTD cast, then transfer it to the AVP for more in-situ bottom mixed layer measurements. By combining the velocity and concentration data, transport of SPM (sediment in this case) in the BML could be determined. Closing a series of sections could yield the net flux of sediment, either on or off the ridge. The OBS was chosen for concentration measurements on the AVP because it fit the size and power requirements. The transmissometer would have been more appropriate, but would not fit without significant changes to the AVP. Packaged independently of all other systems, the OBS was easily moved back and forth from the AVP to the CTD system. The transmissometer was useful in determining full depth profiles of relative SPM concentration. It also allowed the SPM concentration to be compared to the simultaneous CTD data as well as to previous studies of the area.

The OBS unit was modified to detect the levels of SPM concentration below its normal range. Unfortunately, we were never able to calibrate it or make sense of the signals it produced. Also, after about 75 deep cycles it was apparent the light baffle in the sensor head had moved, rendering the instrument useless. The transmissometer, on the other hand, was a stock unit that had been calibrated only six months prior to the cruise. We conducted an air-calibration after the cruise and found no change relative to its pre-cruise calibration value. Therefore, all data from the transmissometer was deemed valid as taken.

The transmissometer measures light attenuation along a narrow path. The attenuation is related to the number and size of particles in the path, thus delivering a relative measure of SPM concentration. In order to change this into an absolute value, some actual reference to the SPM in the water itself must be obtained. The traditional approach is to directly filter water samples and determine a concentration through a pre- and post-filtering weight difference, divided by the volume of water filtered.

Five liter Niskin bottles were used to obtain water samples for oxygen and nutrient observations, although less than one liter was typically taken for these analyses. The remainder was drawn either directly into 4-liter beakers or into 8-liter storage jugs. A measured amount of water was drawn through pre-weighed filters via a vacuum system. The filters chosen were 47 mm diameter Nulceopore polycarbonate membranes with a 0.4 μm diameter pore size. The 47 mm diameter was chosen over the 25 mm diameter because the latter did not allow enough water to flow through in the time available between CTD casts. The filters were dried on board and weighed again at the University of Washington. Theoretically, this yields an SPM concentration in micrograms per liter for each bottle by dividing the weight difference by the amount filtered. Practically, this technique hinged on how well the filters were weighed both before and after the cruise. Unfortunately, the pre-cruise weighing was done poorly resulting in a large amount of random bias error due to static cling of the filters to the electro-balance chamber. The polycarbonate is a hydrophilic material but it takes on a static charge very easily. This problem was resolved for the post-cruise weighing but the pre-cruise errors were too large to make the data useful. However, these filters did provide material for X-ray fluorescence analysis and scanning electron microscope imaging (see Fig. 7).

The calibration curve from a previous study of sediment at the BOR (Haskell, 1991) was used with our transmissometer data to determine the concentration of suspended sediment during the experiment (see Fig. 38). Haskell used the same model transmissometer and produced his calibration in the same fashion we attempted, by directly filtering water samples. His data also have some scatter due to difficulty in pre- and post-weighing filters. However, the data are from the same location and only three years prior to our experiment, so it provides a useful basis for converting our transmissometer readings to SPM concentrations.
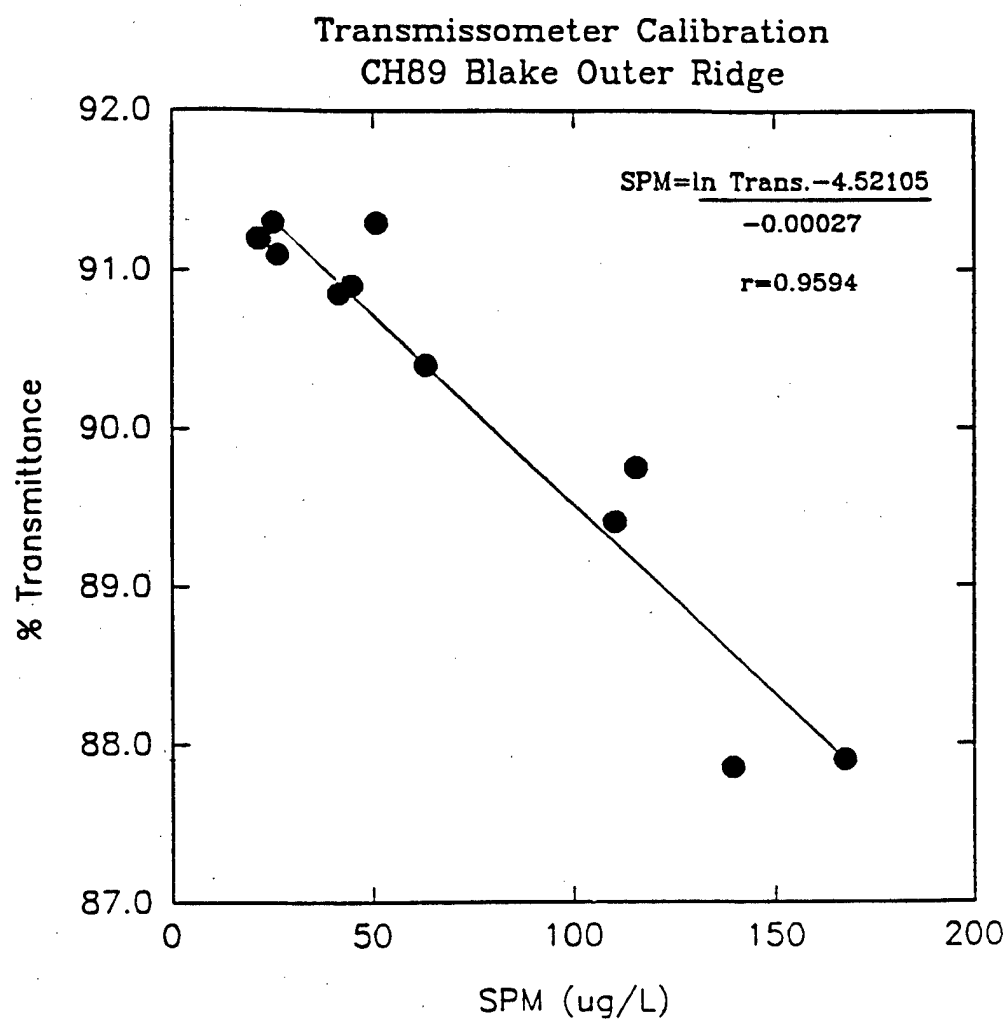
Figure 39: Transmissometer calibration curve from Haskell (1991) for Blake Outer Ridge
and a 25-cm Sea-Tech transmissometer. Also given is the equation relating SPM
concentration to transmittance values as calculated by linear regression of the data
points in the plot.

Appendix D: Data Figures

D.1 Unstable density steps in the bottom mixed layer
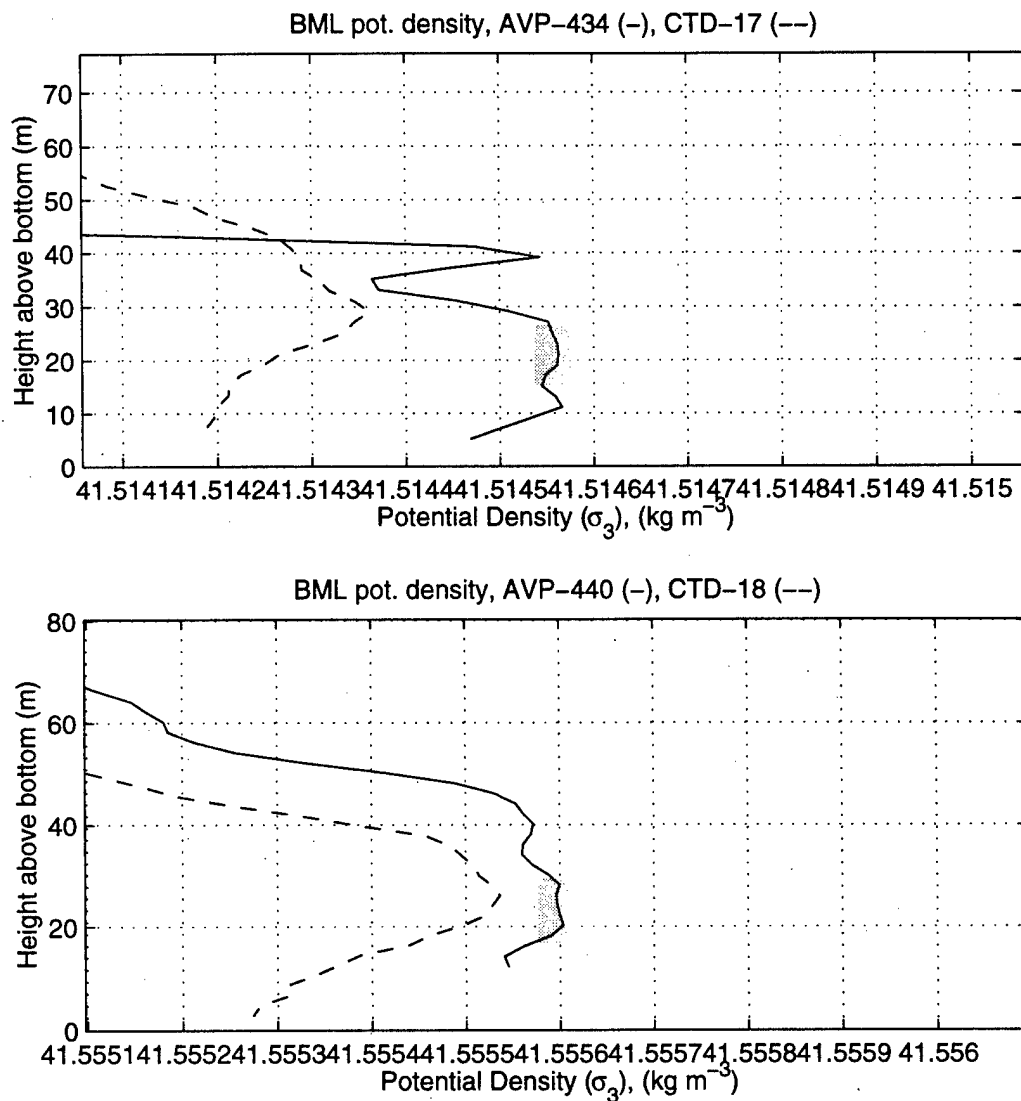
Figure 40: Potential density profile of BML on Section 0. AVP-434 was 16 hours before CTD-17 at Site 0-3. AVP-440 was 4 hours before CTD-18 at Site 0-9.

122
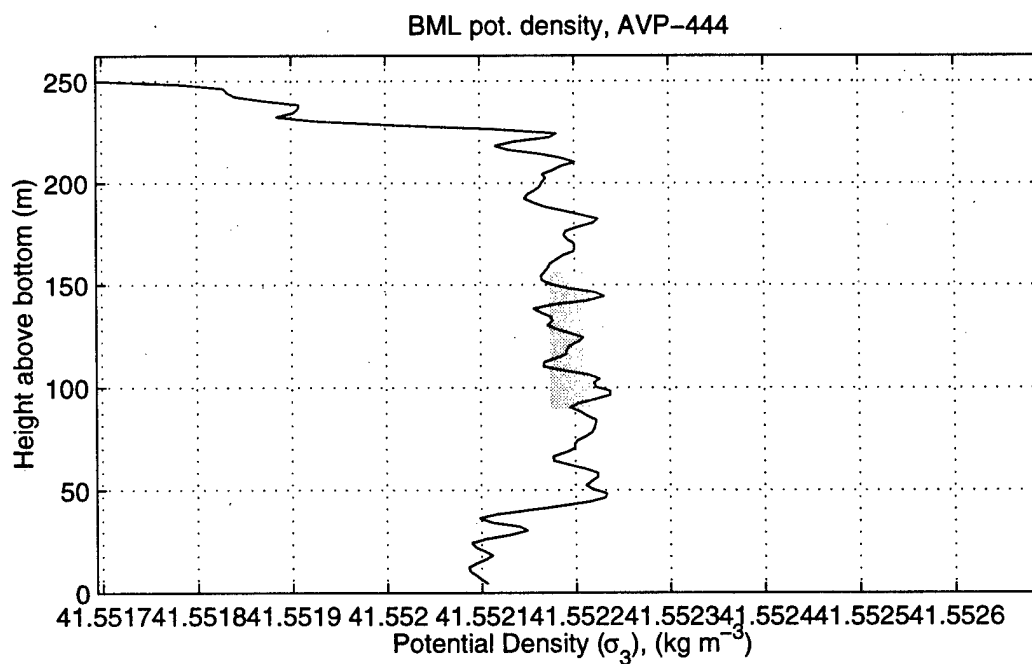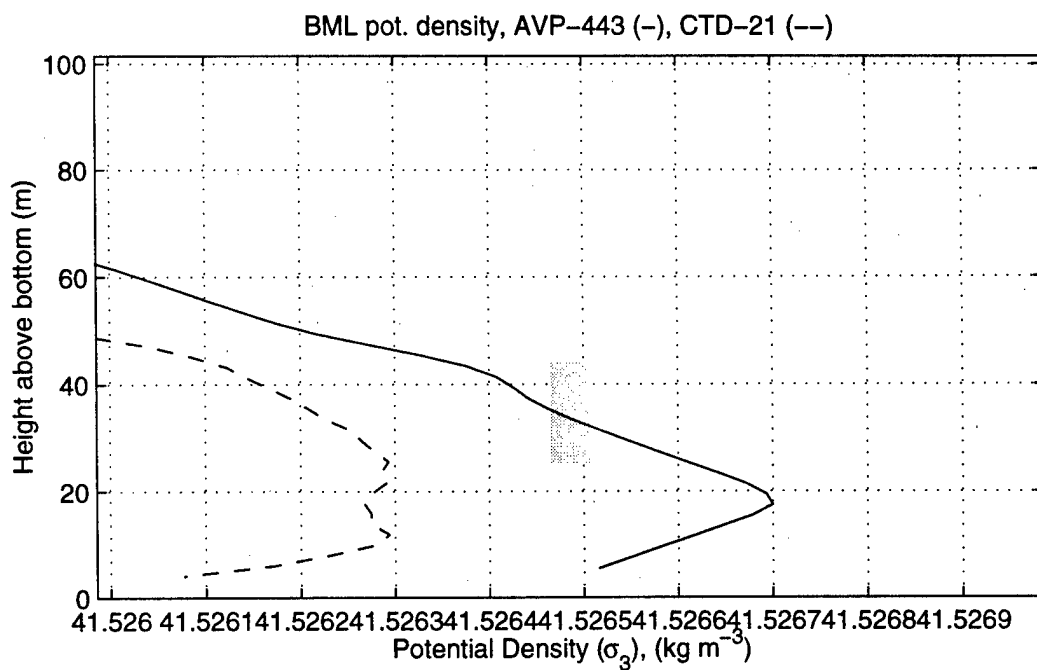
Figure 41: Potential density profile of BML on Section 1. AVP-443 was 8 hours before CTD-21 at Site 1-3. AVP-444 was at Site 1-4 (no CTD cast was made at this station).
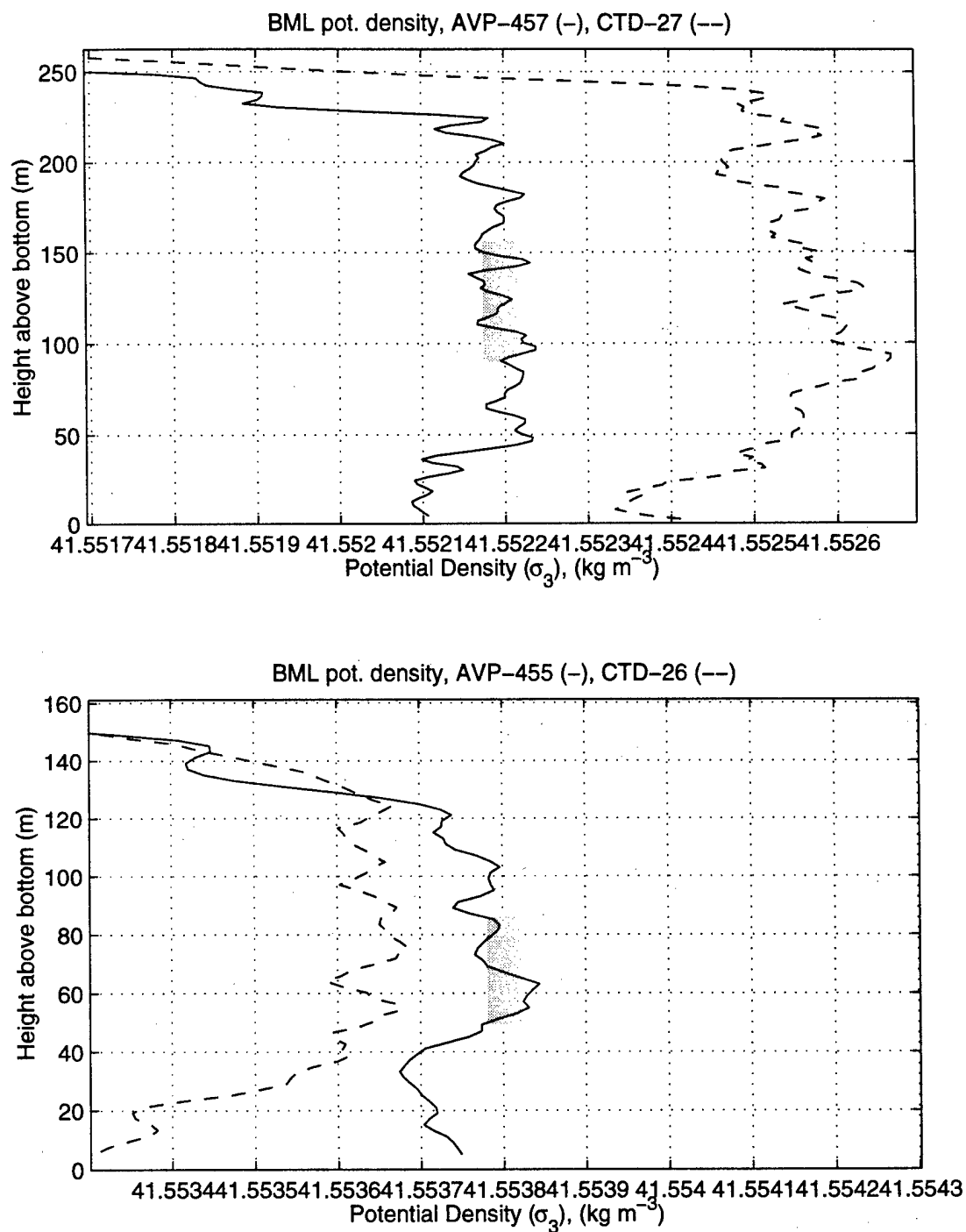
Figure 42: Potential density profile of BML on Section 2. AVP-457 was 6 hours after CTD-27 at Site 2-4. AVP-455 was 4.5 hours before CTD-26 at Site 2-7.
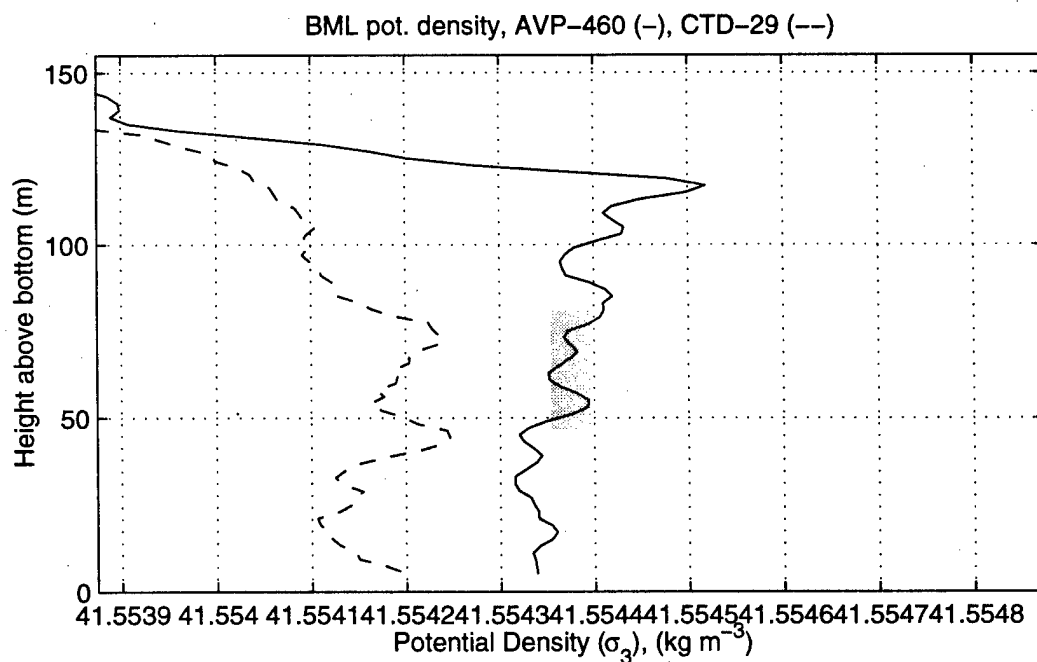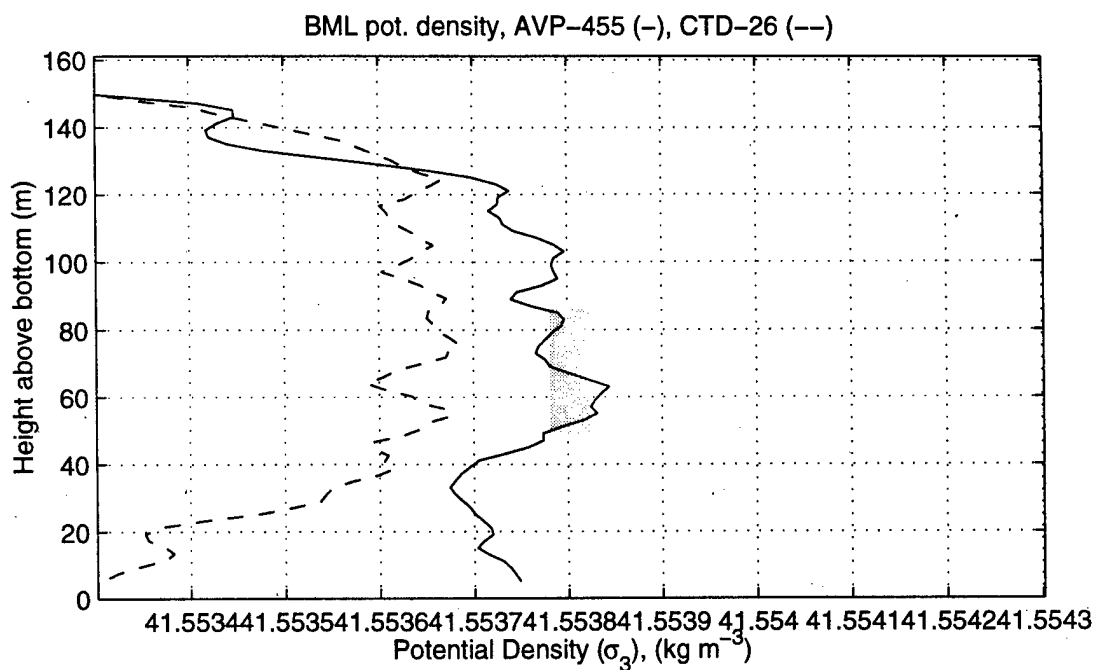
Figure 43: Potential density profile of BML on Section 2. AVP-455 was 26 hours before CTD-29 at Site 2-7. AVP-460 was 4.5 hours before CTD-28 at Site 2-8.
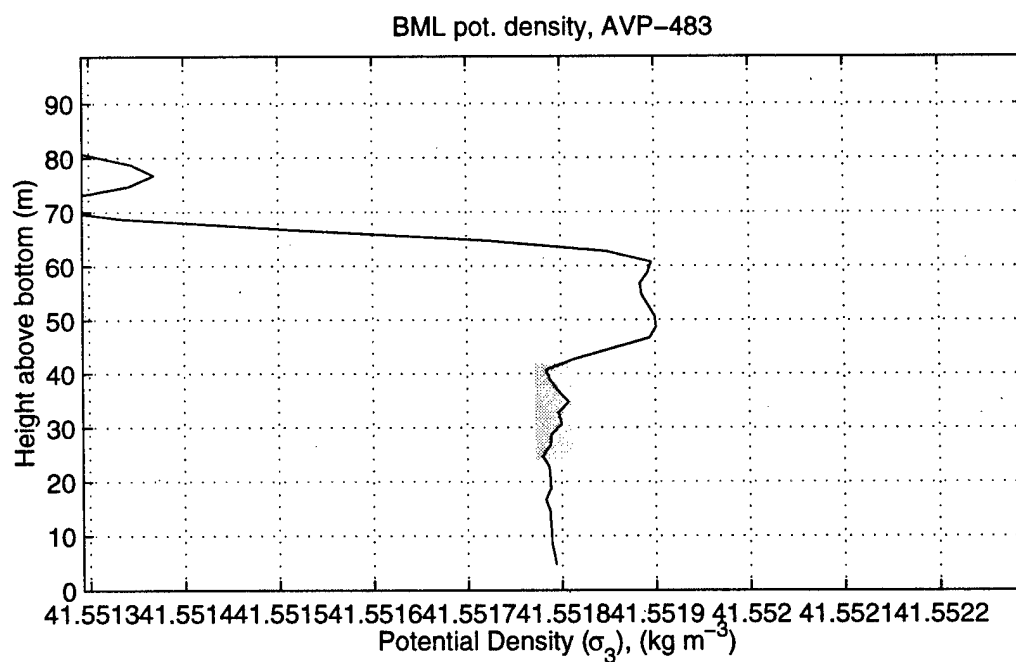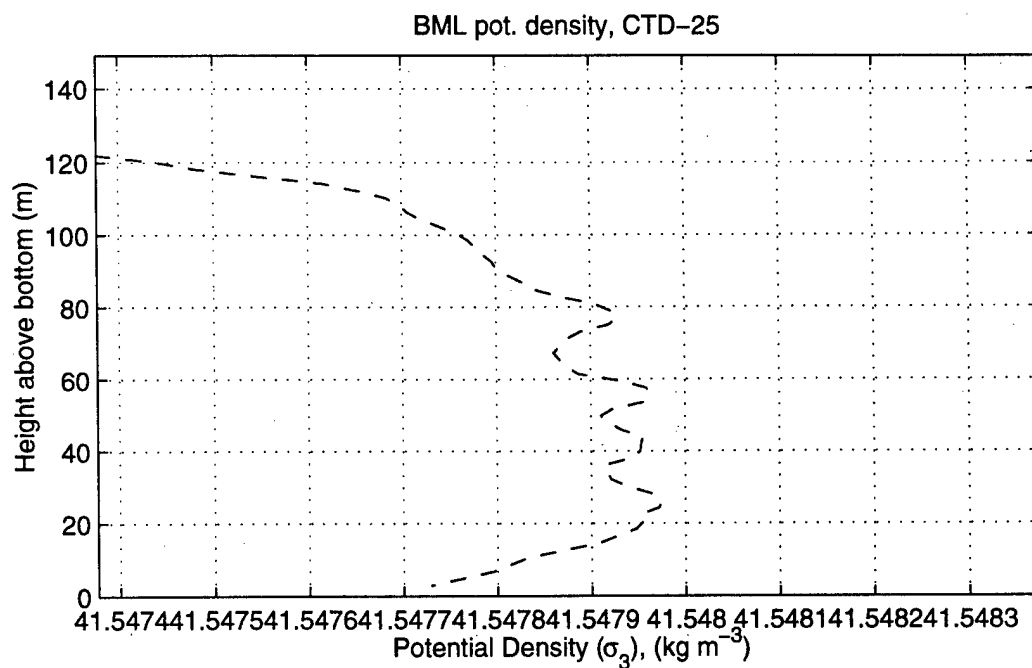
Figure 44: Potential density profile of BML on Section 2. CTD-25 at Site 2-1. AVP-483 was at Site 2-0.

D.2 Contours of density for Sections 0, 1, 2, 5

a) Potential density (σ_θ) contours, (intervals 0.1/0.5 kg m^{-3})

b) Potential density (σ_3) contours, (intervals 0.01/0.05 kg m^{-3})

Section 0

Distance (km)
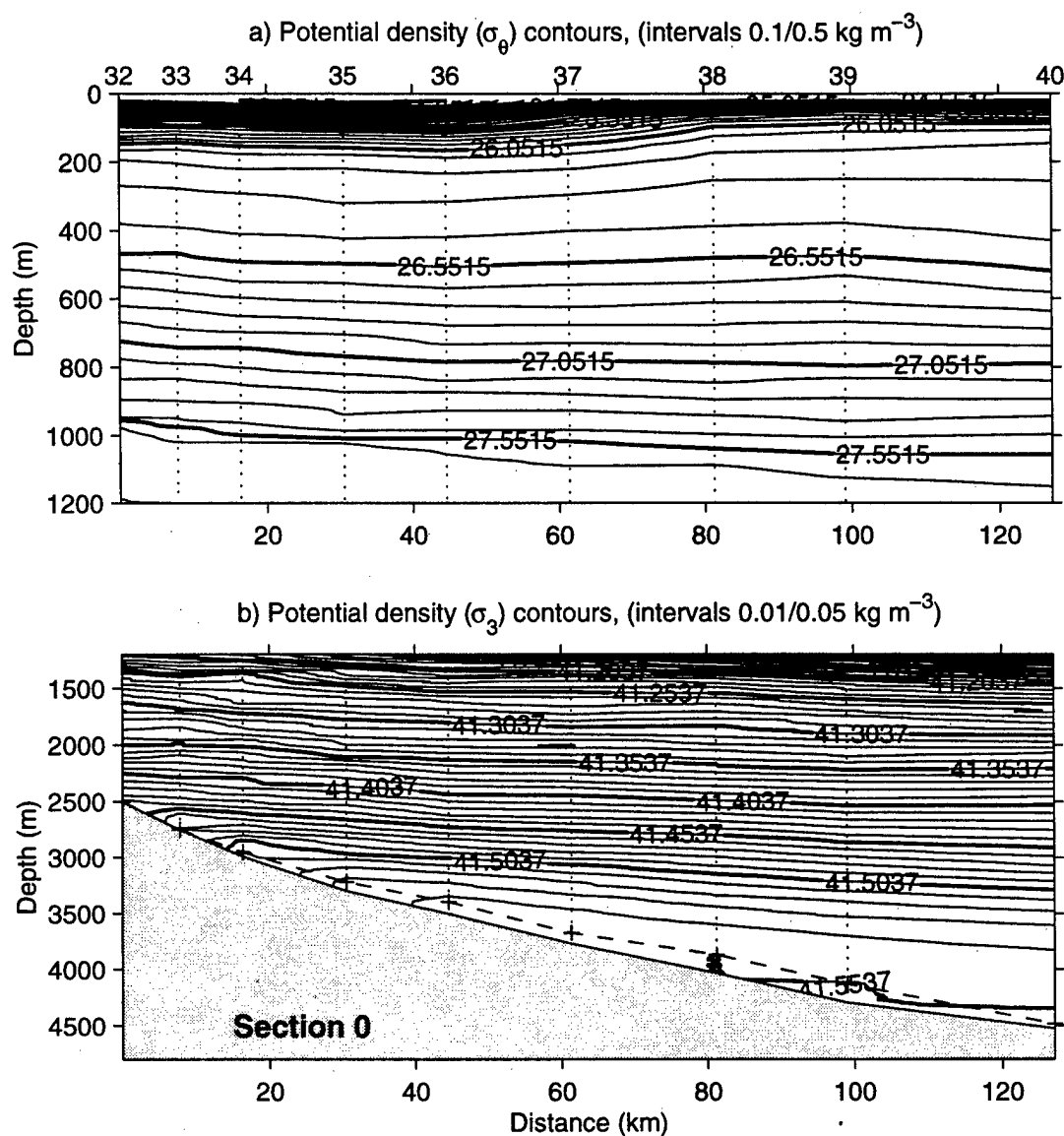
Figure 45: a) Contours of potential density (σ_θ) in upper 1200 m of Section 0. Light lines are intervals of 0.1 kg m^{-3} and heavy lines are 0.5 kg m^{-3}. b) Contours of potential density (σ_3) below 1200 m. Light lines are intervals of 0.01 kg m^{-3} and heavy lines are 0.05 kg m^{-3}.
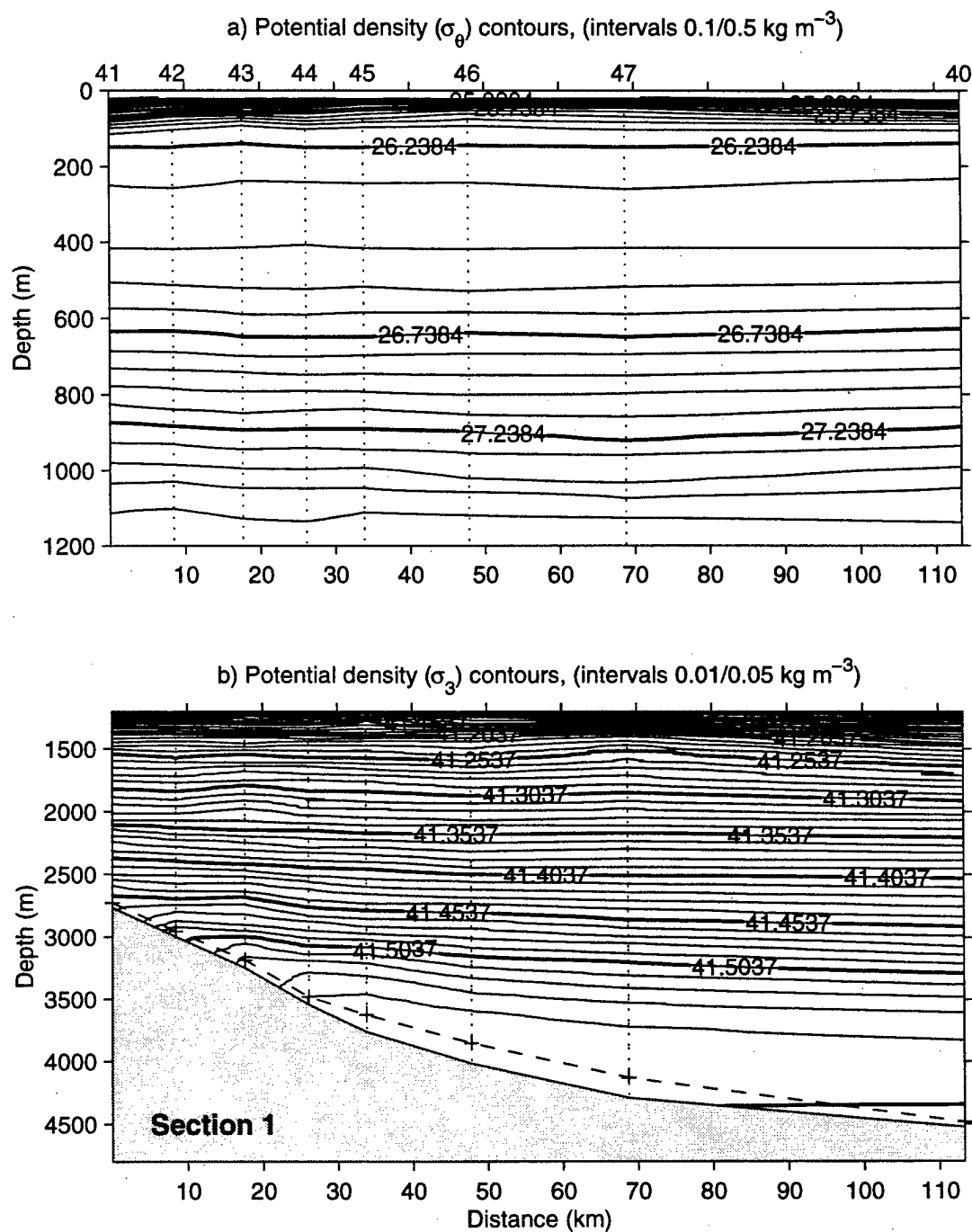
Figure 46: a) Contours of potential density (σ_θ) in upper 1200 m of Section 1. Light lines are intervals of 0.1 kg m^{-3} and heavy lines are 0.5 kg m^{-3}. b) Contours of potential density (σ_3) below 1200 m. Light lines are intervals of 0.01 kg m^{-3} and heavy lines are 0.05 kg m^{-3}.

a) Potential density (σ_θ) contours, (intervals 0.1/0.5 kg m^{-3})

b) Potential density (σ_3) contours, (intervals 0.01/0.05 kg m^{-3})
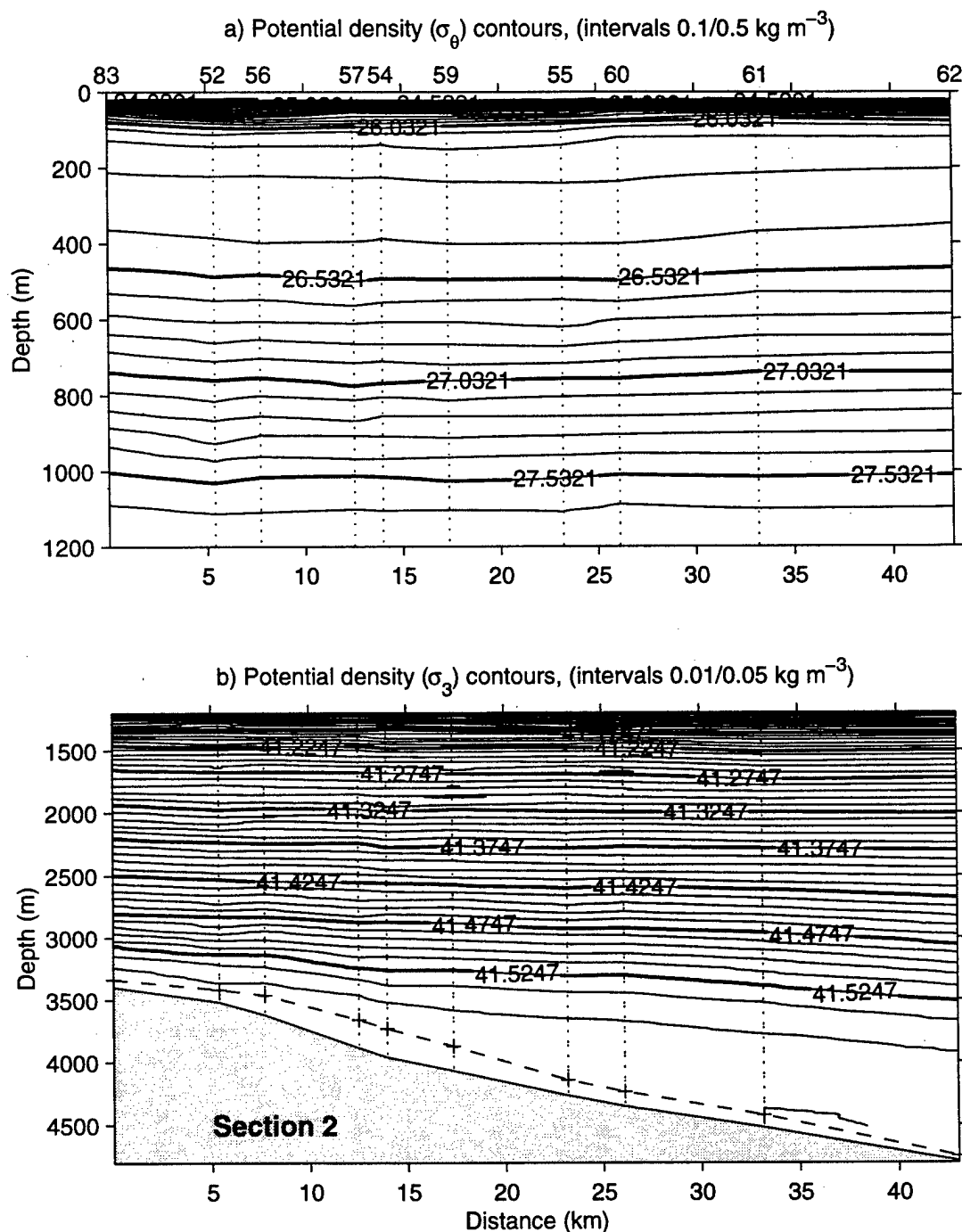
Figure 47: a) Contours of potential density (σ_θ) in upper 1200 m of Section 2. Light lines are intervals of 0.1 kg m^{-3} and heavy lines are 0.5 kg m^{-3}. b) Contours of potential density (σ_3) below 1200 m. Light lines are intervals of 0.01 kg m^{-3} and heavy lines are 0.05 kg m^{-3}.

a) Potential density (σ_θ) contours, (intervals 0.1/0.5 kg m^{-3})

b) Potential density (σ_3) contours, (intervals 0.01/0.05 kg m^{-3})
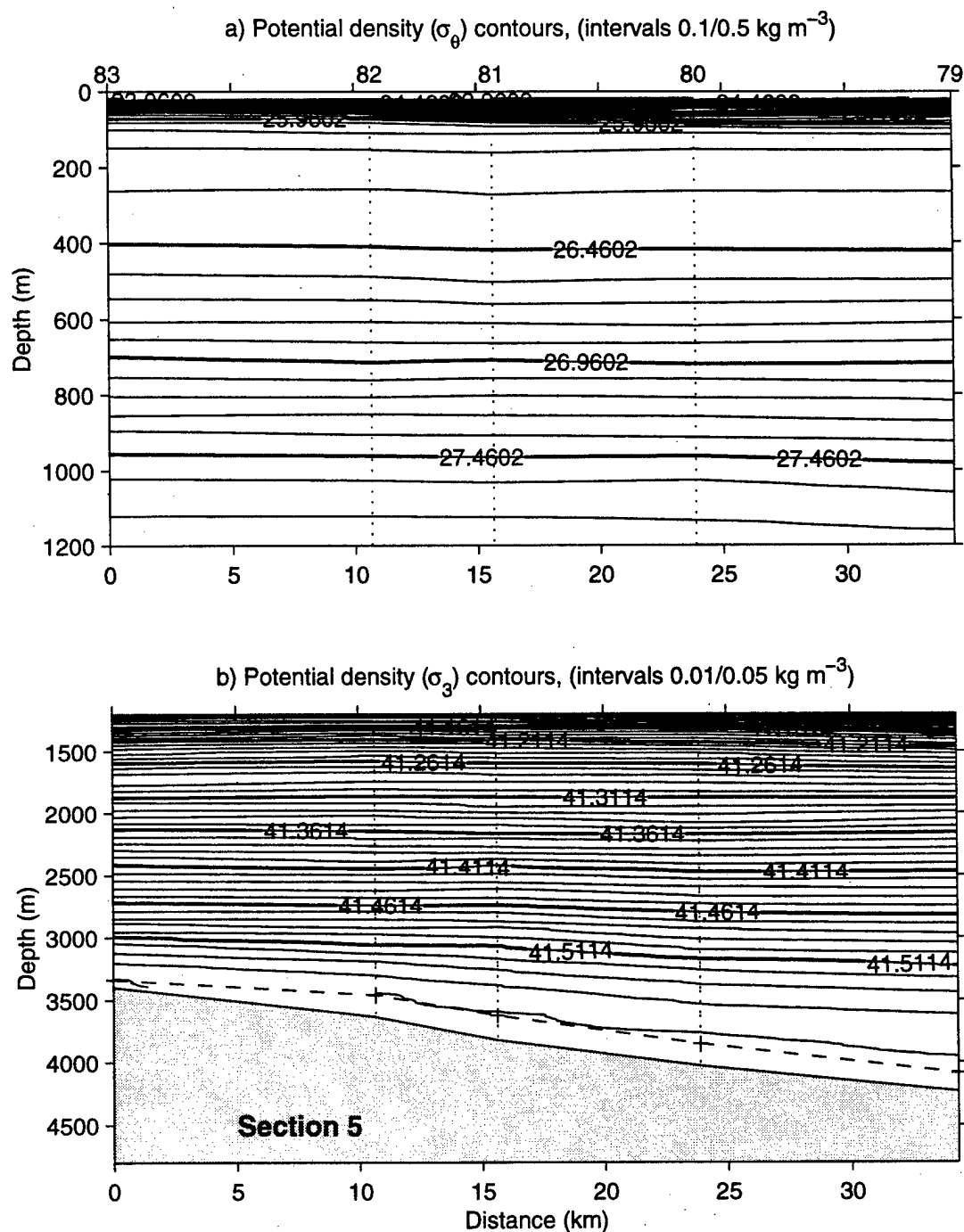
Figure 48: a) Contours of potential density (σ_θ) in upper 1200 m of Section 5. Light lines are intervals of 0.1 kg m^{-3} and heavy lines are 0.5 kg m^{-3}. b) Contours of potential density (σ_3) below 1200 m. Light lines are intervals of 0.01 kg m^{-3} and heavy lines are 0.05 kg m^{-3}.

D.3 Profiles of SPM concentration for Sections 0, 1, 2, 5
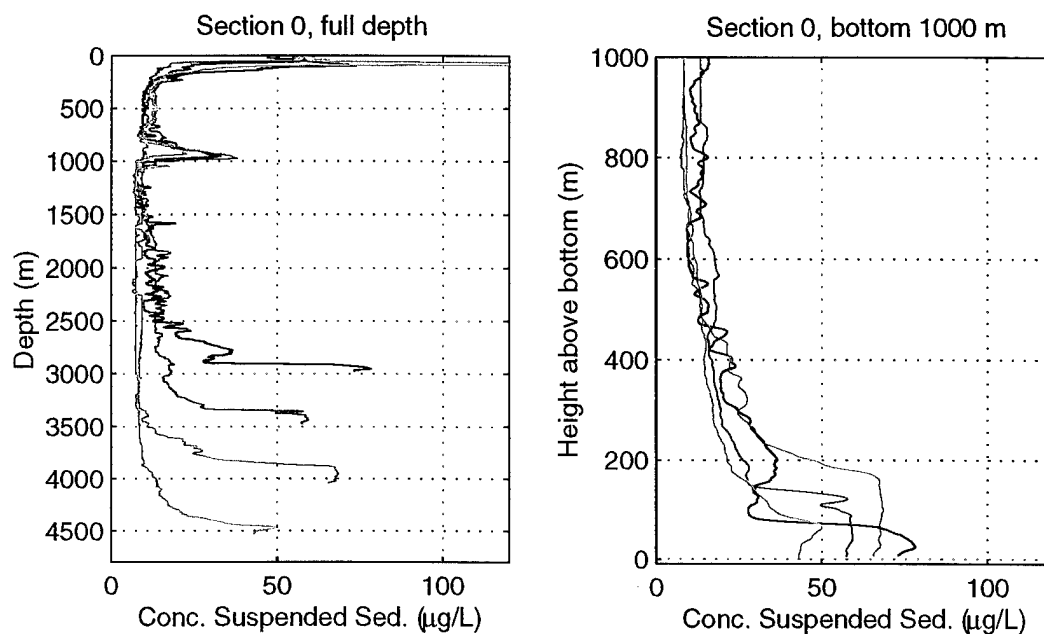
Figure 49: Profiles of suspended sediment concentration for Section 0.
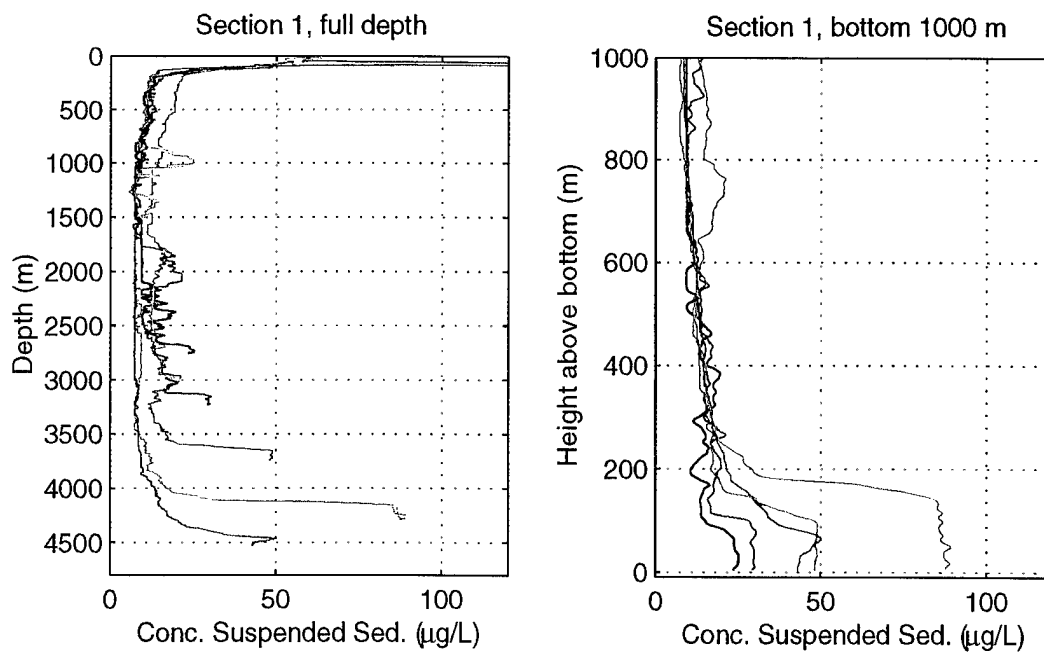
Figure 50: Profiles of suspended sediment concentration for Section 1.
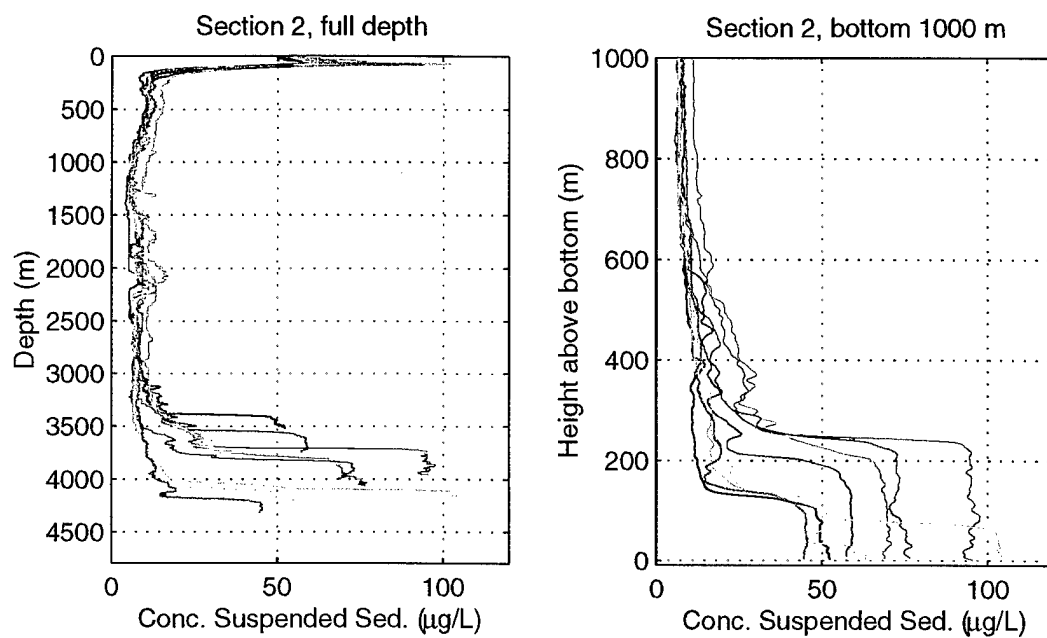
Figure 51: Profiles of suspended sediment concentration for Section 2.
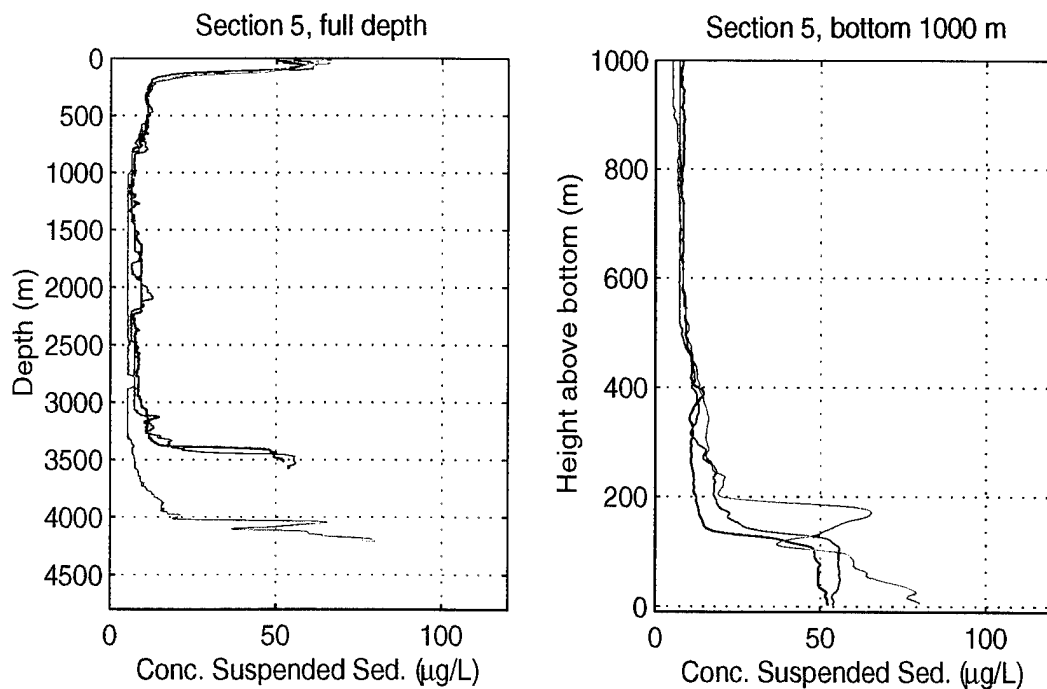
Figure 52: Profiles of suspended sediment concentration for Section 5.

D.4 Potential temperature and salinity curves for Sections 0, 1, 2, 5
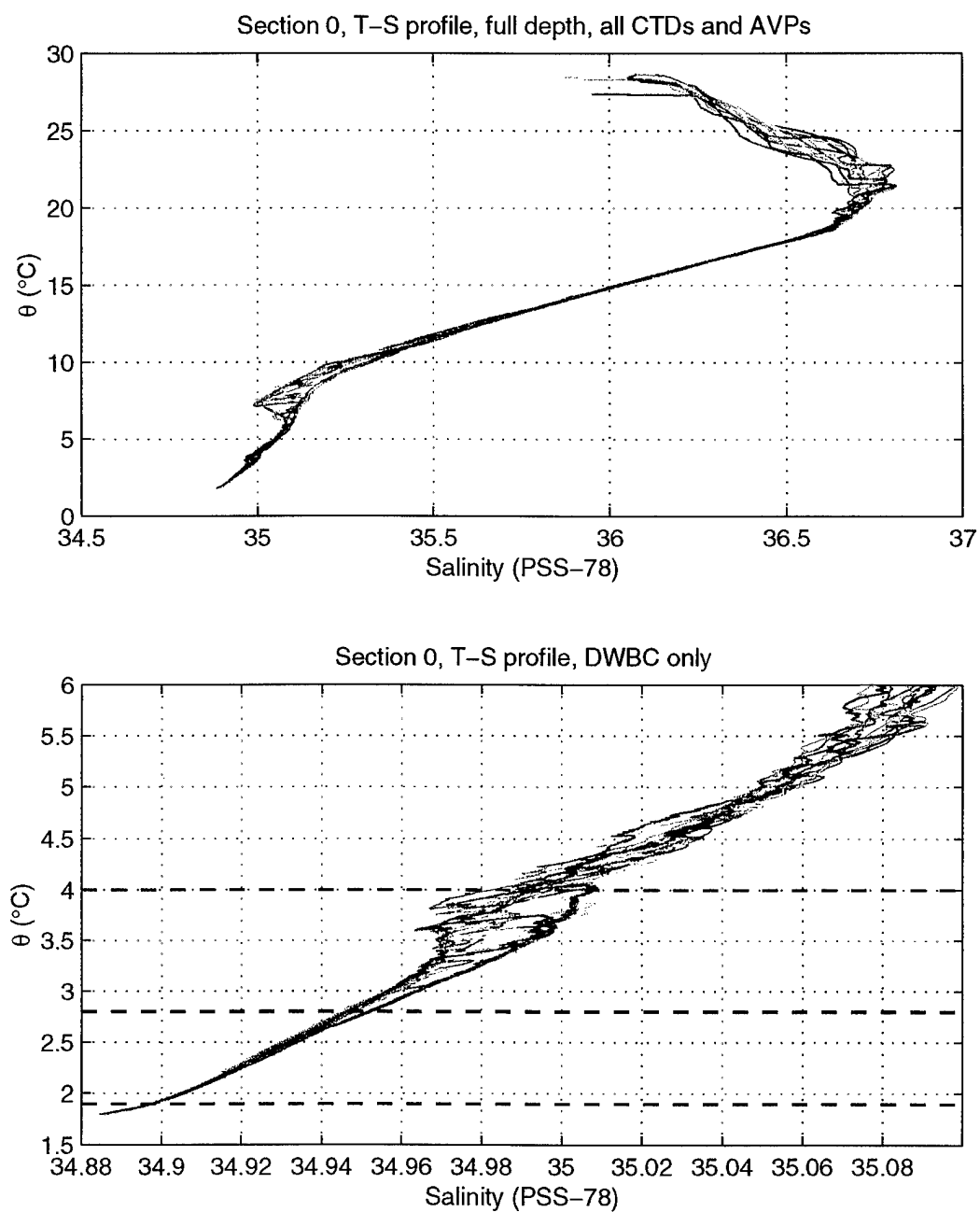
Figure 53: Potential temperature (θ)–Salinity plots for all AVPs and CTDs on Section 0.

Section 1, T–S profile, full depth, all CTDs and AVPs

Section 1, T–S profile, DWBC only
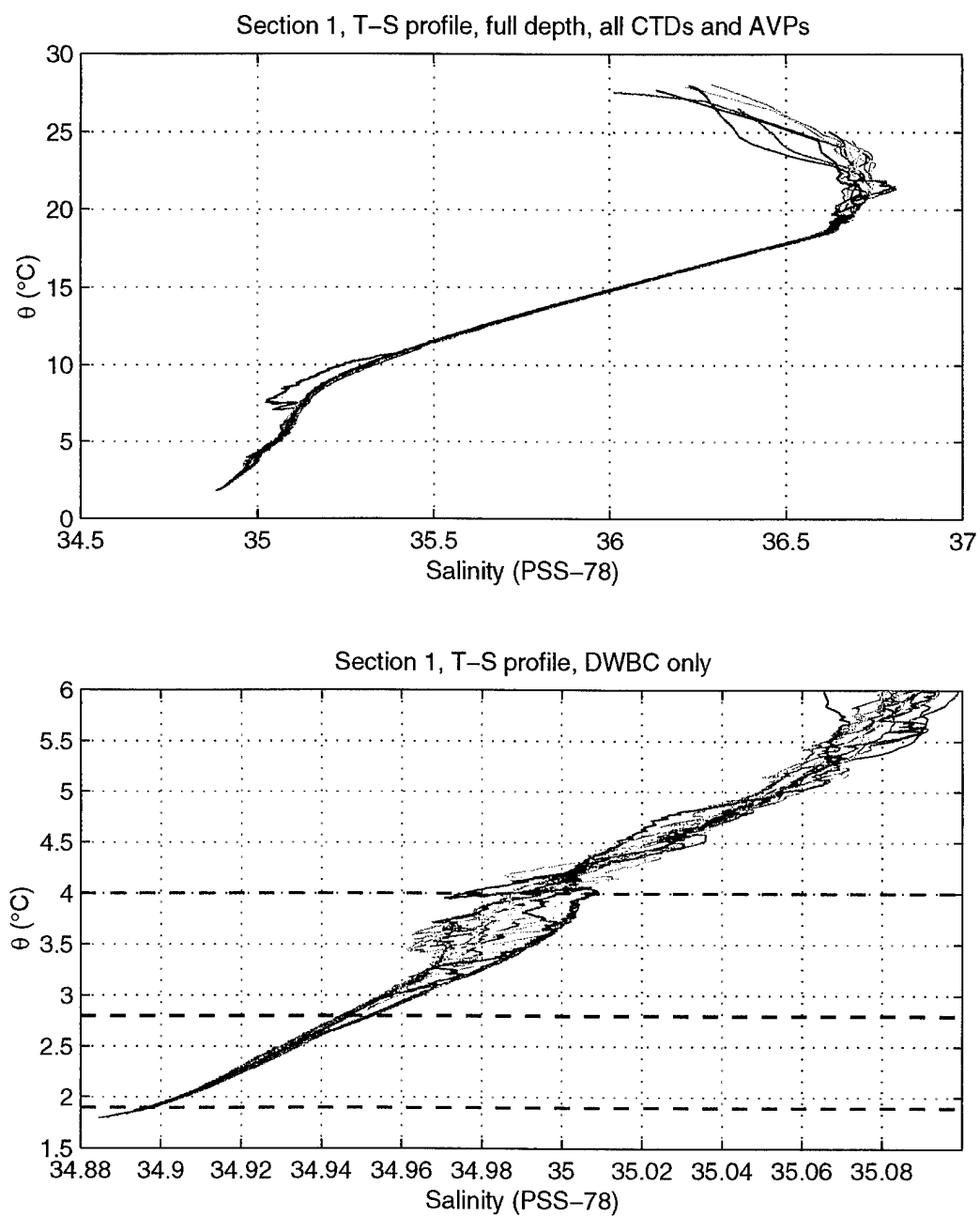
Figure 54: Potential temperature (θ)–Salinity plots for all AVPs and CTDs on Section 1.
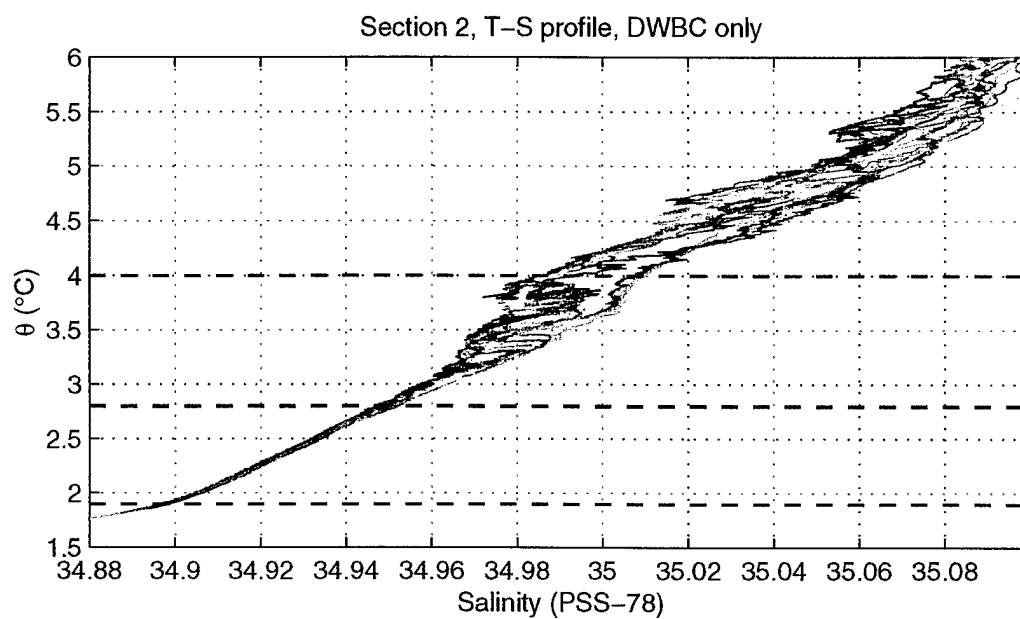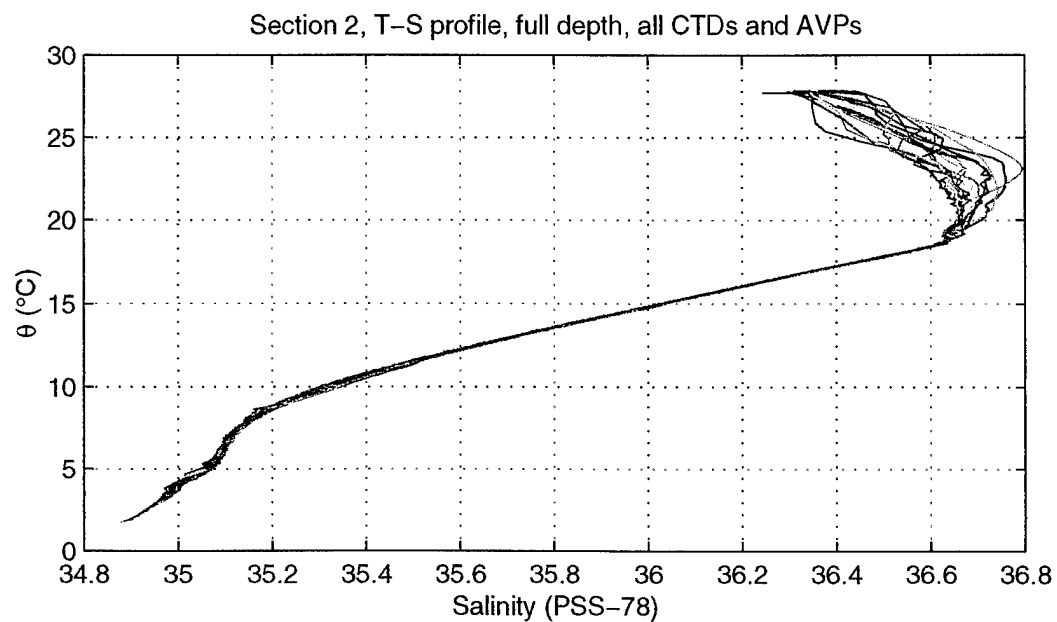
Figure 55: Potential temperature (θ)–Salinity plots for all AVPs and CTDs on Section 2.
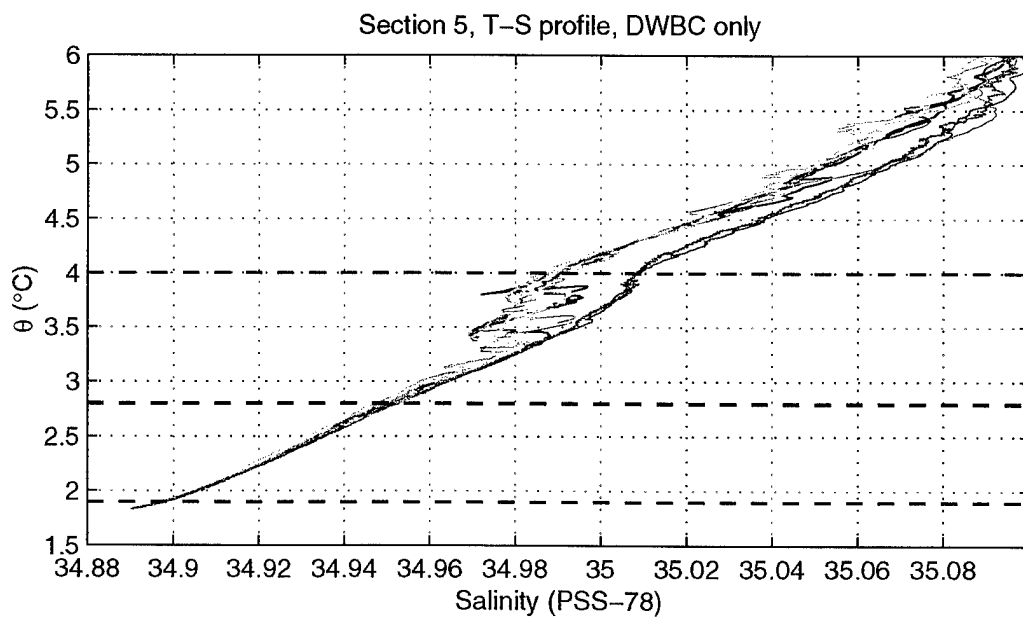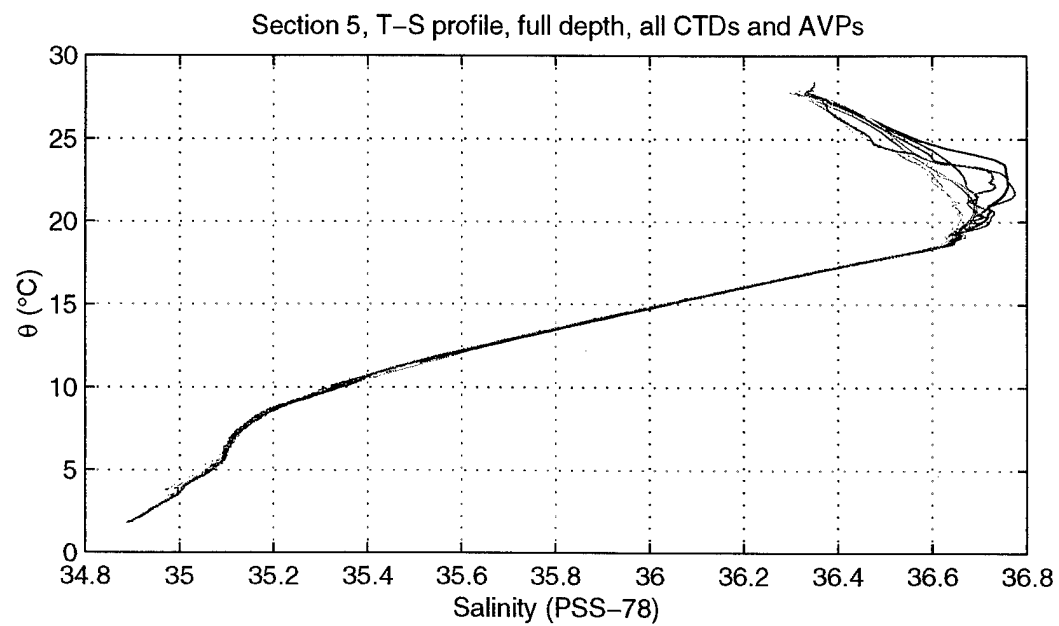
Figure 56: Potential temperature (θ)–Salinity plots for all AVPs and CTDs on Section 5.

D.5 Nutrient profiles in the bottom mixed layers of all CTD casts
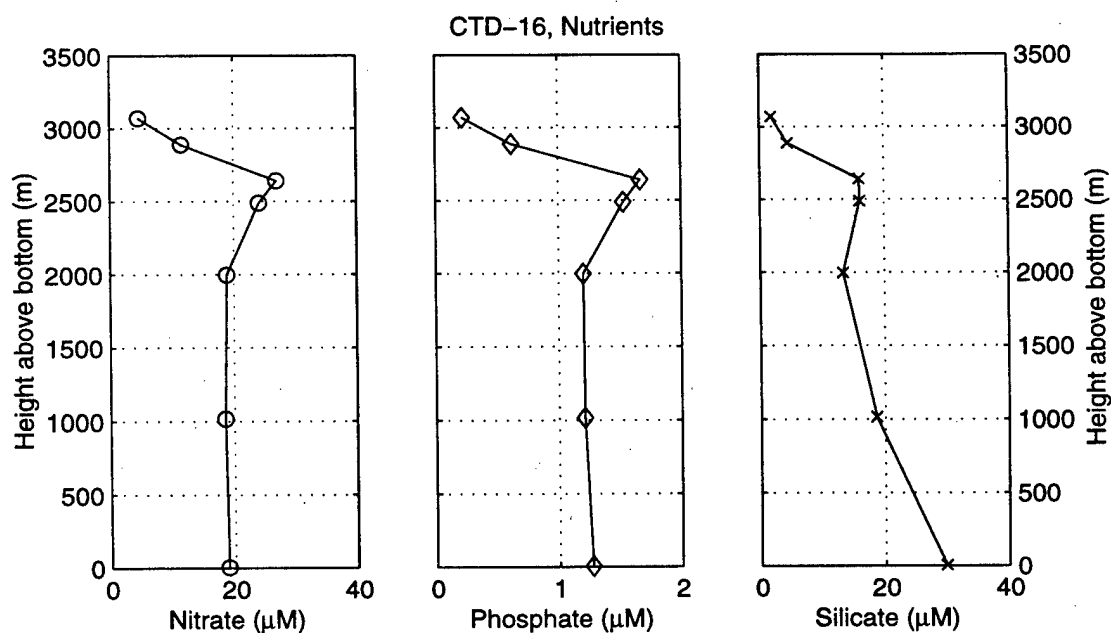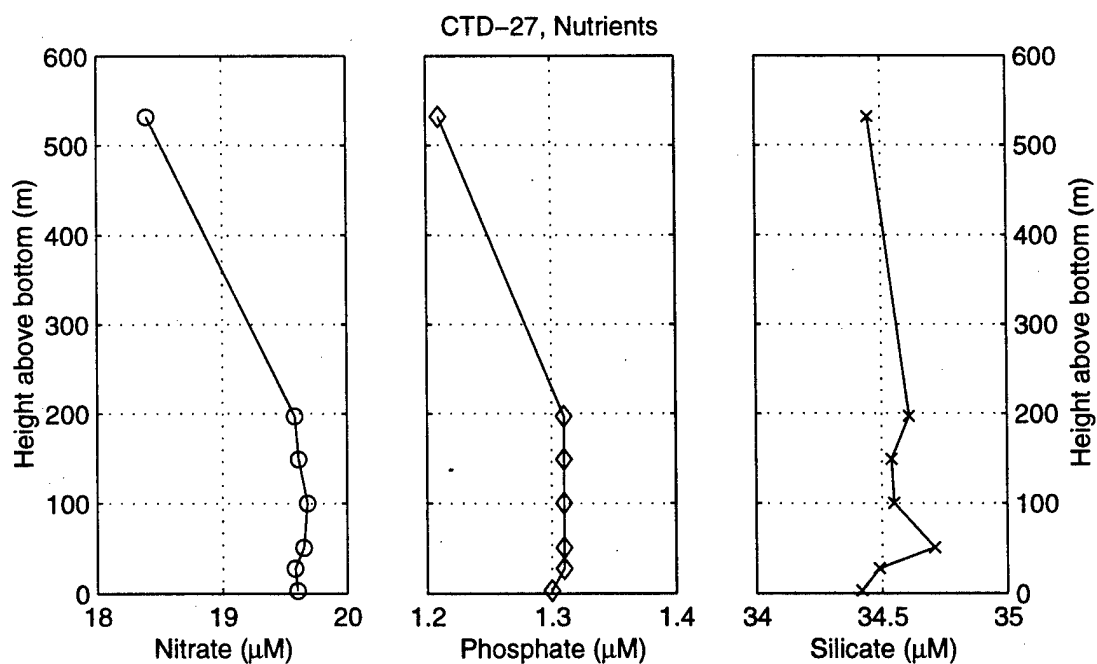

Figure 57: Nutrient profiles for CTD 16, Site 0-5. Data from seven deepest bottles only.
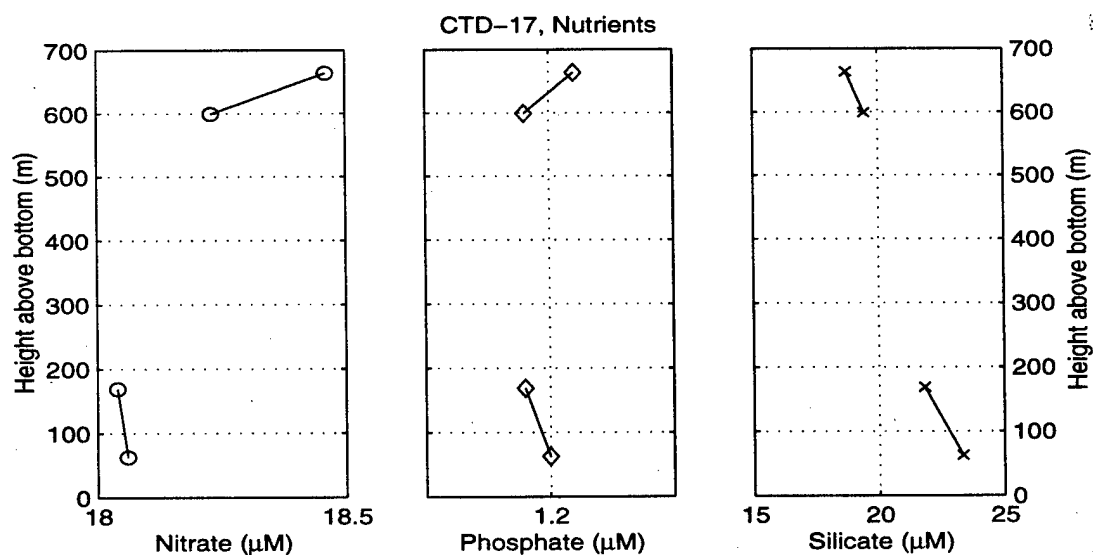
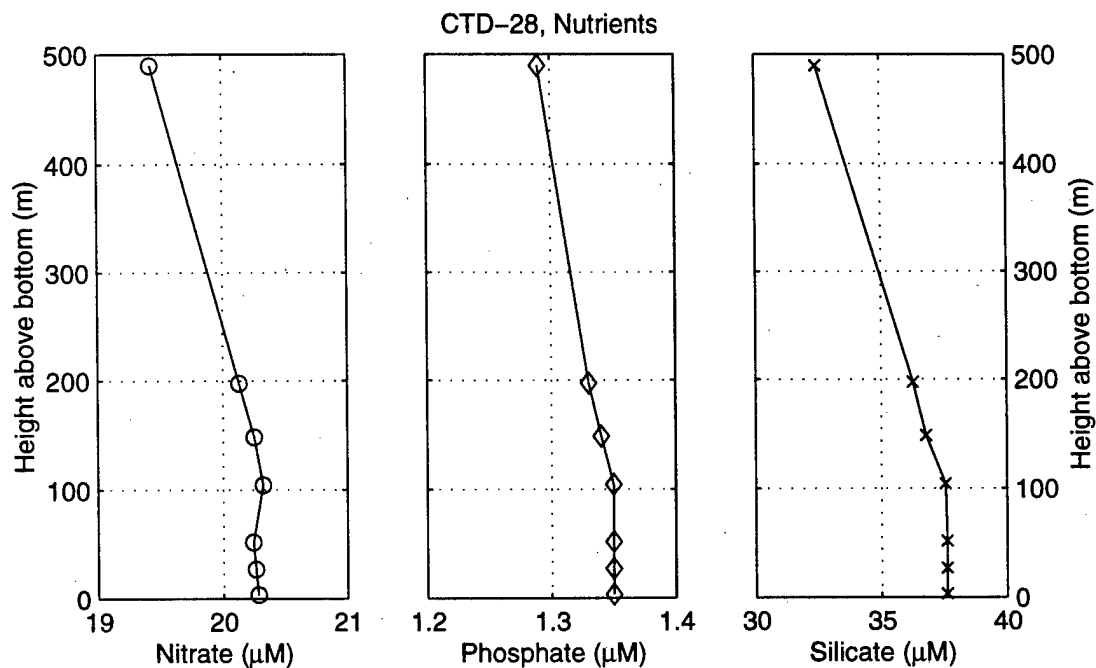Figure 58: Nutrient profiles for CTD 17, Site 0-3. Data from four deepest bottles only.
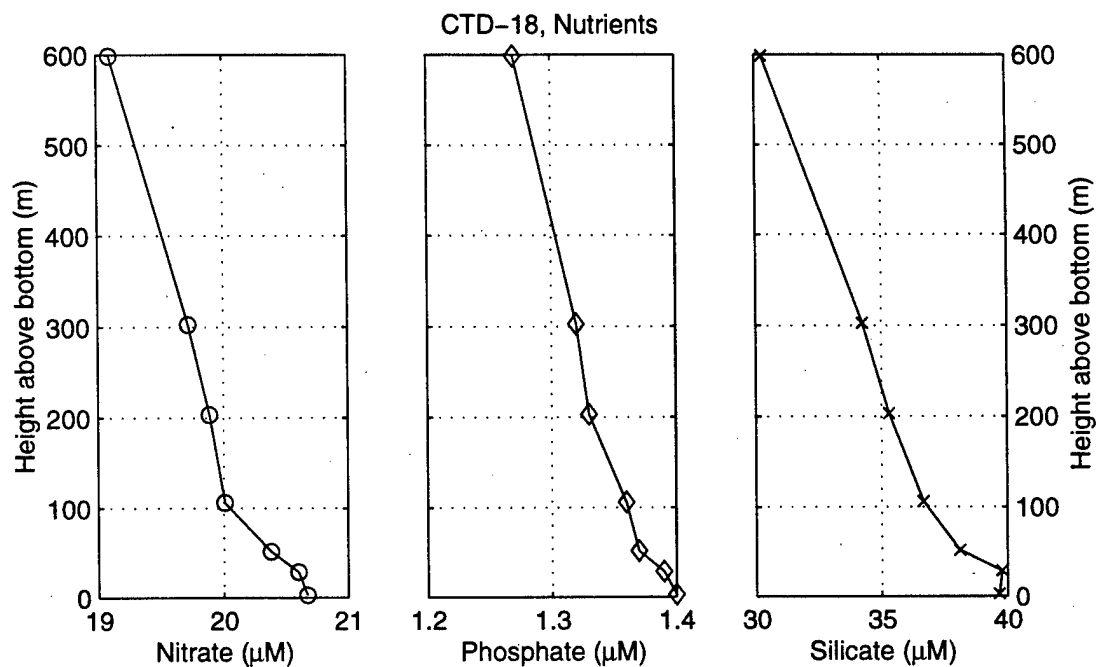
Figure 59: Nutrient profiles for CTD 18, Site 0-9. Data from seven deepest bottles.
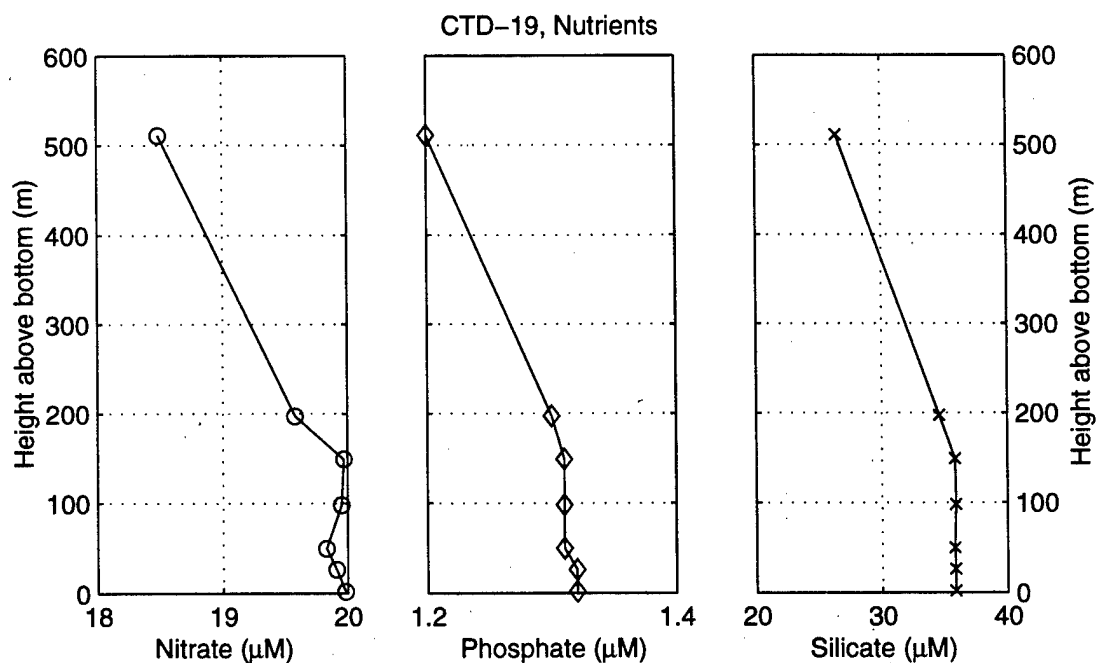
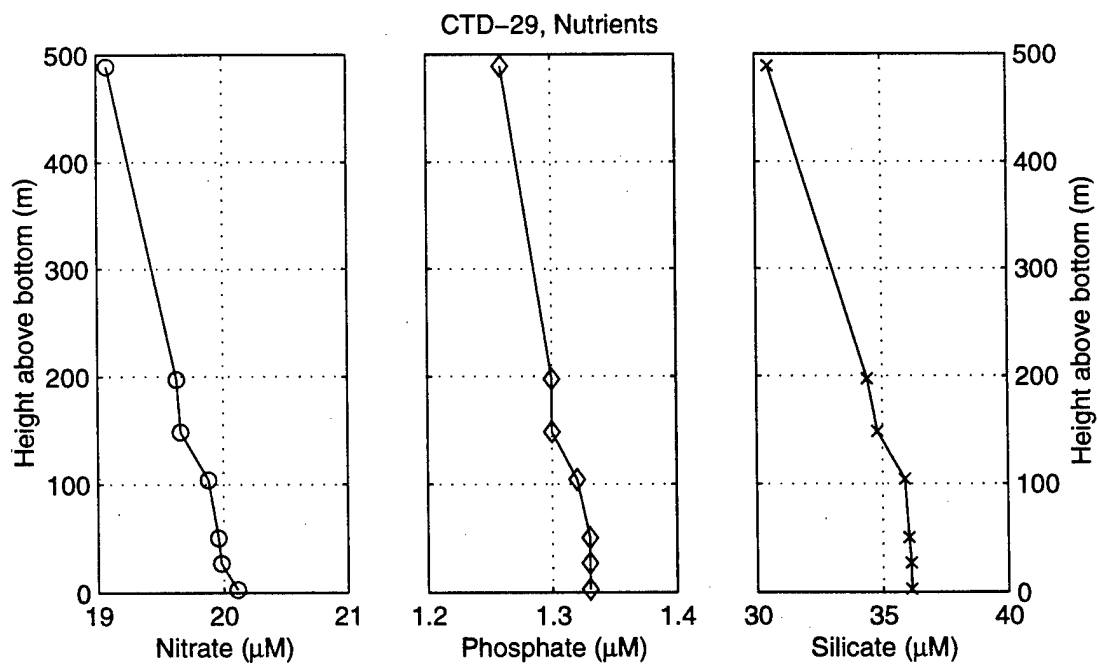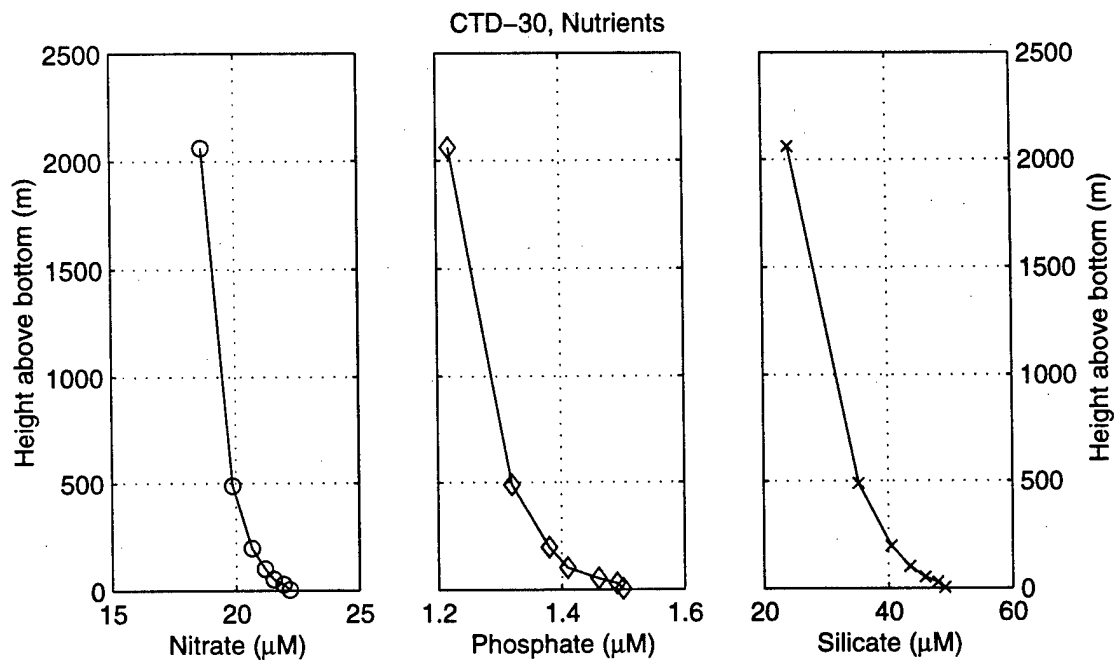Figure 60: Nutrient profiles for CTD 19, Site 0-7. Data from seven deepest bottles only.
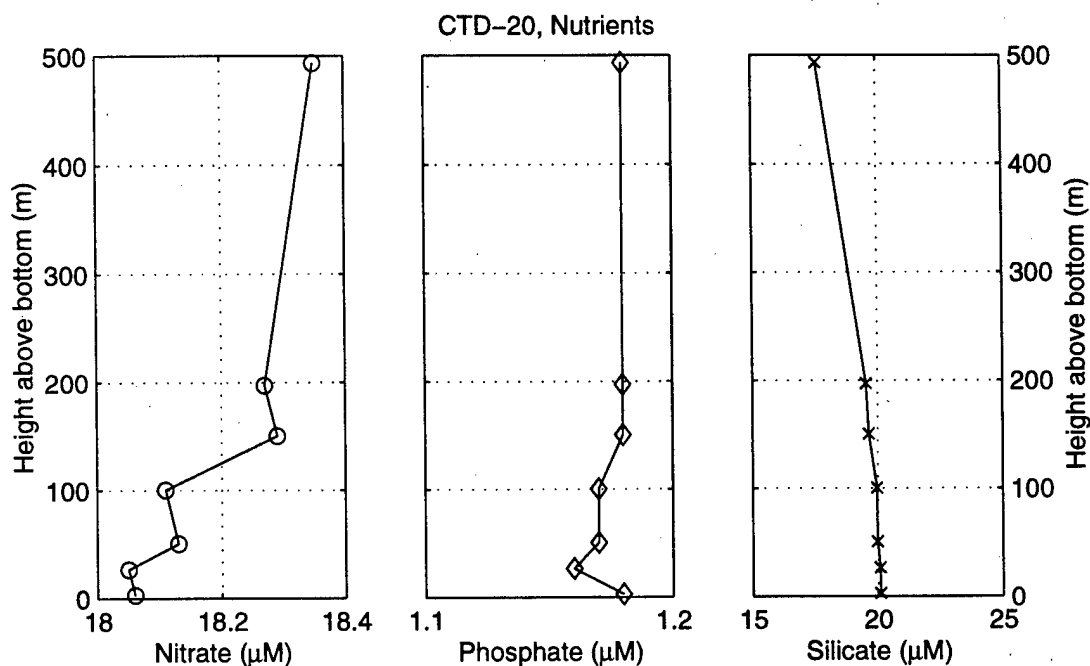
CTD–20, Nutrients

Figure 61: Nutrient profiles for CTD 20, Site 1-1. Data from seven deepest bottles.
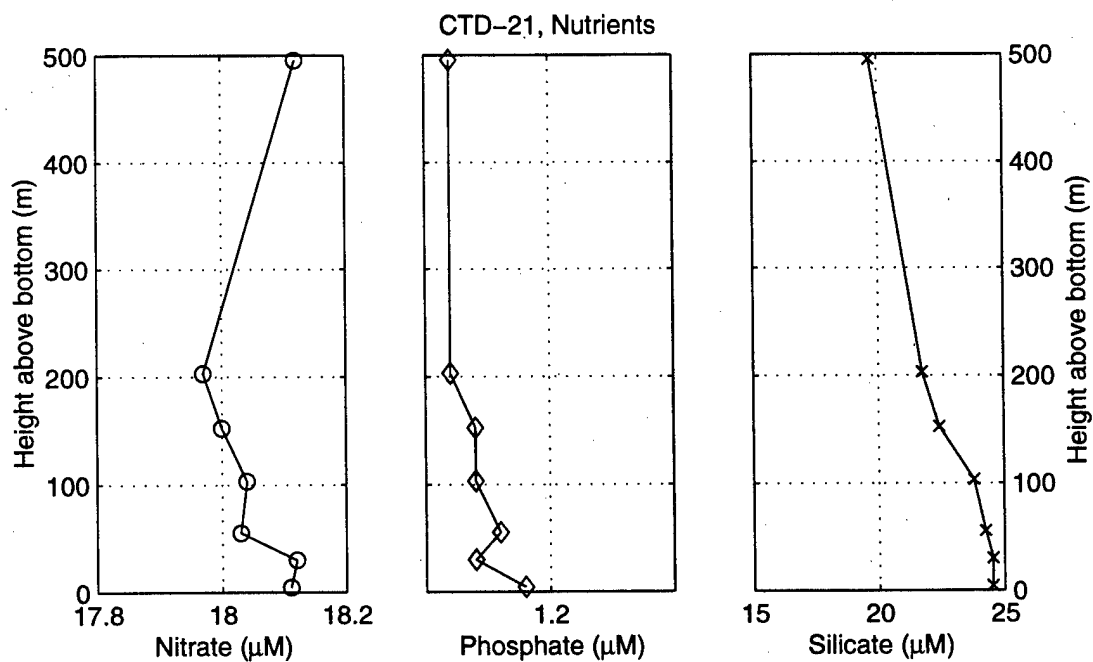
CTD–21, Nutrients

Figure 62: Nutrient profiles for CTD 21, Site 1-3. Data from seven deepest bottles.
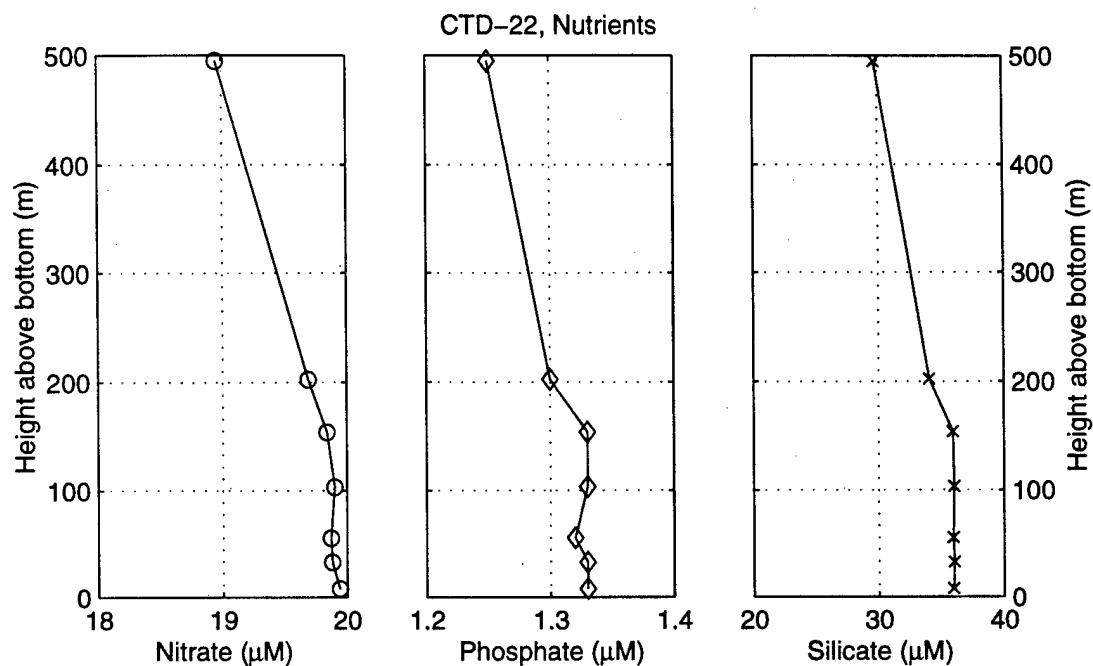
Figure 63: Nutrient profiles for CTD 22, Site 1-7. Data from seven deepest bottles.
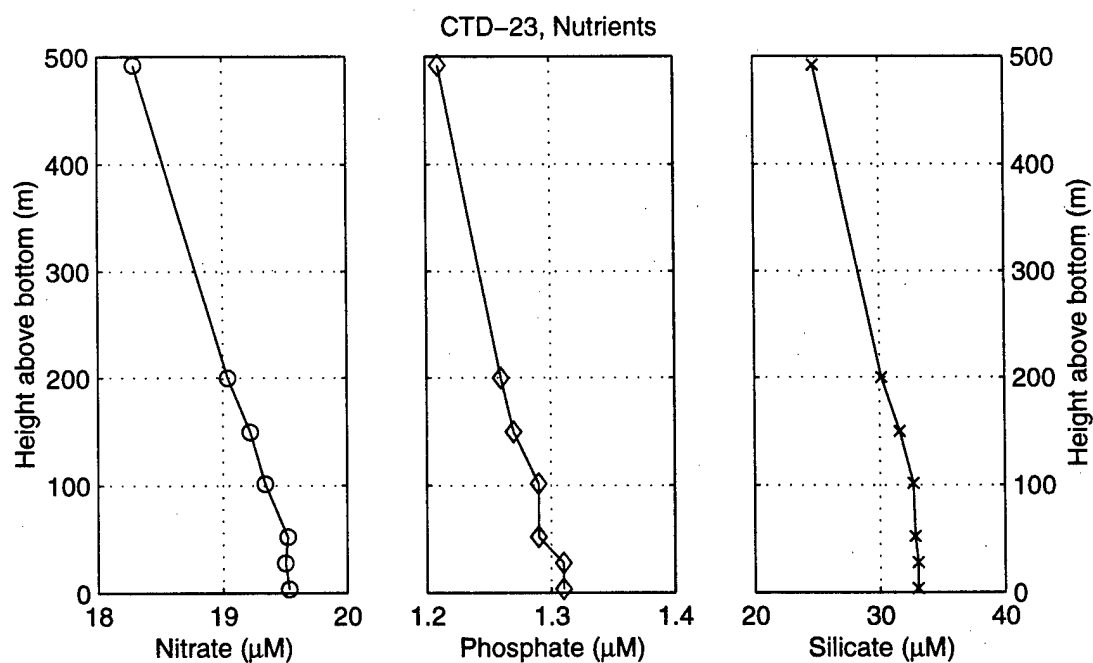
Figure 64: Nutrient profiles for CTD 23, Site 1-5. Data from seven deepest bottles.
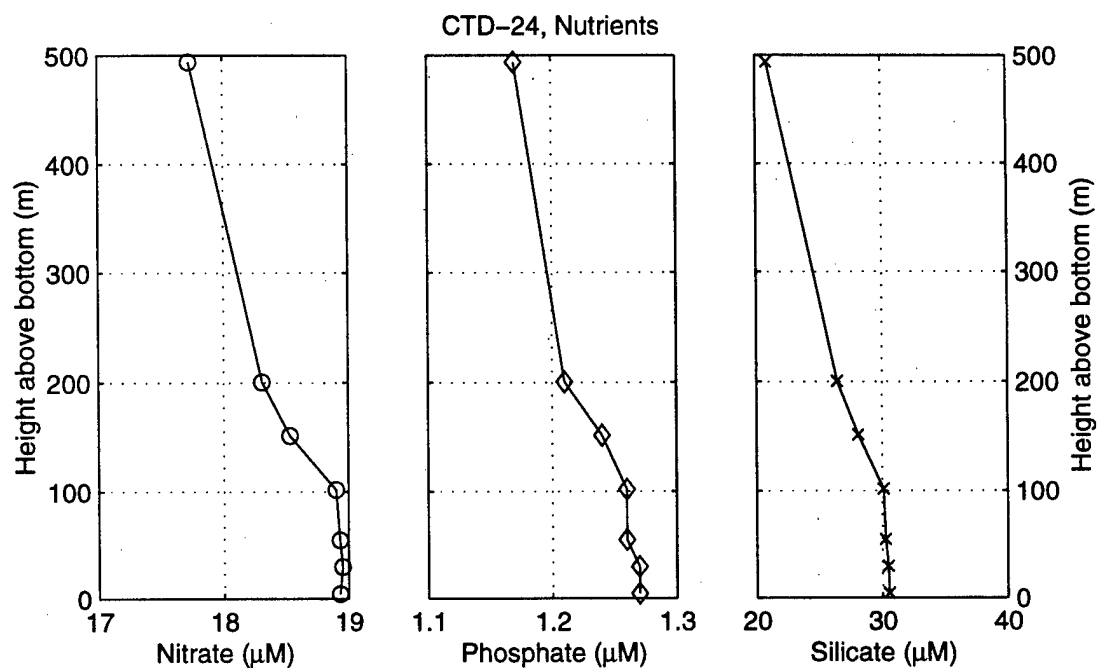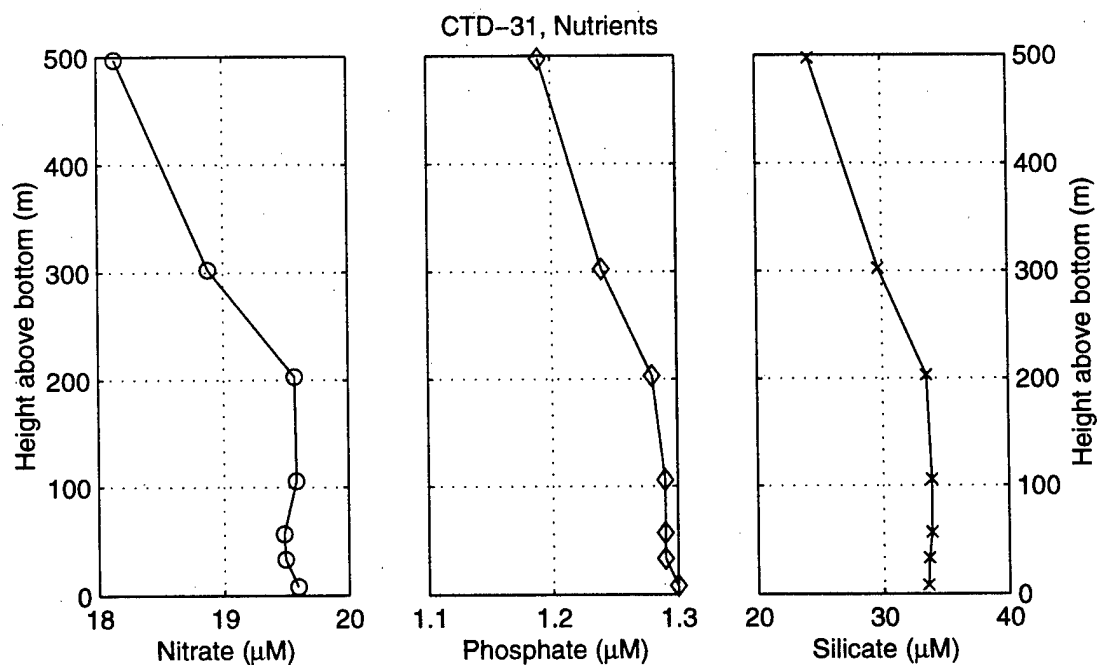
Figure 65: Nutrient profiles for CTD 24, Site R-4. Data from seven deepest bottles.
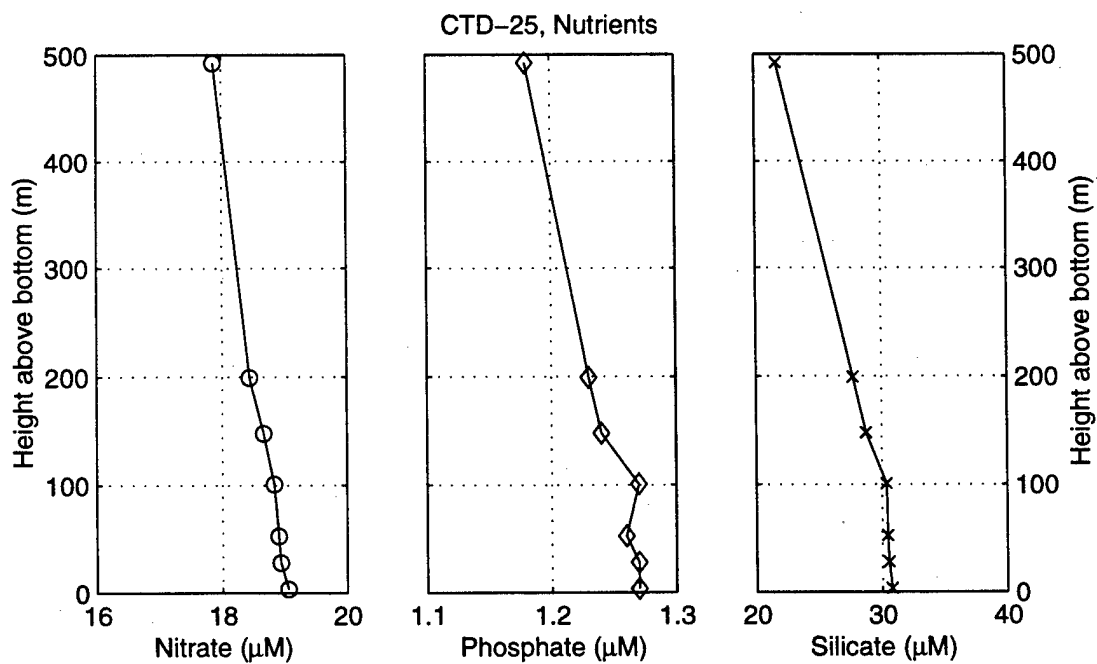
Figure 66: Nutrient profiles for CTD 25, Site 2-1. Data from seven deepest bottles.
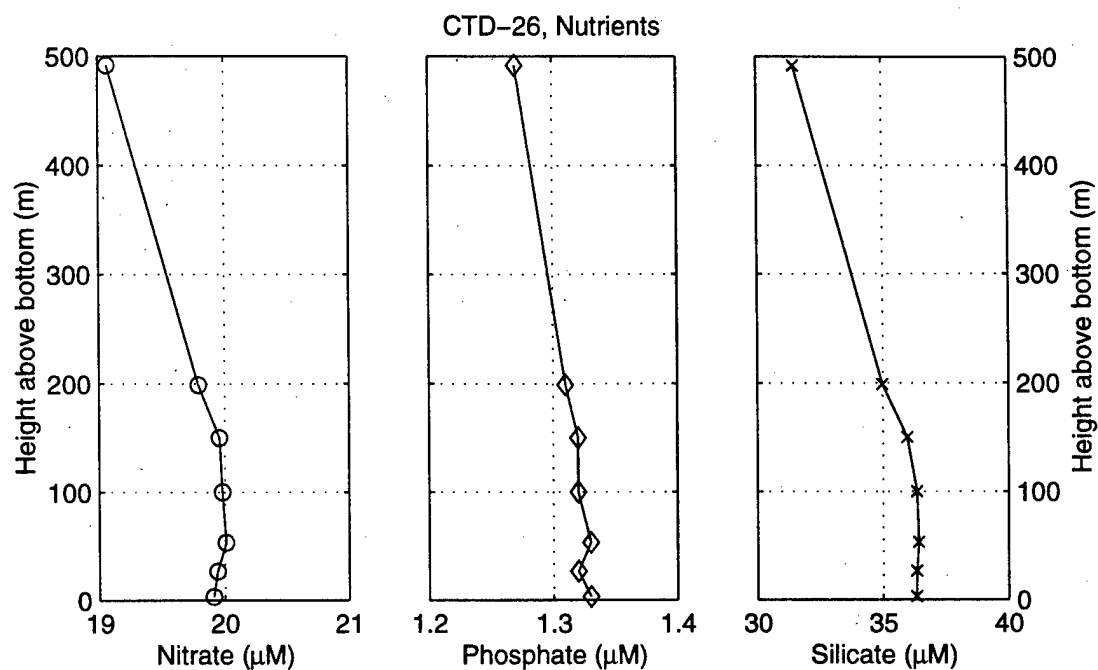
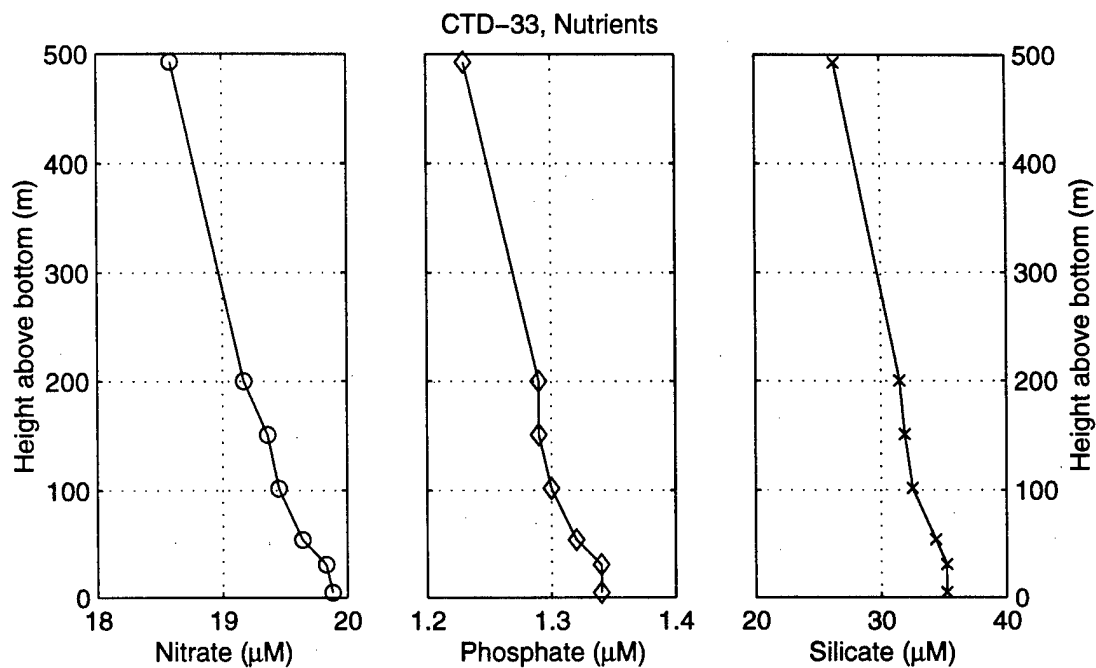Figure 67: Nutrient profiles for CTD 26, Site 2-7. Data from seven deepest bottles.

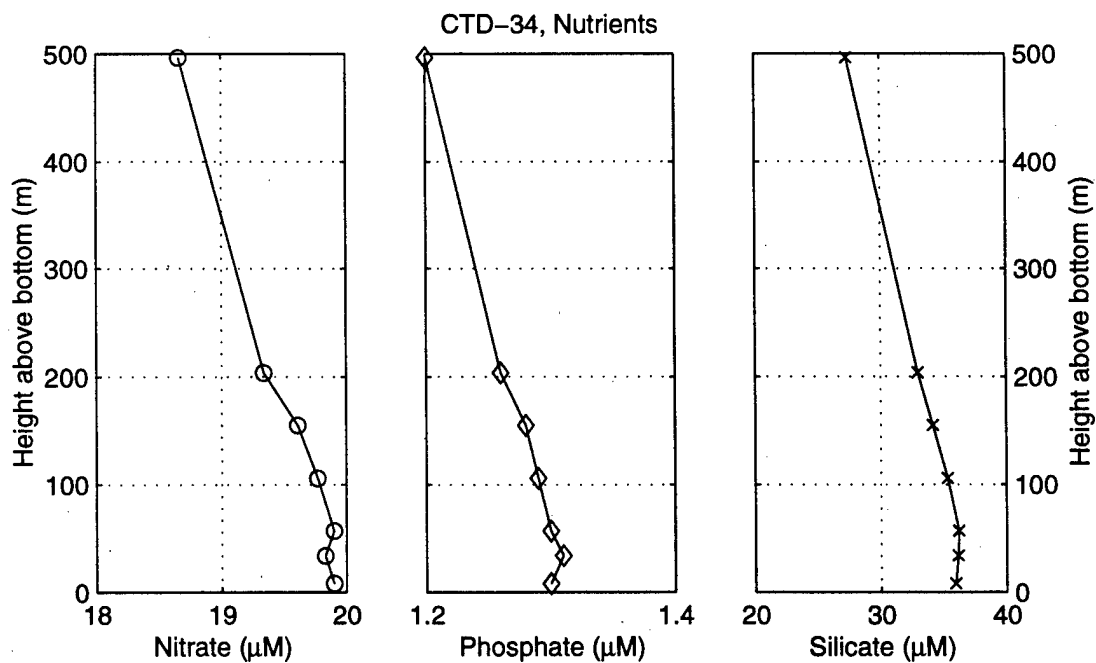Figure 68: Nutrient profiles for CTD 27, Site 2-4. Data from seven deepest bottles.

Figure 69: Nutrient profiles for CTD 28, Site 2-8. Data from seven deepest bottles.

Figure 70: Nutrient profiles for CTD 29, Site 2-7. Data from seven deepest bottles.

Figure 71: Nutrient profiles for CTD 30, Site 2-15. Data from seven deepest bottles.

Figure 72: Nutrient profiles for CTD 31, Site 2-3. Data from seven deepest bottles.

Figure 73: Nutrient profiles for CTD 33, Site 3-4. Data from seven deepest bottles.
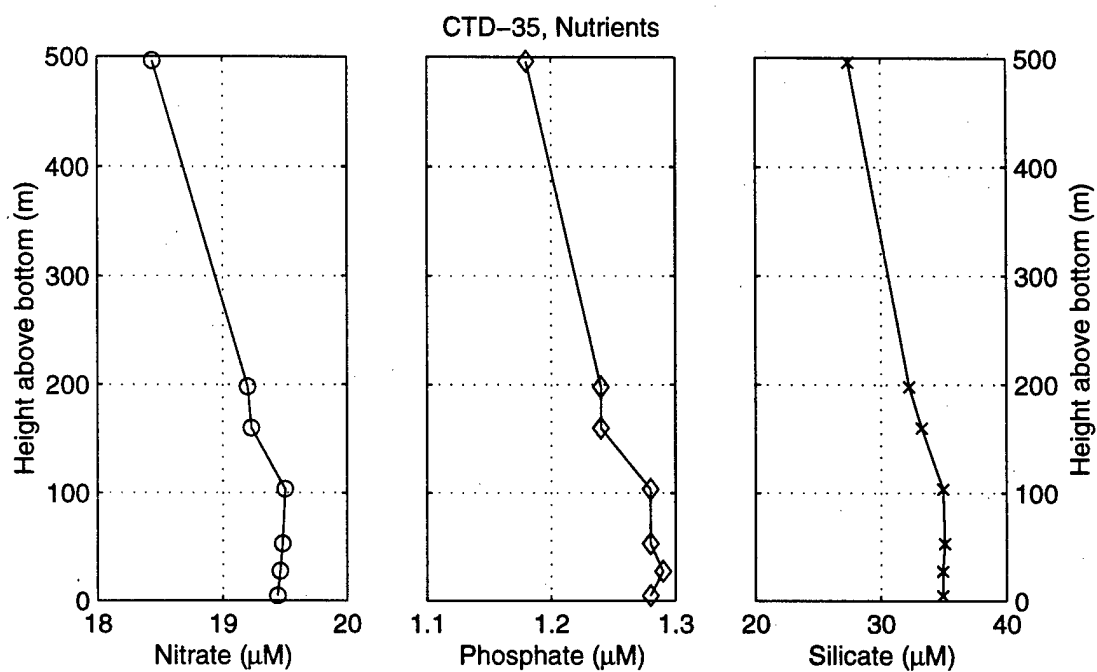

Figure 74: Nutrient profiles for CTD 34, Site 3-5. Data from seven deepest bottles.

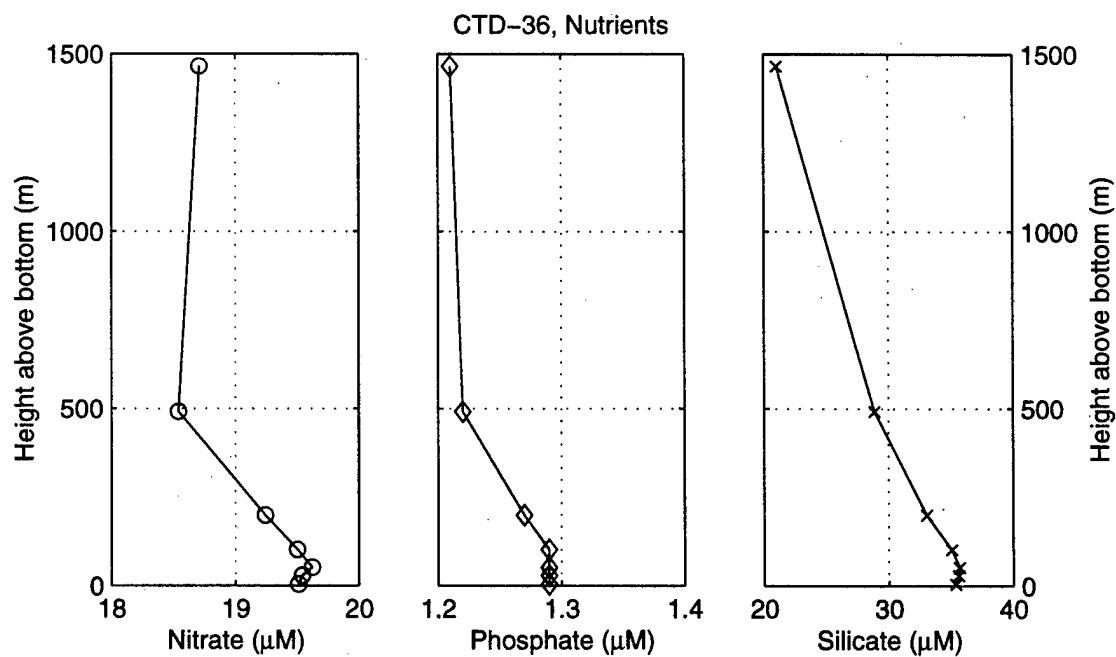Figure 75: Nutrient profiles for CTD 35, Site 4-1. Data from seven deepest bottles.

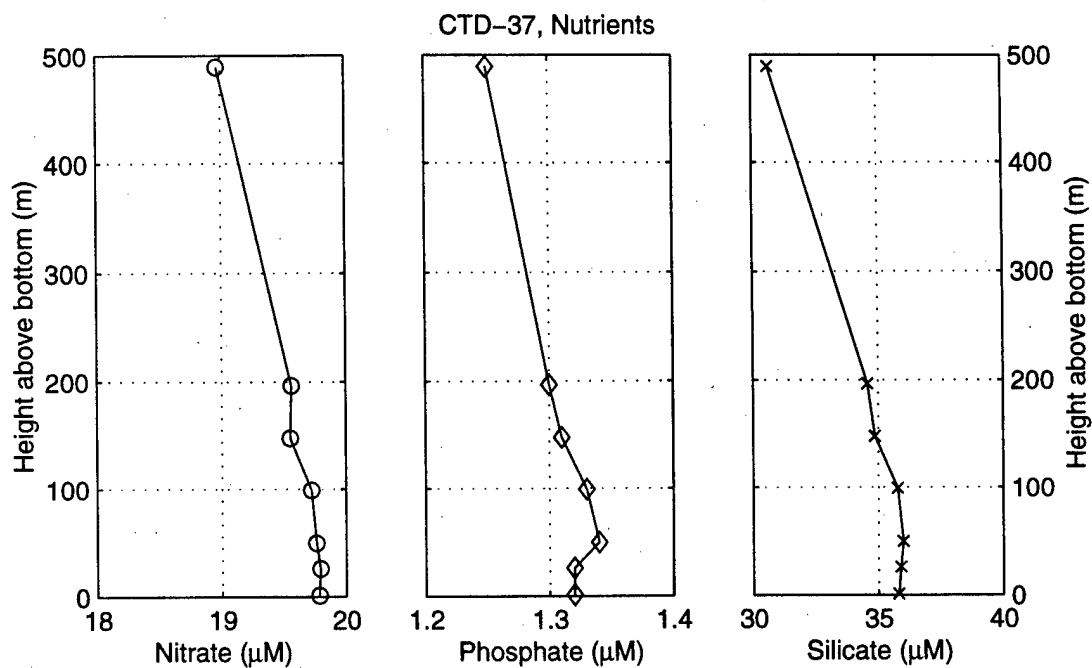Figure 76: Nutrient profiles for CTD 36, Site 4-2. Data from seven deepest bottles.

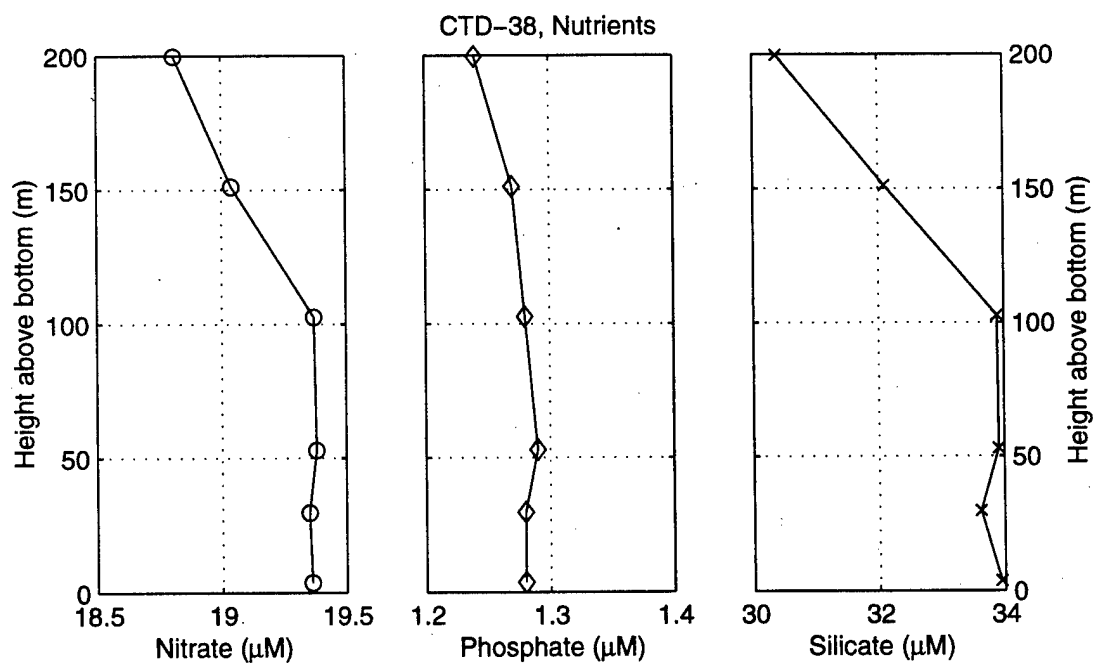Figure 77: Nutrient profiles for CTD 37, Site 5-8. Data from seven deepest bottles.

Figure 78: Nutrient profiles for CTD 38, Site 5-2. Data from seven deepest bottles.
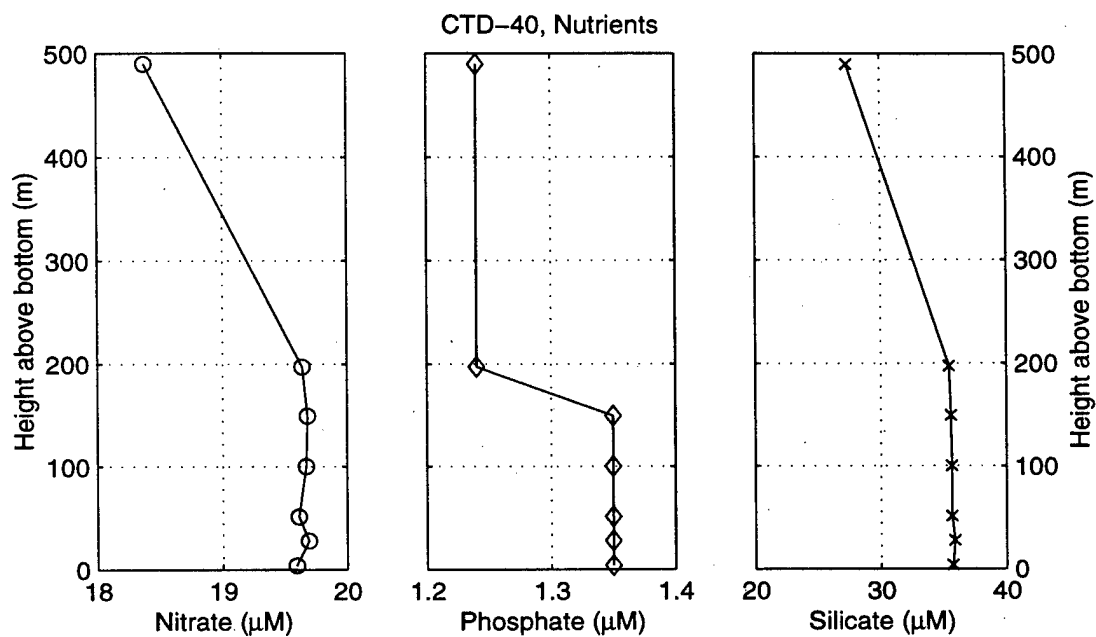
Figure 79: Nutrient profiles for CTD 40, 5 km NW of Site 2-5. Data from seven deepest bottles.
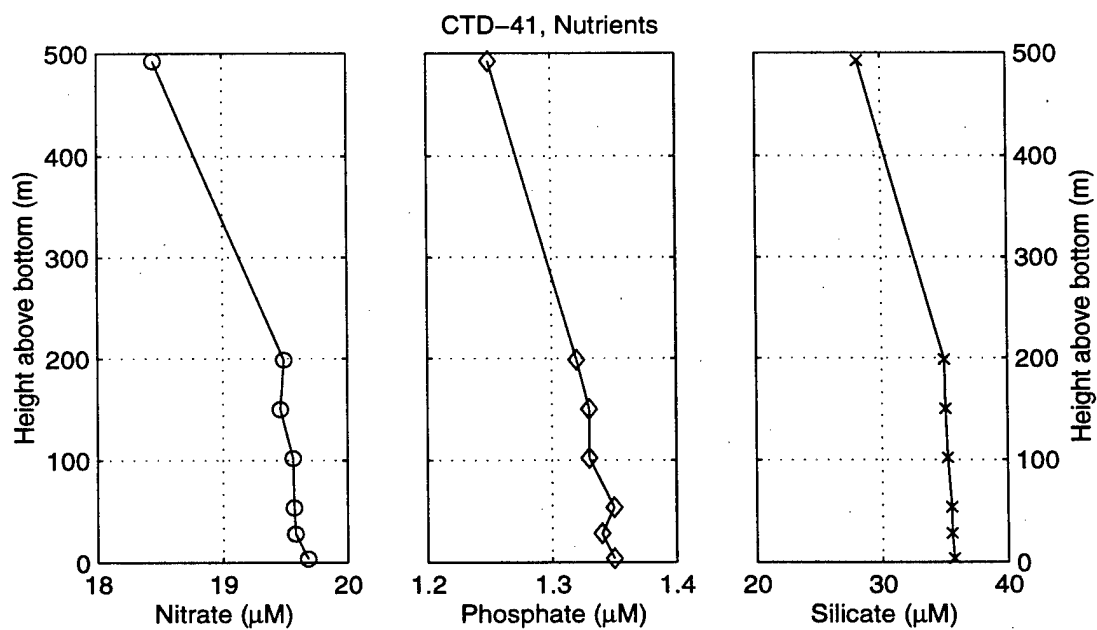

Figure 80: Nutrient profiles for CTD 41, 5 km SE of Site 2-5. Data from seven deepest bottles.

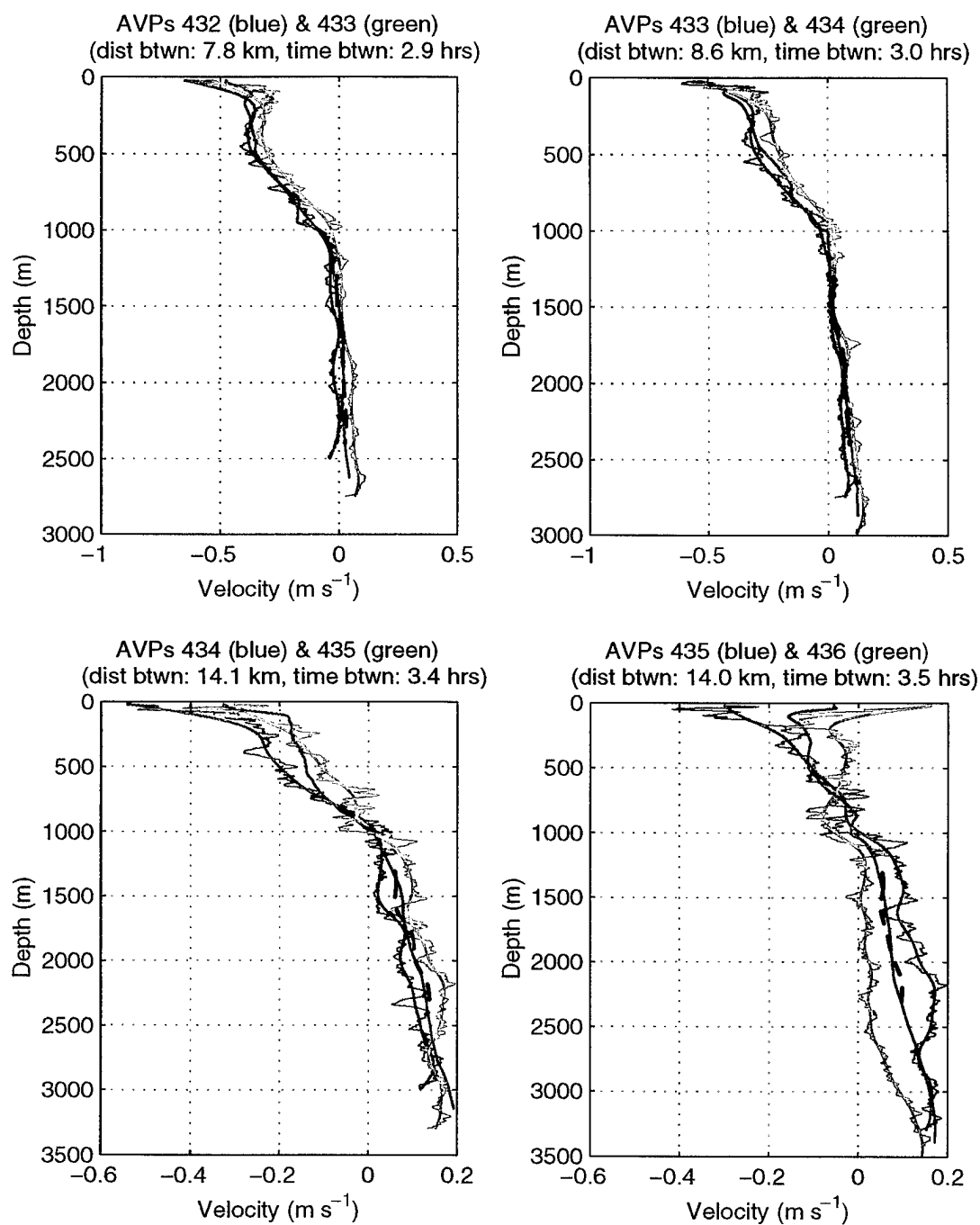## D.6 Absolute and geostrophic velocity profile comparisons

Figure 81: Absolute velocity profiles (blue and green) and referenced geostrophic profile from density data (red) for AVPs 432-436 on Section 0. Reference velocity is indicated by black dashed line in 1300-2400 m depth range. Jagged blue and green lines are 2-m absolute velocity data, smooth lines are filtered over 300 m.

Figure 82: Absolute velocity profiles (blue and green) and referenced geostrophic profile from density data (red) for AVPs 436-440 on Section 0. Reference velocity is indicated by black dashed line in 1300-2400 m depth range. Jagged blue and green lines are 2-m absolute velocity data, smooth lines are filtered over 300 m.

Figure 83: Absolute velocity profiles (blue and green) and referenced geostrophic profile from density data (red) for AVPs 441-445 on Section 1. Reference velocity is indicated by black dashed line in 1300-2400 m depth range. Jagged blue and green lines are 2-m absolute velocity data, smooth lines are filtered over 300 m.
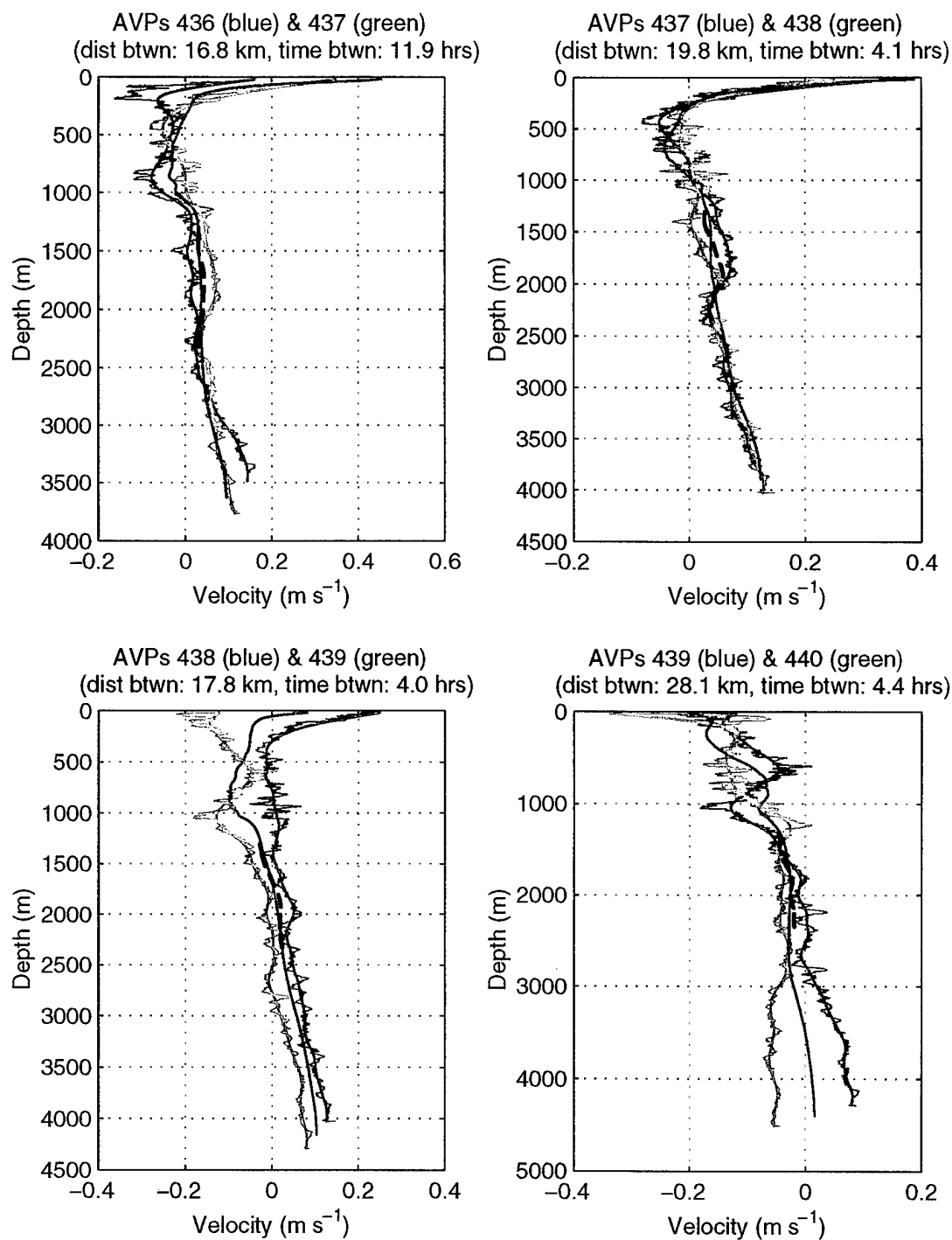
Figure 84: Absolute velocity profiles (blue and green) and referenced geostrophic profile from density data (red) for AVPs 445-440 on Section 1. Reference velocity is indicated by black dashed line in 1300-2400 m depth range. Jagged blue and green lines are 2-m absolute velocity data, smooth lines are filtered over 300 m.
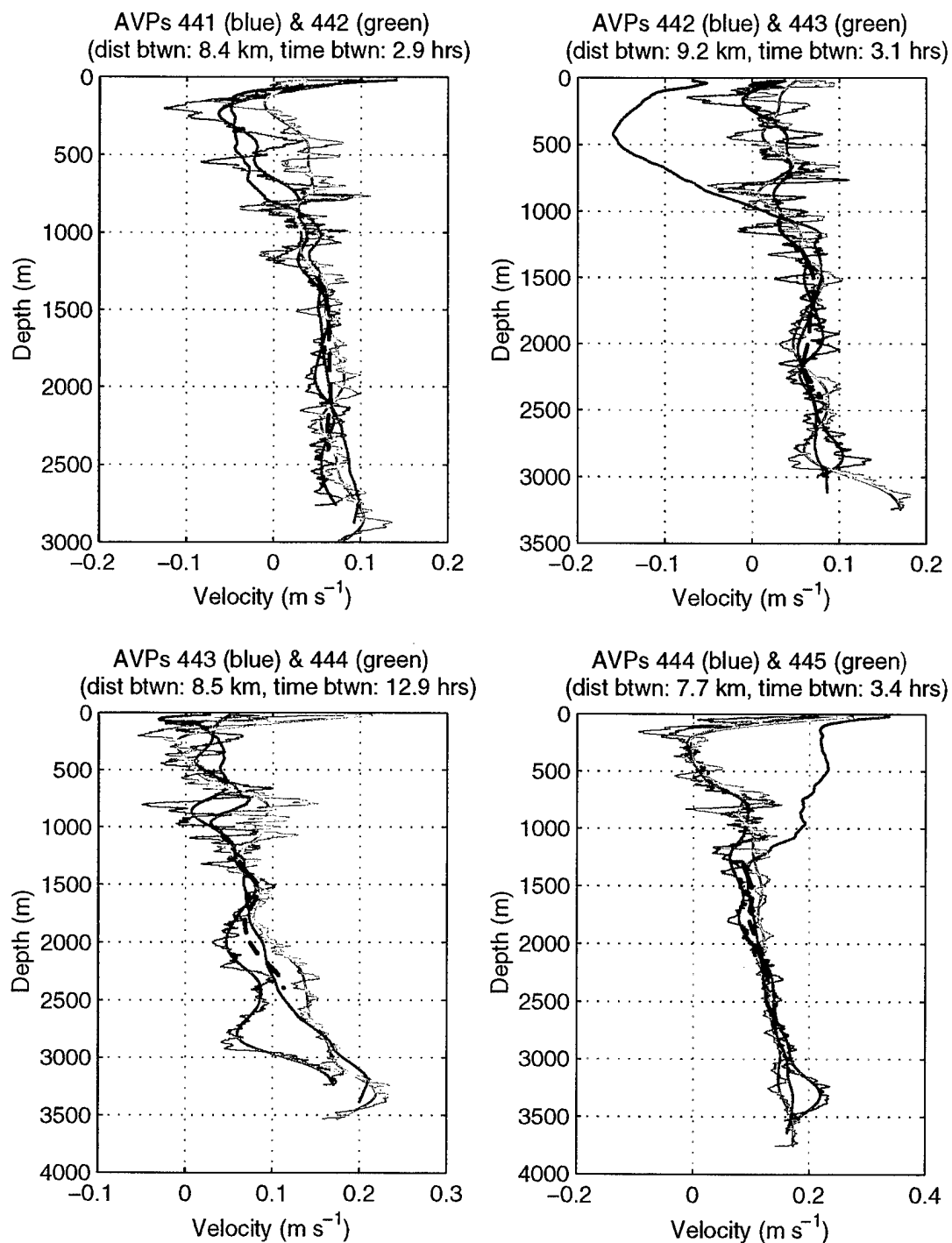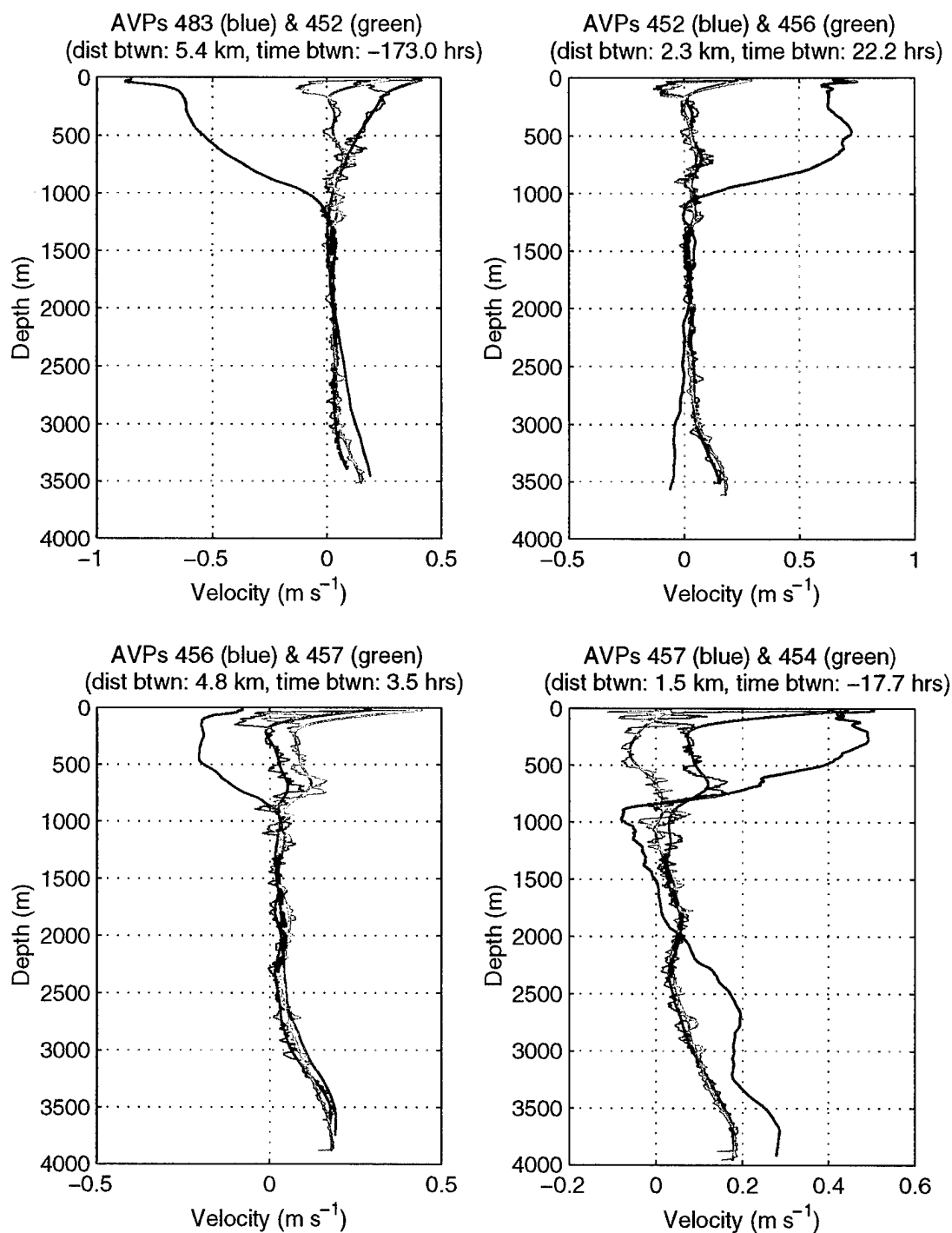
Figure 85: Absolute velocity profiles (blue and green) and referenced geostrophic profile from density data (red) for AVPs 483-454 on Section 2. Reference velocity is indicated by black dashed line in 1300-2400 m depth range. Jagged blue and green lines are 2-m absolute velocity data, smooth lines are filtered over 300 m.
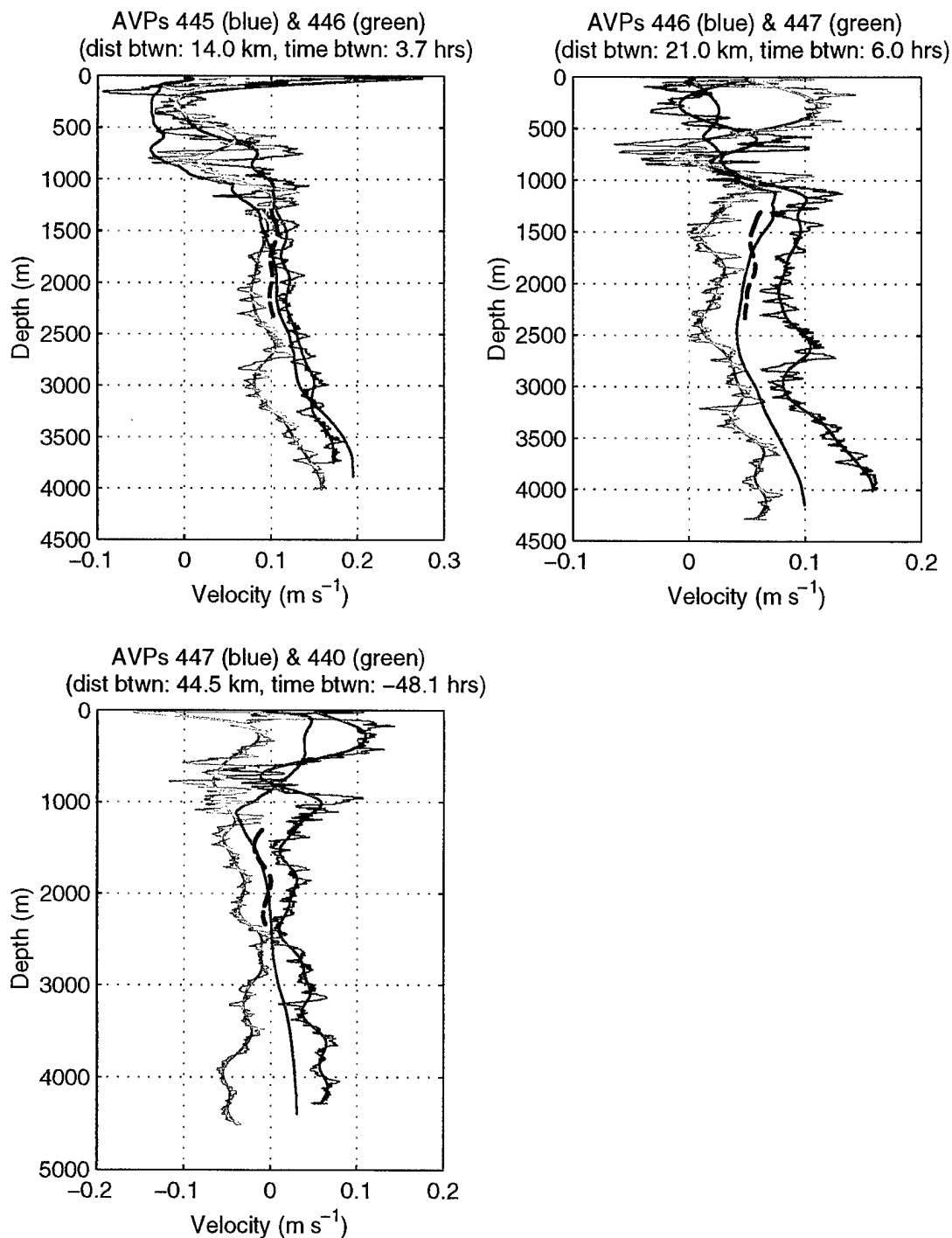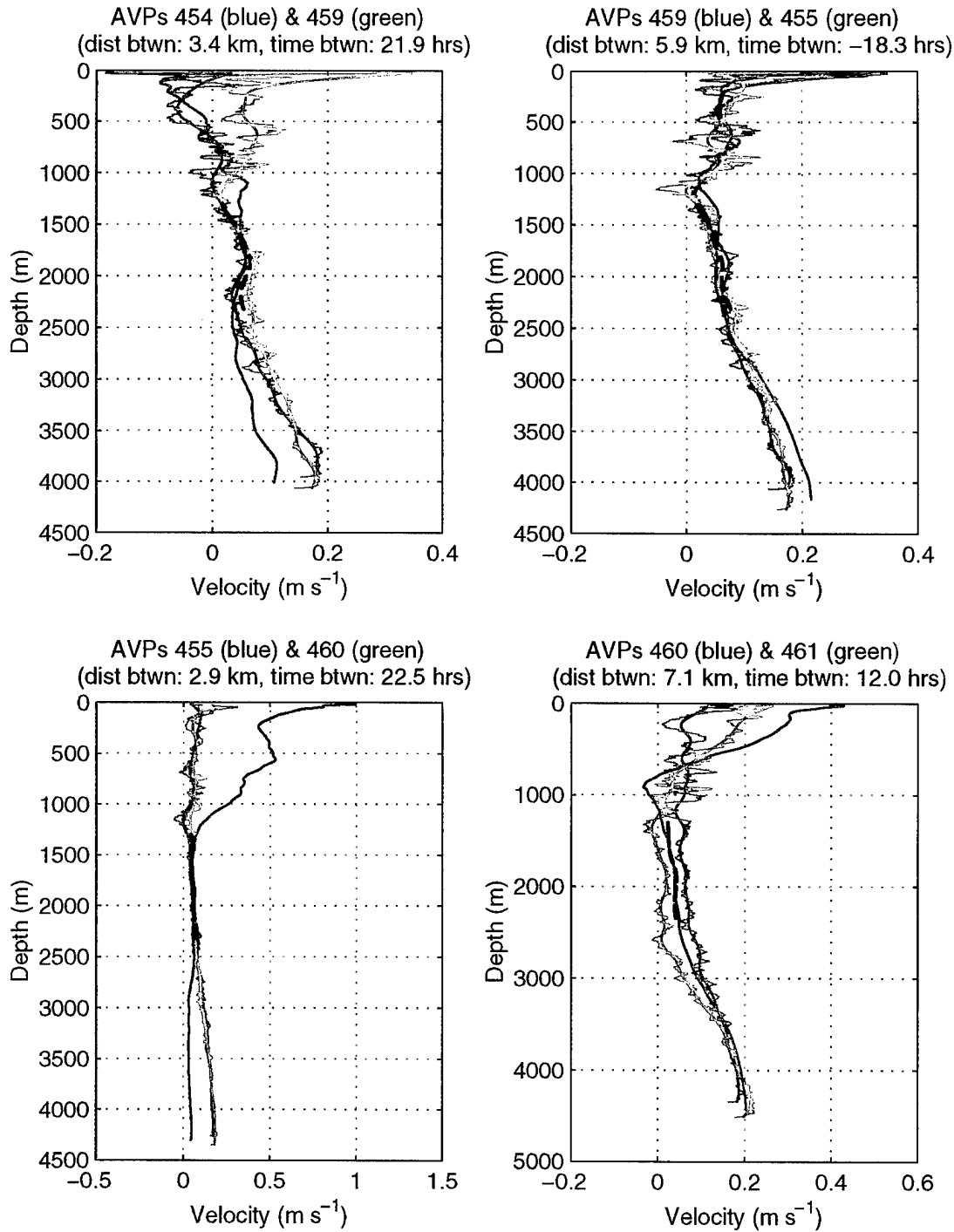
Figure 86: Absolute velocity profiles (blue and green) and referenced geostrophic profile from density data (red) for AVPs 454-461 on Section 2. Reference velocity is indicated by black dashed line in 1300-2400 m depth range. Jagged blue and green lines are 2-m absolute velocity data, smooth lines are filtered over 300 m.

Figure 87: Absolute velocity profiles (blue and green) and referenced geostrophic profile from density data (red) for AVPs 483-479 on Section 5. Reference velocity is indicated by black dashed line in 1300-2400 m depth range. Jagged blue and green lines are 2-m absolute velocity data, smooth lines are filtered over 300 m.
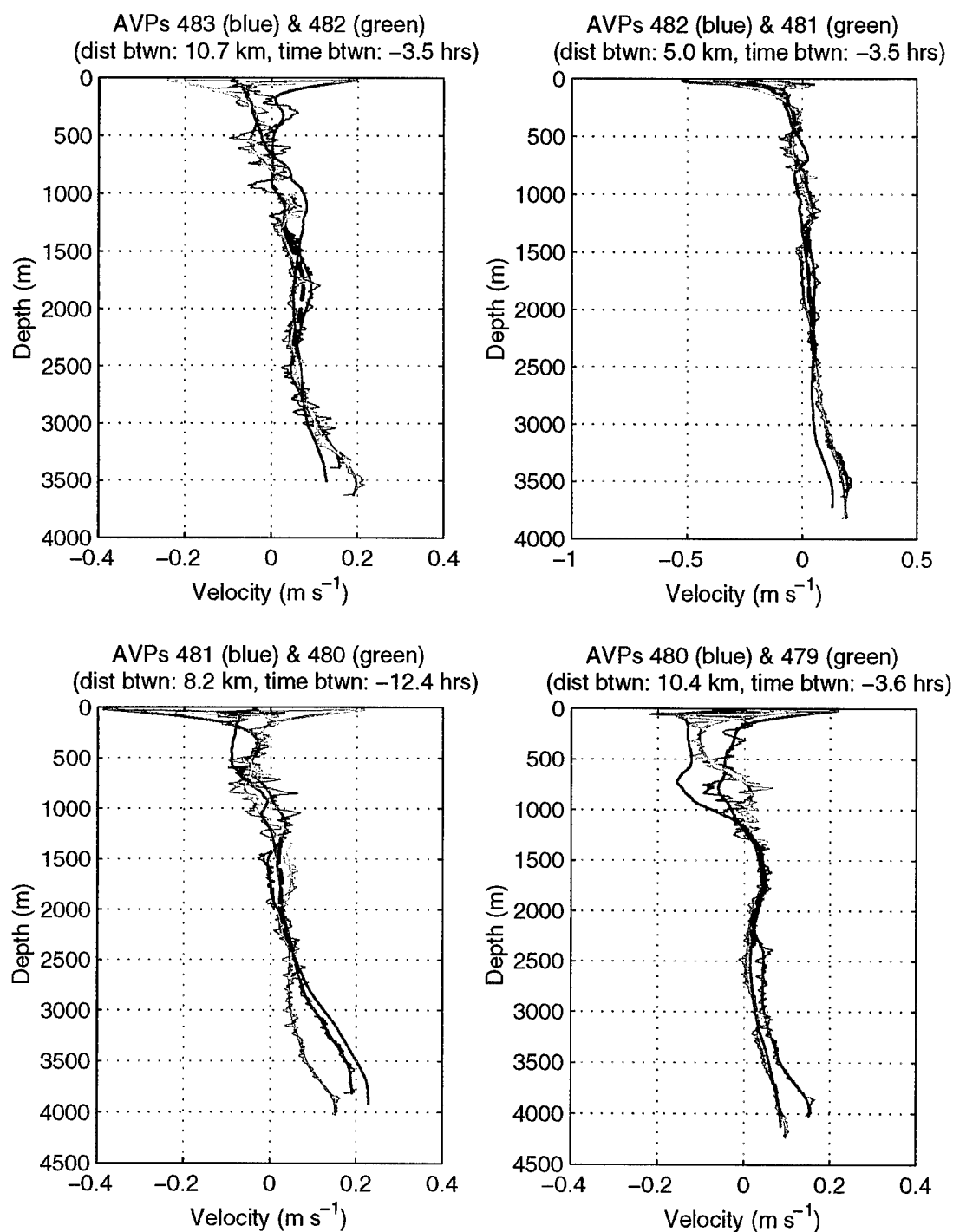
Vita

Frederick R. Stahr

University of Washington

1998

PERSONAL

Fritz Stahr
School of Oceanography
University of Washington
Box 357940
Seattle, Washington, 98195-7940
email: stahr@ocean.washington.edu
phone: 206-543-7886

EDUCATION

B.S., 1981, Stanford University, Stanford, California (Mechanical Engineering)

HONORS AND AWARDS

Office of Naval Research Fellowship recipient (1991)

PUBLICATIONS

Stahr F. R. and T. B. Sanford (1998) Transport and Bottom Boundary Layer Observations of the North Atlantic Deep Western Boundary Current at the Blake Outer Ridge. *Deep-Sea Research II, 46*, (2), in press.

Sanford T. B., M. D. Allison, J. H. Dunlap, T. Lehman, F. R. Stahr, and J. A. Verrall (1996) *R/V Endeavor 239: Cruise Report and Preliminary Results.* Technical Report APL-UW TR 9603, APL, University of Washington.

Davis, R. M., W. E. Humphrey, A. L. Kirschbaum, V. M. Patella, A. L. Shinn, and F. R. Stahr (1986) A new system for automated digital imaging and quantitative analysis of fundus images. Acta Ophthalmol. Proc. (XXV), pp.583-590.

EMPLOYMENT

Teaching Assistant (1994, 1996, present): School of Oceanography, University of Washington, Seattle, Washington.
Graduate and undergraduate classes in Physical Oceanography, Observations, and Fluid Dynamics.

Research Assistant (1994-98): Applied Physics Laboratory,
        University of Washington, Seattle, Washington.
    Assisted in re-design, fabrication and testing of Towed Transport Meter.
    Operated Sea-Bird 911+ CTD system on two month-long research cruises.
    Assisted in writing research proposals and reports.
    Designed and conducted experiment on sediment transport at Blake Outer Ridge.

Senior Mechanical Engineer (1990-91): Lightwave Electronics,
        Mountain View, California.
    Designed and built solid-state lasers for contract and commercial customers.

Mechanical Engineer and Engineering Services Manager (1981-89):
        Humphrey Instruments, San Leandro, California.
    Designed components and systems for various automated ophthalmic
    instrumentation (1981-84). Designed or directed design and fabrication of opto-
    mechanics for innovative retinal imaging and analysis system (1984-89).
    Managed drafting, documentation and machine shop personnel (1988-89).

PROFESSIONAL MEMBERSHIPS

American Geophysical Union
The Oceanography Society

REPORT DOCUMENTATION PAGE

Public reporting burden for this collection of information is estimated to average 1 hour per response, including the time for reviewing instructions, searching existing data sources, gathering and maintaining the data needed, and reviewing the collection of information. Send comments regarding this burden estimate or any other aspect of this collection of information, including suggestions for reducing this burden, to Washington Headquarters Services, Directorate for Information Operations and Reports, 1215 Jefferson Davis Highway, Suite 1204, Arlington, VA 22202-4302, and to the Office of Information and Regulatory Affairs, Office of Management and Budget, Washington, DC 20503.

1. AGENCY USE ONLY (Leave blank)	2. REPORT DATE November 1998	3. REPORT TYPE AND DATES COVERED Technical

4. TITLE AND SUBTITLE

Transport and Bottom Boundary Layer Observations of the North Atlantic Deep Western Boundary Current at the Blake Outer Ridge

5. FUNDING NUMBERS

NSF Grants OCE-9103013, OCE-9116245, and OCE-9503892

6. AUTHOR(S)

Frederick R. Stahr

7. PERFORMING ORGANIZATION NAME(S) AND ADDRESS(ES)

Applied Physics Laboratory
University of Washington
1013 NE 40th Street
Seattle, WA 98105-6698

8. PERFORMING ORGANIZATION REPORT NUMBER

APL-UW TR 9805

9. SPONSORING / MONITORING AGENCY NAME(S) AND ADDRESS(ES)

National Science Foundation
4201 Wilson Blvd.
Arlington, VA 22230

10. SPONSORING / MONITORING AGENCY REPORT NUMBER

11. SUPPLEMENTARY NOTES

12a. DISTRIBUTION / AVAILABILITY STATEMENT

Approved for public release; distribution is unlimited.

12b. DISTRIBUTION CODE

13. ABSTRACT (Maximum 200 words)

The North Atlantic Deep Western Boundary Current (DWBC) was surveyed at the Blake Outer Ridge over 14 days in July and August 1992 to determine its volume transport and to investigate its bottom boundary layer (BBL). This site was chosen because previous investigations showed a strong and bottom-intensified DWBC on the ridge's flanks with a thick BBL. The primary instrument used was the Absolute Velocity Profiler, a free-falling velocity and conductivity-temperature-depth device. Two sections across the width of the current produced volume transports of 17 ± 1 Sv and 18 ± 1 Sv (1 Sv $= 1 \times 10^6$ m^3 s^{-1}) for all water flowing equatorward below a potential temperature of 6°C. Transport values were derived using both absolute velocities and AVP-referenced geostrophic velocities and were the same within experimental uncertainty. Good agreement was found between these results and historical ones when both were similarly bounded and referenced. The mean of a nine-day time series of absolute velocity profiles was the same as the means of year-long current-meter records at three depths in the same location suggesting these observations reflect the mean DWBC. A turbulent planetary BBL was found everywhere under the current. Frictional bottom stress was mostly balanced by an along-stream change in the current's external potential energy evidenced by a change in depth of the velocity core along the ridge. The thickness of the bottom mixed layer (BML) (where density, nutrient, and suspended sediment concentrations asre vertically uniform) was asymmetrical across the current and up to five times thicker than the BBL. There was little velocity shear in the BML above the BBL and the across-slope density gradient was minimal. Observations suggest a combination of processes maintains the thick BML including large-scale turbulence, downwelling Ekman transport in the BBL and up-slope return flow in the BML, and buoyant convection into the BML.

14. SUBJECT TERMS

Deep Western Boundary Current, Bottom Boundary Layer, Blake Outer Ridge, Bottom Mixed Layer, Thermohaline Transport, North Atlantic

15. NUMBER OF PAGES

178

16. PRICE CODE

17. SECURITY CLASSIFICATION OF REPORT	18. SECURITY CLASSIFICATION OF THIS PAGE	19. SECURITY CLASSIFICATION OF ABSTRACT	20. LIMITATION OF ABSTRACT
Unclassified	Unclassified	Unclassified	SAR